



THE UNIVERSITY *of* EDINBURGH

This thesis has been submitted in fulfilment of the requirements for a postgraduate degree (e.g. PhD, MPhil, DClinPsychol) at the University of Edinburgh. Please note the following terms and conditions of use:

This work is protected by copyright and other intellectual property rights, which are retained by the thesis author, unless otherwise stated.

A copy can be downloaded for personal non-commercial research or study, without prior permission or charge.

This thesis cannot be reproduced or quoted extensively from without first obtaining permission in writing from the author.

The content must not be changed in any way or sold commercially in any format or medium without the formal permission of the author.

When referring to this work, full bibliographic details including the author, title, awarding institution and date of the thesis must be given.

NEURONAL CIRCUITS OF
EXPERIENCE-DEPENDENT PLASTICITY
IN THE PRIMARY VISUAL CORTEX

EVELYN DYLDA



Doctor of Philosophy
Center for Integrative Physiology
School of Biomedical Sciences
University of Edinburgh

2018

Supervisors:

Dr. Nathalie Rochefort
Prof. Ian Duguid

Evelyn Dylida: *Neuronal circuits of experience-dependent plasticity in the primary visual cortex*, © 2018

ABSTRACT

Our ability to learn relies on the potential of neuronal networks to change through experience. The primary visual cortex (V1) has become a popular system for studying how experience shapes cortical neuronal networks. Experience-dependent plasticity in V1 has been extensively studied in young animals, revealing that experiences in early postnatal life substantially shape neuronal activity in the developing cortex. In contrast, less is known about how experiences modify the representation of visual stimuli in the adult brain. In addition, adult experience-dependent plasticity remains largely unexplored in neurodevelopmental disorders.

To address this issue, we established a two-photon calcium imaging set-up, suitable for chronic imaging of neuronal activity in awake-behaving mice. We implemented protocols for the reliable expression of genetically encoded calcium indicators (GCaMP6), for the implantation of a chronic cranial window and for the analysis of chronic calcium imaging data. This approach enables us to monitor the activity of hundreds of neurons across days, and up to 4-5 weeks.

We used this technique to determine whether the daily exposure to high-contrast gratings would induce experience-dependent changes in V1 neuronal activity. We monitored the activity of putative excitatory neurons and of three non-overlapping populations of inhibitory interneurons in layer 2/3 of adult mice freely running on a cylindrical treadmill. We compared the results obtained from mice that were exposed daily to either a high-contrast grating or to a grey screen and characterized their neuronal response properties. Our results did not reveal significant differences in neuronal properties between these two groups, suggesting a lack of stimulus-specific plasticity in our experimental conditions. However, we did observe and characterize, in both groups, a wide range of activity changes in individual cells over time.

We finally applied the same method to investigate impairments in experience-dependent plasticity in a mouse model of intellectual disability (ID), caused by synaptic GTPase-activating protein (SynGAP) haploinsufficiency. SynGAP haploinsufficiency is a common *de novo* genetic cause of non-syndromic ID and is considered a Type1 risk for autism spectrum disorders. While the impact of *Syngap* gene mutations has been thoroughly studied at the molecular and cellular levels, neuronal network deficits *in vivo* remain largely unexplored. In this study, we compared *in vivo* neuronal activity before and after monocular deprivation in adult mutant mice and littermate controls. These results revealed differences in baseline network activity between both experimental groups. These impairments in cortical neuronal network activity may underlie sensory and cognitive deficits in patients with *Syngap* gene mutations.

LAY SUMMARY

Throughout our lives, we learn essential skills and gain new knowledge. This information is stored as memories in our brains. Our brains consist of billions of neurons making trillions of connections with each other. These connections are shaped by our experiences and these changes are referred to as experience-dependent plasticity. While experience-dependent plasticity has been extensively studied in young animals, less is known about how experiences shape neuronal networks in the adult brain.

A critical step to study such experience-dependent neuronal changes is to be able to monitor neuronal activity over time: before, during and after an experimentally controlled experience. To do so, we established an advanced imaging technique, named two-photon calcium imaging, allowing us to monitor the activity of individual neurons up to 700 μm deep into the brain tissue of awake animals. This technique enabled us to image the same population of neurons across several days and monitor their activity while we exposed the animal to new sensory experiences. We used the primary visual cortex (V_1), the first cortical area in the brain where visual information is processed, as a model system. We imaged the activity of neurons in V_1 in two groups of mice that were exposed to either a high-contrast grating or a grey screen over 5 consecutive days. We compared the results obtained from both groups and did not find differences in neuronal properties, suggesting a lack of stimulus-specific plasticity in our experimental conditions. However, we did observe and characterize, in both groups, a wide range of activity changes in individual neurons across days.

Additionally, we applied the same technique to investigate experience-dependent plasticity in a mouse model of intellectual disability, caused by a mutation of the gene encoding the synaptic GTPase-activating protein (*Syngap*). *Syngap* gene mutation causes intellectual disability co-occurring with autism spectrum disorders in humans. The impact of *Syngap* gene mutations has been thoroughly studied at the molecular and cellular levels, however, neuronal network deficits *in vivo* remain largely unexplored. We compared results obtained from adult mutant mice and littermate controls and found differences in baseline network activity. These impairments in cortical neuronal network activity may underlie sensory perception deficits that could by themselves alter cognitive abilities in patients with *Syngap* gene mutations.

ACKNOWLEDGEMENTS

I would like to express my sincere thanks to my supervisor Dr. Nathalie Rochefort for the continuous support, as well as for her patience, guidance and encouragement throughout the past four years.

I would also like to thank the rest of my thesis committee: Prof. Ian Duguid and Prof. Peter Kind, for their valuable comments and discussions.

My sincere thanks also goes to Dr. Janelle MP Pakan. Without her continuous support, it would not have been possible to conduct this research.

I also would like to thank my fellow labmates of the Rochefort and Duguid labs for the stimulating discussions, feedback and help.

I also would like to specifically thank Dr. Daumante Suminaite and Gintas Sasnauskas for sharing their home with me whenever I lost mine.

Last but not least, I would like to thank my family, especially my parents, and friends for supporting me throughout this thesis and life in general.

DECLARATION

I declare that this thesis was composed by myself, that the work contained herein is my own except where explicitly stated otherwise in the text, and that this work has not been submitted for any other degree or professional qualification except as specified.

Edinburgh, 05.01.2018

Evelyn Dylida

CONTENTS

Acronyms	xiv
1 GENERAL INTRODUCTION	1
1.1 Why studying neuronal plasticity in mouse V ₁ ?	2
1.2 Anatomy and function of mouse primary visual cortex	4
1.2.1 Organization of the mouse primary visual cortex	4
1.2.2 Neuronal subtypes in mouse V ₁	7
1.2.3 Neuronal activity in mouse V ₁ is modulated by behavioral state	10
1.2.4 Higher visual cortical areas and top-down projections to mouse V ₁	11
1.3 Neuronal plasticity in adult mouse V ₁	12
1.3.1 Functional plasticity	14
1.3.2 Structural plasticity	14
1.4 Experimental paradigms for inducing plasticity in V ₁ of adult mice . .	15
1.4.1 Plasticity induced by retinal lesion and enucleation	15
1.4.2 Plasticity induced by monocular deprivation	16
1.4.3 Plasticity induced by passive viewing protocols	18
1.4.4 Plasticity induced by active viewing protocols (reward or fear experience)	19
1.5 Thesis aims	21
2 IMPLEMENTATION OF A TWO-PHOTON CALCIUM IMAGING SET-UP FOR CHRONIC <i>in-vivo</i> RECORDINGS IN AWAKE BEHAVING MICE	22
2.1 Introduction	22
2.1.1 Genetically encoded fluorescent calcium indicators	23
2.1.2 Principles of two-photon imaging	24
2.2 Establishing a two-photon imaging set-up for imaging in awake mice .	26
2.2.1 Visual stimulation without light contamination	29
2.2.2 Monitoring movement activity	30
2.3 Establishing a reliable cranial window and neuronal labeling	30
2.3.1 Head-plate design	31
2.3.2 Sterile surgery: craniotomy and AAVs injection	31
2.3.3 Labelling of cell-type specific neuronal subpopulations	36
2.4 Establishing tools to analyse two-photon calcium imaging data	36
2.4.1 Correcting for motion artefacts	37
2.4.2 Image segmentation into regions of interest	37
2.4.3 Correction for neuropil contamination and fluorescence signal extraction	38
2.4.4 Analysis of somatic fluorescence changes across days	39

2.5	Discussion	42
2.5.1	A two-photon imaging set-up for chronic <i>in vivo</i> calcium imaging in awake-behaving mice	42
2.5.2	Analysing two-photon calcium imaging data	44
3	BEHAVIORAL STATE MODULATES EXCITATORY AND INHIBITORY NEURONAL ACTIVITY IN THE MOUSE PRIMARY VISUAL CORTEX	48
3.1	Introduction	48
3.2	Material and Methods	49
3.3	Personal contribution disclaimer	50
3.4	Pakan et al. 2016	50
3.5	Discussion	69
4	EFFECT OF REPETITIVE PASSIVE VIEWING OF VISUAL STIMULI ON LAYER 2/3 NEURONAL ACTIVITY IN MOUSE PRIMARY VISUAL CORTEX	72
4.1	Introduction	72
4.2	Material and Methods	73
4.2.1	Animals	74
4.2.2	Habituation of mice to the imaging setup	75
4.2.3	Chronic two-photon imaging protocol	75
4.2.4	Data analysis	76
4.3	Results	77
4.3.1	Similar neuronal response properties of V1 putative excitatory neurons in naive mice from the familiar and control experimental groups	77
4.3.2	The response properties of V1 putative excitatory neurons after the daily exposure to a defined grating are stable on the population level	79
4.3.3	Heterogeneous changes in neuronal response properties at the single cell level	92
4.3.4	Behavioural state-specific modulation of neuronal activity across days	103
4.3.5	Stability and plasticity of interneuron activity across days	108
4.4	Discussion	111
4.4.1	Repetitive passive exposure to sensory stimuli: Adaptation vs Potentiation	112
4.4.2	Experimental limitations	114
4.4.3	Future prospects	115
5	NEURONAL RESPONSE PROPERTIES IN THE ADULT PRIMARY VISUAL CORTEX OF A MOUSE MODEL OF INTELLECTUAL DISABILITY	117
5.1	Introduction	117
5.1.1	SynGAP expression and function	118
5.1.2	Behavioral impairments in SynGAP ^{+/-} mice	119

5.1.3	Cellular impairments in SynGAP ^{+/-} mice	120
5.2	Material and Methods	121
5.2.1	Animals	122
5.2.2	Habituation of mice to the imaging setup	122
5.2.3	Monocular deprivation	122
5.2.4	Chronic two-photon imaging protocol	123
5.2.5	Data analysis	123
5.3	Personal contribution disclaimer	124
5.4	Results	124
5.4.1	Behaviour correlates of SynGAP ^{+/-} mutation	124
5.4.2	Comparison of V ₁ neuronal activity between SynGAP ^{+/-} mice and WT littermates	125
5.4.3	Effect of monocular deprivation on V ₁ neuronal activity in adult SynGAP ^{+/-} mice and WT littermates	131
5.5	Discussion	139
5.5.1	Lower visually evoked activity but higher orientation tuning in V ₁ of SynGAP ^{+/-} mice	139
5.5.2	Behavioural correlates of SynGAP ^{+/-} mutation	140
5.5.3	Heterogeneous changes in monocular responses after seven days of MD in adult SynGAP ^{+/-} mice and WT littermates	141
6	GENERAL DISCUSSION	143
A	APPENDIX	147
A.1	Solutions	147
A.2	Keemink et al. 2018	148
	BIBLIOGRAPHY	160

LIST OF FIGURES

Figure 1.1	Primary visual cortex of mice	5
Figure 1.2	Schematic of the connectivity between interneurons	8
Figure 2.1	Two-photon calcium imaging experimental workflow	23
Figure 2.2	GCaMP6 activation	25
Figure 2.3	Two-photon excitation	25
Figure 2.4	Schemata of the two-photon imaging set-up	28
Figure 2.5	Head-plate design	32
Figure 2.6	Cranial window surgery and head-plate implantation	35
Figure 4.1	Experimental timeline: passive viewing paradigm	74
Figure 4.2	Visual stimulation protocol passive viewing paradigm	76
Figure 4.3	Baseline response properties of putative excitatory neurons on day 1	78
Figure 4.4	Percentage of visually responsive neurons per day	80
Figure 4.5	Stability of population visual responses across days during stationary periods (putative excitatory neurons)	81
Figure 4.6	Individual neuronal responses across days during stationary periods (putative excitatory neurons)	82
Figure 4.7	Example traces of a orientation selective neuron 1	84
Figure 4.8	Example traces of a orientation selective neuron 2	85
Figure 4.9	Response properties of individual neurons across days	86
Figure 4.10	Average population response properties across days	87
Figure 4.11	Percentage of orientation selective neurons per day	88
Figure 4.12	Population response properties across days of all neurons orientation selective on day 1	90
Figure 4.13	Familiar group: population response properties across days of all neurons with a preferred orientation different from the familiar grating on day 1	91
Figure 4.14	Heterogeneous changes in response amplitude across days: familiar group	93
Figure 4.15	Heterogeneous changes in response amplitude across days: control group	94
Figure 4.16	Difference in response amplitude between day 1 and day 5, and day 5 and 6 of putative excitatory neurons	95
Figure 4.17	Changes in OSI magnitude of individual putative excitatory neurons across days	97

Figure 4.18	Average OSI magnitude across days of all neurons orientation selective on at least one day	98
Figure 4.19	Percentage of neurons orientation selective across days	98
Figure 4.20	Average $\Delta F/F_0$ in relation to OSI of individual putative excitatory neurons across days	99
Figure 4.21	Average $\Delta F/F_0$ across days of all neurons orientation selective on at least one day	100
Figure 4.22	Changes in preferred orientation across days	102
Figure 4.23	Amount of running per animal across days	103
Figure 4.24	Stability of population visual responses across days during locomotion periods (putative excitatory neurons)	104
Figure 4.25	Locomotion modulation index across days (putative excitatory neurons), familiar group	105
Figure 4.26	Locomotion modulation index across days (putative excitatory neurons), control group	106
Figure 4.27	Correlation of the total amount of locomotion during the presentation of the familiar stimulus and the amplitude of neuronal responses	107
Figure 4.28	Example traces of inhibitory interneurons	109
Figure 4.29	Changes in $\Delta F/F_0$ during locomotion and stationary periods of all interneurons across days	110
Figure 5.1	Signaling mechanism upon phosphorylation of SynGAP	119
Figure 5.2	Example field of view and example $\Delta F/F_0$ traces before and after MD	125
Figure 5.3	Proportion of time spent running in both experimental groups (SynGAP ^{+/-} mice and WT littermates)	126
Figure 5.4	Number of visually responsive neurons recorded in SynGAP ^{+/-} mice and WT littermates on day 1	127
Figure 5.5	Mean neuronal activity of visually responsive neurons of SynGAP ^{+/-} mice and WT littermates measured on day 1	127
Figure 5.6	Example traces of orientation selective neurons	128
Figure 5.7	OSI and SER of V1 neurons in SynGAP ^{+/-} mice and WT littermates measured on day 1	129
Figure 5.8	LMI of all active neurons of SynGAP ^{+/-} mice and WT littermates measured on day 1	130
Figure 5.9	Changes in number of visually responsive neurons across days in SynGAP ^{+/-} mice and WT littermates during visual stimulation	132
Figure 5.10	Average neuronal activity of SynGAP ^{+/-} mice and WT littermates across days during darkness and visual stimulation	133
Figure 5.11	Changes in LMI across days of SynGAP ^{+/-} mice and WT littermates during visual stimulation	134

Figure 5.12	Changes in fluorescence before and after MD of SynGAP ^{+/-} mice and WT littermates during visual stimulation of the left eye	136
Figure 5.13	Changes in fluorescence before and after MD of SynGAP ^{+/-} mice and WT littermates during visual stimulation of the right eye	137
Figure 5.14	Changes in ODI across days in SynGAP ^{+/-} mice and WT littermates during visual stimulation	138

LIST OF TABLES

Table 1	Artificial cerebrospinal fluid	147
Table 2	Paraformaldehyde solution (4 %)	147

ACRONYMS

AAV	Adeno-associated virus
ACC	Anterior cingulate cortex
ACSF	Artificial cerebral spinal fluid
AMPA	Alpha-amino-3-hydroxy-5-methyl-4-isoxazolepropionic acid
ANOVA	Analysis of variance
ARC	Activity-regulated cytoskeleton-associated protein
ASD	Autism spectrum disorders
AP	Action potential
CaMKII	Ca ²⁺ /calmodulin-dependent protein kinase II
CLSM	Confocal laser scanning microscopy
cpd	Cycles per degree
dLGN	Dorsal lateral geniculate nucleus
DREADDs	Designer receptor exclusively activated by designer drugs
EE	Enriched environment
ERK ₁	Extracellular signal-regulated kinases-1
ERK ₂	Extracellular signal-regulated kinases-2
FISSA	Fast image signal-source separation analysis
fMRI	Functional magnetic resonance imaging
FOV	Field of view
FXS	Fragile X Syndrome
GABA	gamma-Aminobutyric acid
GaAsP	Gallium arsenide phosphide
GECI	Genetically encoded calcium indicator
Hz	Hertz

ID	Intellectual disability
IQ	Intelligence quotient
LC	Locus coeruleus
LFP	Local field potential
LMI	Locomotion modulation index
LOTOS	Low-power temporal oversampling
LSM	Laser-scanning microscopy
LTD	Long-term depression
LTP	Long-term potentiation
M ₂	Secondary motor cortex
MAP	Mitogen-activated protein
MD	Monocular deprivation
MLR	Mesencephalic locomotor region
NA	Numerical aperture
NG	Neurogliaform
NMDA	N-methyl-D-aspartate
NMF	Non-negative matrix factorization
ODI	Ocular dominance index
OSI	Orientation selectivity index
P	Postnatal day
PFA	Paraformaldehyde
PMT	Photomultiplier tube
PSD	Post-synaptic density
PV	Parvalbumin
RasGAP	RasGTPase activating protein
ROI	Regions of interest
RSC	Retrosplenial cortex

S ₁	Primary somatosensory cortex
SER	Stimulus evoked response
SNR	Signal-to-noise ratio
SRP	Stimulus-specific response potentiation
SST	Somatostatin
STDP	Spike-timing dependent plasticity
SynGAP	Synaptic GTPase-activating protein
tdms	Technical data management streaming
TPLSM	Two-photon laser scanning microscopy
V ₁	Primary visual cortex
V ₂	Secondary visual cortex
VEP	Visually evoked potential
VIP	Vasoactive intestinal polypeptide
VR	Virtual reality
WT	Wild-type

GENERAL INTRODUCTION

Neuronal plasticity is the process by which neuronal circuits in the brain implement new structural or functional states. This process can be induced by experience and is believed to be an underlying mechanism for learning and memory formation. Impairments in neuronal plasticity processes often lead to severe malfunctioning of the brain. Various diseases are associated with deficits in neuronal plasticity, such as neurodegenerative diseases (e.g. Alzheimer's disease) and neurodevelopmental diseases (e.g. autism spectrum disorders). Therefore, revealing the underlying processes of neuronal plasticity is an important step towards the understanding and potential treatment of neurodegenerative and neurodevelopmental disorders. In this thesis, we use the primary visual cortex of the mouse brain as a model system to investigate these underlying processes.

Sensory areas are prime areas to study neuronal plasticity because they have been shown to undergo structural and functional changes with sensory experience or after experimentally controlled alterations to sensory systems. Among the sensory areas, the mammalian primary visual cortex (V1) has been extensively studied and hence a lot of knowledge has been gathered about its anatomical and functional organization. The main advantages of V1 as an experimental model to study neuronal responses and plasticity include its accessibility for *in vivo* recordings as well as the precise control of sensory stimuli. Due to its dorsal-posterior cortical location, most parts of V1 are easily experimentally accessible for electrophysiological and imaging experiments. Visual experiences are easily controlled by presenting defined visual stimuli on a computer screen in front of the animal (Niell and Stryker, 2008, Rochefort et al., 2011, Rose et al., 2016). Recent experiments even create whole virtual reality environments (Keller, Bonhoeffer, and Hübener, 2012, Poort et al., 2015, Leinweber et al., 2017).

Since the first experiments by Hubel and Wiesel in the 1960's in cats, the neuronal response properties of neurons in V1 to visual stimulation have been well characterized, including the size and shape of the neuronal receptive fields and their selectivity to the orientation and direction of visual stimuli. More recently, the properties of V1 neurons have been characterized in rodents, including the retinotopic organization (Drager, 1975, Hofer et al., 2006) as well as the precise cytoarchitectural organization (Kerlin et al., 2010, Rudy et al., 2011, Jiang et al., 2015) and most recently, the cell type specific microcircuitry within this cortical region (Pfeffer et al., 2013, Fu et al., 2015). Therefore, V1 has become a popular area to study experience-dependent organizational and functional changes of neuronal circuits induced by alterations of

the environment or sensory inputs (i.e. experience-dependent neuronal plasticity resulting from repetitive sensory experience or sensory deprivation). Overall, the well characterized neuronal anatomy as well as knowledge about the functional properties, in combination with the accessibility for *in vivo* recordings and easy control of sensory input, make V1 a popular model system to investigate experience-dependent plasticity.

After a brief overview of the mouse visual system, this introduction reviews paradigms that are used to induce neuronal plasticity in the primary visual cortex of adult mice as well as current knowledge about neuronal plasticity mechanisms in V1. Finally, the thesis aims are presented.

1.1 WHY STUDYING NEURONAL PLASTICITY IN MOUSE V1 ?

Historically, many of the fundamental studies investigating neuronal plasticity and network function in V1 have been performed in cats (Hubel and Wiesel, 1962, Wiesel and Hubel, 1963a, Blakemore and Sluyters, 1975, Bonhoeffer and Grinvald, 1991) and non-human primates (Hubel and Wiesel, 1968, Motter, 1993, Treue and Martínez Trujillo, 1999, Wang, Sporns, and Burkhalter, 2012). However, in recent years mice have become a popular model organism to study plasticity and network function. This is because mice as model species has several important advantages that are instrumental to the understanding of neuronal circuits. One might assume that the difference in absolute brain size between the mouse and human brain would be a significant disadvantage to using mouse models. However, the small absolute size of the mouse brain enables the monitoring of single cell neuronal activity across large spatial scales simultaneously, even across several cortical areas (Stirman et al., 2014, Smith et al., 2017). This is a great advantage as it enables the investigation of interactions between primary sensory areas and higher cortical areas, a process involved in neuronal plasticity (Makino and Komiyama, 2015, Fiser et al., 2016).

Considering that mice do not rely on their visual senses to the same degree as higher mammals, the mouse visual cortex shows striking similarities to the cortex of higher mammals, such as cats and non-human primates. For instance, the cytoarchitecture of mouse V1 and higher mammal cortices both consist of 6 layers, show a retinotopic organization and are comprised of a mixture of several excitatory and inhibitory neuronal subtypes (Niell and Stryker, 2008). Furthermore, mouse V1 performs similar computational processing to that which occurs in higher mammals, such as orientation and direction selectivity, as well as a similar spatial structure of receptive fields (Niell and Stryker, 2008, Van Hooser, 2007). Additionally, characteristics such as contrast invariant tuning and selectivity for stimulus features, are preserved between mice and humans (Niell and Stryker, 2008). However, regardless of the numerous similarities between mouse V1 and higher mammalian visual systems, there are also some differences. For example, higher order mammals such as cats and non-human

primates have orientation maps (Bonhoeffer and Grinvald, 1991), while mouse V1 is arranged randomly in a "salt-and-pepper" organization (Ohki et al., 2005). Overall, the similarities of mouse V1 with higher mammal primary visual areas are striking and outnumber the differences. Thus, mouse V1 can be used to study basic neuronal processes in V1. However, due to the differences between species, care still needs to be taken when generalising findings to other species (Huberman and Niell, 2011).

Another clear advantage of using mice is the availability and extent of genetic tools. Genetic tools enable the identification of neuronal subtypes, such as specific inhibitory interneuron subclasses, as well as the mapping of neuronal connections, for instance by using Cre-driver transgenic mouse lines. Cre-driver mouse lines express Cre-recombinase in specific neuronal subtypes, hence the expression of proteins can be targeted to specific neuronal subclasses using floxed-stop reporter alleles (Atasoy et al., 2008, O'Connor, Huber, and Svoboda, 2009). This is essential to understand neuronal circuits, since it enables the investigation of the direct contribution of different neuronal subtypes to behavioural output. Furthermore, genetic tools enable the long-term monitoring (from days to weeks) of neuronal activity of large populations of neurons using genetically encoded calcium indicators (GECIs) (Chen et al., 2013). Finally, to fully understand the function and importance of an identified neuronal circuit during behaviour it is important to manipulate the circuit, by activating or deactivating certain parts, and observing the resulting effects on specific elements of behaviour. This is possible using, for example, optogenetic tools (Luo, Callaway, and Svoboda, 2008, Atasoy et al., 2008, O'Connor, Huber, and Svoboda, 2009) or DRE-ADDs (designer receptor exclusively activated by designer drugs) (Armbruster et al., 2007, Smith et al., 2016, Hamm and Yuste, 2016). Ultimately, the human and mouse genomes are very similar (Waterston et al., 2002), and since it is possible to modify mouse genes it is possible to model human diseases in mice.

Another experimental advantage of mice is that multiple head fixed behaviour paradigms have been developed for investigating neuronal activity in awake behaving mice (O'Connor, Huber, and Svoboda, 2009). In contrast to cats or non-human primates, it is possible to place mice on spherical treadmills, which opens a whole new field of studies, such as spatial learning in virtual reality (Dombeck et al., 2007) or behavioural state dependent encoding (Niell and Stryker, 2010).

Finally, practically speaking, mice are small and therefore it is possible to rear numerous mice in a relatively small space. Maintenance expenses, such as food, bedding and cleaning, are cheap compared to those required for higher mammals. Additionally, mice have a high birthrate (approximately one litter every four weeks), which is beneficial for breeding new genetic lines (Huberman and Niell, 2011).

1.2 ANATOMY AND FUNCTION OF MOUSE PRIMARY VISUAL CORTEX

As in all mammals, in mice visual information is detected by photoreceptors located in the retina of the eyes and is then conveyed through the optic nerve to several subcortical and cortical areas (Jeon, Strettoi, and Masland, 1998, Masland, 2001, Huberman and Niell, 2011). One prominent pathway is the connection from the eyes to the dorsal lateral geniculate nucleus (dLGN) and further to the visual cortex. This pathway is very well conserved across species (human (Shapley, 1990), non-human primates (Garey and Powell, 2017), cats (Garey and Powell, 2017), rat (Rubio-Garrido et al., 2009), mouse (Petreanu et al., 2009)).

Neurons of the dLGN, similar to retinal ganglion cells, have centre surround receptive fields and some have recently been shown to be direction selective (Huberman et al., 2009). The largest region of mouse dLGN receives inputs from the contralateral eye and a small portion receives inputs from the ipsilateral eye (Priebe and McGee, 2014). Other subcortical structures besides the dLGN that receive input from the retinal ganglion cells are, for example, the superior colliculus (which control saccadic eye movements) and the midbrain (which controls pupillary reflexes) (Huberman et al., 2008). The dLGN projects mainly to the primary visual cortex (V1) (Petreanu et al., 2009, Constantinople and Bruno, 2013).

1.2.1 *Organization of the mouse primary visual cortex*

The mouse primary visual cortex consists of six layers (Figure 1.1 B). Visual information from the dLGN arrives mainly at layer 4 with extensive inputs also reaching layer 2/3 (Morgenstern, Bourg, and Petreanu, 2016). A few connections between dLGN and V1 neurons are made in layer 1 (Kondo, Yoshida, and Ohki, 2016), 5 and layer 6 of V1 (Garey and Powell, 2017, Petreanu et al., 2009, Constantinople and Bruno, 2013). Afferent inputs from higher order cortical areas to V1 generally avoid layer 4 and mainly target layer 1, 5 and 6 (for review see: Harris and Mrsic-Flogel, 2013, Niell, 2015).

V1 exhibits a canonical circuit for extracting image features. This microcircuit is formed by neurons of different layers that are intracortically connected. Layer 4 neurons send afferent connections to all other layers but most strongly to layer 2/3, and receive only a small amount of efferent input from other layers of V1. Layer 2/3 neurons project to higher order cortical areas and locally to layer 5. Layer 5 neurons also project to higher cortical areas and additionally back to layer 2/3. Finally, layer 6 neurons project to the dLGN and make strong connections with layer 4 inhibitory interneurons (for review see: Harris and Mrsic-Flogel, 2013, Hübener, 2003).

Mouse V1 is divided into a binocular and a monocular area. The binocular area is in the lateral part of V1 and rather small (approximately $\frac{1}{3}$ of V1) because the eyes of mice are located on either side of the mouse head and thus the overlapping binocular

field of view is narrow. The monocular area of V₁ is much bigger and receives input only from the contralateral eye (Drager, 1975) (Figure 1.1 A). Additionally, mouse V₁ has a retinotopic organization; meaning that the mapping of the visual field to the retina is preserved throughout the visual pathway (Drager, 1975). Retinotopic mapping experiments have shown that neurons in the medial area of V₁ respond to stimuli presented in the lateral visual field and neurons in the lateral area of V₁ respond to stimuli presented in the medial visual field. Similarly, neurons in the anterior area of V₁ respond to stimuli presented in the lower visual field and neurons in the posterior area of V₁ respond to stimuli presented in the higher visual field (Schütt, Bonhoeffer, and Hübener, 2002). The formation and maintenance of the retinotopic organization, as well as the monocular and binocular area of V₁, is experience-dependent and is disturbed in mice where V₁ input from both eyes is abolished (for example when one eye is removed) during development (Faguet et al., 2008). Hence, V₁ is often used as model system to investigate changes in anatomical organization induced by experience (Gordon and Stryker, 1996, Faguet et al., 2008).

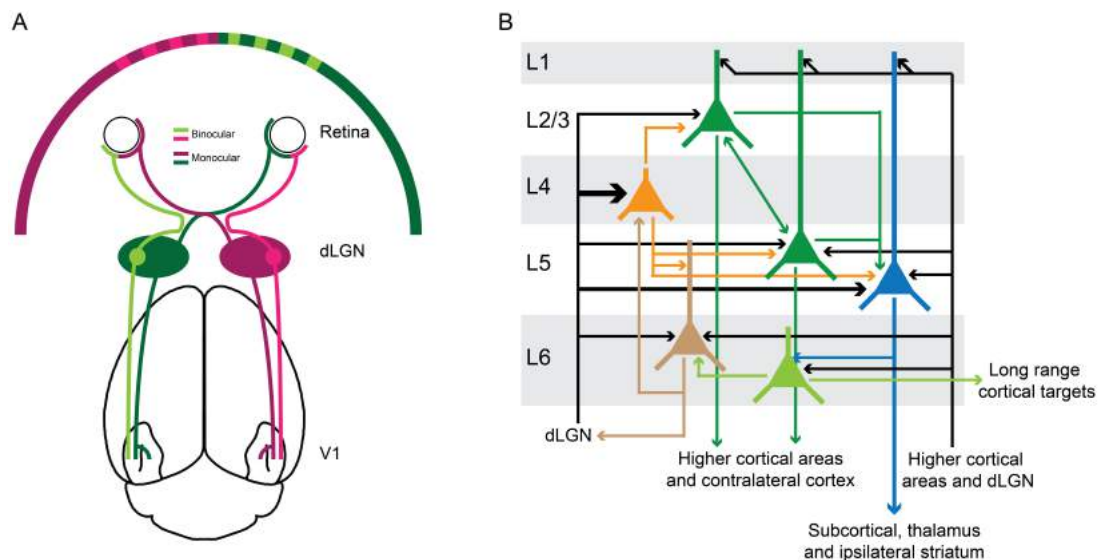


Figure 1.1: Primary visual cortex of mice. A) Schemata of the connections between the eyes and mouse V₁. The lateral binocular area of V₁ receives inputs from both eyes. Medial V₁ receives inputs only from the contralateral eye (monocular area). Monocular and binocular information is separated in the dLGN. B) Schemata showing layer specific connections, as well as inputs and outputs of V₁. Thickness of arrows indicates strength of input. Adapted from Harris and Mrsic-Flogel, 2013.

Unlike in the retina where cells are organized in center-surround receptive fields and thus respond best to round stimuli, neurons in V₁ respond best to elongated lines or bars. Neurons preferentially responding to elongated stimuli are separated into two main groups: simple and complex cells. Simple cells are excited by bars of a specific orientations in a specific position within their receptive field. V₁ rectilinear

fields consist of an excitatory inner zone that is flanked by two inhibitory outer rectilinear fields. These rectilinear fields can be build up from circular center-surround receptive fields as they exist in the retina. Multiple simple cells give inputs to one complex cell. Hence, complex cells have no clearly defined excitatory or inhibitory zones. Therefore, only the orientation of the stimulus is important, but not the position of the stimulus within the receptive field (Drager, 1975, Metin, Godement, and Imbert, 2000, Sohya et al., 2007).

Orientation selectivity in V₁ was first described in cats by Hubel and Wiesel in 1962 and since then multiple studies have found orientation selective neurons in V₁ of mice (Drager, 1975, Niell and Stryker, 2008). Approximately 40 % of neurons in mouse V₁ are orientation selective (Hübener, 2003) and basic feature selectivity seems to be already established before eye opening (Rocheffort et al., 2011). However, orientation selectivity also depends on experience to fully mature. For instance, juvenile rodents have a smaller number of orientation selective neurons compared to adults (Fagiolini et al., 1994, Fagiolini et al., 2003). Mice exposed to only one specific oriented grating during development were shown to express an overrepresentation of layer 2/3 neurons preferentially responding to the experienced orientation (Kreile, Bonhoeffer, and Hübener, 2011). Additionally, the number of neurons orientation selective but not direction selective increases with development (Rocheffort et al., 2011). Furthermore, neuronal connections between neurons are refined after eye opening through visual experience (Ko et al., 2011). It has been shown that neurons preferentially responding to the same features of the visual scene (e.g. same orientated edge) are more likely connected to each other (Ko et al., 2011). These recurrent connections are believed to amplify cortical responses, as well as to prolong the response to a visual stimulus (Lien and Scanziani, 2013, Li et al., 2013). However, there are also connections between neurons which do not respond preferentially to the same features. These non-feature specific connections are believed to occur predominantly between neurons responding to feature combinations that are of behavioural importance and thus enable the amplification of cortical responses to a combination of diverse visual inputs (e.g. different orientations) (Harris and Mrsic-Flogel, 2013).

Unlike in other species (e.g. cats (Bonhoeffer and Grinvald, 1991) or monkeys (Hubel, Wiesel, and Stryker, 1978)), feature selectivity, or more precisely orientation selectivity, in mice is not organized into columns. In mice, orientation selective neurons were shown to be organized in a random "salt-and-pepper" like manner (Ohki et al., 2005). The lack of orientation columns in mice could be explained by a reduced amount of lateral connectivity. However, a recent study described mouse V₁ as organized in mini-columns (Kondo, Yoshida, and Ohki, 2016). A mini-column is a one cell-wide vertical array of cell somata arranged perpendicular to the surface of the cortex (Swindale, 1990). Kondo, Yoshida, and Ohki, 2016 found that neurons with the same orientation preference are arranged in mini-columns, however this clustering is weak, since there are also mini-columns that are composed of neurons not preferring

the same orientation. There have been several hypotheses generated to explain why mice do not have orientation columns (in comparison to higher mammals). One favoured hypothesis is that the small absolute size of mouse V₁ makes it possible for neurons preferring the same orientation to make connections even though they are not organised in columns. Additionally, Kaschube et al., 2010 showed that the spatial organization of orientation columns reflects network self-organization dominated by long-range interactions. Hence, they propose that local rather than long-range circuit formation processes are important to form the random "salt-and-pepper" like organization pattern in mouse V₁. However, as an example, V₁ of tree shrews and ferrets is of similar size as V₁ of squirrels, nevertheless V₁ of tree shrews and ferrets is organised in orientation columns and V₁ of squirrels is not, arguing against that hypothesis and for the idea that orientation maps are not a universal characteristic of V₁ architecture (Humphrey, Skeen, and Norton, 1980, Rao, Toth, and Sur, 1997, Hooser et al., 2005).

1.2.2 Neuronal subtypes in mouse V₁

V₁ neurons, as other cortical neurons, can be divided into two main neuronal subclasses: excitatory neurons and inhibitory interneurons. In V₁, approximately 80 % of the neurons are excitatory neurons and the remaining 20 % are inhibitory neurons (Rudy et al., 2011, Harris and Mrsic-Flogel, 2013). Both categories are comprised of several further subtypes and the identification of these subtypes is an active area of ongoing research.

Excitatory neurons are also often called glutamatergic neurons because they use glutamate as a neurotransmitter or pyramidal cells because of their pyramidal like shape. They usually respond to selective features of a visual stimulus, such as orientation and/or direction of movement. Furthermore, excitatory neurons have been shown to respond preferentially to certain spatial and temporal frequencies (Harris and Mrsic-Flogel, 2013).

Most inhibitory neurons in the cortex use gamma-Aminobutyric acid (GABA) as a neurotransmitter and therefore are called GABAergic neurons. However, there are other inhibitory neurotransmitters such as glycine. Inhibitory neurons in the visual cortex are less selective for stimulus features such as stimulus orientation, but are involved in the modulation of V₁ activity such as behavioural state dependent modulation (Kerlin et al., 2010). Inhibitory neurons can be further divided into subclasses, depending on their morphology, physiology, genetic identity or function (Kepecs and Fishell, 2014, Jiang et al., 2015). Three main non-overlapping interneuron classes in the cortex, identified by the expression of molecular markers, include parvalbumin (PV), somatostatin (SST or SOM) and 5HT_{3A}-receptor-expressing interneurons (Rudy et al., 2011, Jiang et al., 2015). SST interneurons are inhibited by and inhibit VIP and PV inhibitory interneurons. PV inhibitory interneurons additionally inhibit

other PV interneurons, while VIP inhibitory interneurons do not make any further connections (Figure 1.2). These connections between different inhibitory interneurons are also found in other cortical areas. For instance, it was shown that activation of VIP interneurons in auditory cortex suppresses SST activity as well as the activity of a subpopulation of PV interneurons (Pi et al., 2013, for review see: Tremblay, Lee, and Rudy, 2016).

Recent advances in *in vivo* recording techniques as well as molecular tools for labeling specific neuronal subtypes have made it possible to address questions about the influence of cellular subtypes on neuronal computation. Neuronal subtypes can be studied using two-photon imaging in combination with for example Cre-dependent viral expression (Runyan et al., 2010) or fluorescent reporter lines (Zariwala et al., 2011). It is also possible to identify neuronal subtypes posthoc after an experiment using immunohistochemistry (Kerlin et al., 2010).

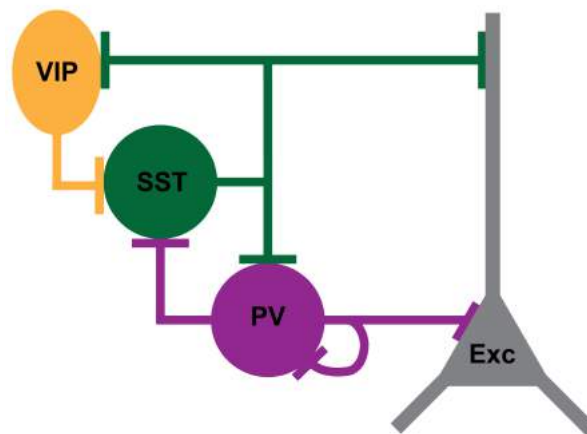


Figure 1.2: Schematic of the connectivity between interneurons. VIP expressing interneurons inhibit preferentially SST expressing interneurons. SST expressing interneurons inhibit VIP and PV expressing interneurons as well as excitatory neurons. PV expressing interneurons inhibit preferentially SST expressing interneurons, excitatory neurons and other PV expressing interneurons. Adapted from Pfeffer et al., 2013.

1.2.2.1 Parvalbumin expressing interneurons

PV expressing interneurons are also called fast spiking cells because they generally spike at high frequencies (up to 150 Hz) (Kawaguchi et al., 1987, Kawaguchi and Kubota, 1997) and account for approximately 40 % of GABAergic interneurons in mouse V1 (Rudy et al., 2011). In general, PV expressing interneurons mainly connect with excitatory neurons and other PV expressing interneurons (Pfeffer et al., 2013) (Figure 1.2). Additionally, PV expressing interneurons were shown to be activated through muscarinic ACh receptors (Alitto and Dan, 2013). On a network level, PV inhibitory interneurons are thought to stabilize the network activity (Pfeffer et al.,

2013). Optogenetic activation of PV expressing interneurons was shown to sharpen orientation tuning as well as to improve performance in an orientation discrimination task (Lee et al., 2012). However, this effect depends strongly on the level of the optogenetically-induced PV interneuron activity, with low levels not resulting in a sharpening of orientation tuning (Atallah et al., 2012, Atallah, Scanziani, and Carandini, 2014).

PV interneurons can be further subdivided into basket cells and chandelier cells (Rudy et al., 2011). There is also evidence that PV expressing interneurons might consist of even more subtypes (for review see: Markram et al., 2004). Basket cells target the cell soma and proximal dendrites of pyramidal cells, while chandelier cells target the axon initial segment (Kawaguchi and Kubota, 1997). Basket cells mediate fast inhibition, and were shown to be important for feedforward inhibition of thalamocortical inputs (Gabernet et al., 2005) and the maintenance of cortical gamma frequency (Cardin et al., 2009). Chandelier cells are found in cortical layers II to VI (Markram et al., 2004), and according to some evidence may have a depolarizing effect on excitatory neurons (Woodruff et al., 2009). However, other studies have only found hyperpolarizing effects of chandelier cells (Glickfeld et al., 2009).

1.2.2.2 *Somatostatin expressing interneurons*

SST interneurons account for 30 % of GABAergic interneurons (Rudy et al., 2011). In general, SST interneurons make connections with excitatory neurons and all other subtypes of inhibitory interneurons, but do not inhibit themselves (Pfeffer et al., 2013, Xu et al., 2013) (Figure 1.2). There have been indications, that SST cells are important for dendritic integration processes (Murayama et al., 2009). SST interneurons can be further subdivided into at least three more subtypes (McGarry et al., 2010).

The main subtype of SST interneuron are Martinotti cells. Martinotti cells arborize and spread horizontally in layer 1, where they mainly target dendritic tufts of excitatory neurons. Even though Martinotti cell soma are found throughout all cortical layers (except layer 1), they are most concentrated in layer 5 (Kawaguchi and Kubota, 1997). They receive most of their inputs from excitatory neurons, with a single excitatory neuron being able to drive Martinotti cells output (Kapfer et al., 2007). Another subtype of SST interneuron is X94 cells. X94 cells were first identified in the primary somatosensory cortex (S1) and were mainly located in layers 4 and 5. In contrast to Martinotti cells, the X94 arborize in layer 4 (Ma et al., 2006). Besides these differences, Martinotti cells and X94 cells can both be driven by cholinergic agonists via muscarinic receptors (Fanselow, Richardson, and Connors, 2008, Kawaguchi, 1997). A third subtype of SST interneuron is calretinin positive neurons. Calretinin and SST positive interneurons are very similar to Martinotti cells, however, they are concentrated in layer 2/3 and have larger horizontally extended dendritic trees (Xu, Roby, and Callaway, 2007).

1.2.2.3 *5HT₃A-receptor-expressing interneurons*

5HT₃A-receptor-expressing interneurons also account for 30 % of GABAergic interneurons and consists of two main groups: neurogliaform cells (NG) and vasoactive intestinal peptide (VIP) expressing cells (Lee et al., 2010, Rudy et al., 2011). 5HT₃A-receptor-expressing cells have been implicated in learning and control of cortical circuits by higher-order cortex and thalamus (Pfeffer et al., 2013). Furthermore, since none of the PV- or SST-expressing interneurons, express the ionotropic serotonin 5HT₃A-receptor, only 5HT₃A-receptor-expressing interneurons such as VIP and NG cells are modulated by serotonin. Additionally, 5HT₃A-receptor-expressing interneurons are also modulated by acetylcholine through nicotinic receptors (Lee et al., 2010). VIP expressing cells account for approximately 40 % of all 5HT₃A-receptor-expressing interneurons and are most densely found in layer 2/3 of the cortex (Lee et al., 2010), where they preferentially target SST expressing interneurons (Lee et al., 2013) (Figure 1.2). VIP expressing interneurons can be further subdivided into at least 4 different subtypes dependent on their morphology (bipolar, bitufted, multipolar) and electrophysiological properties (Miyoshi et al., 2010).

Non-VIP expressing 5HT₃A-receptor-expressing interneurons account for 60 % of the population of 5HT₃A-receptor-expressing interneurons. A big proportion (approximately 80 %) of those neurons co-express reelin (Lee et al., 2010). Most of the non-VIP expressing 5HT₃A-receptor-expressing reelin positive interneurons are neurogliaform cells (NG). NG cells have a small, round soma with multiple radially arranged dendrites and round axonal arbors with fine branches. Their unique morphology makes it easy to identify them (Kawaguchi and Kubota, 1997, Lee et al., 2010). Based on their electrophysiological firing patterns it is suggested that NG cells can also be further subdivided into subtypes (Lee et al., 2010, Miyoshi et al., 2010). In general, NG cells do not specifically target other cells but act through volume transmission (Olah et al., 2009).

1.2.3 *Neuronal activity in mouse V1 is modulated by behavioral state*

Recent studies have shown that the activity of excitatory and inhibitory neurons is not only dependent on visual inputs, but additionally modulated by non-visual stimuli in V1. A growing body of research is investigating how information from multiple modalities (e.g. reward (Shuler and Bear, 2006), attention (Reynolds and Heeger, 2009), and motor action (Saleem et al., 2013)) are integrated in V1.

For example, it has been shown, that the response properties of excitatory and inhibitory neurons in V1 are modulated by locomotion. Specifically, the gain of excitatory neuronal responses to visual stimulation in V1 is increased during locomotion compared to during stationary periods (Fu et al., 2014, Niell and Stryker, 2010).

Studies performing experiments where mice are navigating in a virtual reality envi-

ronment have shown that V₁ neurons integrate visual flow during navigation (Saleem et al., 2013). In addition, a study conducted by Keller, Bonhoeffer, and Hübener, 2012 has shown that a subset of V₁ neurons of mice respond to a mismatch in visual flow and locomotion speed of the mouse (Keller, Bonhoeffer, and Hübener, 2012, Zmarz and Keller, 2016, Leinweber et al., 2017). However, V₁ neurons have also been shown to be responsive, not only to behavioural state (e.g. locomotion versus stationary), but also to changes in the level of arousal (McGinley et al., 2015). Furthermore, it has been shown that V₁ neurons in rodents can accurately predict reward timing (Shuler and Bear, 2006).

Taken together, these findings demonstrate that V₁ is more than just a feature detector. Response properties of V₁ neurons are highly modulated by several modalities, such as behavioural state and arousal. Furthermore, V₁ neurons encode modalities other than features of the visual scene, like reward, speed, and visual flow. The mechanisms underlying the modulation of visual inputs in V₁ by non-sensory aspects remain largely unexplored. Top-down projections from higher visual areas (Larkum, Senn, and Lüscher, 2004) as well as neuromodulatory inputs (Pinto et al., 2013, Polack, Friedman, and Golshani, 2013, Bennett, Arroyo, and Hestrin, 2014) have been shown to contribute to behavioral state modulation of V₁ activity. Top-down inputs arrive to V₁ in layer 1, where they make connections with interneurons and apical tuft dendrites of excitatory neurons. It is believed that top-down inputs increase the probability and number of dendritic calcium spikes. Hence, they are in an ideal position to increase the gain of neuronal activity (Larkum, Senn, and Lüscher, 2004).

1.2.4 Higher visual cortical areas and top-down projections to mouse V₁

Studies in non-human primates have identified two anatomically and functionally separated streams of V₁ projections to higher visual cortical areas, the ventral stream (important for form vision and object recognition) and the dorsal stream (important for perception of motion) (Goodale and Milner, 1992, Wang, Sporns, and Burkhalter, 2012). Mice also show a functional and anatomical separation in ventral and dorsal stream. Two adjacent areas to V₁, the lateral-medial (LM) and latero-intermediate (LI) area, were anatomically identified as equivalent to the ventral stream; and four adjacent areas to V₁, postero-medial (PM), antero-medial (AM), anterior (A), rostro-lateral (RL) and antero-lateral (AL) area, were anatomically identified as equivalent to the dorsal stream (Wang and Burkhalter, 2007, Wang, Sporns, and Burkhalter, 2012). Visual responses of the ventral stream are tuned to orientations (Smith et al., 2017). Dorsal stream neurons were shown to respond significantly more to direction of motion (Marshel et al., 2011). Furthermore, it was shown that the visual preference of the presynaptic bouton coming from V₁ matches the visual preferences of the postsynaptic bouton in V₂. Thus, V₁ neurons projecting to V₂ make functionally specific connections with neurons in V₂ (Glickfeld et al., 2013).

V2 also send projections back to mainly layer 1 of V1 (Larkum, Senn, and Lüscher, 2004). Top-down connections carry a substantial amount of information and are involved in encoding and recall of learned information (Gilbert and Li, 2013). For example, it was shown that top-down projections from V2 LM (part of the ventral stream) facilitates neuronal response of V1 layer 2/3 neurons and this facilitation is specific to the preferred orientation of those neurons (Pafundo et al., 2016, Leinweber et al., 2017). However, not only higher visual areas provide top-down projections to V1. For example, cingulate cortex, which is believed to be involved in learning, sends long-range projections to V1 that increase V1 neuron responses and improve visual discrimination (Zhang et al., 2014). Similarly, retrosplenial cortex, which is also believed to be involved in memory formation, sends long-range projections to V1. A recent study did show that during passive visual stimulation and simultaneously associative learning retrosplenial cortex inputs to layer 2/3 of V1 increase their activity (Makino and Komiyama, 2015). Inactivation of retrosplenial cortex inputs to V1 after learning reversed the learning induced alterations of layer 2/3 neuronal responses (Makino and Komiyama, 2015).

1.3 NEURONAL PLASTICITY IN ADULT MOUSE V1

The developing visual cortex of mice undergoes several stages, each stage defined by several developmental markers such as neuronal cell-type differentiation, circuit maturation and changing levels of neuronal growth factors. During development, the extent to which the visual cortex is plastic changes.

The critical period defines a specific short period during which a certain brain area is especially susceptible to change in response to an adequate sensory input. The onset time of the critical period differs between brain systems and species. Opening of the critical period requires the maturation of inhibitory cortical circuitry (Fagiolini and Hensch, 2000). V1 of mice is especially susceptible to changes in response to visual stimuli between postnatal day 20 and approximately postnatal day 35, although different visual properties mature at varying speeds and ages (for review see Levelt and Hübener, 2012). For instance, between postnatal day 21 and 35 binocularly (ability to focus with both eyes) as well as binocular matching are established in mice V1 (Espinosa and Stryker, 2012). However, the closing process of the critical period is a gradual process (for review see: Levelt and Hübener, 2012). Closure of the critical period in mice V1 is believed to be mediated by extracellular signals. There are three main signals that are believed to trigger the closure of the critical period: the formation of perineuronal nets (PNNs), changes in neuromodulatory inputs and epigenetic regulations (Levelt and Hübener, 2012). The formation of PNNs prevents further axonal growth (McGee et al., 2005) and the intracortical formation of new synapses (Morales, Choi, and Kirkwood, 2002) by either forming a physical barrier or binding and presenting repelling axonal growth factors; hence limiting structural

plasticity. Furthermore, levels of neuromodulatory inputs to the cortex were shown to change during development. For instance, cholinergic and serotonergic inputs are decreased in adult compared to juvenile mice and it was shown that adult mice exhibit enhanced neuronal plasticity after cholinergic or serotonergic inputs are increased (Morishita et al., 2010, Fernando et al., 2008). Additionally, epigenetic regulations such as the reduction in cAMP responsive element binding protein (CREB) mediated gene transcription is believed to be involved in the closure of the critical period. However, the identification of the exact pathway and CRE regulated genes that mediate plasticity is an ongoing field of research (Levelt and Hübener, 2012). Finally, recently it was shown that the closure of the critical period for ocular dominance plasticity is governed by the maturation of silent glutamatergic synapses (Huang et al., 2015). Silent synapses are synapses that do not express AMPA receptors but can be transformed into fully functional synapses through the experience-dependent insertion of AMPA receptors. Mice lacking the postsynaptic density protein-95 (PSD-95), a protein shown to be crucial for the experience-dependent maturation of silent synapses, were shown to display lifelong juvenile ocular dominance plasticity. Hence, the maturation of silent synapses is important for the closure of the critical period.

Today it is well established that, even though the critical period is the time the visual cortex is especially plastic, it is possible to induce neuronal plasticity in the adult visual cortex. Neuronal plasticity induced in adult mice was shown to be less effective, less permanent and often involves less structural reorganization (Levelt and Hübener, 2012). However, several studies show that the adult visual cortex is plastic and depicts structural and functional changes in response to altered visual experience (Sawtell et al., 2003, Cooke and Bear, 2010). Furthermore, it was shown that adult cortical plasticity can be improved. For example, prior experience can enhance adult cortical plasticity (Hofer et al., 2006). Mice raised in an enriched environment (EE) also show enhanced adult cortical plasticity (Scali et al., 2012, Greifzu et al., 2014). Enriched environments are cages that provide mice with enhanced sensory, cognitive and motor stimulation. Enriched stimulation can be achieved by adding complex objects to the environment that provide visual, somatosensory and olfactory stimulation. Furthermore, environmental novelty, such as changing the objects or rearranging of the objects, is important (Nithianantharajah and Hannan, 2006). Experiments did show that different objects influence adult cortical plasticity to different extents, one of the most stimulating environmental enrichments being a running wheel (Kalogeraki et al., 2014, Kalogeraki et al., 2016). Housing adult rats (P70 to P100) for 10 days in an environment completely deprived of visual inputs (e.g. light tight room) was shown to reactivate juvenile-like ocular dominance plasticity, characterised by an increase in open eye responses and a decrease in closed eye responses after a 3 day period of monocular deprivation, accompanied by a reduction of GABA receptors relative to AMPA receptors (He, Hodos, and Quinlan, 2006). A recent study housing adult mice (P138) and old mice (P535) in a light tight room for 10 to 14 days showed an

increase in response to the non-deprived eye after a brief period of monocular deprivation, likely mediated by a reduction of intracortical inhibition, while there was no decrease of deprived eye responses observed, resembling the adult form of ocular dominance plasticity (Stodieck et al., 2014). Furthermore, exposure to patterned visual stimulation was also shown to enhance adult cortical plasticity (Matthies, Balog, and Lehmann, 2013). Finally, as discussed earlier, changes in neuromodulatory inputs (Morishita et al., 2010, Fernando et al., 2008) and epigenetic regulations (Jenks et al., 2017, Levelt and Hübener, 2012) in the direction of the juvenile state were shown to enhance adult neuronal plasticity.

1.3.1 *Functional plasticity*

Functional plasticity describes plasticity mechanisms that change the efficacy of existing neuronal connections and was shown to be present in adult mice (Keck et al., 2013, Barnes et al., 2015a). Functional plasticity mechanisms were first hypothesised by Donald Hebb, who proposed a mechanism by which neurons that fire together enhance their efficacy, a process referred to as Hebbian plasticity (Hebb, 1949). Later experiments revealed that activating the pre-synapse before the post-synapse results in a long-lasting potentiation (long-term potentiation, LTP), while activation of the post-synapse before the pre-synapse results in a long-term depression (LTD) (Frégac et al., 1988, Bi and Poo, 1998). Since LTP and LTD depend on the timing of the pre- and postsynaptic activity it is also termed spike-timing dependent plasticity (STDP) (Froemke and Dan, 2002).

During LTP the connection between two neurons is strengthened, which leads to an increase in activity of the whole network in a positive feedback loop. To avoid that the network becomes hyperactive, individual neurons are able to regulate their activity (homeostatic plasticity) by several mechanisms including but not limited to: synaptic scaling, changes in excitation and inhibition balance and compensatory changes in synapse number (for review see: Turrigiano, 2012, Sammons and Keck, 2015, Keck et al., 2017).

1.3.2 *Structural plasticity*

Structural plasticity describes plasticity mechanisms that involve the physical remodeling of neuronal connections through mechanisms of synapse formation, stabilization and elimination as well as axonal sprouting (for review see: Caroni, Donato, and Muller, 2012). For instance, it was shown that in adult animals after lesioning of the retina, the visually deprived area in V1 experienced axonal sprouting of neurons from adjacent non-deprived visual areas into the deprived visual area (Grutzendler, Kasthuri, and Gan, 2002). Following dendritic spines and filopodia of mouse V1

layer 5 neurons Grutzendler, Kasthuri, and Gan, 2002 did find structural plasticity in juvenile and reduced rates of structural plasticity in adult mice (Holtmaat et al., 2005). A different study, investigating structural changes in the superficial layers of V1 of adult mice *in vivo* without specifically inducing neuronal plasticity, revealed that most of the restructuring is happening at GABAergic arbors, while the dendritic structure of glutamatergic neurons are more stable (Lee et al., 2006). Therefore, structural plasticity in GABAergic inhibitory interneurons might play an important role in adult mouse V1 (Karmarkar and Dan, 2006). However, it was shown that the induction of LTP (functional plasticity mechanism) also induces structural changes in glutamatergic neurons resulting in the formation of new spines (Engert and Bonhoeffer, 1999). Thus, structural and functional plasticity mechanisms can act together to alter neuronal activity. Studies fully abolishing visual experience of one eye (enucleation), did not find structural reorganization of the deprived area in adult mice (Keck et al., 2008).

1.4 EXPERIMENTAL PARADIGMS FOR INDUCING PLASTICITY IN V1 OF ADULT MICE

There are several paradigms for inducing neuronal plasticity in V1 in juvenile and adult mice (for review see: Karmarkar and Dan, 2006). These paradigms can either be non-invasive by altering visual experience or invasive by physically perturb visual experience. In juvenile mice common paradigms for inducing plasticity in V1 are: dark rearing (Blakemore and Sluyters, 1975, Cynader and Mitchell, 1980, Mower, 1991, Fagiolini et al., 1994, Morales, Choi, and Kirkwood, 2002, He, Hodos, and Quinlan, 2006, Rochefort et al., 2009), stripe rearing (Blakemore and Cooper, 1970, Hirsch and Spinelli, 1970, Kreile, Bonhoeffer, and Hübener, 2011) and monocular or binocular deprivation (Gordon and Stryker, 1996, Sawtell et al., 2003, Hofer et al., 2006, Lehmann and Löwel, 2008). In adult mice common paradigms for inducing plasticity in V1 are: retinal lesioning or enucleation (Gilbert and Wiesel, 1992, Darian-Smith and Gilbert, 1994, Das and Gilbert, 1995), Keck et al., 2008, Keck et al., 2013, Barnes et al., 2015a), monocular or binocular deprivation (Gordon and Stryker, 1996, Sawtell et al., 2003, Hofer et al., 2006, Lehmann and Löwel, 2008), passive viewing (Frenkel et al., 2006, Cooke and Bear, 2010, Kaneko, Fu, and Stryker, 2017) and active viewing (Andermann et al., 2010, Poort et al., 2015, Stirman, Townsend, and Smith, 2016).

1.4.1 *Plasticity induced by retinal lesion and enucleation*

Retinal lesions and enucleation deprive the experimental animal from visual inputs, since the sensory cells of the retina will be removed. Precise retinal photo-coagulated lesions are made using a laser and a microscope (Keck et al., 2008). Enucleation can

be achieved by either photo-coagulate the entire retina using multiple confluent laser lesions (Keck et al., 2008), or by removing the eye (Barnes et al., 2015a).

In general, peripheral lesions lead to a loss in input in the lesion projection zone in the nervous system and to a topographical reorganization of the deprived area. Retinal lesions decreased visual cortex activity directly after lesioning. However, in the first two days after lesioning neuronal activity in V1 gradually increases again (Gilbert and Wiesel, 1992, Keck et al., 2013). Neurons that were silenced after lesioning start to represent retinotopic loci from the retina surrounding the lesion. This topographic reorganization of the deprived region is due to processes intrinsic to the cortex such as strengthening of subthreshold inputs and axonal sprouting from close by cortical areas (Darian-Smith and Gilbert, 1994, Das and Gilbert, 1995, Yamahachi et al., 2009, Hickmott, 2010, Sammons and Keck, 2015). Additionally, bouton turnover time increases, indicating the formation and withdrawal of new synapses (Keck et al., 2008, Yamahachi et al., 2009) and the cortex shows a loss in number of inhibitory spines, that were recently described in a subset of inhibitory neurons (Kawaguchi, Karube, and Kubota, 2006, Keck et al., 2011) and form most often synapses with excitatory neurons (Keck et al., 2011). Taken together, loss of peripheral input to the cortex results in two main components of plasticity: reduction of inhibition and the topographical reorganization via the mechanisms of axonal growth and synaptic strengthening (Sammons and Keck, 2015).

Enucleation does not lead to a topographical reorganization of the deprived area (Keck et al., 2008). However, some neurons do recover initial activity levels after the initial silencing. Excitatory neurons recovering after deprivation are most likely correlated before deprivation with other neurons that recover and additionally correlated with a large number of neurons, especially with inhibitory neurons that do not become unresponsive after enucleation (Barnes et al., 2015a). Since V1 also receives input from other regions of the brain (Niell and Stryker, 2010, Andermann et al., 2010, Keller, Bonhoeffer, and Hübener, 2012), another explanation for the recovery of neuronal activity in a subset of neurons after enucleation involves shared top-down inputs from higher cortical areas (Barnes et al., 2015a). Overall, a decrease in synaptic inhibition is observed (Barnes et al., 2015a).

1.4.2 *Plasticity induced by monocular deprivation*

Monocular deprivation (MD) is an invasive paradigm, pioneered by Hubel and Wiesel, to induce neuronal plasticity in the binocular area of the visual cortex (Wiesel and Hubel, 1963b). MD is achieved by suturing the eye lids of the contralateral eye after trimming the lid margins, thus preventing the eye from experiencing any patterned visual stimulation. Importantly, lid closure does not fully abolish vision, differences in illumination are still perceivable (Wiesel and Hubel, 1963a, Wiesel and Hubel, 1963b).

MD was shown to cause morphological alterations in the dLGN and a shift in responses to visual stimuli from the deprived eye to the non-deprived eye. This shift in inputs to V1 from both eyes in favour of the non-deprived eye is called ocular dominance shift (OD shift) (Wiesel and Hubel, 1963a, Wiesel and Hubel, 1963b). OD shifts consist of two separate parts, first the response to the deprived eye decreases. This decrease was shown to result from a withdrawal of thalamocortical projections from the deprived eye (Antonini and Stryker, 1993). Recently it was shown that potentiation of inhibition of fast spiking basket cells onto pyramidal neurons also leads to a decrease in deprived eye responses (Maffei et al., 2006). Second the responses to the non-deprived eye increases. This process was shown to be NMDA receptor dependent, and thus might share common features with LTP (Sawtell et al., 2003, Frenkel and Bear, 2004). Furthermore, it was shown that the decrease and increase in responses of individual neurons depend on the inputs a neuron receives from both eyes (Mrsic-Flogel et al., 2007). A study recording single neuron responses using two-photon calcium imaging could show that neurons receiving significant input from the non-deprived eye displayed an increase in non-deprived eye responses and a decrease in deprived eye responses. Deprived eye responses were shown to decrease within the first 2-3 days of MD, while the increase of response to the non-deprived eye only begin after 3 days of MD (Mrsic-Flogel et al., 2007). However, neurons mainly receiving input from the deprived eye surprisingly increase their responses. This increase is believed to be mediated by homeostatic response compensation, where the decrease in deprived-eye responses triggers a compensatory upscaling of all inputs, keeping the summed visual responses preserved (Mrsic-Flogel et al., 2007).

Early studies performing MD in kittens directly after birth and for three months did show atrophy in the dLGN and a drastic OD shift towards the non-deprived eye as well as little to no recovery after eye opening (Wiesel and Hubel, 1963a, Wiesel and Hubel, 1963b, Wiesel and Hubel, 1964). In mice it was shown that MD of four days performed during the critical period (postnatal day 20 to 35, with a peak sensitivity at approximately P28) in juvenile mice induces a significant OD shift (Gordon and Stryker, 1996, Espinosa and Stryker, 2012), while MD of four days performed in adult mice (P90 and older) does not induces an OD shift (Lehmann and Löwel, 2008). More recent studies performed in adult mice (P90) showed that MD for seven days also induces a significant OD shift (Sawtell et al., 2003, Lehmann and Löwel, 2008). Importantly, it was shown that in adult mice the responses to the non-deprived eye still increases, but the decreased response of the deprived eye is absent (Sawtell et al., 2003, Hofer et al., 2006) and that these changes are less dependent on homeostatic response (Ranson et al., 2012). Additionally, there are indications that the increase in response to the non-deprived eye results from a decrease in inhibition rather than from an increase in excitation in the adult cortex (Yoshimura, Ohmura, and Komatsu, 2003). MD performed in mice older than 110 days did not elicit a significant OD shift (Lehmann and Löwel, 2008). However, it was shown that adult mice, which were

transferred from standard cages into enriched environment cages (EE) at P₁₁₀, did show a significant OD shift after a MD period of 7 days. The observed OD shift in adult mice was likely mediated by reduced levels of intracortical inhibition in mice transferred to EE cages (Greifzu et al., 2014).

In juvenile and adult mice, it was shown that a MD of four to ten days after prior visual experience results in an OD shift which is reversible after re-opening of the deprived eye (Hofer et al., 2006). Experiments performing multiple MDs on the same animal did show that the OD shift induced by the second MD episode is faster and more persistent than the first experienced MD. Furthermore, in adult mice a second OD shift can be induced after a MD period of only 3 days (Hofer et al., 2006). Another study using MD in adult mice showed that following MD spine density is increased in layer 5 neurons of mouse V₁. This effect is persistent after recovery from MD and a second MD episode is not inducing more spine growth. It is suggested that the increased spine density is the underlying mechanism for faster OD shift observed in V₁ during a second MD period (Hofer et al., 2009). Additionally, a chronic imaging study conducted by Rose et al., 2016 found that after an OD shift, individual neurons return to their initial OD state, meaning that neurons responding pre MD preferentially to the stimulation of the non-deprived eye will do so again after recovery from the OD shift induced by MD.

1.4.3 *Plasticity induced by passive viewing protocols*

A non-invasive paradigm to induce plasticity in mouse V₁ consists of repetitive passive viewing of visual stimuli. It was shown that passive viewing of a defined stimulus (e.g. gratings) across consecutive days selectively enhances local field potential (LFP) responses to that stimulus in mouse V₁ (stimulus selective response potentiation, SRP) (Frenkel et al., 2006). Stimulus presentation can be as brief as five to six minutes per day and the maximum change in response amplitude is normally reached after five days (Frenkel et al., 2006, Cooke and Bear, 2010). Furthermore, it was shown that repetitive presentation with a sequence of different oriented gratings for five consecutive days leads to an enhanced response in LFP magnitude in V₁ (Gavornik and Bear, 2014b). This increase in LFP magnitude is highly specific for stimulus order and timing. The specificity for stimulus order and timing is so strong that omitting stimulus from the sequence will elicit the same response as elicit by the presentation of the full sequence (Gavornik and Bear, 2014b). SRP manifests behaviourally as long-term behavioural habituation to the specific stimulus (orientation-selective habituation, OSH) (Cooke et al., 2015). Using extracellular electrophysiological recordings, no change in the number of neurons responding preferentially to the presented stimulus was found, but neurons preferentially responding to the presented stimulus increased their preference to that particular stimulus (Frenkel et al., 2006). Similar results were obtained from studies conducted in monkeys (Schoups et al., 2001). In

contrast to those studies, a recent study using two-photon imaging reported stimulus specific response potentiation at the single neuron level in mouse V1 that strongly depended on locomotion; potentiation was only observed in mice that were running during stimulus presentation (Kaneko, Fu, and Stryker, 2017).

SRP was shown to occur in V1 of juvenile as well as adult mice, while in both ages the largest increase in LFP is recorded in thalamo-recipient layer 4 (Frenkel et al., 2006). Furthermore, SRP was shown to be NMDA receptor dependent and likely requires the activity dependent insertion of AMPA receptors in the post membrane and thus shares similarities with LTP (Frenkel et al., 2006, Cooke and Bear, 2010). Additionally, SRP was shown to be abolished in mice lacking the activity-regulated cytoskeleton-associated protein (ARC), which is known to be important for long-lasting LTP in the hippocampus (McCurry et al., 2010). Hence, the SRP paradigm induces long-lasting changes in V1 that are likely mediated by LTP like plasticity mechanisms, enabling the investigation of neuronal plasticity using a non-invasive paradigm (Cooke and Bear, 2014, Gavornik and Bear, 2014a).

Similarly, using functional magnetic resonance imaging (fMRI) it was shown in humans that repeated exposure to a defined visual stimulus leads to an increase in activation of the primary visual cortex. This increase goes along with a lower threshold to detect the presented stimulus, which is a form of perceptual learning (Furmanski, Schluppeck, and Engel, 2014). Furthermore, if human subjects were trained in a discrimination task and presented repetitively with the same grating they improved performance across days and this improvement is stimulus specific (Fiorentini and Berardi, 1980, Schoups, Vogels, and Orban, 1995).

1.4.4 *Plasticity induced by active viewing protocols (reward or fear experience)*

In contrast to passive viewing paradigms there are also active viewing paradigms that engage the experimental animal in a task. To engage an animal in a learning task it is important to motivate the animal. Motivation can either be achieved by using a reward for successful completion of the task or a punishment for unsuccessful completion of the task. Using rewards or punishments to motivate mice to participate in a learning task, enables the investigation of learning and memory formation as well as retrieval mechanisms during and after the learning process.

In the past, multiple different substances were used as rewards, such as sweet soy milk (Poort et al., 2015), water to drink (Andermann et al., 2010, Guo et al., 2014, Dent, Isles, and Humby, 2014) or food (Stirman, Townsend, and Smith, 2016). While sweet soy milk is an extra treat for mice and thus is sometimes sufficient to motivate mice to participate in a task, water and food rewards are only sufficient, if mice are on restriction (e.g. deprived of water or food) and motivated to obtain the water or food reward. If mice are on food or water restriction it is important to constantly monitor their body weight to avoid starving. Fluid rewards can be easily delivered

using a computer-controlled spout (Andermann et al., 2010, Guo et al., 2014). Reward delivery can be triggered by for example licking of the spout (Andermann et al., 2010, Poort et al., 2015) or by touching of a touch screen (Stirman, Townsend, and Smith, 2016). Using rewards, mice can be trained in a go/no-go task to either discriminate between gratings of different orientations (with one being the rewarded grating) (Andermann et al., 2010), or to discriminate different moving stimuli using a random dot kinematogram (Stirman, Townsend, and Smith, 2016). A rewarded go/no-go discrimination task was also shown to be successful if mice are in a virtual reality environment (Poort et al., 2015). Mice also engage in forced choice based perceptual decision tasks using a dual lick port for reward (Guo et al., 2014, Marbach and Zador, 2016). Another commonly used paradigm to motivate an animal to engage in a learning task is the association of a punishment or fear experience when the task is not completed successfully. In general, anything perceived as an aversive stimulus by mice can be used as punishment or fear experience. For example, Makino and Komiyama, 2015 used a tail shock (0.5 seconds, 0.6 mA) to motivate mice to run. An incorrectly executed task can also be indicated by presenting an air puff to the head of the mouse (Andermann et al., 2010). Finally, a time out period, which pauses the experiment and prevents mice from starting a new trial to gain a reward, was also shown to be effective as a punishment (Aoki et al., 2017).

Using a reward paradigm Leinweber et al., 2017 trained mice to navigate a VR environment. Using this approach, they showed that top-down projections from the secondary motor cortex (M2) as well as the adjacent area A24b (part of the anterior cingulate cortex (ACC)) conveys motor related signals to V1, and that the activity pattern of the ACC projections to V1 started to become correlated with visual flow after mice were trained to navigate through the VR environment (Leinweber et al., 2017). A study conducted by Makino and Komiyama, 2015 using a fear experience also showed that during learning bottom-up inputs to V1 weakened, while top-down inputs from the retrosplenial cortex (RSC) became stronger. However, active viewing protocols using either rewards or fear experiences are not only used to motivate an animal, the reward or fear experience itself often also induces experience-dependent changes in neuronal activity. A recent study demonstrated that the reward timing itself is also encoded in mouse V1 and that learning of the rewarded behaviour depends on cholinergic inputs from the basal forebrain, suggesting that these inputs to V1 convey information about the outcome of a specific behaviour (Chubykin et al., 2013). Taken together, the results obtained using active viewing protocols indicated that learning might be accompanied by a shift in the balance between bottom-up and top-down inputs to V1 (Makino and Komiyama, 2015).

1.5 THESIS AIMS

The overarching topic of this thesis is to contribute to the understanding of neuronal circuit function and plasticity in the adult primary visual cortex of awake behaving mice. We used chronic two-photon imaging in awake behaving mice in order to characterise neuronal response properties of excitatory neurons, as well as inhibitory interneurons before, during and after the induction of experience-dependent plasticity. As a proxy for neuronal activity, a genetically encoded fluorescent calcium indicator (GCaMP6) was used. Using two-photon calcium imaging, it is possible to follow the same population of neurons across consecutive days, thus enabling the tracking of changes in neuronal activity during experience-dependent plasticity.

First, we determined the baseline activity of neuronal circuits in V1 during behavioural state changes. We studied the effect of locomotion on neuronal activity of excitatory neurons as well as on three non-overlapping inhibitory interneuron subclasses (PV-, SST-, and VIP interneurons). Then, we investigated neuronal plasticity using a passive viewing paradigm in wild-type mice, to reveal changes in neuronal activity levels of individual neurons across days. We used a protocol of 5 min of passive exposure to an oriented grating for 5 consecutive days, monitoring the activity of single neurons before, during and after this experience. Finally, neuronal plasticity was investigated in a mouse model of intellectual disability and autism spectrum disorders to reveal potential impairments associated with the mutation of the *Syngap* gene in adult mice. We compared baseline neuronal activity, as well as neuronal activity after seven days of MD, between SynGAP^{+/-} mice and wild-type littermates.

IMPLEMENTATION OF A TWO-PHOTON CALCIUM IMAGING SET-UP FOR CHRONIC *IN-VIVO* RECORDINGS IN AWAKE BEHAVING MICE

2.1 INTRODUCTION

To investigate experience-dependent plasticity mechanisms in the brain, it is essential to compare the state of the brain before and after plasticity was induced. Past work, investigating experience-dependent plasticity, was mainly conducted using anatomical or electrophysiological methods. However, using anatomical methods such as histology, limits the experiment to the comparison of naive versus trained mice brains of different experimental animals, and additionally does not yield any information about changes in functionality of the brain. Electrophysiological studies using chronically implanted silicon probes, enables the comparison of neuronal activity before and after the induction of experience-dependent plasticity in the same animal, albeit not containing any information about neuronal subtypes. Furthermore, using electrophysiological methods does not always allow for the identification of specific individual neurons, preventing the monitoring of individual neurons across time.

To achieve the aims of this thesis, we used *in vivo* chronic two-photon imaging in combination with genetically encoded calcium indicators (GECI). Combining both techniques enabled us to monitor the activity of neuronal populations with single cell resolution across several days and weeks in awake behaving mice (Andermann et al., 2010). This allows us to investigate changes in neuronal response properties of identified individual neurons over time, and hence enables us to monitor their activity before, during and after an experimentally-controlled experience. The change in fluorescence of the GECIs, induced by an increase of intracellular free calcium triggered by neuronal activity, is used as a proxy readout for neuronal activity (for review see: Tian, Andrew Hires, and Looger, 2012).

During my PhD, I together with Dr. Rochefort and Dr. Jia established an *in vivo* resonant-scanning two-photon microscope for imaging of awake-behaving mice. I also independently developed a reliable surgical procedure, optimised for performing stable chronic *in vivo* two-photon imaging and contributed to the development of standardised analysis tools for large imaging datasets.

In the following chapter I will first introduce the basic principles of two-photon microscopy and GECI. I will describe the resonant scanning two-photon imaging set-up established in the lab, used for all imaging experiments included in this thesis. I then describe the critical steps of the experimental procedure (surgical procedure

and image acquisition, (Figure 2.1). Finally, I present the data analysis workflow including the steps I contributed to establish for the reliable and standardized analysis of chronic two-photon imaging data.

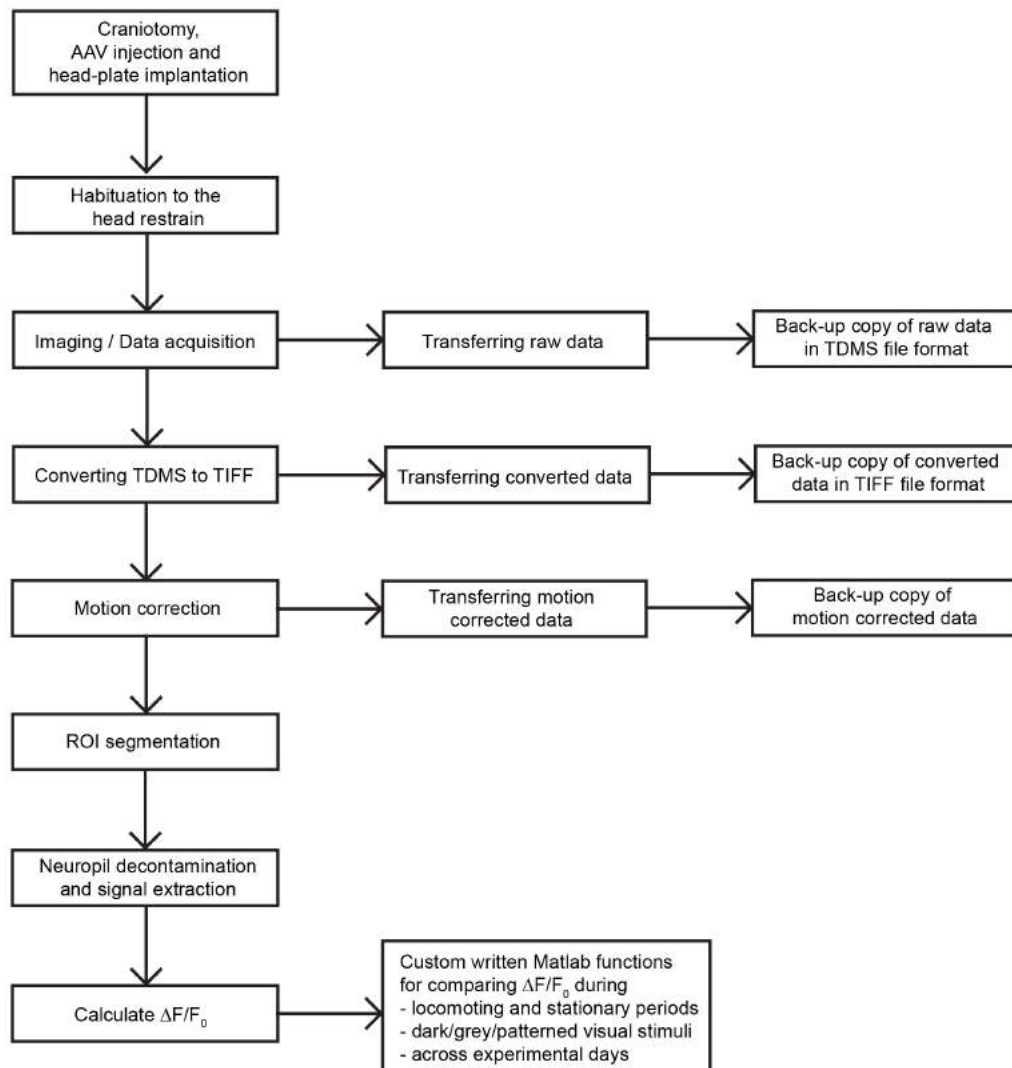


Figure 2.1: Two-photon calcium imaging experimental workflow: Schematic showing the workflow and data management plan of a chronic two-photon calcium imaging experiment.

2.1.1.1 Genetically encoded fluorescent calcium indicators

In resting conditions, neurons maintain very low free cytoplasmic calcium (Ca^{2+}) levels. When an action potential (AP) is generated, Ca^{2+} influx is triggered through voltage gated calcium channels and through the release of Ca^{2+} from internal Ca^{2+} stores. The resulting increase in free cytoplasmic Ca^{2+} concentration can be mea-

sured using GECI's. GECIs consist of a calcium binding protein (calmodulin, CaM), a peptide (M13) and a fluorescent protein. When Ca^{2+} ions bind to the CaM-M13 domain, the CaM-M13 domain undergoes a conformational change that causes an increase in fluorescence (Figure 2.2). The resulting change in fluorescence is used as a proxy of the spiking activity of individual neurons (Adams, 2010, Tian, Andrew Hires, and Looger, 2012, Looger and Griesbeck, 2012).

Currently, the most widely used GECI are GCaMPs, which consist, in addition to the calcium binding protein CaM and the M13 peptide, of a circularly permuted enhanced green fluorescent protein (cpEGFP). For all experiments GCaMP6 was expressed under the human synapsin-1 promoter exclusively in neurons through adeno-associated virus (AAV) injections. For all experiments the most recently developed GCaMP calcium sensor, GCaMP6s and GCaMP6f; both differing in their kinetics were used. The kinetics determine the rise and decay time and thus define the temporal resolution of the calcium sensor. GCaMP6s has the highest affinity for Ca^{2+} and hence has a very high detection rate for single APs (nearly 100 % *in vivo*, Chen et al., 2013). However, due to its slow rise and decay time (rise time: 179 ± 23 ms, decay time: 550 ± 52 ms), GCaMP6s can not temporally resolve a sequence of successive APs that are separated by less than approximately 179 ms (Chen et al., 2013). GCaMP6f has approximately a 4 fold faster rise and a 3.9 fold faster decay time than GCaMP6s. Thus, it has a better temporal resolution in resolving single APs than GCaMP6s. Specifically, GCaMP6f can resolve individual APs when separated by at least 50 to 75 milliseconds (rise time of GCaMP6f). However, the faster rise and decay time are associated with a lower affinity for Ca^{2+} ions compared to GCaMP6s. Hence, it fails to detect single APs in 15 % of the cases (*in vivo*) (Chen et al., 2013, Ding et al., 2014). Overall, due to the high AP detection efficiency of both calcium indicators as well as the stable expression across weeks, GCaMP6 is perfectly suited for the use in chronic two-photon imaging experiments. However, virus expressing can differ depending on the neuronal subtype and individual neurons (Nathanson et al., 2009). Additionally, expression levels increase over time, and eventually cause cell damage, thus limiting the time-window for imaging experiments. GCaMP6 expression level depends on several factors such as viral titre, volume of AAV injection and GECI promoter (Chen et al., 2013).

2.1.2 Principles of two-photon imaging

Two-photon calcium imaging is based on the principle that a fluorescent molecule is excited with two low energy photons instead of one high energy photon (e.g., one-photon excitation) (for review see: Potter, 1996, Denk and Svoboda, 1997, Zipfel, Williams, and Webb, 2003, Denk, Piston, and Webb, 2006, Svoboda and Yasuda, 2006, Kerr and Denk, 2008). Therefore, two photons have to be absorbed simultaneously by a fluorophore. When a photon is excited, it is moved from its ground state to its

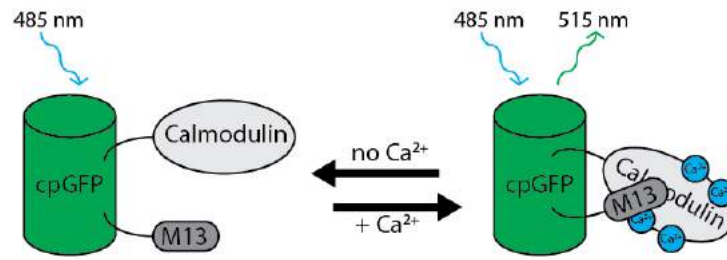


Figure 2.2: GCaMP6 activation: GCaMP6 consists of a cpGFP, M13 protein and a calcium binding calmodulin domain. If Ca^{2+} ions bind to the CaM-M13 domain, the CaM-M13 domain undergoes a conformational change, causing a conformational change and thus an increase in fluorescence that is physically detectable.

excited state and will emit light when returning back to its ground state (Figure 2.3). The principle of two-photon absorption was first proposed by Göppert-Mayer, 1930 and could first be tested in 1961 after the invention of the laser (Kaiser and Garrett, 1961). Experiments in 1962 (Abella, 1962), demonstrated two-photon absorption using a ruby maser (precursor of a laser) to excite cesium vapor and in 1963 Petricolas, Goldsborough, and Rieckhoff, 1963 achieved two-photon excitation in organic crystals.

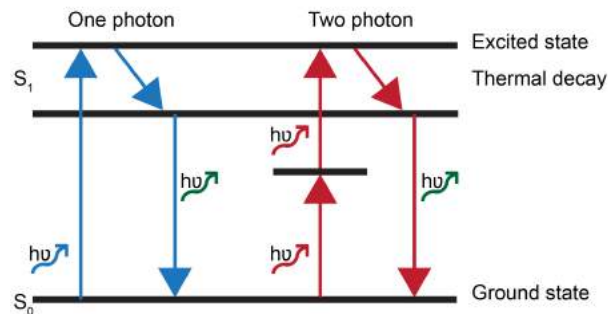


Figure 2.3: Two-photon excitation: Jablonski diagram showing one-photon excitation (left) and two-photon excitation (right). Left: Fluorophore is excited by absorbing one high energy photon. Right: Fluorophore is excited by absorbing two low energy photons. The two photons are absorbed nearly simultaneously and thus, are combining their energy to excite the fluorophore.

Two-photon calcium imaging was pioneered by Winfried Denk in 1990, when he was working in the laboratory of Watt W. Webb at Cornell University (Denk, Strickler, and Webb, 1990). By combining two-photon excitation and laser-scanning microscopy (LSM), Denk and colleagues built the first two-photon imaging set-up to excite fluorophores in living tissue. This was a great step forward for science because it enabled scientists for the first time to monitor the activity of individual neurons in alive animals. Nowadays, it is possible to image up to 1 mm deep into living brain tissue (Theer, Hasan, and Denk, 2003 Denk, Strickler, and Webb, 1990, for review see Helm-

chen and Denk, 2005).

The basic elements of a two-photon laser scanning microscope are: a femtosecond pulsed laser, scan mirrors, a Pockel cell, a tube lens, dichroic mirrors, an objective and at least one photomultiplier tube (PMT) to detect photons. The PMT is connected to a computer to produce a digital image based on the detected photons (Mertz, 2005).

Under normal conditions, the probability that two-photon excitation takes place is very low (in sunlight rhodamine B, a very good absorber, is expected to absorb two photons every 10 million years) (Denk and Svoboda, 1997). The probability is significantly increased by focusing a laser beam spatially as well as temporally. The laser beam is focused spatially using an objective. The highest spatial concentration of the laser beam is achieved by completely back-filling the objective. Since the laser beam is Gaussian-shaped it is beneficial to slightly overfill the back aperture. Under filling of the back aperture will result in an increase in power transmission, but lead to a decrease in resolution due to a broadening of the focal volume. To adjust the diameter of the laser beam to the back aperture a beam expander is used. The laser beam is focused temporally using a femtosecond pulsed laser (pulse duration 100 fs, repetition rate of 100 MHz) (Denk, Strickler, and Webb, 1990 Helmchen and Denk, 2005).

The spatial and temporal concentration of the laser beam results in a very small focal volume, which provides an optical sectioning effect, resulting in high resolution (Denk, Strickler, and Webb, 1990). Thus, two-photon calcium imaging can be used to image populations of neurons with single cell resolution as well as single dendrites and spines.

Additionally, the probability of two-photon excitation outside the focal volume is very low, resulting in nearly no out-of-focus excitation. As a consequence, there is only a small amount of photobleaching below and above the imaged focal plane. Furthermore, as there is no out-of-focus excitation, all emitted photons can be collected as signal, increasing the total photon yield (Denk, 2007). To collect as many photons as possible, it is beneficial to use an objective with a high numerical aperture (NA). The NA defines the range of angles from which an objective can collect photons. The higher the NA, the wider the angle (Oheim et al., 2001).

2.2 ESTABLISHING A TWO-PHOTON IMAGING SET-UP FOR IMAGING IN AWAKE MICE

There are different ways of setting up a system for two-photon calcium imaging. There are commercially available imaging set-ups (e.g., Zeiss, Leica, Femtonics) or an existing confocal microscope can be turned into a two-photon imaging microscope (Denk, 2007). The two-photon imaging microscope used to conduct all experiments described in this thesis was custom-made using mechanical devices from Scientifica and commercially available optical parts (ThorLabs, UK) (Chen et al., 2012). Together with Dr Rochefort and Dr Jia, I contributed to build the set-up, mounting the compo-

nents on the anti-vibration table and aligning the laser path. The set-up is a LOTOS (low-power temporal oversampling) based two-photon imaging set-up, comprising a Coherent LaVisionS Ti:sapphire laser, a 12 kHz resonant scanner and 2 GaAsP PMTs. Using a LOTOS based two-photon imaging set-up enables the data acquisition at high frame rates (e.g. between 20 to 200 frames per second), and thus only relatively low-excitation laser power is needed. Therefore, the main advantage of high speed imaging using a 12 kHz scanner is the reduction of photodamage during long or consecutive imaging sessions (Chen et al., 2012). The two-photon system was set up, tested and calibrated together with Dr. Janelle Pakan and Dr. Nathalie Rochefort for *in-vivo* two-photon imaging recordings in awake-behaving mice (modeled after Dombeck et al., 2007).

A schematic of the laser paths of the custom-built resonant scanning two-photon microscope that was used for all experiments is shown in Figure 2.4. The tunable femtosecond pulsed (75 fs) Ti:sapphire laser (LaVisionS, Coherent) is operating at 100 MHz and has a tunable wavelength range between 700 and 1060 nm. For all experiments, GCaMP6 was excited using a laser wavelength of 920 nm. The average output power of the laser is 1 Watt and the laser power under the objective at a wavelength of 920 nm is between 0 and 198 mW depending on the settings of the Pockel cell (Figure 2.4). For *in vivo* experiments, the laser power under the objective should not exceed 60 mW (Jackson et al., 2016). For the experiments included in this thesis the power under the objective was on average 55 mW. The laser power reaching the sample can be adjusted using a Pockel cell (Denk, Piston, and Webb, 2006) (Figure 2.4). The Pockel cell is a voltage controlled electro-optical modulator and operates at a timescale of microseconds. Therefore, Pockel cells are able to modulate laser power throughput very fast and thus are ideally suited to operate in combination with the LOTOS based imaging set-up (Denk, Piston, and Webb, 2006). Afterwards, the size of the laser beam is adapted to the size of the back aperture of the objective using a beam expander. This is necessary to spatially concentrate the laser beam to gain the best possible resolution for imaging (Helmchen and Denk, 2005).

The microscope base contains two scan heads, a telescope, dichroic mirrors and the PMTs. The scan heads are needed to direct the laser beam across the sample in x and y direction. The scanner moving the beam in y direction is a galvo scanner and the scanner moving the laser beam in x direction is a resonant scanner, operating at 12 kHz. This allows us to sample at high frequencies with the aim to limit photodamage. The first set of experiments was performed using a 40x Nikon objective (Nikon NIR Apo 40x/0.80 W, Japan). Later experiments were performed using a 25x Olympus objective (Olympus XL PlanN 25x/1.05 WMP, Japan). The FOV using the 40x Nikon objective was 240 x 240 μm and the FOV using the 25x Olympus objective was 384 x 384 μm .

The set-up comprises two PMTs to enable the simultaneous imaging of two fluorescent molecules. PMTs are highly sensitive photon detectors used to capture all available emitted photons. A dichroic mirror was used to separate excitation and fluorescence. Dichroic mirrors are able to do so by separating different wavelengths (Denk, Piston, and Webb, 2006). To protect the sample and the PMTs from the laser beam in between imaging trials a mechanical shutter, controlled by the imaging software, is used (Figure 2.4).

The output of the PMTs was recorded by an imaging software developed by Dr Hongbo Jia (LotosScan 1.4, Beijing ABORO-Tech Co. Ltd) as tdms (technical data management streaming) files. For *in vivo* imaging experiments, the mouse was placed on a cylindrical treadmill and head-fixed by a custom-built head restrain system. The initial design of the wheel and head fixation system was developed by Dr. Duguid's laboratory for *in vivo* patch clamp recordings in awake mice and the design was adapted for the two-photon imaging set-up.

The following sections will describe how the visual stimulus was presented and the behavioral state of the experimental animal monitored.

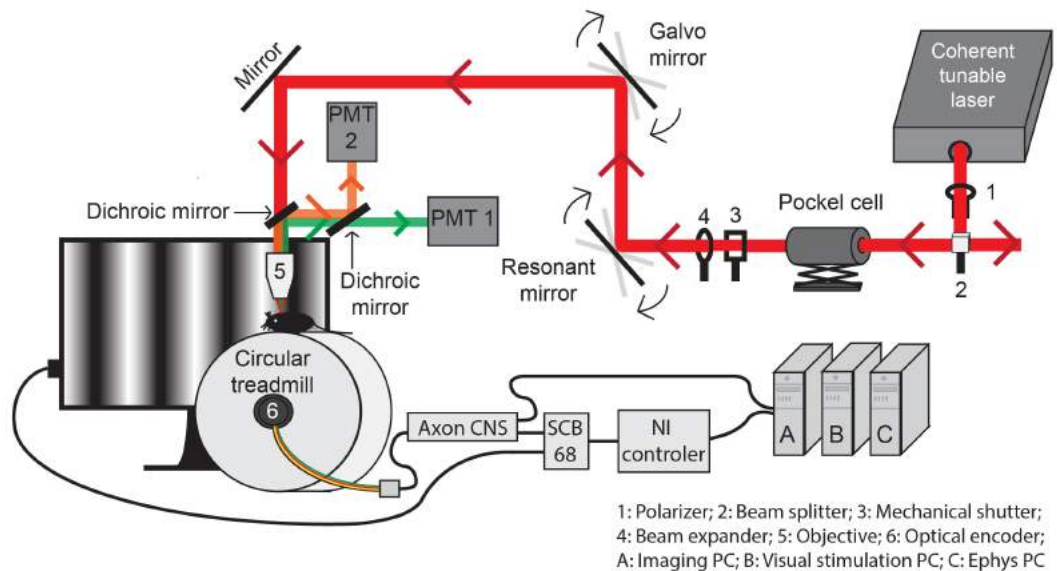


Figure 2.4: Schemata of the two-photon imaging set-up: The laser beam was generated by a tunable laser and directed through a beam polarizer and afterwards split into two laser beams by a beam splitter. Thus, one laser is used for two two-photon set-ups. Then the laser beam was directed through a Pockel cell, a beam expander and a mechanical shutter. Finally, the laser beam was directed through an objective and focused towards the sample. The laser beam was moved across the sample by a 12 kHz resonant scanner (x-axis) and a galvo scanner (y-axis). The mouse is fixed by a custom-built head restrain system and placed on a cylindrical treadmill. The speed of the treadmill was detected by an optical encoder and recorded by an Axon CNS device (Molecular Devices). Visual stimuli were presented using a screen placed at a 20 cm distance in front of the mouse. Imaging data, wheel speed and visual stimulation were recorded simultaneously.

2.2.1 *Visual stimulation without light contamination*

The emitted light from GCaMP6 labeled neurons was collected by PMTs. As discussed earlier, two-photon excitation takes place only in the focal imaging plane and hence, all emitted photons can be collected as signal. To do so, PMTs are operated in whole-field configuration (without a pinhole). PMTs are highly sensitive photon detectors and therefore the emitted photons from the fluorescent markers of interest are easily contaminated by ambient light. To reduce light contamination from ambient light sources two-photon microscopes are either shielded using a casing or operated in dark rooms. However, for a lot of experiments it is necessary to present a visual stimulus, e.g., experiments investigating the activity of the visual cortex or experiments where mice are navigating through a virtual reality environment (Dombeck et al., 2007), and the visual stimulus is a strong source of ambient light contamination.

Light contamination arising from the visual stimulus can be fully abolished by synchronising the light output of the screen to the turnaround points of the resonant scanner (Leinweber et al., 2014). Since there is no data acquired during the turnaround time of the laser beam, there will be no light contamination arising from the stimulus during data acquisition. The two-photon microscope used in this study consists of a 12 kHz resonant scanner, which is turning at a frequency of 24 kHz. Hence, the screen presenting the visual stimulus was modified to flicker at a rate of 24 kHz, triggered by the resonant scanner. The flickering rate is well beyond the flicker fusion threshold mice are able to perceive and thus the presented visual stimulus looks coherent to the mouse (Leinweber et al., 2014).

Nevertheless, since there is still light contamination during the turnaround time of the laser that can cause significant damage to the PMTs, the area between the objective and the head-plate was shielded with black tape, significantly reducing the amount of ambient light reaching the PMTs.

The screen was connected to a PC (VisStimPC, Figure 2.4) and stimulus presentation was triggered by the LotosScan 1.4 imaging software (Beijing ABORO-Tech Co. Ltd). The brightness of the screen was set to 30 lux. The visual stimulus was created using the Psychophysics Toolbox package (Brainard, 1997) for MATLAB (Mathworks, MA) and displayed on an LCD monitor (51 × 29 cm, Dell, UK, model number P2412Hb, 100-240 V, 50-60Hz, 1.2 A). For the experiments discussed in Chapter 3 square-wave stationary (4 to 5 seconds) and moving (2 seconds) grating stimuli of 8 different orientations (0°, 45°, 90°, 135°, 180°, 225°, 270°, 315°) were presented. For the experiments discussed in Chapter 4 and Chapter 5 phase-reversing (1 Hz, 3 seconds) sinusoidal grating stimuli of 4 different orientations (0°, 45°, 90°, 135°) were presented. In all experiments the inter-stimulus interval was a isoluminant grey screen.

2.2.2 Monitoring movement activity

During the experiments mice were head restrained and placed on a circular treadmill (Dombeck et al., 2007). The circular treadmill was made of a 20 cm diameter polystyrene cylinder, mounted on a ball-bearing axis. Movements of mice were monitored by recording mice's running speed on the circular treadmill using an optical encoder (E7P, 250cpr, Pewatron, Switzerland). The output of the optical encoder was recorded by the Clampfit 10.3 software (Axon CNS Multiclamp 700B). The software records the binary output from the optical encoder (square-wave signal, 12 kHz sampling frequency). Since the output of 12000 sampling points per second is 300 times the sampling frequency of the image acquisition (40 Hz), the optical encoder signal was down-sampled by 300 to meet the sampling frequency of the imaging (Pakan et al., 2016).

The binned signal was used to calculate the wheel speed. For the analysis of effect of locomotion on neuronal activity, different behavioural state types were defined as follows: stationary corresponded to periods where instantaneous speed (as measured at the 40 Hz sampling rate) was less than 0.1 cm/s; locomotion corresponded to periods meeting three criteria: instantaneous speed \geq 0.1 cm/s, 0.25Hz lowpass filtered speed \geq 0.1cm/s, and an average speed \geq 0.1cm/s over a 2 second window centered at this point in time (Pakan et al., 2016). Hence, brief periods of movement and transition periods between stationary and locomotion were excluded from further analysis.

2.3 ESTABLISHING A RELIABLE CRANIAL WINDOW AND NEURONAL LABELING

To achieve high quality *in vivo* chronic two-photon imaging with cellular resolution, the cranial window and neuronal labeling quality are crucial. Imaging depth strongly depends on a clear and clean cranial window to reduce auto fluorescence and light scattering at the surface of the brain. If the surgery and window implant are not conducted under aseptic conditions, inflammation will decrease imaging quality across days. In addition, stability of the focal plane during imaging recordings strongly depends on the head fixation as well as the cranial window. I have established a reliable protocol for a surgical procedure that is optimised for performing stable *in vivo* chronic two-photon calcium imaging experiments. All procedures were approved by the University of Edinburgh animal welfare committee, and were performed under a UK Home Office project license.

2.3.1 *Head-plate design*

Head-plates were designed with the help of Dr. Lukas Fischer (Rochefort laboratory) using a free software (Autodesk inventor 2017, Autodesk inventor Inc., USA) and were then manufactured by Proto Labs (UK). All head-plates were made of aluminum (AlSi10Mg) and weight less than 0.5 g. Each head-plate has a middle part with a hole and two arms which connect with a screw-nut to the head restrain system (Figure 2.5 A, B, C). Head-plates were designed in such a way, that the diameter of the hole was as big as possible to create enough space for the cranial window and the objective, and at the same time, having as much surface area of the head-plate as possible attaching to the skull to achieve a stable fixation of the head-plate. The two arms of the head-plate were designed long enough to create space between the objective and the screw nut that was used to fix the head-plate to the head restrain system to protect the objective from damage. At the same time, for stability reasons, the arms of the head-plate should not be too long. Head-plates can be reused several times after being cleaned from debris using dental acrylic liquid (Paladur, Heraeus Kulzer GmbH, Germany) and after being autoclaved.

I contributed to the testing and the development of different versions of head-plate designs, with the aim to achieve stable experimental imaging conditions as well as an optimal access to the cranial window with the objective. For experiments using the 40x objective a head-plate with a 6 mm off-centered hole and 7 mm long arms was used (Figure 2.5 D). For experiments using the 25x objective a head-plate with a 8 mm centered hole and 11 mm long arms was used (Figure 2.5 E).

2.3.2 *Sterile surgery: craniotomy and AAVs injection*

Cranial window implantation and GECI injection were performed in one surgery two to three weeks prior to imaging. For the surgery a binocular (Leica M80), a cold light source (KL 1500 LCD, Zeiss, Germany) and sterile gloves (Sterile indigo nitrile examination gloves, HandSafe, UK) as well as an autoclaved head-plate and three sterile tissues (Kleenex, UK) were prepared. The surgery area was disinfected (AZOWIPE, Synergyhealth LTD, UK) and artificial cerebrospinal fluid (ACSF (Appendix A), approx. 30 ml, brought to room temperature and filtered (Minisart, sterile single use filter unit, sartorius stedim biotech, Germany) provided.

Then, mice were moved from their home cage to an anesthesia chamber (univentor, uv401) and anesthetized using 4 % Isoflurane (IsoFlo, Abbott Laboratories, UK). Superfluous Isoflurane was removed using an active scavenging unit (VetTech Solutions LTD, UK) connected to an anesthetic gas absorber (Cardiff Aldasorber, Shirley Aldred & Co LTD, UK). The head was shaved (Wahl model 9966, Wahl clipper corporation, USA) and loose fur removed (air duster hfc free, Office depot, UK).

The mouse was then fixed in a stereotaxic frame (David Kopf Instruments, CA, USA)

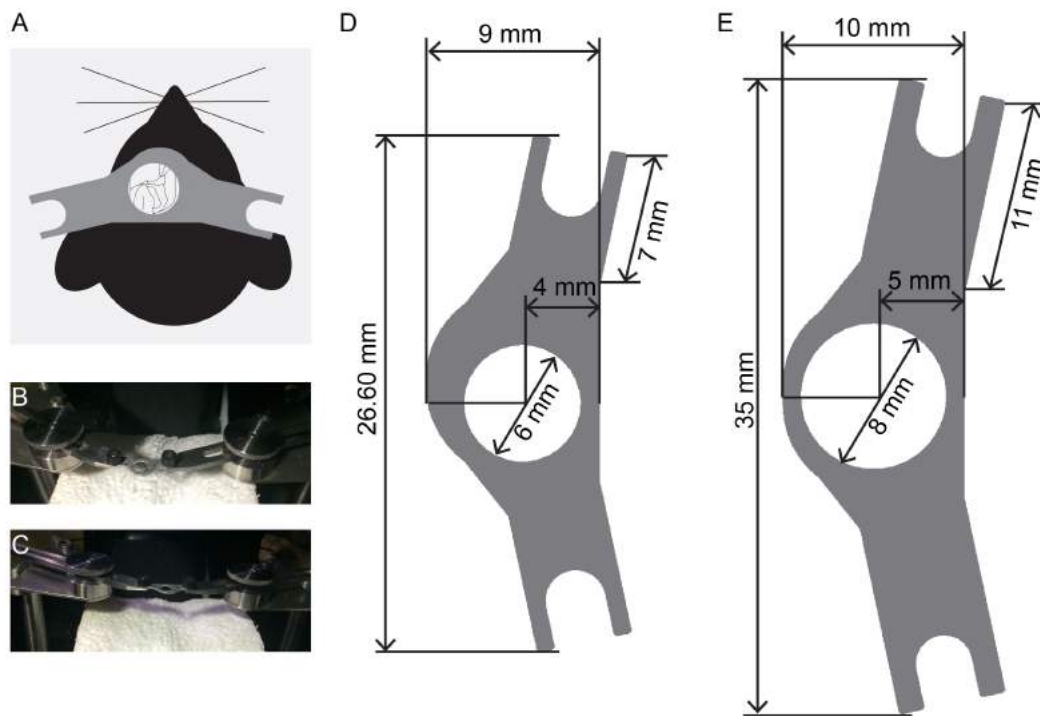


Figure 2.5: Head-plate design for stable head fixation under two-photon imaging set-up: A) Schematic showing the head-plate attached to a mouse head. B) Pictures of a head-plate fixed in head-restraint, front view. C) Pictures of a head-plate fixed in head restraint, top view. D) Model of the head-plate used for experiments using the 40x objective. E) Model of the head-plate used for experiments using the 25x objective.

and Isoflurane supply was reduced to 1.8 to 2 %. Since, anesthetized mice do not regulate their body temperature, mice were placed on a heating pad (Beurer HK95, Beurer GmbH, Germany). During the whole course of the surgery breathing rate and body temperature were monitored. The eyes of the mouse were covered with an opaque eye cream (Bepanthen, Bayer, Germany) to prevent dehydration of the eyes. An analgesic (1 ml/ 20 mg mouse Buprenorphine (Vetergesic), diluted 1:10 with injectable water (Water for Injections 100 % v/v, Norbrook Laboratories Limited, Northern Ireland), a corticosteroid (1 ml/ 20 mg mouse Dexamethasone, Rapidexon, Dechra, to diminish brain swelling) and a non-steroidal anti-inflammatory drug (1 ml/ 20 mg mouse Carprofen, Carprieve 5.0 %, Norbrook, to prevent inflammation) was injected subcutaneously.

Before removing the scalp using scissors (no. 5 forceps, Fine Science Tools, UK) the scalp was disinfected with surgical scrub (Videne surgical scrub, ECOLAB, UK, dilution 1:10 with sterile ringer, Viaflo Ringer's solution for infusion, Baxter healthcare LTD, UK). The edges of the skin were glued to the skull using a tissue adhesive (3M Vetbond, Animal Care Products, USA). The exposed skull was scratched with a scalpel (Stainless steel surgical blade, Swann-Morton LTD, UK) to remove debris and

improve head-plate attachment. The skull was disinfected with ethanol (70% Ethanol absolute, AnalaR NORMAPUR, VWR chemicals, UK) and the primary visual cortex (-2.3 to -5.0 from bregma and between 1.75 to 3.5 lateral from mid-line) marked. To create more surface area for better head-plate attachment, the muscle in the back of the head were gently push back with sterile cotton swaps (Technical Service Consultants Ltd, UK) and blunt forceps (Figure 2.6 A).

Afterwards, a square shaped cranial window (between 4 mm lateral to 1 mm lateral from midline and between -3.8 mm and -2.5 mm posterior to bregma) was drilled (Volvere Vmax NE120, NSK, 2000 cycles/min, Japan; drill head: H1 204 005, Komet Dental, Germany). When the outline of the cranial window became visible drilling was paused and a template of the outlines drawn using disinfected parafilm (Parafilm M laboratory film PM-996, Pechiney plastic packaging, USA) (Figure 2.6 A). The template was used to cut a coverglass (Menzel-Glaeser, 24x32 mm size 0, Germany), fitting the cranial window using a diamond tipped pen (Miller straight diamond tipped retractable stainless steel scribe, RS components LTD, UK) (Figure 2.6 D).

Before drilling continued, the injection pipette (3.5" Drummond #3-000-203-G/X, Drummond Scientific, USA) was prepared. Pipettes were pulled (Narishige PC-10, UK) and back-filled with mineral oil (Mineral Oil M5904-5ML, Sigma-Aldrich, Germany). Injections were made with a Nanoject (Nanoject II, Drummond Scientific, USA). The tip of the pipette was cut, approx. 2 μ l of the mineral oil was ejected and the injection pipette filled with an AAV construct containing the calcium sensitive molecule GCaMP6 (1:10 dilution in ACSF).

Afterwards, drilling was continued until the skull was thinned and the bone removed with fine forceps; avoiding mechanical damage and bleeding (Figure 2.6 B). The exposed brain surface was covered with ACSF to prevent dehydration. The injection pipette was positioned approximately -3.0 mm posterior from bregma and 3.5 mm lateral from midline (binocular V1), at a vertical angle of 10° and a horizontal angle of 10° from midline. Injections were made at 3 depths (500 μ m, 400 μ m and 300 μ m deep, 100 μ l total, 4.6 nl each 30 seconds).

After removal of the injection pipette the coverglass, prepared earlier, was gently pushed down onto the brain surface (Figure 2.6 C). The coverglass was fixed in place using super glue (Loctite super glue power flex, Henkel Limited, Germany), which was applied with a fine injection needle (Monoject, standard hypodermic needle, 0.305 mm x 1.9 cm, Covidien, USA) to the edges of coverglass and skull. It is important to push the coverglass until the glue is entirely solid, to avoid a cavity between brain and coverglass; since this could lead to bone regrowth and diminish imaging quality.

A sterile head-plate was attached to the skull using the same super glue. The head-plate should be horizontally even and the cranial window in the middle. Afterwards, dental acrylic (Paladur, Heraeus Kulzer GmbH, Germany, 63 ml powder mixed with 125 ml liquid) was applied using a sterile syringe (BD Plastipak 1 ml, Becton, Dickin-

son and Company Limited, Ireland; Hypodermic needle, 1.2 mm x 40 mm 18G, B.Braun Melsungen AG, Germany). Exposed parts of the skull were covered with glue and the cranial window was cleaned using a sterile injection needle (BD Micro-lance 3, 0.45 mm x 10.0 mm 26G, Becton, Dickinson and Company Limited, Ireland) (Figure 2.6 D). Before the mouse was removed from the anesthesia, 0.5 ml of a sterile Ringer's solution per 20g mouse (Viaflo Ringer's solution for infusion, Baxter) was subcutaneously injected and the eye cream was gently removed from the eyes. For recovery, the mouse was placed alone in a cage on a heating pad, and when the mouse was able to walk straightforward it was moved back to its home cage.

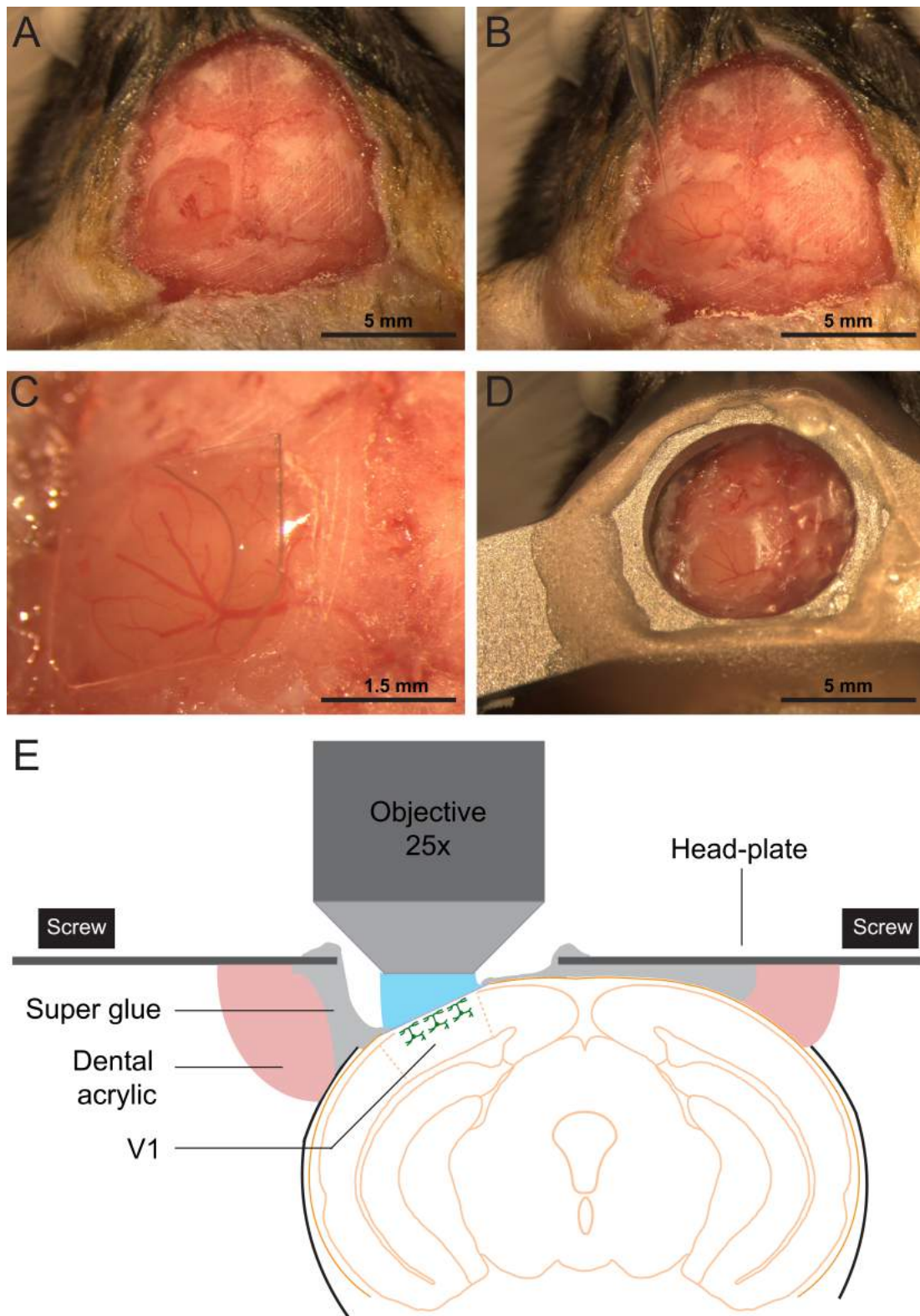


Figure 2.6: Cranial window surgery and head-plate implantation. Mouse is anesthetised and fixed in a stereotaxic frame. A) Picture of exposed skull after scalp removal, with cranial window outlined above V1. B) Cranial window opened (skull removed, brain surface exposed) and injection pipette. C) Glass coverslip fitted to the cranial window. D) Closed cranial window. Glass coverslip glued and head-plate attached. E) Schematic showing a coronal section through a mouse brain with cranial window and head-plate.

2.3.3 Labelling of cell-type specific neuronal subpopulations

In all experiments described in this thesis, neuronal populations were labeled using GCaMP6 expressed under the human synapsin-1 promoter. We used AAVs to deliver GCaMP6s (AAV1. Syn. GCaMP6s. WPRE. SV40), GCaMP6f (AAV1. Syn. GCaMP6f. WPRE. SV40) and flex-GCaMP6s (AAV1. Syn. Flex. GCaMP6f. WPRE. SV40), all acquired from the University of Pennsylvania Vector Core (PA, USA). GCaMP6s was expressed exclusively in neurons and flex-GCaMP6f was expressed exclusively in neurons, which contained cre-recombinase. Parvalbumin-, Somatostatin-, and Vasoactive intestinal polypeptide- cre mice lines (PV-Cre, SST-Cre, VIP-Cre) enabled us to investigate the neuronal activity of these specific inhibitory neuronal subpopulations (Taniguchi et al., 2011, Pakan et al., 2016).

All used cre-driver transgenic mice lines have been obtained from Jackson Laboratory (ME, USA): Pvalb<tm1(cre)Arbr> (PV-Cre), [RRID: IMSR_JAX:008069], Sst<tm2.1(cre)Zjh> (SST-Cre) [RRID: IMSR_JAX:013044], Vip<tm1(cre)Zjh> (VIP-Cre) [RRID: IMSR_JAX:010908]. Cell type specific expression of a red fluorescent marker (tdTomato) was achieved by cross-breeding these cre-driver mouse lines with homozygote Rosa-CAGLSL-tdTomato [RRID: IMSR_JAX:007914] mice. Thus, all neurons containing cre-recombinase were labeled with tdTomato (PVtdTom, SSTtdTom, VIPtdTom), allowing for identification of one specific inhibitory subtype, while the whole neuronal population was labeled with the GCaMP6 (green fluorescence).

2.4 ESTABLISHING TOOLS TO ANALYSE TWO-PHOTON CALCIUM IMAGING DATA

In this study, *in vivo* chronic two-photon calcium imaging was used to monitor experience-dependent changes in neuronal activity over several days (up to 7 days). During each imaging experiment, large amounts of imaging data (on the order of 100 GB per experimental hour) were recorded, thus effective data handling and storage solutions had to be implemented. Furthermore, quantitative changes in fluorescence, used as a proxy for neuronal activity, need to be extracted in a robust and accurate way. This analysis typically involves motion correction, image segmentation into regions of interests (ROIs), and signal extraction. I contributed to the development and testing of each of the three analysis steps that I am presenting in the following sections.

In the present work, two-photon imaging data were recorded with a LabView based software (LotosScan 1.4, Beijing ABORO-Tech Co. Ltd) at a sampling frequency of 40 Hz. All files were saved as image sequences in tdms format and for further analysis files were converted into image sequences in tiff file format using a custom written image format converter based on LabView. In the following chapters I will describe a method to correct for x-y motion artefacts and a reliable way to match neurons across

several days. Furthermore, I will explain a method to correct for neuropil contamination and how the $\Delta F/F_0$ signal was calculated.

2.4.1 *Correcting for motion artefacts*

A problem arising with the application of two-photon calcium imaging *in vivo* in awake-behaving mice, are motion artefacts. During an experiment, movements of the animal cause time-dependent displacements of the imaged brain region relative to the microscope. This will introduce substantial artefacts into the imaging data, which makes it impossible to extract the calcium signal of interest. There are two types of movement artefacts: inter-frame distortions and frame to frame displacement. Inter-frame distortions mainly occur when the data is acquired at a low sampling frequency and can be avoided by acquiring the data at higher sampling frequencies. For this thesis, the calcium imaging data were acquired at 40 Hz hence, there were no inter-frame distortions. Frame to frame displacements can not be avoided using high sampling frequencies.

To correct for frame to frame displacements image sequences were loaded into Fiji (Fiji, ImageJ 1.48, USA) using MatLab (MatLab 2015a/2015b/2016a, The MathWorks Inc, USA). Afterwards, 2D plane translation-based image alignment (SIMA 1.2.0, sequential image analysis, (Kaifosh et al., 2014)) was used to correct for frame to frame displacements. Only the GCaMP6 signal collected by PMT number 1 was used for motion correction. The stable tdTomato signal collected by PMT number 2 was only used for motion correction, if motion correction using the GCaMP6 signal failed. This happened, when the GCaMP6 labeling was very sparse.

2.4.2 *Image segmentation into regions of interest*

After motion correction, image sequences were loaded into Fiji (Fiji, ImageJ 1.48, USA), down-sampled to 20 Hz (to improve the signal to noise ratio) and regions of interest (ROI), corresponding to neuronal cell bodies, were selected manually using the polygon tool of Fiji. The first ROI was a small rectangle drawn in a dark region of the image, containing the background signal. The second ROI was a large rectangle spanning the whole field of view (FOV), containing the summed signal of the FOV (including the neuropil). All following ROIs demarcated neurons. The total number of neurons per FOV varied between 70 to 300 neurons for GCaMP6s injections, depending on imaging quality and FOV size.

It is challenging to ensure that each ROI is marking the same neuron across consecutive days, since not all neurons are active each day and the imaged FOV was slightly twisted between experimental days. To ensure each ROI was marking the same neuron across days, it was necessary to reliably identify each neuron each day

by checking the motion corrected imaging sequences. If it was not possible to retrieve the location of a ROI reliably or a ROI was retrieved in less than 2 out of 7 imaging days, the ROI was dismissed from the data set.

In some cases, two or more ROIs were overlapping. In this case only non-overlapping areas of each neuron were selected and became part of the ROI. As a consequence, each ROI contained only the signal of one neuron. Neurons were excluded from further analysis, if it was not possible to draw non-overlapping ROIs. Neurons also were excluded from further analysis, if the remaining non-overlapping ROI would have been too small to extract a reliable signal. Finally, ROI coordinates for each ROI per trial were saved as zip folders.

We did not use automated ROI detection to define the ROIs. This is because most of the tested automated ROI detection algorithms hitherto available still needed manual checking, which was very time consuming. Furthermore, for further analysis it was important to keep the ROI numbers the same, i.e. each ROI needs to define the same neuron across days, which was not possible to achieve with the tested automated ROI segmentation tool at the time of the experiments.

2.4.3 *Correction for neuropil contamination and fluorescence signal extraction*

Following motion correction, images are processed in order to extract the fluorescence changes across time within each ROI. However, the fluorescence signal of each ROI is often contaminated by the neuropil signal. The neuropil signal consists of dendrites and synapses that surround the somas of individual ROIs. Additionally, nearby neuronal cell bodies are a source of signal contamination. It is important to correct for neuropil contamination because the neuropil itself is responding to stimuli (e.g. visual or behavioural) and thus when not removed, is influencing the final readout of the extracted signal (Lee et al., 2017).

To correct for neuropil contamination motion corrected image sequences and ROI coordinates were automatically loaded into Fiji (Fiji, ImageJ 1.48, USA) using Python (WinPython 2.7.10.3) and contamination was removed using non-negative matrix factorization (NMF). NMF is a low rank matrix decomposition method based on blind source separation and used for demixing spatially overlapping signal sources (Kim and Park, 2007), as implemented in the FISSA toolbox (Fast Image Signal-source Separation Analysis), developed by the Rochefort laboratory. Spatially overlapping signal sources are separated by estimating positive signals that best explain the recorded contaminated signal. For the purpose of demixing the spatially overlapping signal sources, four additional regions surrounding each ROI marking a neuron were automatically drawn (radius of 50 pixels from the center of the neuron). Those additional ROIs contain neuropil signal as well as signal from adjacent neurons. The algorithm was set to find a minimum of two and a maximum of five underlying signals using the data extracted from the neuronal ROI and the four additionally created ROIs.

Each of the underlying signals is compared to the signal of the neuronal ROI, and the best matching underlying signal is saved as the neuropil corrected neuronal signal. I have contributed to the testing of different versions of NMF based methods and the final version is summarized in a manuscript (Keemink S.W., Lowe S.C., Pakan J.M.P., Dylida E., Van Rossum M. and Rochefort N.L., FISSA: A neuropil decontamination toolbox for calcium imaging signals, Scientific Reports, 2018).

The mean fluorescence signal, obtained after neuropil decontamination, is used to calculate the $\Delta F/F_0$ signal. Baseline fluorescence F_0 was computed for individual neurons by taking the lowest 5th percentile of the smoothed $F(t)$ (1 Hz lowpass, zero-phase, 60th-order FIR filter) across all trials recorded on each day. Hence, baseline F_0 was the same for computing the change in fluorescence of trials recorded in darkness and during visual stimulation. ΔF relative to baseline ($\Delta F/F_0$) has been calculated by taking the difference between F and F_0 and dividing by F_0 .

2.4.4 *Analysis of somatic fluorescence changes across days*

$\Delta F/F_0$ was analysed using custom written MatLab scripts (MatLab 2016a, The MathWorks Inc, USA) (Pakan et al., 2016). Measured $\Delta F/F_0$ values across time were separated by stimulus and movement conditions and averaged across trials. Stimulus conditions were defined by the grating orientation presented (0° , 45° , 90° , 135° , isoluminant grey screen) and movement conditions were defined by the behavioural state of the animal (i.e. stationary or locomotion).

Neurons that did not reach an average maximum $\Delta F/F_0$ amplitude of $0.2 \Delta F/F_0$ in at least one stimulus condition (gratings) were termed unresponsive and dismissed from further analysis. Visual responsive neurons were determined by using an ANOVA (analysis of variance). Neurons showing a significant difference in $\Delta F/F_0$ between any of the five visual stimulus conditions (0° , 45° , 90° , 135° , grey), or between the visual stimulation and the dark on any of the first 3 orientation mapping days (day 1, day 5 or day 6), were termed visual responsive neurons.

Orientation selectivity (neurons preferentially responding to gratings of a specific orientation) was determined by calculating an orientation selectivity index (OSI) using the mean $\Delta F/F_0$ of each neuron to each presented grating. The OSI index was calculated as follows:

$$\text{OSI} = \frac{\text{pref} - \text{ortho}}{\text{pref} + \text{ortho}} \quad (1)$$

where

pref Average $\Delta F/F_0$ for the preferred orientation of gratings

ortho Average $\Delta F/F_0$ for the orientation orthogonal to the preferred orientation

The oriented grating for which a given neuron responded with the highest mean $\Delta F/F_0$ amplitude was defined as the preferred orientation.

Furthermore, because experiments in awake behaving animals involve many ongoing and changing behavioural influences, in order to specifically determine the effect that a visual stimulus has on the activity of neurons, stimulus-evoked responses were quantified by calculating a stimulus-evoked response index (SER). The activity in the stimulus period is normalized to the directly preceding non-stimulus (grey) period. The SER was calculated as follows:

$$\text{SER} = \frac{\text{stim}_{(i)} - \text{grey}_{(i)}}{\text{stim}_{(i)} + \text{grey}_{(i)}} \quad (2)$$

where

stim Average $\Delta F/F_0$ during a single stimulus presentation (oriented grating)

grey Average $\Delta F/F_0$ during directly preceding grey screen presentation

Finally, neuronal responses evoked by the locomotion of the mouse were quantified by calculating a locomotion modulation index (LMI). Locomotion periods were separated from stationary periods as described earlier (chapter 2.2.2) using the wheel speed (stationary: instantaneous speed less than 0.1 cm/s; Locomotion: instantaneous speed ≥ 0.1 cm/s, 0.25Hz lowpass filtered speed ≥ 0.1 cm/s, and an average speed ≥ 0.1 cm/s over a 2 second window centered at this point in time). The LMI was calculated as follows:

$$\text{LMI} = \frac{R_L - R_S}{R_L + R_S} \quad (3)$$

where

R_L Average $\Delta F/F_0$ during locomotion periods

R_S Average $\Delta F/F_0$ during stationary periods

2.5 DISCUSSION

2.5.1 *A two-photon imaging set-up for chronic in vivo calcium imaging in awake-behaving mice*

The established resonant scanning two-photon imaging set-up is a reliable setup for chronic *in vivo* imaging in awake-behaving mice. The two-photon set-up is now used routinely in the Rochefort laboratory to reach layer 5 of V1 (up to 600 μm deep) using the calcium sensor GCaMP6. Furthermore, it is possible to image up to 300 neurons simultaneously using a 25x objective (Olympus XL PlanN 25x/1.05 WMP, Japan). The design of the head fixation and head-plates ensure the stability required for somatic and dendritic imaging in awake-mice. Taken together, the custom-built set-up is ideal for performing *in vivo* chronic two photon imaging experiments.

Nevertheless, since this two-photon microscope was built many new developments have been made in the field of *in vivo* two-photon imaging. Two major aims of these technical developments are improving imaging depth and increasing the number of neurons sampled per experiment.

Currently, it is possible to image up to 1 mm deep into highly scattering tissue *in vivo* (Theer, Hasan, and Denk, 2003). This was achieved by developing better optics and the development of specialized objectives for two-photon imaging, as well as by the improvement of GECIs. Recently, red GECIs have been developed to further improve deep imaging. Red fluorescent molecules are excited by, and emit photons at, higher wavelengths than green fluorescent molecules. Thus, they have a better signal transduction in highly scattering tissue due to their longer emission wavelength and thus penetrate deeper (Inoue et al., 2014, Dana et al., 2016). However, GECI are expressed differently in different neuronal subtypes and expression levels rise overtime until they cause neuronal cell death (Chen et al., 2013). Transgenic mice lines were developed that do not show signs of neuronal cell death. But unfortunately, expression levels are often to faint for *in vivo* imaging applications (Peron, Chen, and Svoboda, 2015).

Additionally, even with all the progress made in improving GECI for deep imaging, their slow kinetics compared to neuronal spikes is still a major disadvantage. Hence, it is currently not possible to resolve fast consecutive APs using GECIs and, therefore, changes in spiking activity of individual neurons can not be resolved (Yaksi and Friedrich, 2006). In contrast, voltage sensitive proteins have faster kinetics and thus are able to resolve spiking activity (Song, Barnes, and Knöpfel, 2017). Recent generations of voltage sensitive proteins are genetically encoded and can be expressed under cell-specific promoters, enabling the investigation of neuronal subpopulations (Dimitrov et al., 2007) and are suitable for *in vivo* imaging applications (Akemann et al., 2010). However, at the single neuron level the sensitivity of voltage sensitive proteins

is much lower compared to GECIs. This is because voltage changes need to be sensed across the cell membrane and only a limited number of proteins can be inserted into the cell membrane, compared to calcium sensitive molecules that can be expressed in high numbers in the soma (Peron, Chen, and Svoboda, 2015). Therefore, voltage sensitive proteins are currently not suited for imaging applications where single neuron resolution is needed (Knöpfel, 2012).

Recent developments of two-photon imaging microscopes significantly increased the number of simultaneously recorded neurons per imaging session using either wide-field two-photon imaging microscopes or scanning of multiple focal planes. Wide-field two-photon imaging microscopes were developed using large numerical aperture objectives (Stirman et al., 2016) or by using a resonant scanner in series with a galvo scanner (Sofroniew et al., 2016). Scanning of multiple focal planes can be achieved by using different approaches, such as: variable focus lenses, piezoelectric translators to move the objective, small lightweight mirrors or acousto-optic deflectors (Ji, Freeman, and Smith, 2016, Dal Maschio et al., 2011).

For instance, Stirman et al., 2016 developed a two-photon imaging setup providing access to multiple cortical areas simultaneously using two laser beams that are independently repositionable in x and y , within a field of view larger than 9.0 mm^2 . This enables simultaneous imaging of single-cell resolution neuronal activity in different brain areas. By using two electronically tunable lenses, one for each laser beam, it is possible to also image neuronal activity in different depths, for example, across multiple cortical layers. In contrast, the two-photon imaging setup designed by Andermann et al., 2010 uses a piezo-scanner to image multiple focal planes. This setup is capable of imaging neuronal activity in a volume of about $150 \mu\text{m} \times 150 \mu\text{m} \times 45 \mu\text{m}$ (Andermann et al., 2010, Kerlin et al., 2010). However, using a piezoelectric scanner to adjust the focus of the objective is a slow process. The two-photon imaging setup developed by Sofroniew et al., 2016 uses a rapid remote focusing unit to allow for simultaneous imaging in different cortical depths. The rapid remote focusing unit is made of a light weight mirror that is moved to focus between different cortical depths, and thus the objective does not need to be adjusted.

Finally, Katona et al., 2012 designed a two-photon imaging setup capable of imaging a 3D volume of $700 \mu\text{m} \times 700 \mu\text{m} \times 1400 \mu\text{m}$, using acousto-optical deflectors (AODs). AODs use soundwaves to deflect laser beams and thus, are faster than mechanical galvanometer mirrors. To achieve such a large z scanning range, they physically separated the x - y scanning unit from the z scanning unit. Acquiring two-photon imaging data in a 3D volume makes it possible to follow neurons of interest even if the z plane of the neuron changes across time (for example due to movement artefacts induced by locomotion) (Katona et al., 2012). However, it is still challenging to analyse the data, since AOD systems are not capable of performing continuous line scans but rather acquire the data by pointing the laser beam voxel by voxel across the

sample. Therefore, due to movement of the imaged tissue each imaging point can be shifted in relation to the previous acquired point (Nadella et al., 2016). To overcome this problem two solutions were explored. Cotton et al., 2013 developed an AOD based volume scanning two-photon microscope which is also capable of tracking the motion of the tissue (e.g. mouse brain), and thus it is possible to correct for motion artefacts in the z plane. Nadella et al., 2016 developed a AOD based volume scanning two-photon microscope that can perform continuous line scanning across the sample and thus acquiring spatial information around the ROI. Therefore, using the acquired spatial information around the ROI allows for the correction of movement artefacts after data acquisition (Nadella et al., 2016).

There is a constant progress to further improve two-photon imaging techniques to answer fundamental questions about neuronal circuit functions of the brain. New GECIs with an improved signal to noise ratio to enable shorter dwell times and faster imaging will aid the imaging of larger samples. At the same time, new two-photon imaging microscopes enabling the imaging of an increasing number of neurons are developed (up to 10,000 neurons per mouse (Peron et al., 2015)). Overall, after two decades since the first *in vivo* two-photon calcium imaging experiments were performed (Svoboda et al., 1997), the field of two-photon imaging is still moving forward and improving image quality and quantity with the aim to understand how the brain works.

2.5.2 *Analysing two-photon calcium imaging data*

The analysis of two photon calcium imaging data is not yet standardised across laboratories and generally each laboratory uses their own method to calculate $\Delta F/F_0$ with slightly different parameters. Hence, comprehensive documentation of the way individual datasets are analysed is important. The data acquired for this thesis were analysed using published MatLab and Python packages, in order to standardise the procedure as much as possible (i.e., minimize user-dependent steps). Nevertheless, since not all analysis steps are standardised and published yet, custom written MatLab scripts were used in addition.

In the past years several packages were made open source and became freely available to the imaging community. For example, there are multiple open source packages available for correcting motion artefacts in imaging datasets (Dombeck et al., 2007, Kaifosh et al., 2014). However, standardised open source packages are not available for all analysis steps. For instance, ROI segmentation is not yet fully standardised and automated. Different laboratories employ different manual or semi-manual ROI segmentation techniques. For example, one way to determine a ROI is to define the whole area of the neuron as a ROI, including the area without fluorescence (nucleus of the neuron) (Pakan et al., 2016). A different approach defines only the outer,

ring shaped fluorescent area (cytoplasm) as a ROI (Chen et al., 2013, Kaneko, Fu, and Stryker, 2017). Recently, morphology based and activity based ROI segmentation algorithms were developed and made freely available (Mukamel, Nimmerjahn, and Schnitzer, 2009, Peron, Chen, and Svoboda, 2015). However, even though ROI segmentation is more standardised using an algorithm, there are still user defined inputs as well as the need for a final manual inspection.

Recent initiatives have been aimed at standardizing two-photon analysis methods for neuropil decontamination. One method is to subtract the neuropil signal from the somatic signal (Chen et al., 2013). A disadvantage of this subtraction method is that in cases where the neuropil signal is larger than the somatic signal, the signal can become negative after subtraction. This can be overcome by manually adjusting the subtraction parameters for each dataset, but this type of user input and manual adjustment is not ideal for large datasets. A different method uses signal source separation, such as independent component analysis (ICA) (Stetter et al., 2000, Mukamel, Nimmerjahn, and Schnitzer, 2009), non-negative matrix factorization (NMF) (Maruyama et al., 2014, Keemink et al., in revision), or physiological model-based NMF (Pnevmatikakis et al., 2016, Pachitariu et al., 2016). These methods are mostly automated, however there are still many parameters that can be adapted. Therefore, a fully standardised method is currently still unavailable.

For all experiments conducted for this thesis motion correction was performed using an open-source software SIMA (SIMA 1.2.0, sequential image analysis, (Kaifosh et al., 2014)). SIMA performs fully automated motion correction of image sequences and does not need extensive manual user input. Furthermore, FISSA (Keemink et al., in review), was used to correct for neuropil contamination. The advantage of FISSA is that it is comparatively fast and does not require manual user input. Furthermore, FISSA does not make any assumptions about signal dynamics, thus can be used for a variety of calcium signals obtained from different neuronal subtypes. However, FISSA does not include an automated ROI detection method, hence ROIs were delineated manually.

Besides differences between laboratories in the three main steps for extracting the final fluorescent signal, there are also substantial differences in the calculation of the change in fluorescence ($\Delta F/F_0$) and the further analysis of this signal.

Even though the calculation of $\Delta F/F_0$ follows a standardised formula, different laboratories define the baseline fluorescence (F_0) in different ways. For example, F_0 can be defined by taking a certain lowest percentile of the whole fluorescence trace. However, the absolute value chosen is arbitrary and varies between laboratories (e.g. Pakan et al., 2016, lowest fifth percentile; Roth et al., 2015, median between the 10th and 70th percentile). Other laboratories define the average change in fluorescence immediately before the stimulus onset as F_0 (Kaneko, Fu, and Stryker, 2017). Standardizing these methods will be important to ensure that the ultimate signal produced from calcium

imaging data is directly comparable across laboratories and publications.

After the calculation of $\Delta F/F_0$, often not all neurons will be taken into further consideration. Inactive or only sparsely active neurons may be dismissed from the dataset, which can bias datasets to include only highly active neurons, providing a misrepresentation of total network activity. "Responsive" neurons can also be defined in different ways, for example either defining a threshold of minimum response amplitude or using statistical measures such as the skewness of $\Delta F/F_0$ values. An arbitrary defined threshold of minimum response amplitude has been used widely in the past. For example, Kaneko, Fu, and Stryker, 2017 only includes neurons in further analysis that reach an average response amplitude ($\Delta F/F_0$) above 25 % during the presentation of its preferred orientation, while Ranson, 2016 uses a threshold of at least 30 % minimum response amplitude to the preferred orientation. Other laboratories use a combination of thresholds. For example, responsive neurons can be defined as neurons that reach a minimum response amplitude ($\Delta F/F_0$) of 0.05 to their preferred orientation and in addition had a significant (ANOVA, $p < 0.01$) response during patterned stimulus presentation (Ohki et al., 2005, Hillier et al., 2017). In contrast, Roth et al., 2015 uses the skewness to define responsive neurons. Skewness is a measure of asymmetry of a distribution, hence a responding neuron will have a skewed distribution of $\Delta F/F_0$ values. However, similar to the previous described measure, an arbitrary threshold has to be defined. For example, Roth et al., 2015 defines responsive neurons as neurons that have a skewness value of above 1. Furthermore, tonically responsive neurons also have low skewness values, and thus will not be defined as responsive neurons. Therefore, because of the lack of a specifically defined signal outcome (i.e. an action potential spike), calcium imaging signal analysis can be very subjective, and the definition of what constitutes a neuronal response highly variable; moving forward, these definitions should be standardised across laboratories.

Furthermore, different measures to evaluate neuronal response, such as OSI, differ between laboratories, potentially introducing further bias. To date the two most commonly used OSI formulas are either using the ratio between the response magnitude to the preferred orientation and the response magnitude to the orthogonal grating (Niell and Stryker, 2008, Grienberger et al., 2012, Smith et al., 2013, Roth et al., 2015, Kaneko, Fu, and Stryker, 2017), or the circular variance (Ringach, Shapley, and Hawken, 2002, Kerlin et al., 2010, Hillier et al., 2017). While the circular variance takes the response magnitude to all presented gratings into account, the ratio only depends on the difference between the preferred orientation and the orthogonal. Therefore, OSI calculated using the ratio instead of the circular variance are likely higher on average. However, highly orientation selective neurons will have similar OSI values independent on the formula used. Better definitions of when it is appropriate to use each method will greatly increase the likelihood that the appropriate method is used for each experiment (e.g. see Mazurek, Kager, and Van Hooser, 2014).

Finally, recent research aims to extract neuronal spiking activity from calcium imaging data. However, extracting spikes from calcium data can be an unreliable process and the accuracy depends on several factors. Therefore, for the data analysed in my thesis I did not extract single spikes from the calcium data. For one, the temporal resolution of the used calcium indicator GCaMP6s is not optimal to resolve single spikes (rise time: 179 ± 23 ms, decay time: 550 ± 52 ms). Furthermore, to extract single spikes, it is highly beneficial to have, in addition to the calcium imaging data, ground truth electrophysiological data (which was not recorded for the datasets discussed in this thesis) to “train” the spike inference algorithm and enhance the inference process by providing the mathematical algorithm with data about calcium transient to spike output relationship for the specific microscope with which the data was collected. Without this calibrating information, extracting spikes is a complex process, that affords the adjustment of several parameters of the spike inference algorithm to extract the spikes as accurately as possible, all done blindly without the knowledge of the ground truth. This is currently the project of another PhD student in a lab which the Rochefort lab is collaborating with (Hennig Lab); however, this project is in an early phase. Additionally, there are currently many labs developing more sophisticated methods for spike inference from calcium imaging data (Deneux et al., 2016, Friedrich, Zhou, and Paninski, 2017, Pnevmatikakis et al., 2016); however, there is currently no consensus in the field as to the best method or whether any current methods are reliable enough across many different imaging systems and neuronal cell types - this will be an ongoing focus of research in the coming years.

The advancements made in microscopy techniques as well as the development of improved markers for neuronal activity will enable even more comprehensive studies of the brain. Hence, the amount of data generated in a single experiment will further increase and therefore it is more topical than ever to address the problem of a common way of data analysis. Different laboratories have started to address this issue and begun to develop open-source two-photon imaging analysis software packages that integrate all analysis steps (for example see Mukamel, Nimmerjahn, and Schnitzer, 2009, Kaifosh et al., 2014, Pnevmatikakis et al., 2016, Pachitariu et al., 2016, Romano et al., 2017). However, these packages are not fully automatized and often need to be adapted to specific needs. Therefore, further progress in the field of data analysis is needed until biases arising from different analysis methods are fully abolished.

BEHAVIORAL STATE MODULATES EXCITATORY AND INHIBITORY NEURONAL ACTIVITY IN THE MOUSE PRIMARY VISUAL CORTEX

3.1 INTRODUCTION

This thesis investigates properties of experience-dependent neuronal plasticity in the visual cortex. To fully understand the effect of experience on sensory processing it is important to perform these experiments in awake-behaving animals; however, how the perception of sensory stimuli can be modulated by the behavioural state of the animal is not entirely clear. Conducting these experiments in awake-behaving animals has the advantage that there are no side effects induced by general anesthesia, such as reduced inhibition in the cortex (Harris and Thiele, 2011, Haider, Häusser, and Carandini, 2013). In order to determine the effect that experience has on the activity of neuronal circuits in awake-behaving animals, it is important to first establish the effects that behavioural state changes can have on the microcircuitry in the primary visual cortex (V1). To this aim, we first defined the baseline neuronal response properties of V1 neurons by examining cell-type specific responses to changes in behavioural state.

Whether an animal is in a state of quiet wakefulness or active locomotion, affects neuronal responses in the cortex. Recently, recordings in awake-behaving mice have shown that the response properties of V1 neurons in layer 2/3 are highly modulated by behavioural state (Niell and Stryker, 2010, Petersen and Crochet, 2013, Bennett, Arroyo, and Hestrin, 2014, McGinley et al., 2015). Recordings of neuronal response properties of excitatory neurons have shown an increased gain of visual responses while the animal was running compared to when the animal was stationary (Niell and Stryker, 2010, Keller, Bonhoeffer, and Hübener, 2012, Bennett, Arroyo, and Hestrin, 2013, Polack, Friedman, and Golshani, 2013, Saleem et al., 2013, Erisken et al., 2014, Reimer et al., 2014). Vasoactive intestinal peptide (VIP) expressing inhibitory interneurons have been found to be strongly activated during locomotion periods of the animal (Fu et al., 2014, Reimer et al., 2014, Jackson et al., 2016). While VIP interneurons have been shown to have very few direct connections to excitatory neurons in V1, they do project strongly to somatostatin (SST) expressing inhibitory interneurons, which in turn inhibit pyramidal cell dendrites (Pfeffer et al., 2013, Jiang et al., 2015). Thus, a disinhibition model, where locomotion increases the activity of VIP interneurons that leads to a decrease of activity of SST interneurons and ultimately alleviating the inhibition on excitatory neurons, has been proposed as a possible mechanism for

the gain increase of excitatory neurons during locomotion (Fu et al., 2014). However, another study conducting electrophysiological recordings of neuronal response properties during visual stimulation, has shown a depolarization of SST interneuron membrane potential during locomotion, which would be in contradiction to the proposed disinhibition model (Polack, Friedman, and Golshani, 2013).

Since the observations of interneuron activity of Fu et al., 2014 were made in darkness and the observations of Polack, Friedman, and Golshani, 2013 during visual stimulation, a possible explanation for the discrepancy would be that V1 neuronal responses to locomotion are context-dependent. In this chapter, I present our publication from 2016, "Behavioral-state modulation of inhibition is context-dependent and cell type specific in mouse visual cortex" (Pakan et al., 2016). We tested the hypothesis that the modulation of neuronal response properties by locomotion in V1 of mice depends on the sensory context (Pakan et al., 2016). Towards this aim, we used *in vivo* two-photon calcium imaging to record neuronal response properties of layer 2/3 and layer 4 excitatory neurons as well as VIP-, SST- and PV-expressing interneurons during both visual stimulation and darkness, in awake-behaving mice.

3.2 MATERIAL AND METHODS

Two-photon calcium imaging data were acquired using the same two-photon imaging set-up and visual stimulation that are described in Chapter 2. For a detailed method description also see the method section of the paper, Pakan et al., 2016. Briefly, SST-, VIP-, and PV- expressing interneurons were labelled by GCaMP6 through AAV injections in either Cre-driver transgenic mice (AAV1.Syn.Flex.GCaMP6f.WPRE.SV40) or in Cre-driver mice cross-bred with Rosa-CAG-LSL-tdTomato mice (AAV1.Syn.GCaMP6f.WPRE.SV40). To label specifically Ca²⁺/calmodulin-dependent protein kinase II (CaMKII) expressing neurons, C57Bl/6 wild-type mice were injected with AAV1.CaMKIIo.4.Cre.SV40 in combination with AAV1.Syn.Flex.GCaMP6f.WPRE.SV40.

An AAV construct driving the expression of GCaMP6f or GCaMP6s, was injected into V1 two to three weeks prior to imaging. A cranial window above V1 was made either at the day of AAV injection or one to two days before imaging. Visual stimulation trials consisted of stationary full-field square-wave gratings for four to five seconds and the corresponding drifting phase for 2 seconds (0.03 cpd (cycles per degree), 1 Hz, 8 equally spaced directions in randomized order, contrast 80 %, mean luminance 37 cd/m²). Each trial started and ended with an isoluminant grey screen. Additional data was obtained during the presentation of an isoluminant grey screen preceding the presentation of each oriented grating for five seconds (0.03 cpd, 1 Hz, 4 equally spaced orientations in randomized order, contrast 80 %, mean luminance 37 cd/m²). All recordings were made in awake-behaving mice, able to run voluntarily on a circular treadmill.

3.3 PERSONAL CONTRIBUTION DISCLAIMER

I personally contributed to the acquisition of two-photon calcium imaging data in 12 animals (5 PV-, 4 VIP- and 3 SST-Cre driver mice), which were then included in layer 2/3 data for the manuscript (specifically, Figure 2 (including supplements), Figure 3 (including supplements) and layer 2/3 data for Figure 4).

3.4 PAKAN ET AL. 2016

Janelle M. P. Pakan, Scott C. Lowe, **Evelyn Dylida**, Sander W. Keemink, Stephen P. Currie, Christopher A. Coutts, and Nathalie L. Rochefort. "Behavioral-state modulation of inhibition is context-dependent and cell type specific in mouse visual cortex." In: *eLife* 5.AUGUST (2016). issn: 2050084X. doi: 10.7554/eLife.14985.

The article was published under a Creative Commons Attribution license (also known as a CC-BY license), and is free to use, reproduce and distribute (unless otherwise noted), for commercial and noncommercial purposes (subject to citation of the original source in accordance with the CC-BY license).



Behavioral-state modulation of inhibition is context-dependent and cell type specific in mouse visual cortex

Janelle MP Pakan¹, Scott C Lowe², Evelyn Dylida¹, Sander W Keemink^{2,3}, Stephen P Currie¹, Christopher A Coutts¹, Nathalie L Rochefort^{1*}

¹Centre for Integrative Physiology, School of Biomedical Sciences, University of Edinburgh, Edinburgh, United Kingdom; ²Institute for Adaptive and Neural Computation, School of Informatics, University of Edinburgh, Edinburgh, United Kingdom; ³Bernstein Center Freiburg, Faculty of Biology, University of Freiburg, Freiburg, Germany

Abstract Cortical responses to sensory stimuli are modulated by behavioral state. In the primary visual cortex (V1), visual responses of pyramidal neurons increase during locomotion. This response gain was suggested to be mediated through inhibitory neurons, resulting in the disinhibition of pyramidal neurons. Using in vivo two-photon calcium imaging in layers 2/3 and 4 in mouse V1, we reveal that locomotion increases the activity of vasoactive intestinal peptide (VIP), somatostatin (SST) and parvalbumin (PV)-positive interneurons during visual stimulation, challenging the disinhibition model. In darkness, while most VIP and PV neurons remained locomotion responsive, SST and excitatory neurons were largely non-responsive. Context-dependent locomotion responses were found in each cell type, with the highest proportion among SST neurons. These findings establish that modulation of neuronal activity by locomotion is context-dependent and contest the generality of a disinhibitory circuit for gain control of sensory responses by behavioral state.

DOI: 10.7554/eLife.14985.001

*For correspondence:
 n.rochefort@ed.ac.uk

Competing interests: The authors declare that no competing interests exist.

Funding: See page 16

Received: 03 February 2016

Accepted: 22 August 2016

Published: 23 August 2016

Reviewing editor: Thomas D Mrcic-Flogel, University of Basel, Switzerland

© Copyright Pakan et al. This article is distributed under the terms of the [Creative Commons Attribution License](https://creativecommons.org/licenses/by/4.0/), which permits unrestricted use and redistribution provided that the original author and source are credited.

Introduction

Sensory perceptions are modulated by the context in which they are experienced. In primary sensory areas, neuronal responses to sensory inputs are also modulated by behavioral states, including level of arousal, attention and locomotion (Iriki et al., 1996; Petersen and Crochet, 2013; Bennett et al., 2014; McGinley et al., 2015). In vivo recordings in awake mice have shown that locomotion modulates the response properties of neurons in the primary visual cortex (V1), resulting in an increased gain of excitatory neuron responses to visual stimuli (Niell and Stryker, 2010; Keller et al., 2012; Bennett et al., 2013; Polack et al., 2013; Saleem et al., 2013; Erisken et al., 2014; Reimer et al., 2014). However, the neuronal circuits underlying this response modulation are unclear.

Recent studies have revealed that a specific subclass of inhibitory neurons, expressing vasoactive intestinal peptide (VIP), strongly increase their activity during locomotion (Fu et al., 2014; Reimer et al., 2014; Jackson et al., 2016). VIP neurons mainly inhibit a second class of inhibitory neurons, expressing somatostatin (SST; Figure 1A; Pfeffer et al., 2013; Jiang et al., 2015; Urban-Ciecko and Barth, 2016). It has been proposed that cholinergic activation of VIP neurons during locomotion would inhibit SST neurons, alleviating inhibition onto excitatory neurons and, as a consequence, increase the gain of excitatory neuron visual responses (Figure 1B; Fu et al., 2014). However, a previous study has reported an increase of SST spiking activity in layer 2/3 during locomotion (Polack et al., 2013), an observation that challenges the hypothesis of an SST-cell mediated

eLife digest How we perceive what we see depends on the context in which we see it, such as what we are doing at the time. For example, we perceive a park landscape differently when we are running through it than when we are sitting on a park bench. Behavior can also alter neuronal responses in the brain. Indeed, the neurons in the part of the brain that receives information related to vision (known as the visual cortex) respond differently to visual stimuli when an animal is moving compared to when the animal is still. However, while some recent studies revealed that specific types of neurons become more or less responsive during movement, others reported the opposite results.

One hypothesis that would explain these contradictory findings would be if the way that behavior, in this case movement, affects neuronal responses also depends on the external context in which the movement happens. Now, Pakan et al. have tested this hypothesis by imaging the activity of different types of neurons in the primary visual cortex of mice that were either running on a treadmill or staying still. The experiments were conducted in two different contexts: in total darkness (in which the mice could not see) and in the presence of display screens (which provided the mice with visual stimulation).

Pakan et al. confirmed that running does indeed affect the activity of specific neurons in different ways in different contexts. For example, when the mice received visual stimulation, the three main classes of neurons that send inhibitory signals in the visual cortex became more active during running. However, when the mouse ran in the dark, two of these neuron types became more active during running while the third type of neuron was unresponsive. This finding reveals more about the dynamic nature of inhibitory activity that strongly depends on the animal's behaviour. It also shows how these neurons influence the excitatory neurons in the visual cortex, which send information to the rest of the brain for further processing towards perception.

The next step will be to identify what precise mechanism makes these neurons respond differently in unique contexts, and to tease apart how these movement-dependent signals affect the way animals perceive visual stimuli.

DOI: [10.7554/eLife.14985.002](https://doi.org/10.7554/eLife.14985.002)

disinhibitory circuit. The aforementioned recordings of SST neuronal activity were acquired in different sensory contexts, either in darkness or during the presentation of visual stimuli. One hypothesis that would explain the discrepancies between these results is that V1 neuronal responses to locomotion are context-dependent.

In this study, we tested this hypothesis by directly comparing the locomotion responses of excitatory and inhibitory neurons in darkness and during visual stimulation. We used two-photon calcium imaging to monitor the activity of excitatory neurons as well as of three non-overlapping populations of inhibitory neurons (VIP, SST and parvalbumin [PV] neurons) in layer 2/3 and layer 4 of V1 in awake behaving mice. Our results show that during visual stimulation these three classes of interneurons increase their activity with locomotion, challenging the model of a disinhibitory circuit mediated through SST neurons. We found that locomotion affects the activity of inhibitory circuits differently in darkness and during visual stimulation, revealing a context-dependent, cell type specific response to locomotion in V1. The highest proportion of context-dependent responses to locomotion was found among SST neurons, which play a central role in V1 microcircuits. We suggest alternative mechanisms of how locomotion modulates the neuronal activity in V1, highlighting the dynamic nature of interneurons function that strongly depends on the behavioral context of the animal.

Results

We compared the modulation of neuronal activity by locomotion in the mouse primary visual cortex (V1), between two different sensory contexts: darkness and visual stimulation. To do this, we used two-photon calcium imaging in head-fixed mice that ran freely on a cylindrical treadmill (Figure 1C). The relative changes in somatic fluorescence of the genetically-encoded calcium indicator GCaMP6f were used as a non-linear readout of the neuronal spiking activity (Chen et al., 2013). Inhibitory neuronal subtypes were labeled by injecting adeno-associated viruses (AAVs) into V1 of Cre-

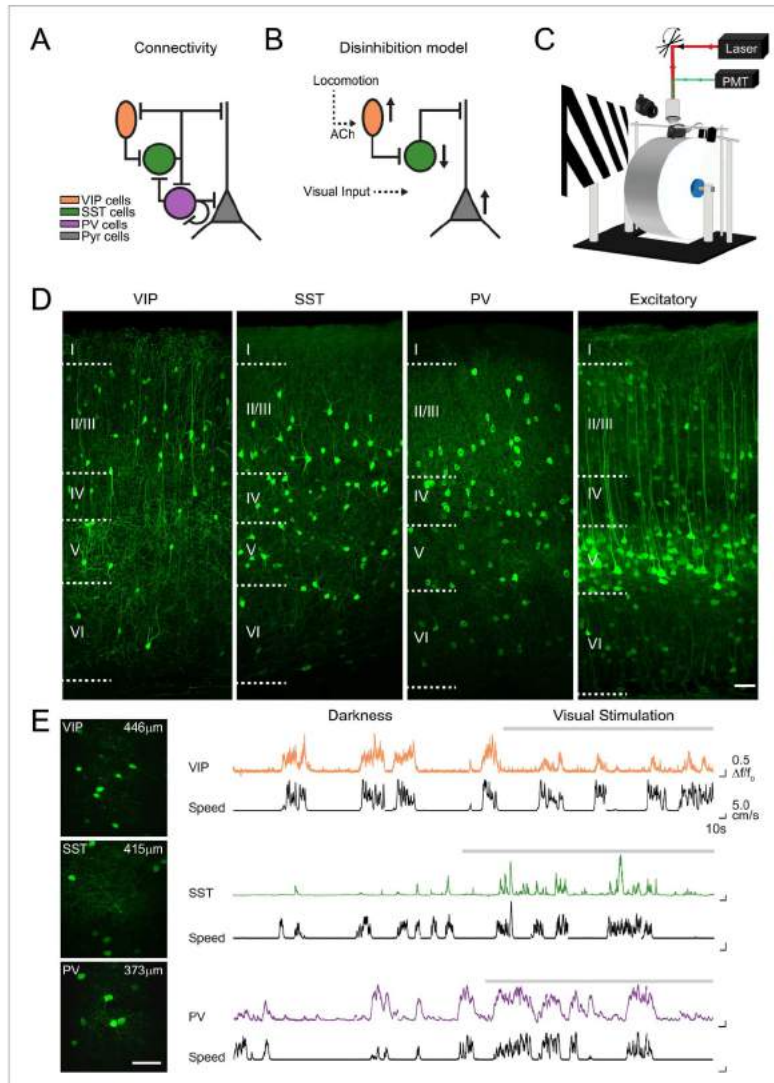


Figure 1. Imaging locomotion responses of excitatory and inhibitory neurons in mouse V1. (A) Schematic of the connectivity between pyramidal neurons (Pyr) and subtypes of inhibitory neurons, vasoactive intestinal peptide (VIP), somatostatin (SST) and parvalbumin (PV) expressing neurons, established from *in vitro* studies in V1 (Pfeffer et al., 2013; Jiang et al., 2015). (B) Proposed disinhibition model: locomotion activates VIP neurons through cholinergic (ACh) inputs, SST neurons are inhibited, which leads to a disinhibition of Pyr neurons and an increase in the gain of visual responses. Figure 1 continued on next page

Figure 1 continued

during locomotion (Fu et al., 2014). (C) Experimental set-up for two-photon calcium imaging in V1 of awake-behaving mice. Mice are head-fixed and can run freely on a cylindrical treadmill either during the presentation of a visual stimulus (oriented gratings) or in darkness. (D) Confocal images of 50 μm thick coronal sections showing cell type specific GCaMP6f expression in VIP, SST and PV-positive inhibitory neurons as well as in CaMKII-positive excitatory populations. Boundaries between cortical layers are indicated. (E) Left panel, in vivo two-photon images of VIP, SST and PV neurons labelled with GCaMP6f; cortical depth of imaging is indicated. Right panel, example calcium transients ($\Delta F/F_0$, colored traces) of single VIP, SST and PV neurons, imaged in darkness and during visual stimulation with oriented gratings (grey bar above trace), and aligned with the corresponding running speed (cm/s, black traces). Scale bars on images, 50 μm .

DOI: 10.7554/eLife.14985.003

recombinase transgenic mice (PV-, SST-, or VIP-Cre mice) for the Cre-inducible expression of the genetically-encoded calcium indicator GCaMP6f (Figure 1D–E; Chen et al., 2013). To image excitatory neurons, we co-injected a floxed version of GCaMP6f and an AAV where Cre expression is driven by a CaMKII promoter, into C57/BL6 mice. After 2–3 weeks of expression, we recorded the running speed and GCaMP6f signals simultaneously, both in total darkness and during visual stimulation (Figure 1E).

Layer 2/3 celltype-specific responses to locomotion differ in darkness and during visual stimulation

Excitatory neurons

We quantified, for each excitatory neuron ($n = 1124$ in 12 mice), the mean amplitude of calcium transients during locomotion periods and stationary periods, both during visual stimulation (drifting gratings) and in darkness (Figure 2A(i),B(i)). In agreement with previous electrophysiological observations (Niell and Stryker, 2010; Keller et al., 2012; Bennett et al., 2013; Polack et al., 2013; Saleem et al., 2013; Erisken et al., 2014; Reimer et al., 2014), we observed that, on average, locomotion increased the amplitude of calcium transients in excitatory neurons during visual stimulation (Figure 2B(i), Figure 2—figure supplement 1B(i)) mean change in fluorescence [$\Delta F/F_0$] = 0.12 ± 0.02 locomotion versus 0.07 ± 0.01 stationary; $p < 0.001$, $n = 12$, Wilcoxon signed rank test). We quantified the effect of locomotion by calculating a locomotion modulation index (LMI) for each neuron, corresponding to the difference between the mean $\Delta F/F_0$ during locomotion (R_L) and stationary (R_S) periods, normalized by the sum of the mean $\Delta F/F_0$ during both behavioral states (LMI = $(R_L - R_S)/(R_L + R_S)$). An LMI equal to 0 indicates no difference between locomotion and stationary periods, while an LMI equal to 0.5 indicates that the average amplitude of calcium transients was three times higher during locomotion than during stationary periods. Comparing the distribution of LMIs between the two sensory contexts, we found that the modulation of the activity of excitatory neurons by locomotion was significantly different in darkness compared to visual stimulation (Figure 2C(i),D(i); mean of median LMI: 0.07 ± 0.02 darkness versus 0.19 ± 0.02 visual stimulation; $p = 0.001$, $n = 12$, Kruskal–Wallis test). During visual stimulation, 47 \pm 4% of excitatory neurons were significantly locomotion responsive (see Materials and methods for locomotion responsive criteria), compared with 28 \pm 4% in darkness. Additionally, in the dark, a small proportion of neurons were inhibited by locomotion, decreasing their activity during locomotion periods relative to stationary periods (10 \pm 1% of neurons).

VIP neurons

As reported in previous studies (Fu et al., 2014; Reimer et al., 2014; Jackson et al., 2016), we found that VIP neurons ($n = 210$ in 12 mice) strongly responded to locomotion (Figure 1E and Figure 2A(ii),B(ii)). This was true both in darkness (mean $\Delta F/F_0 = 0.51 \pm 0.12$ locomotion versus 0.10 ± 0.03 stationary; $p < 0.001$, $n = 12$, Wilcoxon signed rank test) as well as during visual stimulation (mean $\Delta F/F_0 = 0.42 \pm 0.14$ locomotion versus 0.09 ± 0.02 stationary; $p < 0.001$, $n = 12$) with no significant difference in the average LMI between sensory contexts (Figure 2C(ii),D(ii)), mean of median LMI: 0.60 ± 0.05 darkness versus 0.49 ± 0.06 visual stimulation; $p = 0.106$, $n = 12$, Kruskal–Wallis test; see also Figure 2—figure supplement 1B(ii)). A high proportion of VIP neurons were significantly locomotion responsive in both sensory contexts (85 \pm 7% in darkness and 79 \pm 6% during visual stimulation).

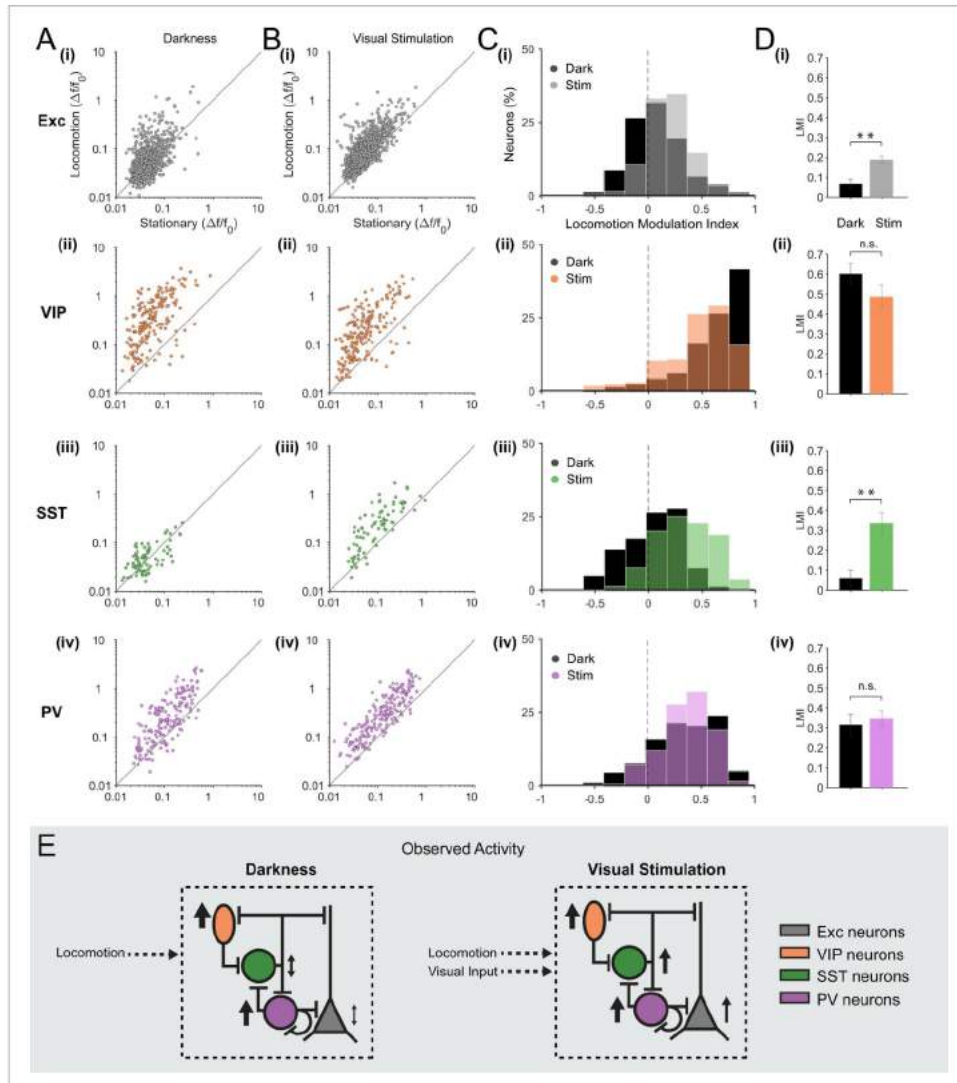


Figure 2. Locomotion differentially modulates excitatory and inhibitory neuronal responses in darkness and during visual stimulation in V1 layer 2/3. (A–B) Scatter plots of the mean amplitude of fluorescence changes ($\Delta F/F_0$) of each neuron for locomotion periods versus stationary periods, in darkness (A) and during visual stimulation (oriented gratings) (B); (i) excitatory cells (Exc), $n = 1124$; (ii) VIP, $n = 210$; (iii) SST, $n = 79$; (iv) PV, $n = 199$ neurons. (C) Histograms of the distribution of locomotion modulation indices (LMI = $(R_L - R_S)/(R_L + R_S)$), where R_L and R_S are the mean $\Delta F/F_0$ during locomotion and stationary periods, respectively. (D) Bar graphs of the mean LMI for each neuron type. (E) Schematic diagram of the observed activity. *Figure 2 continued on next page*

Figure 2 continued

stationary periods, respectively), for each cell type, in darkness (Dark, black) and during visual stimulation (Stim, colored). An LMI equal to 0 indicates no difference between locomotion and stationary periods, while an LMI equal to 0.5 indicates that the average amplitude of calcium transients was three times higher during locomotion than during stationary periods. (D) Mean of the median LMI per animal and s.e.m. ** $p < 0.01$, n.s., not significant ($p > 0.05$); $n = 12$ (i), 12 (ii), 11 (iii), 13 (iv) mice; Kruskal–Wallis test. (E) Schematic representation of the results. Size and direction of the arrows indicate the average response per cell type during locomotion (increasing or decreasing activity). In darkness, SST and excitatory neurons were largely non-responsive to locomotion while VIP and PV neurons were strongly activated by locomotion. However, during visual stimulation, locomotion increases the responses of excitatory neurons as well as of the three classes of inhibitory neurons (VIP, SST and PV).

DOI: 10.7554/eLife.14985.004

The following figure supplements are available for figure 2:

Figure supplement 1. Modulation of excitatory and inhibitory neurons responses by locomotion during the presentation of patterned (oriented gratings) and non-patterned (grey screen) visual stimuli.

DOI: 10.7554/eLife.14985.005

Figure supplement 2. Cross correlation of fluorescence changes ($\Delta F/F_0$) with running speed.

DOI: 10.7554/eLife.14985.006

Figure supplement 3. Visual responsiveness of excitatory and inhibitory neurons during stationary and locomotion periods.

DOI: 10.7554/eLife.14985.007

In order to compare our results directly with previous findings (Fu et al., 2014), we calculated the cross-correlation between VIP calcium signals and running speed. We confirmed the presence of a single positive peak around time zero, both in darkness and during visual stimulation (Figure 2—figure supplement 2A(ii)). We also observed a lower amplitude during visual stimulation but this decrease was not significant (mean zero-time correlation: 0.26 ± 0.04 in darkness versus 0.20 ± 0.02 during visual stimulation; $p = 0.225$, $n = 12$, Kruskal–Wallis test; Figure 2—figure supplement 2C). Similarly, the mean $\Delta F/F_0$ (Figure 2—figure supplement 3C(ii)) and the mean LMI (Figure 2D(ii)) of VIP neurons also decreased during visual stimulation, without reaching significance (mean $\Delta F/F_0 = 0.51 \pm 0.12$ in darkness versus 0.42 ± 0.14 during visual stimulation; $p = 0.151$, $n = 12$, Wilcoxon signed rank test).

SST neurons

In contrast to VIP neurons, responses of SST neurons ($n = 79$ in 11 mice) to locomotion were found to be highly context-dependent. During visual stimulation, the mean $\Delta F/F_0$ during locomotion periods was significantly higher than during stationary periods (Figure 2B(iii), Figure 2—figure supplement 1B(iii); mean $\Delta F/F_0 = 0.25 \pm 0.05$ locomotion versus 0.10 ± 0.03 stationary; $p = 0.001$, $n = 11$, Wilcoxon signed rank test). However, in darkness, SST neurons were either non-responsive, increased or even decreased their activity during locomotion with, on average, no significant difference between locomotion and stationary periods (Figure 2A(iii), Figure 2—figure supplement 1B(iii); mean $\Delta F/F_0 = 0.06 \pm 0.02$ locomotion versus 0.06 ± 0.01 stationary; $p = 0.102$, $n = 11$, Wilcoxon signed rank test). As a result, the modulation of SST neuron responses by locomotion was found to be significantly different across sensory contexts (Figure 2C(iii), D(iii)), mean of median LMI: 0.06 ± 0.04 darkness versus 0.33 ± 0.06 visual stimulation; $p = 0.002$, $n = 11$, Kruskal–Wallis test). During visual stimulation, $63 \pm 7\%$ of SST neurons were significantly locomotion responsive (increasing their activity) and only $4 \pm 3\%$ were decreasing their activity during locomotion. In darkness, the percentage of neurons increasing their activity dropped to $24 \pm 6\%$ with an additional $11 \pm 5\%$ of SST neurons decreasing their activity during locomotion.

In line with these results, the cross-correlation between SST calcium transients and running speed significantly increased during visual stimulation compared to darkness (mean zero-time correlation = 0.04 ± 0.01 in darkness versus 0.13 ± 0.01 during visual stimulation; $p = 0.001$, $n = 11$, Kruskal–Wallis test; Figure 2—figure supplement 2C). Notably, SST neurons were strongly responsive to visual stimulation (Figure 2—figure supplement 3(iii); mean $\Delta F/F_0$ during locomotion = 0.06 ± 0.02 darkness versus 0.25 ± 0.05 visual stimulation; $p = 0.001$, $n = 11$, Wilcoxon signed rank test). These results indicate that most SST neurons respond to visual stimuli and, in addition to this visual response, they become responsive to locomotion. In darkness, however, they have low spontaneous activity and are largely non-responsive to locomotion (Figure 2E).

PV neurons

Finally, PV neurons ($n = 199$ in 13 mice) were strongly responsive to locomotion in both sensory contexts (Figure 2A(iv),B(iv), Figure 2—figure supplement 1B(iv); dark: mean $\Delta F/F_0 = 0.33 \pm 0.07$ locomotion versus 0.13 ± 0.02 stationary; $p=0.001$; visual stimulation: mean $\Delta F/F_0 = 0.41 \pm 0.08$ locomotion versus 0.16 ± 0.03 stationary; $p<0.0001$; $n = 13$ Wilcoxon signed rank test), with no significant difference between sensory conditions (Figure 1E, Figure 2C(iv),D(iv); mean of median LMI: 0.32 ± 0.06 darkness versus 0.35 ± 0.04 visual stimulation; $p=0.663$, $n = 13$, Kruskal–Wallis test). Similarly, the cross-correlation between running speed and calcium transients showed a positive peak around time zero both in darkness and during visual stimulation, with no significant difference ($p=0.778$; $n = 13$, Kruskal–Wallis test; Figure 2—figure supplement 2).

Modulation of neuronal responses by locomotion during patterned and non-patterned visual stimuli

Isoluminant grey screen stimulation is commonly used to record so called ‘spontaneous activity’ of neurons in the visual cortex. Since our results showed different locomotion responses in the dark and during the presentation of drifting gratings, we tested whether this difference was due to the presence of patterned visual stimuli or, more simply, to the presence of light (Figure 2—figure supplement 1). We quantified the amplitude of fluorescence changes during stationary and locomotion periods in all three contexts: darkness, grey screen and drifting gratings. We did not find any significant difference for any of the inhibitory populations (VIP, SST and PV neurons) between the two types of visual stimulation (gratings vs grey screen; Figure 2—figure supplement 1C). For excitatory neurons, we found a lower LMI during the presentation of a grey screen than during drifting grating presentation (mean of median LMI: 0.17 ± 0.02 grey versus 0.19 ± 0.02 visual stimulation; $p=0.033$, $n = 12$, Kruskal–Wallis test; Figure 2—figure supplement 1C(i)). Locomotion responses for each type of visual stimulus (gratings vs grey screen) were still significantly higher than during darkness (mean of median LMI: 0.07 ± 0.02 dark versus 0.17 ± 0.02 grey; $p=0.007$, $n = 12$, Kruskal–Wallis test) (Figure 2—figure supplement 1C(i)). These results indicate that, during visual stimulation and independently of the presence of patterned visual stimuli, excitatory, VIP, SST and PV neurons show increased activity during locomotion.

Diversity of context-dependent locomotion responses within cell types

While comparisons of a neuronal population’s LMI distribution (Figure 2C) indicates how, on average, that cell type is modulated by locomotion in different sensory contexts, it does not provide information about the context-dependent responses of single neurons. For instance, the average LMI could be the same in darkness and during visual stimulation even though individual neurons may have large changes in their LMI, which cancel out when considering the population as a whole.

In order to show the diversity of locomotion responses within each neuronal subtype, we examined the LMI value in darkness versus during visual stimulation for each neuron (Figure 3A). Neurons near the identity line show context-independent locomotion responses (similar LMI in darkness and during visual stimulation), while the other neurons changed their response to locomotion from one context to another (context-dependent responses). We first quantified this diversity by calculating the difference between the LMI value during visual stimulation and the LMI value in darkness for each neuron (Figure 3B). These results confirmed that VIP neurons displayed mainly context-independent locomotion responses (Figure 3B(ii), narrow distribution, centered around 0), while locomotion responses of SST neurons were mainly context dependent (Figure 3B(iii), broad distribution shifted towards positive values). Both excitatory and PV neuronal populations included a diversity of locomotion responses (broad distributions). To quantify the proportions of context-independent and context-dependent neurons in each cell type, we first determined the variability of the locomotion responses for each context by comparing neuronal responses across odd and even locomotion periods (Figure 3—figure supplement 1; see Materials and methods). We found high correlation values for all neuronal populations, both in darkness and during visual stimulation ($0.676 < R < 0.944$; $p<0.0001$), indicating a general low variability of the responses across different locomotion periods in both contexts. We determined the proportion of context-dependent neurons meeting two criteria: i) with a response that was significantly different across contexts (neurons distance from the identity line in Figure 3A, to estimate the error on the LMI in both dark and stimulated conditions for

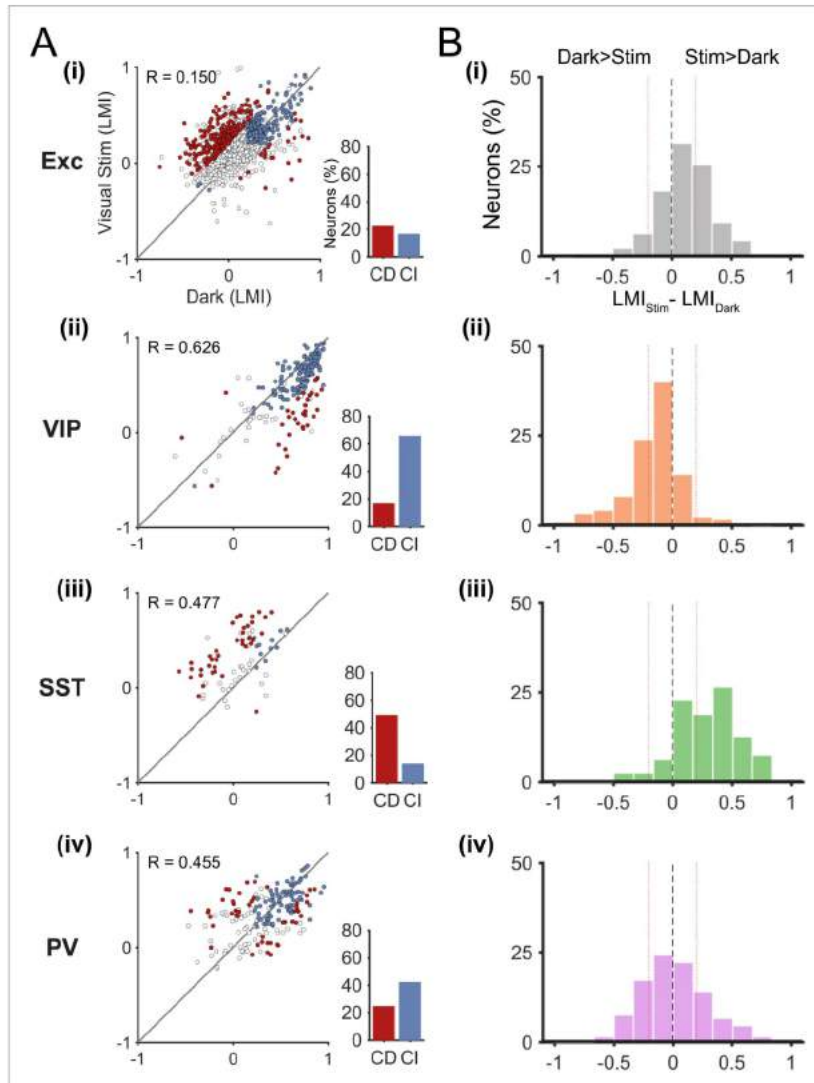


Figure 3. Context-dependent responses to locomotion of individual excitatory and inhibitory neurons in layer 2/3. (A) Left panels, scatter plots of the locomotion modulation index (LMI) of individual neurons in darkness versus during visual stimulation (gratings) with an associated Pearson correlation coefficient (R-values). Context-dependent (CD; red) and context-independent (CI; blue) locomotion responsive neurons are highlighted. Context dependency was defined for each neuron by its distance from the identity line and the variability of its locomotion responses (see Materials and Figure 3 continued on next page

Figure 3 continued

methods and **Figure 3—figure supplement 1**). Neurons that were either non-responsive to locomotion or responded unreliably are shown as open circles. Right panels, percentages of context-dependent (CD) and context-independent (CI) neurons for each neuronal subtype. Note the high proportion of CI VIP neurons (66%), the high proportion of CD SST neurons (49%), and the diversity of both PV and excitatory (Exc) neurons. **(B)** Histograms of the difference between the LMI value in darkness and during visual stimulation ($LMI_{\text{Stim}} - LMI_{\text{Dark}}$) for each neuronal population. Negative values indicate increased responses to locomotion in darkness compared with visual stimulation, positive numbers indicate increased responses to locomotion during visual stimulation, and numbers close to 0 (within red lines; $-0.2 < LMI_{\text{Stim}} - LMI_{\text{Dark}} < 0.2$) indicate context-independent responses.

DOI: 10.7554/eLife.14985.008

The following figure supplements are available for figure 3:

Figure supplement 1. Variability of locomotion responses in darkness and during visual stimulation.

DOI: 10.7554/eLife.14985.009

Figure supplement 2. Representative examples of calcium transients ($\Delta F/F_0$) of context-independent and context-dependent neurons, in darkness and during visual stimulation with oriented gratings (grey bar above trace).

DOI: 10.7554/eLife.14985.010

each neuron, bootstrapping was employed (see Materials and methods)), and ii) with low variability of locomotion responses (**Figure 3—figure supplement 1**).

These results confirm that most VIP neurons were context-independent, remaining locomotion-responsive in both sensory contexts (66%), with only 17% of neurons showing context-dependent responses (**Figure 3A(ii)**, **Figure 3—figure supplement 2**). The proportion of context-dependent neurons was the highest among SST neurons, with 49% of neurons showing context-dependent responses to locomotion (**Figure 3A(iii)**, **Figure 3—figure supplement 2**). Both excitatory and PV neurons had approximately the same proportion of context-dependent neurons (22% for excitatory and 25% for PV neurons) (**Figure 3A(i)**, (iv)).

Finally, we tested whether context-dependent neurons differ from context-independent ones with regard to the following characteristics: percentage of visually responsive neurons, orientation selectivity and direction selectivity. We did not find any significant difference in any neuronal population (comparisons between context-dependent and context independent neurons for each cell type, OSI, $p > 0.261$; DSI $p > 0.093$, Kruskal–Wallis test), suggesting that the mechanisms underlying the modulation of locomotion responses differ from those determining the selectivity of visual responses.

Layer 4 excitatory and inhibitory responses to locomotion are similar to layer 2/3

Layer 2/3 neurons receive sensory information from excitatory neurons in layer 4, the main thalamo-recipient layer, as well as top-down information from higher cortical areas (Niell, 2015). In addition, these neurons receive subcortical inputs from the dorsal lateral geniculate nucleus as well as neuromodulatory inputs (Polack et al., 2013; Fu et al., 2014; Lee et al., 2014). Context-dependent locomotion responses of layer 2/3 neurons may thus come from one of these distinct inputs or from a combination of them. By using the same approach as for layer 2/3 neurons, we recorded locomotion responses in layer 4 neurons (excitatory $n = 331$; VIP $n = 57$; SST $n = 74$; PV $n = 109$; in 6, 4, 6 and 6 mice, respectively). As in layer 2/3, we used local injections of AAVs into V1 for the Cre-inducible expression of the genetically-encoded calcium indicator GCaMP6f. However, we observed that on average the GCaMP6f labelling in layer 4 was sparser than in layer 2/3 (**Figure 1D**). Thus, we cannot exclude that we preferentially labelled subtypes of layer 4 neurons in which transduction efficiency with these AAV vectors would be higher. The quantification of locomotion responses showed no significant difference between layer 2/3 and layer 4 neurons, in any cell type, both in darkness and during visual stimulation (**Figure 4B,C**). The results showed a higher mean LMI value for PV neurons in layer 4 (0.45 ± 0.04) compared to layer 2/3 (0.35 ± 0.04) during visual stimulation. However, this did not reach significance; $p = 0.058$, Mann-Whitney U-test). In addition, the results showed similar proportions of context-dependent responses in layer 4 as described in layer 2/3 (**Figure 4A**, see also **Figure 3A**; context-dependent neurons: Exc, L2/3: 22%, L4: 17%; VIP, L2/3: 17%, L4: 26%; SST, L2/3: 49%, L4: 42%; PV, L2/3: 25%, L4: 23%).

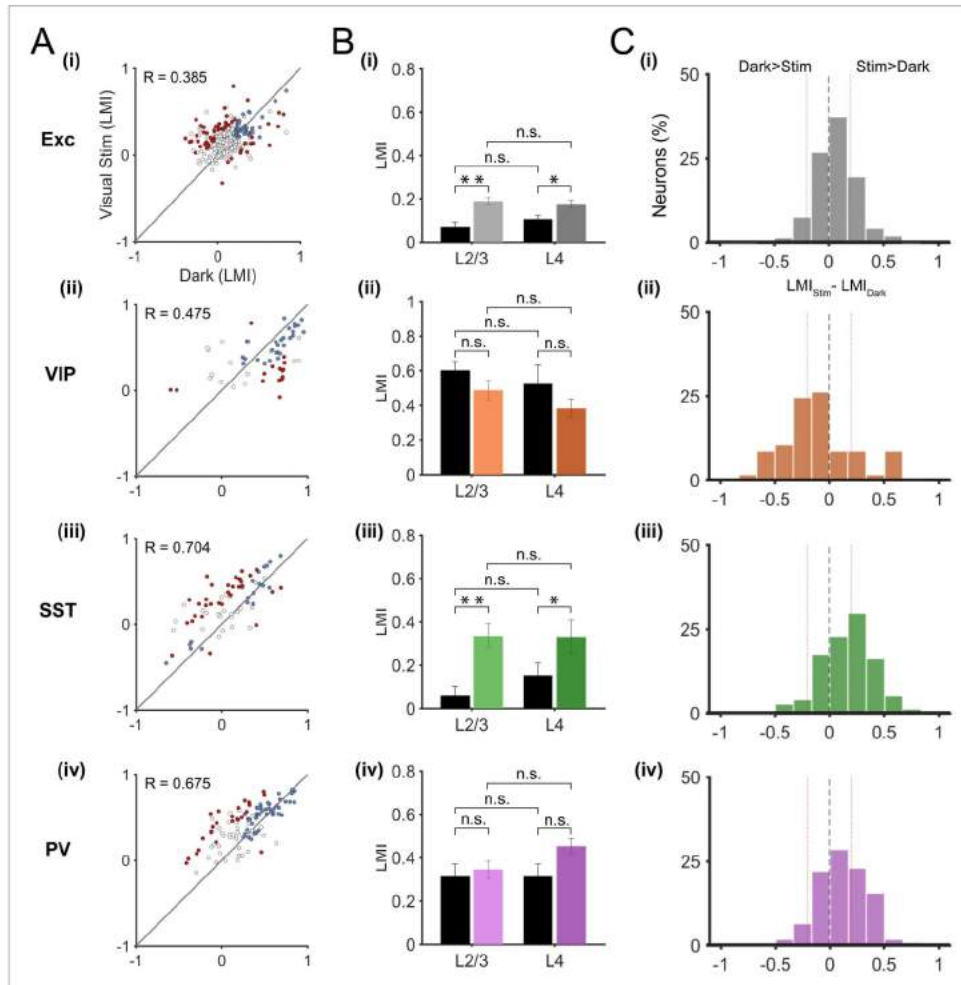


Figure 4. Locomotion responses of individual inhibitory and excitatory neurons in V1 cortical layer 4. **(A)** Scatter plots of locomotion modulation index (LMI) of individual neurons in darkness versus during visual stimulation (oriented gratings), with associated Pearson correlation coefficient (R -values) for excitatory (Exc; $n = 331$), VIP ($n = 57$), SST ($n = 74$), and PV ($n = 109$) neurons. Context-dependent (red) and context-independent (blue) locomotion responsive neurons are highlighted. Context dependency per neuron was defined by its distance from the identity line and its variability to locomotion periods (see Materials and methods). Neurons that were either non-responsive to locomotion or responded unreliably are shown as open circles. **(B)** Mean of the median LMI per animal and s.e.m. for layer 2/3 (L2/3) as well as layer 4 (L4), in darkness (Dark, black bars) and during visual stimulation (Stim, colored bars) for Exc (L2/3, $n = 12$; L4, $n = 6$), VIP (L2/3, $n = 12$; L4, $n = 4$), SST (L2/3, $n = 11$; L4, $n = 6$), and PV (L2/3, $n = 13$; L4, $n = 6$) mice. Within each cell type, there was no significant difference (n.s., $p > 0.05$, Mann-Whitney U test) between the median LMI across layers in either context (darkness: Exc, $p = 0.151$; VIP, $p = 0.521$; SST, $p = 0.350$; PV, $p = 0.966$; visual stimulation: Exc, $p = 0.750$; VIP, $p = 0.133$; SST, $p = 0.961$; PV, $p = 0.058$). **(C)** Histograms of the

Figure 4 continued on next page

Figure 4 continued

difference between the LMI value in darkness and during visual stimulation ($LMI_{\text{Stim}} - LMI_{\text{Dark}}$) for each cell type. Negative values indicate increased responses to locomotion in the dark compared with visual stimulation, positive numbers indicate increased responses to locomotion during visual stimulation, and numbers close to 0 (within red lines; $-0.2 < LMI_{\text{Stim}} - LMI_{\text{Dark}} < 0.2$) indicate context-independent responses.

DOI: 10.7554/eLife.14985.011

Discussion

The increased gain of visual responses during locomotion provides a model to elucidate the circuit mechanisms underlying behavioral-state dependent changes of sensory responses. In this study, we found that the modulation of neuronal activity by locomotion is context-dependent and cell type specific, in layer 2/3 and layer 4 of mouse V1. During periods of visual stimulation, locomotion increases the activity of excitatory neurons as well as of three classes of inhibitory neurons (VIP, SST, PV; Figure 2E). These results indicate that the enhancement of excitatory neuron visual responses during locomotion does not result from the inhibition of SST neurons, in mouse V1. Our findings thus challenge the generality of a disinhibitory circuit involving VIP, SST and pyramidal neurons for the gain control of sensory responses by behavioral state.

Relationship between somatic fluorescence changes and spiking activity in different neuronal types and behavioral contexts

In this study, we used the relative changes in fluorescence of the genetically-encoded calcium indicator GCaMP6f as a reporter of the spiking activity of cortical neurons (Chen et al., 2013). For a given fluorescent calcium indicator, the relationship between the amplitude of somatic fluorescence changes and the number of spikes can be affected by a number of factors including the concentration of calcium buffers in the soma, the balance between calcium influx and efflux as well as calcium release from internal stores (Grienberger et al., 2012). Consequently, potential confounding factors in the present study would be (1) different intracellular calcium dynamics in different types of inhibitory neurons as well as (2) a higher increase of cytosolic free calcium concentration for the same number of spikes during locomotion compared to stationary periods. Considering that neuromodulators can regulate calcium influx (Fucile, 2004; Shen and Yakel, 2009), this second possibility may result from the action of neuromodulators released during locomotion that would increase the amount of calcium entering the neuron in response to each spike. In that case, for the same number of spikes, the increase in fluorescence of our calcium indicator would be higher during locomotion than during stationary periods.

Without an independent readout of the spiking activity for each neuronal type in each behavioral context, we cannot exclude that the relationship between fluorescence transients and the number of spikes differ between different neurons and different contexts. However, the comparison of our results (mean $\Delta F/F_0$, Figure 2—figure supplement 1B, 'stim' column) with spiking frequencies published in a previous study (see Supplementary Table 3 of Polack et al., 2013) in mouse V1 strongly suggests that somatic GCaMP6f fluorescence changes do reflect changes in spiking activity related to locomotion. For the same neuronal populations (layer 2/3 Excitatory, SST and PV neurons; layer 4 Excitatory neurons) and visual stimulation condition (drifting gratings), both data sets show the same relative change in signal during locomotion compared to stationary periods (corresponding to an approximate doubling of activity during locomotion for all three cell types). This similarity suggests that somatic GCaMP6f fluorescence changes during locomotion do reflect changes in spiking activity, at least in these cell types during visual stimulation.

Comparison with previous findings: locomotion responses differ in darkness and during visual stimulation

In this study, we found that SST activity increased with locomotion during visual stimulation. This is in line with previous electrophysiological recordings of SST neurons (Polack et al., 2013) but in contradiction with the current disinhibitory model that relies on the inhibition of SST neurons during locomotion (Figure 1B; Fu et al., 2014). Our results provide an explanation for these discrepancies since the aforementioned electrophysiological recordings were acquired during visual stimulation whereas imaging of SST activity was done in the dark (Fu et al., 2014). The disinhibitory model was

based on the assumption that the locomotion-driven response of SST neurons would be similar in the dark and during visual stimulation (Fu et al., 2014). The same assumption was made in the interpretation of membrane potential fluctuations of VIP and SST neurons recorded during the presentation of a blank screen (Reimer et al., 2014). While VIP neurons were reliably depolarized during running, the SST population was heterogeneous. The authors distinguished two populations of SST interneurons (see Supplementary Figure 5C of Reimer et al., 2014): Type I cells were inhibited by running while Type II cells were depolarized. Importantly, spiking activity of SST neurons was not reported and it is thus not clear how the membrane potential fluctuations relate to spiking activity.

Our findings regarding the locomotion responses of SST neurons in darkness are consistent with the previous imaging study performed in similar conditions (Figure 2—figure supplement 2 of the present study compared to Figure 3 and Figure S3 of Fu et al., 2014) as well as with the heterogeneity of membrane potential fluctuations of SST neurons during locomotion (Reimer et al., 2014). We cannot exclude the possibility that a disinhibitory circuit may underlie the activity of a small fraction of neurons in darkness: the majority of VIP neurons increase their activity with locomotion, while a small proportion of SST neurons are inhibited during locomotion, potentially leading to the increase in activity of some pyramidal neurons. However, the results obtained in darkness show that the majority of SST neurons are not responsive to locomotion at all, challenging the generality of a disinhibitory circuit acting through the inhibition of SST neurons. With visual stimulation, the inconsistency of the disinhibitory model is even stronger since the vast majority of SST neurons increase their activity with locomotion (see Figure 2B(iii)). Consequently, the results obtained during visual stimulation (present study and Polack et al., 2013) are incompatible with a model in which VIP neurons disinhibit excitatory neurons by inhibiting SST neurons. Additionally, while the vast majority of VIP neurons are context-independent with regard to their locomotion response, excitatory neurons show significantly increased locomotion responses during visual stimulation compared to darkness conditions. Therefore, the context-dependent responses of excitatory neurons do not result from a disinhibitory circuit initiated by VIP neurons.

An appealing aspect of the disinhibitory model was the idea of a canonical circuit for gain modulation of sensory responses (Pi et al., 2013). While the connectivity may be canonical, we show that the circuit activity can strongly differ depending on the behavioral context. Therefore, functional properties of inhibitory neurons should not be generalized from one context to the next, and caution should be taken when inferring connectivity from functional recordings obtained in a specific behavioral context.

Alternative circuit mechanisms for behavioral-state modulation of visual responses in V1

Our results indicate that, in addition to the activation of VIP neurons during locomotion, other pathways are involved in linking locomotion and visual responses in V1. We suggest that neuromodulatory inputs triggered by locomotion would not only activate VIP neurons through nicotinic acetylcholine receptors as previously shown (Alitto and Dan, 2012; Arroyo et al., 2014; Fu et al., 2014), but would also directly activate PV, SST, and excitatory neurons. Previous work has demonstrated cholinergic facilitation of cortical inhibitory neurons (Kawaguchi, 1997; Xiang et al., 1998; Arroyo et al., 2012; Alitto and Dan, 2012), including SST neurons (Kawaguchi, 1997; Fanselow et al., 2008; Xu et al., 2013; Chen et al., 2015). Similarly, in vitro studies have shown that norepinephrine can depolarize both excitatory (McCormick et al., 1993; Kirkwood et al., 1999) and inhibitory (Kawaguchi and Shindou, 1998) cortical neurons. Finally, in vivo studies have shown that neuromodulatory inputs, cholinergic and noradrenergic, can control the gain and signal-to-noise ratio of V1 excitatory neurons during locomotion (Pinto et al., 2013; Polack et al., 2013; Bennett et al., 2014; Lee et al., 2014). We suggest that in darkness, the effect of neuromodulatory inputs remains subthreshold in SST neurons. During visual stimulation, SST neurons are strongly activated and the effect of neuromodulatory inputs becomes suprathreshold. In agreement with the known intra-cortical connectivity in mouse V1 (Figure 1A; Pfeffer et al., 2013; Jiang et al., 2015), our findings support this neuromodulatory hypothesis. In darkness, VIP and PV neurons are activated by locomotion and inhibit SST and excitatory neurons, preventing their activation by locomotion-dependent inputs. During visual stimulation, SST and excitatory neurons are activated: they overcome the intra-cortical inhibition by VIP and PV neurons and become responsive to direct locomotion-dependent inputs. Since SST neurons provide the main intra-cortical input to VIP neurons

(Pfeffer et al., 2013) and are strongly visually-responsive, they likely inhibit VIP neurons (or a sub-population of VIP neurons) during visual stimulation. This is consistent with the decrease in activity of a portion of VIP neurons that was observed during visual stimulation (Fu et al., 2014; see also Figure 2—figure supplement 3B(ii)).

An alternative or complementary hypothesis to the neuromodulatory pathway is that the modulation of visual inputs by locomotion already takes place in subcortical nuclei, such that the thalamo-cortical inputs received by excitatory neurons, and potentially SST neurons, would convey the increased gain of visual responses during locomotion. Indeed, recent studies have shown that projections from the dorsal lateral geniculate nucleus (Erisken et al., 2014; Roth et al., 2016) and from the thalamic latero-posterior nucleus (Roth et al., 2016) to V1 both convey locomotion signals.

The diversity of context-dependent responses to locomotion within SST, PV and, to a lesser extent, VIP populations indicates that there are functional sub-types within each of these interneuron populations. Based on a comprehensive analysis of morphological and electrophysiological properties of inhibitory neurons, a recent in vitro study has identified seven distinct types of cortical interneurons in layer 2/3 (Jiang et al., 2015). Further, in vivo characterization of the activity of these sub-types will be necessary to identify how these populations relate to the different context-dependent responses identified in the present study.

Materials and methods

Animals

Three Cre-driver transgenic mice lines were used to label inhibitory interneurons: *Sst*<tm2.1(cre)Zjh> (SST-Cre) [RRID:IMSR_JAX:013044], *Pvalb*<tm1(cre)Arbr> (PV-Cre) [RRID:IMSR_JAX:008069], *Vip*<tm1(cre)Zjh> (VIP-Cre) [RRID:IMSR_JAX:010908], all originally obtained from Jackson Laboratory, ME, USA. These lines were cross-bred with *Rosa-CAG-LSL-tdTomato* [RRID:IMSR_JAX:007914] mice. C57Bl/6 wild type mice (Jackson Laboratory, ME) were used for virus injections targeting the expression of GCaMP6 in CaMKII-expressing neurons. Mice were group housed (typically 2–4 mice) and both male and female mice were used for the experiments. All procedures were approved by the University of Edinburgh animal welfare committee, and were performed under a UK Home Office project license.

Surgical procedures

Virus injections

For virus injections, 8- to 10-week-old mice were anesthetized with isoflurane (4% for induction and 1–2% maintenance during surgery) and mounted on a stereotaxic frame (David Kopf Instruments, CA). Eye cream was applied to protect the eyes (Bepanthen, Bayer, Germany) and analgesics were injected subcutaneously (Vetergesic, buprenorphine, 0.1 mg/kg of body weight). After an incision was made in the scalp, the bone surface was cleaned and a small craniotomy was performed over the left V1 (3.5 mm lateral and 1 mm anterior to lambda with an injection pipette inserted 70° from vertical and 30° from midline). Adeno-associated viruses (AAVs) were injected using a pipette with 20 µm tip diameter (Nanoject, Drummond Scientific, PA) at a speed of 10 nl min⁻¹ at three different depths (around 250, 400, and 600 µm deep; 50 nl per site). AAVs used in this study include: AAV1.Syn.Flex.GCaMP6f.WPRE.SV40 to label SST, PV, and VIP cells in Cre-driver transgenic mice as well as AAV1.Syn.GCaMP6f.WPRE.SV40 in tdTomato crosses (see above) and AAV1.CaMKII0.4.Cre.SV40 with AAV1.Syn.Flex.GCaMP6f.WPRE.SV40 in C57Bl/6 wild type mice (all AAVs acquired from the University of Pennsylvania Vector Core, PA). After each injection, pipettes were left in situ for an additional 5 min to prevent backflow. The skin was then sutured and mice were monitored until they recovered from anesthesia. The animals were returned to their home cage for 2–3 weeks.

Head-plate and imaging window

Mice were anesthetized with isoflurane (4% for induction and 1–2% maintenance during surgery) and mounted in a stereotaxic frame. Eye cream was applied to protect the eyes (Bepanthen, Bayer, Germany), analgesics and anti-inflammatory drugs were injected subcutaneously (Vetergesic, buprenorphine, 0.1 mg/kg of body weight, carprofen, 0.15 mg, and dexamethasone, 2 µg). A section of scalp was removed and the underlying bone was cleaned before a craniotomy (around 2 × 2 mm) was

made over the left V1 (centered around 2.5 mm lateral and 0.5 mm anterior to lambda). The craniotomy was then sealed with a glass cover slip and fixed with cyano-acrylic glue. A custom-built headpost was implanted on the exposed skull with glue and cemented with dental acrylic (Paladur, Heraeus Kulzer, Germany).

Two-photon calcium imaging

Imaging was performed using a custom-built resonant scanning two-photon microscope with a Ti:Sapphire pulsing laser (Chameleon Vision-S, Coherent, CA, USA; < 70 fs pulse width, 80 MHz repetition rate) tuned to 920 nm. Using a 40X objective (0.8 NA, Nikon), 600×600 pixel images with a field-of-view of 250 × 250 μm were acquired at 40 Hz with custom-programmed LabVIEW based software (version 8.2; National Instruments, UK).

We used two-photon calcium imaging in head-fixed mice that ran freely on a cylindrical treadmill (Figure 1C; Dombeck et al., 2007). Habituation and imaging started 2–3 weeks after AAV injection. Mice were habituated to head-fixation in the dark for 45 min and began to run freely on a polystyrene cylinder (20 cm diameter, on a ball-bearing mounted axis). The mice's running speed on the circular treadmill was continuously monitored using an optical encoder (E7P, 250cpr, Pewatron, Switzerland) connected to a data acquisition device (National Instrument, UK) with custom-written software in LabView (National Instrument, UK) and analyzed in MATLAB (Mathworks, MA). Mice could run freely and spent on average $26 \pm 2\%$ of the time running in the dark and $41 \pm 2\%$ during visual stimulation (n = 48 mice, 51 sessions).

Two-photon imaging was performed at 2–3 focal planes per mouse, at cortical depths between 130 and 350 μm for L2/3 neurons and 350–500 μm for L4 neurons (cortical layers were confirmed on histological sections, see below). Laser power at the brain surface was kept below 50 mW. Mice with excessive brain movement artifacts were excluded. At each focal plane (n = 100 fields of view), 8–12 trials (60 s duration) were acquired in total darkness and 12–20 trials acquired during visual stimulation, with dark and visual stimulation trials randomly interleaved.

Visual stimuli were generated using the Psychophysics Toolbox package (Brainard, 1997) for MATLAB (Mathworks, MA) and displayed on an LCD monitor (51 × 29 cm, Dell, UK) placed 20 cm from the right eye, covering $104^\circ \times 72^\circ$ of the visual field. Visual stimulation trials consisted of stationary full-field square-wave gratings for 4–5 s and the corresponding drifting phase for 2 s (0.03 cpd, 1 Hz, 8 equally spaced directions in randomized order, contrast 80%, mean luminance 37 cd/m²). Each trial started and ended with a grey screen (isoluminance). Additional grey screen data were obtained during the presentation of an isoluminant grey screen for 5–15 s preceding the presentation of each oriented grating for 5 s (0.03 cpd, 1 Hz, 4 equally spaced orientations in randomized order, contrast 80%, mean luminance 37 cd/m²).

At the end of the imaging session, red retrograde beads (Lumafuor, USA) were injected either at the surface or at 2 different focal planes at which neurons had been imaged. This red labelling was used as a structural landmark in histological sections to confirm which cortical layers had been imaged.

Histology

Animals were transcardially perfused with 0.9% saline and 4% PFA in phosphate buffer (0.1 M). Brains were sliced with a vibratome (50 μm thick) and rinsed in phosphate buffered saline (PBS). The slices were then mounted and counterstained with either DAPI (Vectashield mounting medium, Vector Labs, UK) or NeuroTrace 640/660 fluorescent Nissl stain (1:2000; RRID:nlx_152414, Life Technologies, NY) and coverslipped. Sections were imaged with a confocal microscope (Nikon A1R, Nikon Instruments, UK) to define the boundaries of cortical layers and localize the retrograde beads injected at the imaged focal planes in vivo.

Data analysis

Image analysis

To correct for brain motion after image acquisition, we used 2D plane translation-based image alignment (SIMA 1.2.0, sequential image analysis; Kaifosh et al., 2014). Regions of interest (ROIs) corresponding to neuronal cell bodies were selected manually by inspecting down-sampled frames (2 Hz), as well as the maximum intensity projection of each imaging stack (60 s trial). The pixel intensity

within each ROI was averaged to create a raw fluorescence time series $F(t)$. Baseline fluorescence F_0 was computed for each neuron by taking the fifth percentile of the smoothed $F(t)$ (1 Hz lowpass, zero-phase, 60th-order FIR filter) over each trial ($F_0(t)$), averaged across all trials. As a consequence, the same baseline F_0 was used for computing the changes in fluorescence in darkness and during visual stimulation. The change in fluorescence relative to baseline, $\Delta F/F_0$ was computed by taking the difference between F and $F_0(t)$ and dividing by F_0 . In order to remove neuropil contamination, we used nonnegative matrix factorization (NMF), which is a low rank matrix decomposition method used for demixing spatially overlapping signal sources (Kim and Park, 2007; Langville et al., 2014), as implemented in NMF 1.2.1 (Žitnik and Zupan, 2012). The Python toolboxes were run with WinPython 2.7.10.3. All further analyses were performed using custom-written scripts in MATLAB (MathWorks, MA).

Analysis of locomotion responses

Changes in the position of the cylindrical treadmill (sampled at 12,000 Hz) were interpolated onto a downsampled rate of 40 Hz, matching the sampling rate of the two-photon imaging. To define stationary and locomotion periods we used the following criteria. Stationary corresponded to periods where the instantaneous speed (as measured at the 40 Hz sampling rate) was less than 0.1 cm/s. Locomotion corresponded to periods meeting three criteria: instantaneous speed ≥ 0.1 cm/s, 0.25 Hz lowpass filtered speed ≥ 0.1 cm/s, and an average speed ≥ 0.1 cm/s over a 2 s window centered at this point in time. Any inter-locomotion interval shorter than 500 ms was also labelled as locomotion. Stationary periods less than 3 s after or 0.2 s before a period of locomotion were removed from the analysis. The locomotion modulation index (LMI) was defined as the difference between the mean $\Delta F/F_0$ during locomotion (R_L) and stationary (R_S) periods, normalized by the sum of both values: $LMI = (R_L - R_S)/(R_L + R_S)$.

To estimate the error on the LMI in both dark and stimulated conditions for each neuron, bootstrapping with sample replacement was employed. We binned the signal into 1 s bins, each of which had only one visual stimulus and one behavioral activity (locomotion or stationary) throughout its duration. For each 1 s bin, we took the mean $\Delta F/F_0$ and regarded this value as a single sample. For periods of time which had a single stimulus and behavioral activity persisted for longer than 1 s, additional samples were drawn with intervals of no less than 2 s. This interval duration was selected based on the autocorrelation of the calcium fluorescence signal, which took approximately 2 s to fall to 0.5. The average correlation between consecutive samples of the same stimulus and activity condition was computed as a weighted average over all conditions, and was found to be $R = 0.35$. We then randomly selected samples of $\Delta F/F_0$ with replacement from our original set of samples. The number of samples selected in each bootstrap resample (65% = 1-R) was reduced from the total number of samples available to reflect the fact that our samples were not completely independent. This process was repeated 10000 times to obtain 95% confidence intervals for significance tests for each neuron individually. A neuron was considered significantly locomotion responsive if its 95% confidence interval was significantly different from an LMI of 0 and its value exceeded an LMI of 0.2 (at least 50% change in $\Delta F/F_0$ between locomotion and stationary).

To evaluate the variability of locomotion responses in a given context (dark or visual stimulation) for each neuron, we divided the data in two halves: we calculated separate LMI values for all odd and for all even locomotion periods (Figure 3—figure supplement 1). Neurons with the highest variability of locomotion responses were identified based on the difference between odd and even LMI values for each neuronal population. The 5% most variable neurons (i.e. neurons that fall outside the red dashed lines Figure 3—figure supplement 1 for either dark or visual stimulation) were excluded from being defined as context-dependent.

Statistics

The error bars in all graphs indicate standard error of the mean (s.e.m.) and statistics were performed with two-tailed tests. Unless otherwise stated, for statistical tests comparing the average $\Delta F/F_0$ of neurons between two contexts or behavioral states (in darkness versus during visual stimulation, or stationary versus locomotion periods) we used Wilcoxon signed-rank tests. For statistical tests comparing the distribution of LMIs and cross-correlations between visual stimulation contexts

we used the Kruskal–Wallis test (one-way ANOVA on ranks). For statistical tests comparing $\Delta F/F_0$ values across different layers, Mann–Whitney U tests were used.

For statistical tests we used the number of animals as our sample size because neuronal responses from the same mouse may be correlated and not represent independent samples. Therefore, comparing measures across neurons, rather than across animals, would incorrectly inflate the degrees of freedom with the risk of false positive results for detecting significant differences (Galbraith *et al.*, 2010). This is especially relevant for 2-photon imaging studies where data from a large number of neurons are collected from a small number of animals.

Acknowledgements

We thank Ian Duguid and his research group for advice and support on recordings in awake mice. We thank Matt Nolan and Ian Duguid for comments on earlier versions of the manuscript. We thank the GENIE Program and the Janelia Research Campus, specifically V Jayaraman, R Kerr, D Kim, L Looger, and K Svoboda, for making GCaMP6 available.

Additional information

Funding

Funder	Grant reference number	Author
European Commission	Marie Curie Actions (FP7), IEF 624461	Janelle MP Pakan
University Of Edinburgh	Doctoral Training Centre in Neuroinformatics	Scott C Lowe
University Of Edinburgh	Graduate School of Life Sciences	Evelyn Dylida
Engineering and Physical Sciences Research Council	Doctoral Training Centre in Neuroinformatics, EP/F500385/1	Sander W Keemink
European Commission	EuroSpin Erasmus Mundus Program	Sander W Keemink
Engineering and Physical Sciences Research Council	Doctoral Training Centre in Neuroinformatics, BB/F529254/1	Sander W Keemink
European Commission	Marie Curie Actions (FP7), MC-CIG 631770	Nathalie L Rochefort
Patrick Wild Centre		Nathalie L Rochefort
The Shirley Foundation		Nathalie L Rochefort
R5 MacDonald Charitable Trust	Seedcorn Grant 21	Nathalie L Rochefort
Wellcome Trust	Sir Henry Dale fellowship, 102857/Z/13/Z	Nathalie L Rochefort
University Of Edinburgh	Chancellor's fellow starting grant	Nathalie L Rochefort
Wellcome Trust	Sir Henry Dale fellowship, 102857/Z/13/Z	Nathalie L Rochefort
Royal Society	Sir Henry Dale fellowship, 102857/Z/13/Z	Nathalie L Rochefort

The funders had no role in study design, data collection and interpretation, or the decision to submit the work for publication.

Author contributions

JMPP, Conception and design, Acquired the data, Analysed and interpreted the data, Revised the manuscript; SCL, Developed the NMF-based neuropil correction method and analysed the data; ED,

Acquired and analysed the data; SWK, Developed the NMF-based neuropil correction method; SPC, Acquired data; CAC, Analyzed the data; NLR, Designed the experiments, Acquired the data, Analysed and interpreted the data, Wrote the manuscript with input from all authors

Author ORCIDs

Janelle MP Pakan, <http://orcid.org/0000-0001-9384-8067>

Evelyn Dylida, <http://orcid.org/0000-0002-1883-4498>

Nathalie L Rochefort, <http://orcid.org/0000-0002-3498-6221>

Ethics

Animal experimentation: All procedures were approved by the University of Edinburgh animal welfare committee, and were performed under a UK Home Office Project License (PPL No. 60/4570).

References

- Allitto HJ, Dan Y. 2012. Cell-type-specific modulation of neocortical activity by basal forebrain input. *Frontiers in Systems Neuroscience* **6**:79. doi: [10.3389/fnsys.2012.00079](https://doi.org/10.3389/fnsys.2012.00079)
- Arroyo S, Bennett C, Aziz D, Brown SP, Hestrin S. 2012. Prolonged disynaptic inhibition in the cortex mediated by slow, non- $\alpha 7$ nicotinic excitation of a specific subset of cortical interneurons. *Journal of Neuroscience* **32**:3859–3864. doi: [10.1523/JNEUROSCI.0115-12.2012](https://doi.org/10.1523/JNEUROSCI.0115-12.2012)
- Arroyo S, Bennett C, Hestrin S. 2014. Nicotinic modulation of cortical circuits. *Frontiers in Neural Circuits* **8**:30. doi: [10.3389/fncir.2014.00030](https://doi.org/10.3389/fncir.2014.00030)
- Bennett C, Arroyo S, Hestrin S. 2013. Subthreshold mechanisms underlying state-dependent modulation of visual responses. *Neuron* **80**:350–357. doi: [10.1016/j.neuron.2013.08.007](https://doi.org/10.1016/j.neuron.2013.08.007)
- Bennett C, Arroyo S, Hestrin S. 2014. Controlling brain states. *Neuron* **83**:260–261. doi: [10.1016/j.neuron.2014.07.007](https://doi.org/10.1016/j.neuron.2014.07.007)
- Brainard DH. 1997. The psychophysics toolbox. *Spatial Vision* **10**:433–436. doi: [10.1163/156856897X00357](https://doi.org/10.1163/156856897X00357)
- Chen N, Sugihara H, Sur M. 2015. An acetylcholine-activated microcircuit drives temporal dynamics of cortical activity. *Nature Neuroscience* **18**:892–902. doi: [10.1038/nn.4002](https://doi.org/10.1038/nn.4002)
- Chen TW, Wardill TJ, Sun Y, Pulver SR, Renninger SL, Baohan A, Schreiter ER, Kerr RA, Orger MB, Jayaraman V, Looger LL, Svoboda K, Kim DS, Chen WTJ. 2013. Ultrasensitive fluorescent proteins for imaging neuronal activity. *Nature* **499**:295–300. doi: [10.1038/nature12354](https://doi.org/10.1038/nature12354)
- Dombbeck DA, Khabbaz AN, Collman F, Adelman TL, Tank DW. 2007. Imaging large-scale neural activity with cellular resolution in awake, mobile mice. *Neuron* **56**:43–57. doi: [10.1016/j.neuron.2007.08.003](https://doi.org/10.1016/j.neuron.2007.08.003)
- Erisken S, Vaicelunaite A, Jurjut O, Fiorini M, Katzner S, Busse L. 2014. Effects of locomotion extend throughout the mouse early visual system. *Current Biology* **24**:2899–2907. doi: [10.1016/j.cub.2014.10.045](https://doi.org/10.1016/j.cub.2014.10.045)
- Fanselow EE, Richardson KA, Connors BW. 2008. Selective, state-dependent activation of somatostatin-expressing inhibitory interneurons in mouse neocortex. *Journal of Neurophysiology* **100**:2640–2652. doi: [10.1152/jn.90691.2008](https://doi.org/10.1152/jn.90691.2008)
- Fu Y, Tucciarone JM, Espinosa JS, Sheng N, Darcy DP, Nicoll RA, Huang ZJ, Stryker MP. 2014. A cortical circuit for gain control by behavioral state. *Cell* **156**:1139–1152. doi: [10.1016/j.cell.2014.01.050](https://doi.org/10.1016/j.cell.2014.01.050)
- Fucile S. 2004. Ca²⁺ permeability of nicotinic acetylcholine receptors. *Cell Calcium* **35**:1–8. doi: [10.1016/j.ceca.2003.08.006](https://doi.org/10.1016/j.ceca.2003.08.006)
- Galbraith S, Daniel JA, Vissel B. 2010. A study of clustered data and approaches to its analysis. *Journal of Neuroscience* **30**:10601–10608. doi: [10.1523/JNEUROSCI.0362-10.2010](https://doi.org/10.1523/JNEUROSCI.0362-10.2010)
- Grienberger C, Rochefort NL, Adelsberger H, Henning HA, Hill DN, Reichwald J, Staufenbiel M, Konnerth A. 2012. Staged decline of neuronal function in vivo in an animal model of Alzheimer's disease. *Nature Communications* **3**:774. doi: [10.1038/ncomms1783](https://doi.org/10.1038/ncomms1783)
- Iriki A, Tanaka M, Iwamura Y. 1996. Attention-induced neuronal activity in the monkey somatosensory cortex revealed by pupillometrics. *Neuroscience Research* **25**:173–181. doi: [10.1016/0168-0102\(96\)01043-7](https://doi.org/10.1016/0168-0102(96)01043-7)
- Jackson J, Ayzenshtat I, Karnani MM, Yuste R. 2016. VIP+ interneurons control neocortical activity across brain states. *Journal of Neurophysiology* **115**:3008–3017. doi: [10.1152/jn.01124.2015](https://doi.org/10.1152/jn.01124.2015)
- Jiang X, Shen S, Cadwell CR, Berens P, Sinz F, Ecker AS, Patel S, Tolias AS. 2015. Principles of connectivity among morphologically defined cell types in adult neocortex. *Science* **350**:aac9462. doi: [10.1126/science.aac9462](https://doi.org/10.1126/science.aac9462)
- Kaifosh P, Zaremba JD, Danielson NB, Losonczy A. 2014. SIMA: Python software for analysis of dynamic fluorescence imaging data. *Frontiers in Neuroinformatics* **8**:80. doi: [10.3389/fninf.2014.00080](https://doi.org/10.3389/fninf.2014.00080)
- Kawaguchi Y, Shindou T. 1998. Noradrenergic excitation and inhibition of GABAergic cell types in rat frontal cortex. *Journal of Neurophysiology* **79**:6963–6976.
- Kawaguchi Y. 1997. Selective cholinergic modulation of cortical GABAergic cell subtypes. *Journal of Neurophysiology* **78**:1743–1747.
- Keller GB, Bonhoeffer T, Hübener M. 2012. Sensorimotor mismatch signals in primary visual cortex of the behaving mouse. *Neuron* **74**:809–815. doi: [10.1016/j.neuron.2012.03.040](https://doi.org/10.1016/j.neuron.2012.03.040)

- Kim H, Park H. 2007. Sparse non-negative matrix factorizations via alternating non-negativity-constrained least squares for microarray data analysis. *Bioinformatics* **23**:1495–1502. doi: [10.1093/bioinformatics/btm134](https://doi.org/10.1093/bioinformatics/btm134)
- Kirkwood A, Rozas C, Kirkwood J, Perez F, Bear MF. 1999. Modulation of long-term synaptic depression in visual cortex by acetylcholine and norepinephrine. *Journal of Neuroscience* **19**:1599–1609.
- Langville AN, Meyer CD, Albright R, Cox J, Duling D. 2014. Algorithms, initializations, and convergence for the nonnegative matrix factorization. *ArXiv:1407.7299*.
- Lee AM, Hoy JL, Bonci A, Wilbrecht L, Stryker MP, Niell CM. 2014. Identification of a brainstem circuit regulating visual cortical state in parallel with locomotion. *Neuron* **83**:455–466. doi: [10.1016/j.neuron.2014.06.031](https://doi.org/10.1016/j.neuron.2014.06.031)
- McCormick DA, Wang Z, Huguenard J. 1993. Neurotransmitter control of neocortical neuronal activity and excitability. *Cerebral Cortex* **3**:387–398. doi: [10.1093/cercor/3.5.387](https://doi.org/10.1093/cercor/3.5.387)
- McGinley MJ, Vinck M, Reimer J, Batista-Brito R, Zaghera E, Cadwell CR, Tolias AS, Cardin JA, McCormick DA. 2015. Waking State: Rapid Variations Modulate Neural and Behavioral Responses. *Neuron* **87**:1143–1161. doi: [10.1016/j.neuron.2015.09.012](https://doi.org/10.1016/j.neuron.2015.09.012)
- Niell CM, Stryker MP. 2010. Modulation of visual responses by behavioral state in mouse visual cortex. *Neuron* **65**:472–479. doi: [10.1016/j.neuron.2010.01.033](https://doi.org/10.1016/j.neuron.2010.01.033)
- Niell CM. 2015. Cell types, circuits, and receptive fields in the mouse visual cortex. *Annual Review of Neuroscience* **38**:413–431. doi: [10.1146/annurev-neuro-071714-033807](https://doi.org/10.1146/annurev-neuro-071714-033807)
- Petersen CC, Crochet S. 2013. Synaptic computation and sensory processing in neocortical layer 2/3. *Neuron* **78**:28–48. doi: [10.1016/j.neuron.2013.03.020](https://doi.org/10.1016/j.neuron.2013.03.020)
- Pfeffer CK, Xue M, He M, Huang ZJ, Scanziani M. 2013. Inhibition of inhibition in visual cortex: the logic of connections between molecularly distinct interneurons. *Nature Neuroscience* **16**:1068–1076. doi: [10.1038/nn.3446](https://doi.org/10.1038/nn.3446)
- Pi HJ, Hangya B, Kvitsiani D, Sanders JI, Huang ZJ, Kepecs A. 2013. Cortical interneurons that specialize in disinhibitory control. *Nature* **503**:521–524. doi: [10.1038/nature12676](https://doi.org/10.1038/nature12676)
- Pinto L, Goard MJ, Estandian D, Xu M, Kwan AC, Lee SH, Harrison TC, Feng G, Dan Y. 2013. Fast modulation of visual perception by basal forebrain cholinergic neurons. *Nature Neuroscience* **16**:1857–1863. doi: [10.1038/nn.3552](https://doi.org/10.1038/nn.3552)
- Polack PO, Friedman J, Golshani P. 2013. Cellular mechanisms of brain state-dependent gain modulation in visual cortex. *Nature Neuroscience* **16**:1331–1339. doi: [10.1038/nn.3464](https://doi.org/10.1038/nn.3464)
- Reimer J, Froudarakis E, Cadwell CR, Yatsenko D, Denfield GH, Tolias AS. 2014. Pupil fluctuations track fast switching of cortical states during quiet wakefulness. *Neuron* **84**:355–362. doi: [10.1016/j.neuron.2014.09.033](https://doi.org/10.1016/j.neuron.2014.09.033)
- Roth MM, Dahmen JC, Muir DR, Imhof F, Martini FJ, Hofer SB. 2016. Thalamic nuclei convey diverse contextual information to layer 1 of visual cortex. *Nature Neuroscience* **19**:299–307. doi: [10.1038/nn.4197](https://doi.org/10.1038/nn.4197)
- Saleem AB, Ayaz A, Jeffery KJ, Harris KD, Carandini M. 2013. Integration of visual motion and locomotion in mouse visual cortex. *Nature Neuroscience* **16**:1864–1869. doi: [10.1038/nn.3567](https://doi.org/10.1038/nn.3567)
- Shen JX, Yakel JL. 2009. Nicotinic acetylcholine receptor-mediated calcium signaling in the nervous system. *Acta Pharmacologica Sinica* **30**:673–680. doi: [10.1038/aps.2009.64](https://doi.org/10.1038/aps.2009.64)
- Urban-Ciecko J, Barth AL. 2016. Somatostatin-expressing neurons in cortical networks. *Nature Reviews Neuroscience* **17**. doi: [10.1038/nrn.2016.53](https://doi.org/10.1038/nrn.2016.53)
- Xiang Z, Huguenard JR, Prince DA. 1998. Cholinergic switching within neocortical inhibitory networks. *Science* **281**:985–988. doi: [10.1126/science.281.5379.985](https://doi.org/10.1126/science.281.5379.985)
- Xu H, Jeong HY, Tremblay R, Rudy B. 2013. Neocortical somatostatin-expressing GABAergic interneurons disinhibit the thalamorecipient layer 4. *Neuron* **77**:155–167. doi: [10.1016/j.neuron.2012.11.004](https://doi.org/10.1016/j.neuron.2012.11.004)
- Žitnik M, Zupan B. 2012. NMF: a python library for nonnegative matrix factorization. *Journal of Machine Learning Research* **13**:849–853.

3.5 DISCUSSION

In summary, we found that modulation of neuronal activity is behavioural state dependent and cell type specific in layer 2/3 and 4 of mouse V1. During visual stimulation excitatory as well as SST-, VIP-, and PV- expressing interneurons, show an increase in gain of neuronal responses during locomotion. During darkness only VIP and PV interneurons show significantly increased activity during locomotion. The majority of excitatory neurons as well as SST inhibitory neurons were not locomotion responsive during darkness.

A possible mechanism believed to play a role in the increase in gain of excitatory neurons are neuromodulatory inputs to V1. Previous studies have shown that cortical neurons (excitatory and inhibitory neurons) can be modulated by cholinergic (Arroyo, Bennett, and Hestrin, 2014, Fu et al., 2014) as well as noradrenergic inputs (McCormick, Wang, and Huguenard, 1993). Several suggestions about the origin of the modulatory inputs to the cortex have been made. For instance, V1 receives cholinergic inputs from the basal forebrain (Lee et al., 2014) and noradrenergic inputs from the locus coeruleus (LC) (Polack, Friedman, and Golshani, 2013). It is conceivable, that neuromodulatory inputs onto SST inhibitory neurons remain subthreshold during darkness and during visual stimulation neuromodulatory inputs become suprathreshold. Thus, during darkness VIP inhibitory interneurons are activated with locomotion and inhibit SST inhibitory interneurons (also shown in: Reimer et al., 2014). During visual stimulation, the neuromodulatory inputs onto SST neurons depolarize the membrane potential and allow SST expressing interneurons to overcome the inhibition from the VIP expressing interneurons during locomotion (also shown in: Polack, Friedman, and Golshani, 2013). At the same time, SST interneurons, which target VIP interneurons (Pfeffer et al., 2013), will inhibit a subpopulation of VIP interneurons. This is consistent with the decrease in activity of a portion of VIP interneurons that was observed during visual stimulation. Similarly, PV inhibitory interneurons are activated during darkness and inhibit excitatory neurons. During visual stimulation neuromodulatory inputs onto excitatory neurons can depolarise the membrane potential of excitatory neurons and thus, visual inputs become suprathreshold and excitatory neurons can overcome the inhibition from the PV expressing interneurons. Furthermore, SST inhibitory interneurons also target PV expressing interneurons. Thus, during visual stimulation, when SST interneurons are activated they can inhibit PV expressing interneurons and might decrease the inhibition of PV expressing interneurons onto excitatory neurons. In this way, this dynamic microcircuitry within V1 may ultimately lead to a gain in pyramidal responses to visual stimulation during locomotion.

Alternatively, recent findings that projections from sub-cortical nuclei convey locomotion signals to V1, suggest that modulation of visual inputs may already happen in sub-cortical areas (Erisken et al., 2014, Roth et al., 2015). For example, Erisken et

al., 2014 found that locomotion modulates firing rates of the dorsolateral geniculate nucleus (dLGN) of the thalamus. This effect might originate from corticogeniculate feedback (Erisken et al., 2014) or be mediated by neuromodulatory mechanisms such as cholinergic projections from other subcortical areas encoding locomotion (e.g. mesencephalic locomotor region (MLR)) (Lee et al., 2014). In contrast, a second study did not find changes in neuronal responses induced by locomotion in the dLGN (Niell and Stryker, 2010). However, both studies analysed their data for different measures. The study conducted by Niell and Stryker, 2010 reported only spike count per second and did not find a difference between stationary and locomotion periods, while the study conducted by Erisken et al., 2014 reported that dLGN neurons are tuned to the speed of the animal and showed an onset response to locomotion. Additionally, to the direct projections from the MLR, the locus coeruleus (LC) is also believed to innervate the dLGN as well as the MLR itself. LC is the main source of noradrenaline in the cortex, and noradrenaline was shown to likely contribute to the modulation of V1 responses during locomotion (Polack, Friedman, and Golshani, 2013). In general, it is clear now that there is not only one source of modulation but likely several different pathways are involved. The contribution of the individual pathways to the behavioural state dependent modulation of neuronal activity in V1 remains to be elucidated in future studies (Bennett, Arroyo, and Hestrin, 2014).

Behavioural state dependent modulation of neuronal activity was shown to be cell-type specific. However, the responses properties observed especially in SST expressing and PV expressing interneurons were diverse, indicating that there are functional subtypes within each of the interneuron populations (Pakan et al., 2016). For example, SST expressing interneurons can be divided at least in three subclasses (Martinotti cells, X94 cells and calretinin positive SST interneurons; see chapter 1.1.3) and PV expressing interneurons can be further subdivided into basket cells and chandelier cells (Rudy et al., 2011; see chapter 1.1.3). Additionally, it was recently shown that SST expressing interneurons are modulated in a layer specific manner in behaving mice. Specifically, layer 2/3 SST expressing interneurons were suppressed and layer 4 SST expressing interneurons strongly activated during whisking (Muñoz et al., 2017). Therefore, further studies are needed to elucidate differences in response properties of neurons that are part of the same neuronal subclass.

Finally, most of the studies investigating neuronal modulation induced by locomotion did so by presenting the mice with a visual stimulus not coupled to visual flow. However, recent studies did investigate behavioural state dependent neuronal modulation in mice navigating through a virtual reality (VR) environment, thus creating a realistic visual flow when the animal is running (Keller, Bonhoeffer, and Hübener, 2012, Zmarz and Keller, 2016). They found that a subpopulation of neurons in mouse V1 responds to a mismatch between locomotion and visual feedback. Therefore, they suggested that motor-related and visual inputs are used for predictive coding strategies (Keller, Bonhoeffer, and Hübener, 2012). Further studies have shown that the

secondary motor cortex as well as the adjacent area A24b (part of the anterior cingulate cortex (ACC)) send projections to V1 that convey motor related signals. The activity of these projections was shown to be highly correlated with locomotion in mice not trained to navigate through a VR environment. However, after the mouse became trained in the VR environment the activity pattern of the ACC projections to V1 started to become correlated with visual flow, which is in line with the suggested predictive coding mechanism (Leinweber et al., 2017). Therefore, it is likely that the aim of behavioural state dependent modulation of V1 responses goes beyond the function of only increasing the accuracy of the representation of visual information in V1 as shown earlier (Bennett, Arroyo, and Hestrin, 2013, Dadarlat and Stryker, 2017). Hence, future studies are needed either in VR environments or in freely moving animals to further elucidate the role of locomotion dependent modulation of V1 neuronal responses.

EFFECT OF REPETITIVE PASSIVE VIEWING OF VISUAL STIMULI ON LAYER 2/3 NEURONAL ACTIVITY IN MOUSE PRIMARY VISUAL CORTEX

4.1 INTRODUCTION

Important functional properties of the primary visual cortex (V_1) of mice develop already during the first two postnatal weeks before eye opening driven by waves of spontaneous retinal activity (Cang et al., 2005). Another study found that network activity in V_1 changes from a dense mode before eye opening to a sparse mode after eye opening (Rochefort et al., 2009). This switch in neuronal activity pattern was shown to be governed by intrinsic signals and the onset triggered by visual experience. Furthermore, after eye opening neuronal response properties of individual neurons, such as direction selectivity, are further modified by visual experience (Rochefort et al., 2011). Sensory experiences are also known to induce a form of plasticity called experience-dependent plasticity. Several recent studies have investigated the impact of a daily brief presentation of a visual stimulus on neuronal activity in adult V_1 of mice (passive viewing protocol). This protocol allows studying plasticity in intact neuronal circuits (not affected by sensory deprivation or lesions) and does not involve any reward. Electrophysiological recordings performed *in vivo* in awake mice head-fixed and sitting in a tube have revealed a stimulus-specific potentiation of visually-evoked potentials (VEP) in mouse V_1 , following the daily brief (five to six minutes) presentation of an oriented grating over five consecutive days. This increase in response magnitude was shown to be long lasting (across weeks) and NMDA receptor dependent, thus sharing similarities with long-term potentiation (LTP) (Frenkel et al., 2006, Cooke and Bear, 2010, Cooke and Bear, 2014). Furthermore, this stimulus-specific potentiation in V_1 neuronal responses was accompanied by a behavioural habituation to the presented stimulus (Cooke et al., 2015).

However, another study performing recordings of individual neurons using *in vivo* two-photon calcium imaging in running mice showed that a daily brief presentation of a visual stimulus over five consecutive days induced a decrease in number of visually responsive neurons, resulting in an overall decrease in visually evoked responses across days (Makino and Komiyama, 2015). These results were challenged by a third study, also using *in vivo* two-photon calcium imaging but showing a stimulus-specific increase in response magnitude to the presented grating. This stimulus-specific increase in response magnitude was only seen in mice that were voluntarily running during grating presentation for at least one hour (total of 10 hours presentation) (Ka-

neko, Fu, and Stryker, 2017), and thus not in line with the findings by Frenkel et al., 2006 who found a stimulus-specific increase in stationary mice (sitting in a tube). Therefore, the experience-dependent effects induced by the passive viewing of a defined visual stimulus across multiple days and the impact of behavioural state (e.g. locomotion) on this process remains to be elucidated.

In this study, we investigated the stability and plasticity of visual responses of V1 neurons in adult mice across consecutive days. We used *in vivo* two-photon calcium imaging in awake mice that were able to run freely on a circular treadmill. Using cre-driver mouse lines, response properties of putative excitatory as well as of three non-overlapping inhibitory interneuron cell-types were recorded. Mice were presented with four different grating stimuli to map the preferred orientation of individual neurons, on the first day of imaging as well as five and six days later. During the first five days, mice were divided in two experimental groups: group one was presented daily with an isoluminant grey screen (control group) and the second group was presented daily with one defined oriented grating (familiar group). We investigated whether orientation selective neurons in V1 increase (potentiation) or decrease (adaptation) either in the total number of neurons preferring a specific orientation, or in overall response magnitude of orientation selective neurons. Finally, we investigated whether the modulation of neuronal responses by locomotion changed across days. Overall, we found no significant difference in visual responses of layer 2/3 neurons of mouse V1 between the animals exposed daily to a drifting grating (familiar group) and the animals exposed daily to an isoluminant grey screen in similar conditions (control group) on day 1 and day 5. However, individual cells exhibited highly heterogeneous responses across days, with some neurons increasing their activity and other neurons decreasing their activity in response to oriented gratings. This may reflect an experience-dependent reshaping of neuronal ensembles.

4.2 MATERIAL AND METHODS

For all experiments discussed in this chapter we used the experimental protocol (e.g. surgery: virus injection, cranial window and head-plate attachment) and two-photon imaging setup described in Chapter 2. Briefly, two to three weeks prior to imaging, a cranial window surgery was performed and AAVs were injected locally in binocular V1 in order to express the genetically encoded calcium indicator GCaMP6s (AAV1.Syn.GCaMP6s.WPRE.SV40; Penn Vector Core). Mice were imaged for six consecutive days and again after a 7-day break (imaging day 14). On day 1, 5, 6 and 14 orientation-selectivity was mapped and on day 1 to 5 mice were exposed to a specific stimulus protocol (Figure 4.1). At the end of the experiment mice were transcardially perfused. All procedures were approved by the University of Edinburgh animal welfare committee, and performed under a UK Home Office project license.

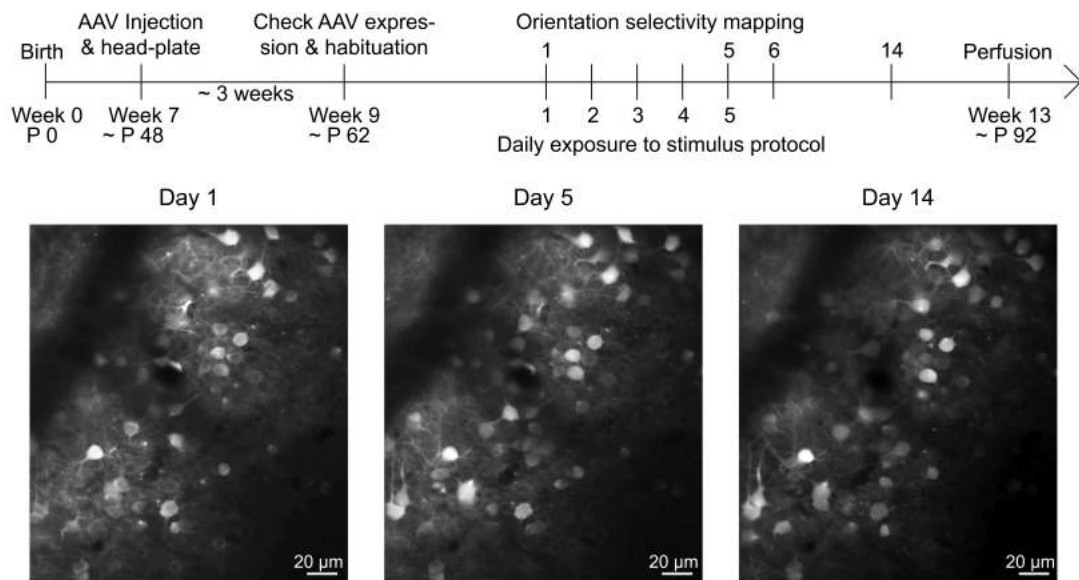


Figure 4.1: Experimental timeline: Timeline of a chronic two-photon imaging experiment. At approximately P48 a cranial window surgery was performed, mice were injected with an AAV that drives the expression of GCaMP6s, and a head-plate was mounted. Approximately three weeks later, mice were habituated to the two-photon imaging setup and the head-restraint. Mice were imaged for six consecutive days and again after 7 days (day 14). Orientation-selectivity was mapped on day 1, 5, 6, 14; and on day 1 to 5 mice were exposed to the specific stimulus, either a grey screen for group 1 or a specific grating (familiar grating) for group 2. Pictures show example of *in vivo* two-photon images of a given field of view from one mouse showing the same population of GCaMP6 labelled neurons on day 1, 5 and 14.

4.2.1 Animals

Both male and female mice were used for the experiments. Animals were housed in groups of two to four mice in conventional cages. In some cases, male mice were single housed due to extensive territorial behavior. Water and food was provided *ad libitum*. Mice were held on a 12/12 hour light/dark cycle.

To investigate a defined sub-population of inhibitory neurons, Pvalb<tm1(cre)Arbr> (PV-Cre), [RRID: IMSR_JAX: 008069], Sst<tm2.1(cre)Zjh> (SST-Cre)[RRID: IMSR_JAX: 013044] and Vip<tm1(cre)Zjh> (VIP-Cre)[RRID: IMSR_JAX: 010908] mice were cross breed with Rosa-CAGLSL-tdTomato [RRID: IMSR_JAX: 007914] mice, resulting in mouse lines having either PV-, SST-, or VIP-expressing inhibitory interneurons labelled with tdTomato. All neurons were labelled using GCaMP6s expressed under a synapsin promotor (AAV1.Syn.GCaMP6s.WPRE.SV40; Penn Vector Core). In three mice PV expressing interneurons were identified by injecting Pvalb<tm1(cre)Arbr> (PV-Cre), [RRID: IMSR_JAX:008069] mice with a cre-dependent version of a tdTomato expressing virus (AAV-CAG-FLEX-tdTomato; UNC Gene Therapy), while all neurons were labelled with GCaMP6s expressed under a synapsin promotor (AAV1.Syn.GCaMP6s.WPRE.SV40; Penn Vector Core). In two mice (one PV-cre and one VIP-cre),

only interneurons were labelled by injecting a cre-dependent GCaMP6s construct (AAV1.Syn.Flex.GCaMP6s.WPRE.SV40; Penn Vector Core).

All control experiments were done using *Sst*<tm2.1(cre)Zjh> (SST-Cre) [RRID: IMSR_JAX:013044] mice cross bred with *Rosa-CAGLSL-tdTomato* [RRID: IMSR_JAX:007914].

4.2.2 *Habituation of mice to the imaging setup*

Mice were habituated to be head restrained for approximately 20 minutes per day for at least one day (and a maximum of 3 days) before the first imaging day. For this, mice were head-fixed in the two-photon setup and left in the dark, free to run on a circular treadmill. The habituation session was also used to check the cranial window and the neuronal labelling. To habituate the mice to the noise of the mechanical shutter, the shutter was opened and closed several times during the habituation session.

4.2.3 *Chronic two-photon imaging protocol*

Orientation-selectivity was determined on day 1, 5, 6 and 14 by presenting sinusoidal phase-reversing gratings of four different orientations (0° , 45° , 90° , 135°). Gratings were presented in randomised order for 3 seconds with a 4 second isoluminant grey screen period between single gratings (Figure 4.2 A). Additionally, data were no visual stimulus was presented (black screen; dark trials) were recorded. Each trial was 72 seconds long.

Neuronal plasticity was induced by presenting a defined sinusoidal phase-reversing grating for 19 trials per day (total of 5 minutes) for five consecutive days (day 1 to day 5). This grating is referred to as the familiar grating. Each trial consisted of four presentations of the familiar grating for 4 seconds, interleaved with the presentation of an isoluminant grey screen. The presentation length of the isoluminant grey screen was randomised (length between 5-15 seconds), in order to avoid predictability of the occurrence of the grating stimulus. The orientation of the familiar grating was either 0° or 90° and chosen randomly between these two (Figure 4.2 B and C). Sinusoidal gratings were phase-reversing at a frequency of 1 Hz and presented with a cycle per degree of 0.03 or 0.05. Hence, in 5 minutes (300 seconds) stimulation period per day, 300 phase-reversals were presented, which were 100 reversals more than needed to induce reliable changes in visually evoked potentials (Frenkel et al., 2006). For control experiments mice were presented with an isoluminant grey screen for five consecutive days for 22.2 minutes per day (Figure 4.2 D). Screen contrast was 80 % and mean luminance 37 cd/m^2 .

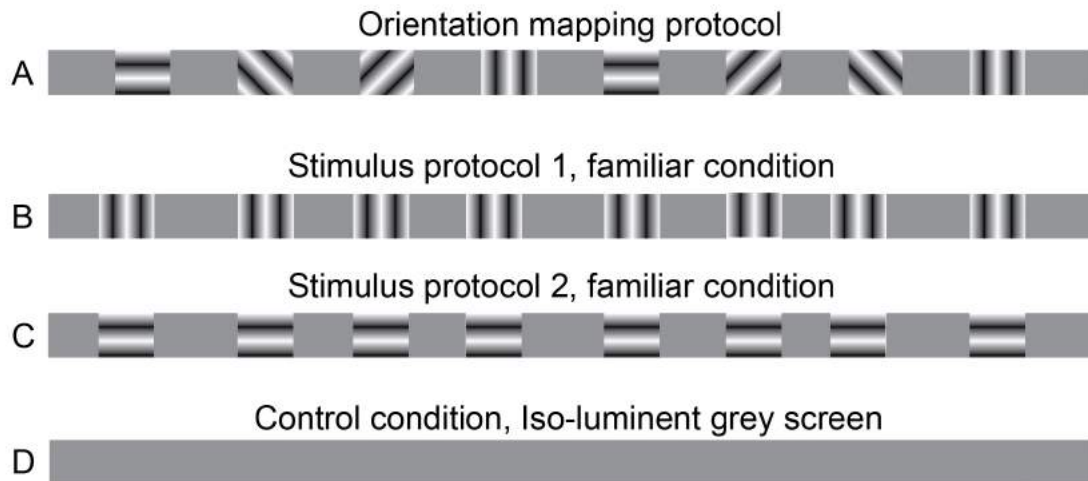


Figure 4.2: Visual stimulation protocol: A) Orientation mapping protocol: mice were presented with a sequence of four different (0° , 45° , 90° , 135°) oriented sinusoidal phase-reversing gratings (1 Hz, 0.03 or 0.05 cpd (cycles per degree)). Each grating was presented for 3 seconds. One trial was 72 seconds long and each grating was presented 2 times per trial. Between gratings an isoluminant grey screen was presented (5 seconds). 16 to 20 trials were presented per day. B) and C) Stimulus protocol familiar condition. Individual mice were presented either with stimulus protocol 1 (B) or with stimulus protocol 2 (C). Each trial consisted of 4 times 4 second presentation of a defined grating (either 0° (B) or 90° (C)). Between grating presentations, an isoluminant grey screen was presented for random durations, in order to avoid predictability of the occurrence of the grating stimulus. The total duration of each trial was 72 seconds and 19 trials were presented per day. D) Stimulus protocol control condition: Presentation of an isoluminant grey screen, for 72 seconds per trial, 19 trials per day.

4.2.4 Data analysis

Acquired data were analysed as described in [Chapter 2](#) of this thesis. Briefly, 2D plane translational-based image alignment (SIMA 1.2.0, Kaifosh et al., 2014) was used to correct for motion artefacts. Next, regions of interests (ROI) corresponding to neuronal somata were manually selected and pixel intensity within individual ROIs averaged for each imaging frame across time. $\Delta F/F_0$ signal was calculated by taking the difference between F (raw fluorescent signal) and F_0 (baseline fluorescence), and divided by F_0 . Neuropil decontamination was performed using non-negative matrix factorization (NMF) run through FISSA (Keemink et al., 2018). Behavioural state (e.g. stationary versus locomotion) was determined by monitoring the speed of the circular treadmill. Visual responsive neurons, stimulus-evoked response (SER), orientation selectivity index (OSI), and locomotion modulation index (LMI) were defined as described in [Chapter 2](#).

4.3 RESULTS

In total 21 mice were presented with the familiar stimulus over five consecutive days. Four animals were excluded due to a decrease in imaging quality across days. The remaining 17 adult mice (average age P77 at day 1 of imaging) had all neurons labelled with GCaMP6 and a subpopulation of inhibitory interneurons labelled with a red fluorescent protein (tdTomato). In total 1407 neurons were imaged, out of which: 1295 are putative excitatory neurons (15 mice), 33 are PV interneurons (6 mice), 32 are SST interneurons (6 mice) and 47 are VIP interneurons (5 mice). For the control condition, V1 neurons were imaged in 3 mice with a total of 363 putative excitatory neurons. Putative excitatory neurons are assumed to be excitatory neurons because they constitute the overwhelming majority of neurons in the cortex (>80 %; Rudy et al., 2011, Harris and Mrsic-Flogel, 2013), but it cannot be excluded that this population also contains inhibitory interneurons.

In order to avoid any bias introduced by an increase in the responsiveness of neurons during locomotion, as described in the previous chapter (Chapter 3), we analysed the data acquired during stationary and locomotion periods separately. The results obtained during stationary periods are presented first, followed by the specific effects of locomotion on neuronal activity. Furthermore, all results include only those neurons that were defined as "active" (average minimum $\Delta F/F_0 > 0.2$ during grating presentation) on day 1, 5, 6 and 14 (see Chapter 2).

4.3.1 *Similar neuronal response properties of V1 putative excitatory neurons in naive mice from the familiar and control experimental groups*

We first established the baseline neuronal response properties of putative excitatory neurons that were visually responsive on day 1 for both the familiar and control experimental group. All data shown were collected during stationary periods.

As expected, we found no significant difference in the total number of visually responsive neurons between the familiar and the control experimental group (Figure 4.3 A). Similarly, we found no significant difference in either the average amplitude of visual responses (mean $\Delta F/F_0$) during stationary periods between the familiar and the control experimental group (Figure 4.3 B) or in the stimulus-evoked response amplitude (SER) (Figure 4.3 C) between the familiar and the control group.

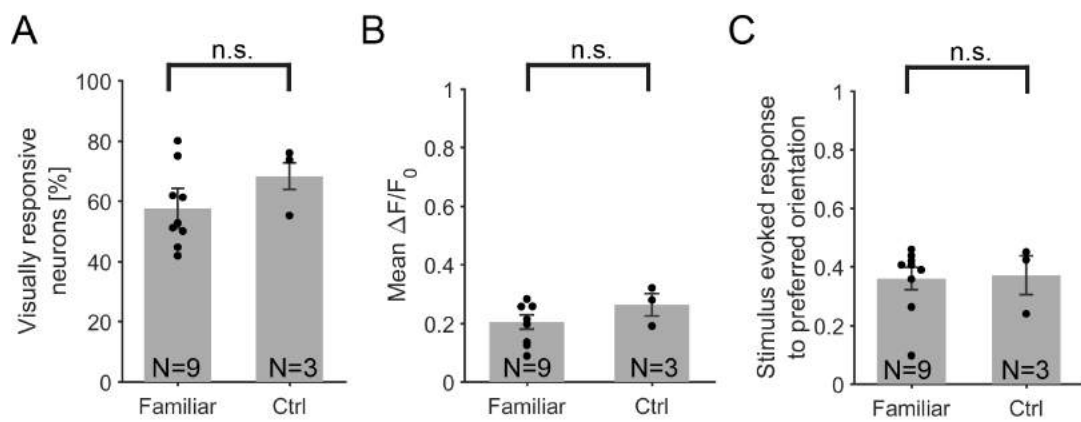


Figure 4.3: Baseline response properties of putative excitatory neurons on day 1, in both the familiar and control experimental group. A) Percentage of visually responsive neurons. B) Average amplitude of fluorescence changes (mean $\Delta F/F_0$) to the preferred orientation during stationary periods. C) Average amplitude of SER to preferred orientation. Black dots represent mean $\Delta F/F_0$ per animal. Error bars indicate s.e.m.; n.s., non-significant, $p > 0.05$, Mann-Whitney U-test.

4.3.2 *The response properties of V1 putative excitatory neurons after the daily exposure to a defined grating are stable on the population level*

4.3.2.1 *Visual responsiveness across days*

We quantified the percentage of visually responsive neurons per day, for both the familiar (Figure 4.4 A) and control group (Figure 4.4 B) during stationary periods. For the familiar experimental group, we found a significant decrease in the number of visually responsive neurons between day 1 and day 5, as well as between day 1 and day 6, with no significant difference in the number of visually responsive neurons between day 5 and day 6 (Figure 4.4 A). For the control group, although there was a large drop in the number of visually responsive neurons on day 5, the difference was not significant, likely due to the small number of animals (N=3) (Figure 4.4 B). Furthermore, there was an increase in number of visually responsive neurons on day 6 compared to day 5, but on average still less visually responsive neurons on day 6 than on day 1. In fact, two of the three recorded animals displayed nearly the same amount of visually responsive neurons on day 1 and day 6, while the decrease in number mainly resulted from one animal (mouse 1: $d_1=55\%$, $d_5=50\%$; mouse 2: $d_1=74\%$, $d_5=71\%$; mouse 3: $d_1=76\%$, $d_5=29\%$). Overall, the decrease in number of visually responsive neurons between day 1 and day 5 is more than twice as high in the control group compared to the familiar group (control group: 40 %, familiar group: 15 %). However, the decrease in number of visually responsive neurons between day 1 and day 6 is approximately the same in both experimental groups (control group: 18 %, familiar group: 16 %).

We then compared the average amplitude ($\Delta F/F_0$) of visually evoked responses of all neurons that were visually responsive on at least one day (day 1, 5 or 6) (Figure 4.5). We found no significant difference in $\Delta F/F_0$ of visually evoked responses for either the familiar group (Figure 4.5 A-C) or the control group (Figure 4.5 D-F), between day 1, 5 and 6. Altogether, these results indicate that although there was a decrease in the proportion of visually responsive neurons between day 1 and day 5, the average population response to visual stimulation in general (regardless of the orientation of the visual grating) was stable across days in both experimental groups.

Furthermore, the mean response amplitude of individual neurons across days was plotted (Figure 4.6 A), showing a large spread in mean response amplitude of individual neurons. However, the range of response amplitudes is similar across days. Following individual neuronal responses across days revealed that some neurons increase their overall response amplitude to visual stimulation, while other neurons decreased their response amplitude and still others did not displayed no change (Figure 4.6 B). Additionally, some neurons display heterogeneous changes across multiple days. For instance, some neurons show a decrease in response amplitude between day 1 and day 5 and an increase in response amplitude between day 5 and day 6, while other

neurons displayed an increase in response amplitude between day 1 and day 5 and a decrease in response amplitude between day 5 and 6 (Figure 4.6 B).

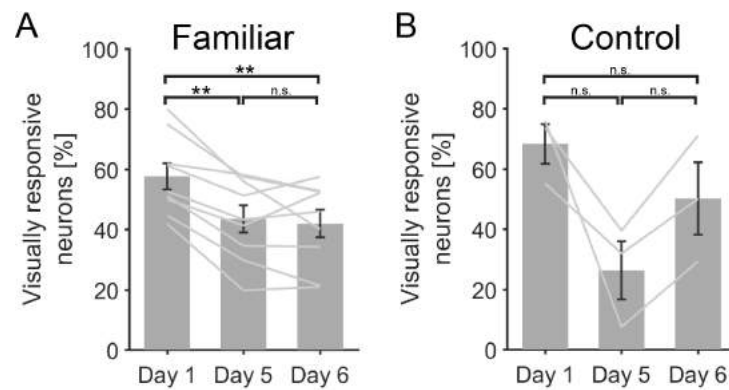


Figure 4.4: Percentage of visually responsive neurons per day. A) Familiar group (N=9). B) Control group (N=3). Grey lines represent the average value per animal per day. Error bars indicate s.e.m.; n.s., non-significant, $p > 0.05$, **, significant, $p < 0.01$, Wilcoxon signed rank test.

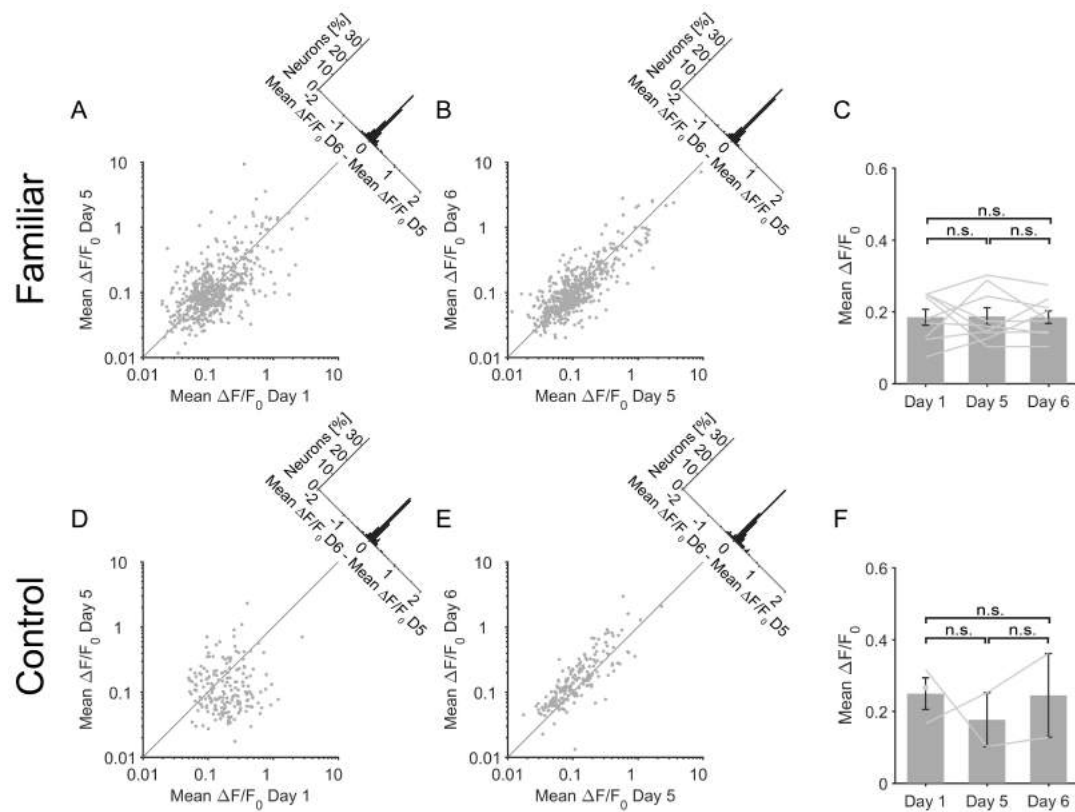


Figure 4.5: Stability of population visual responses across days (putative excitatory neurons) in both familiar (A, B, C) and control group (D, E, F) during stationary periods. A) and B) Scatter plots of the average amplitude of fluorescence changes ($\Delta F/F_0$) of each neuron visually responsive on at least one day (day 1, 5 or 6). A) Day 1 against day 5. B) Day 5 against day 6. C) Average response amplitude ($\Delta F/F_0$) of all neurons visually responsive on at least one day (day 1, 5 or 6) during stationary periods. D), E) and F) Date presented as in A), B) and C) for control group (grey screen). Grey lines represent the average value per animal per day. Error bars indicate s.e.m.; n.s., non-significant, $p > 0.05$, Wilcoxon signed rank test.

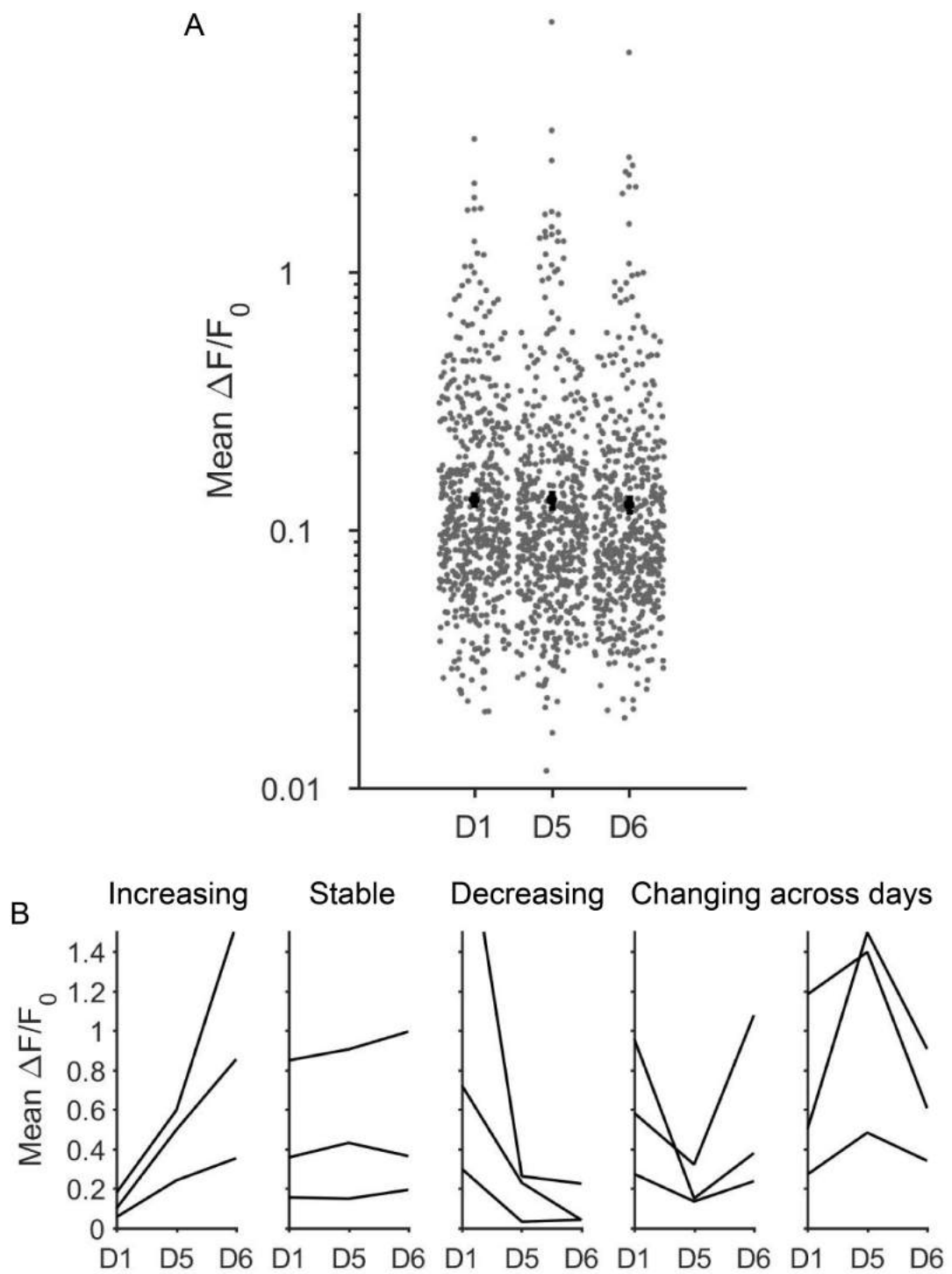


Figure 4.6: Individual neuronal responses across days during stationary periods. A) Shows the neuronal response of individual neurons to visual stimulation across days. Grey dots: individual neurons. Black dots: Mean across all neurons. B) Shows the neuronal response of example neurons across days.

4.3.2.2 *Neuronal responses to preferred orientation across days*

Next, we investigated stimulus-specific changes over days. Mice of the familiar group were stimulated for 5 consecutive days with a defined grating (the "familiar stimulus"). For some neurons, this given grating corresponded to their preferred orientation, as assessed on day 1 (Figure 4.7 A(i)), while other neurons had a different orientation preference (Figure 4.8 B(i)). For the neurons preferring the familiar grating on day 1, the stimulus-evoked response (SER) to the familiar grating remained high across all days (Figure 4.7 A(ii)), while the SER of the neurons with a different orientation preference on day 1 was consistently low across days (Figure 4.8 B(ii)). As can be seen in Figure 4.7 and Figure 4.8, both example neurons remained highly orientation tuned to their preferred orientation before and after the repetitive stimulation with the familiar grating (example neuron 1: day 1 OSI=0.79, day 5 OSI=0.81, day 6 OSI=0.82, day 14 OSI=0.60; example neuron 2: day 1 OSI=0.78, day 5 OSI=0.64, day 6 OSI=0.70, day 14 OSI=0.60) (Figure 4.7 A(iii) and Figure 4.8 B(iii)). Therefore, the repetitive presentation of an orthogonally oriented stimulus did not change the orientation tuning of this highly selective neuron (example neuron 2, Figure 4.8).

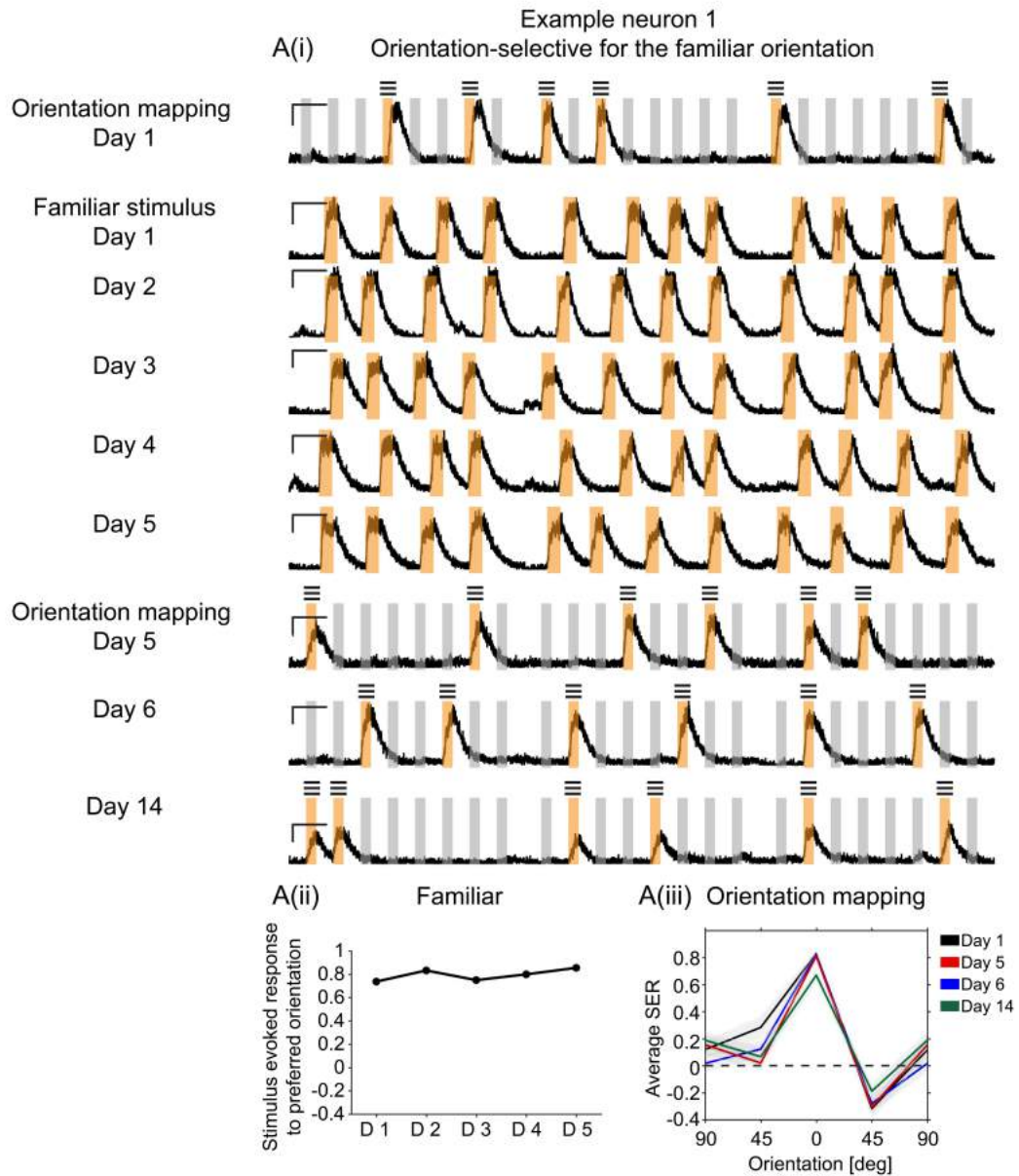


Figure 4.7: Example traces of a orientation selective neuron. A(i) shows the $\Delta F/F_0$ to each oriented grating for a neuron orientation selective for the familiar grating. First trace: day 1 orientation mapping; second to sixth trace: responses to familiar grating on day 1 to day 5; seventh to ninth trace: orientation mapping on day 5, 6 and 14. Orange squares indicate the presentation of a grating stimulus. Black arrows indicate presentation of the preferred grating of the neuron. A(ii): Stimulus-evoked response to the familiar grating on day 1 to day 5. A(iii): Tuning curve of each example neuron acquired during orientation mapping on day 1 (black trace), day 5 (red trace), day 6 (blue trace) and day 14 (green trace). Preferred orientation normalized to 0.

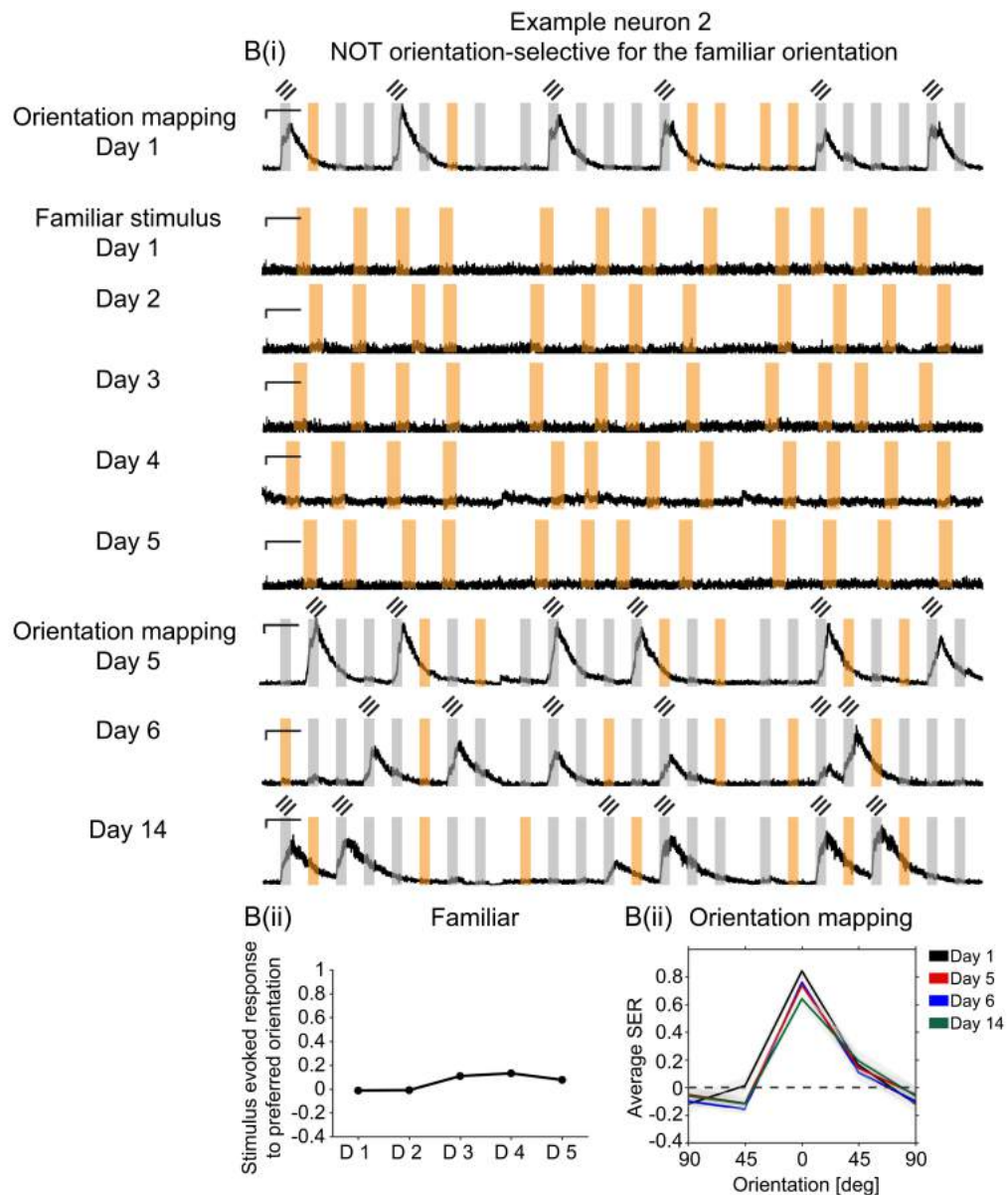


Figure 4.8: Example traces of an orientation selective neuron. B(i) shows the $\Delta F/F_0$ to each oriented grating for a neuron orientation selective for an orthogonal grating. First trace: day 1 orientation mapping; second to sixth trace: responses to familiar grating on day 1 to day 5; seventh to ninth trace: orientation mapping on day 5, 6 and 14. Orange squares indicate the presentation of a grating stimulus. Black arrows indicate presentation of the preferred grating of the neuron. B(ii): Stimulus-evoked response to the familiar grating on day 1 to day 5. B(iii): Tuning curve of each example neuron acquired during orientation mapping on day 1 (black trace), day 5 (red trace), day 6 (blue trace) and day 14 (green trace). Preferred orientation normalized to 0.

We then compared the responses to the preferred orientation of all neurons that were visually responsive as well as orientation selective ($OSI > 0.3$ for any grating) on at least one day (day 1, 5 or 6) (Figure 4.9). We found no significant difference in $\Delta F/F_0$ for either the familiar group (Figure 4.10 A) or the control group (Figure 4.10 B), indicating that the average population response of all orientation selective neurons to their preferred orientation was stable across days, regardless of whether the animal had passively viewed a specific stimulus repetitively or not.

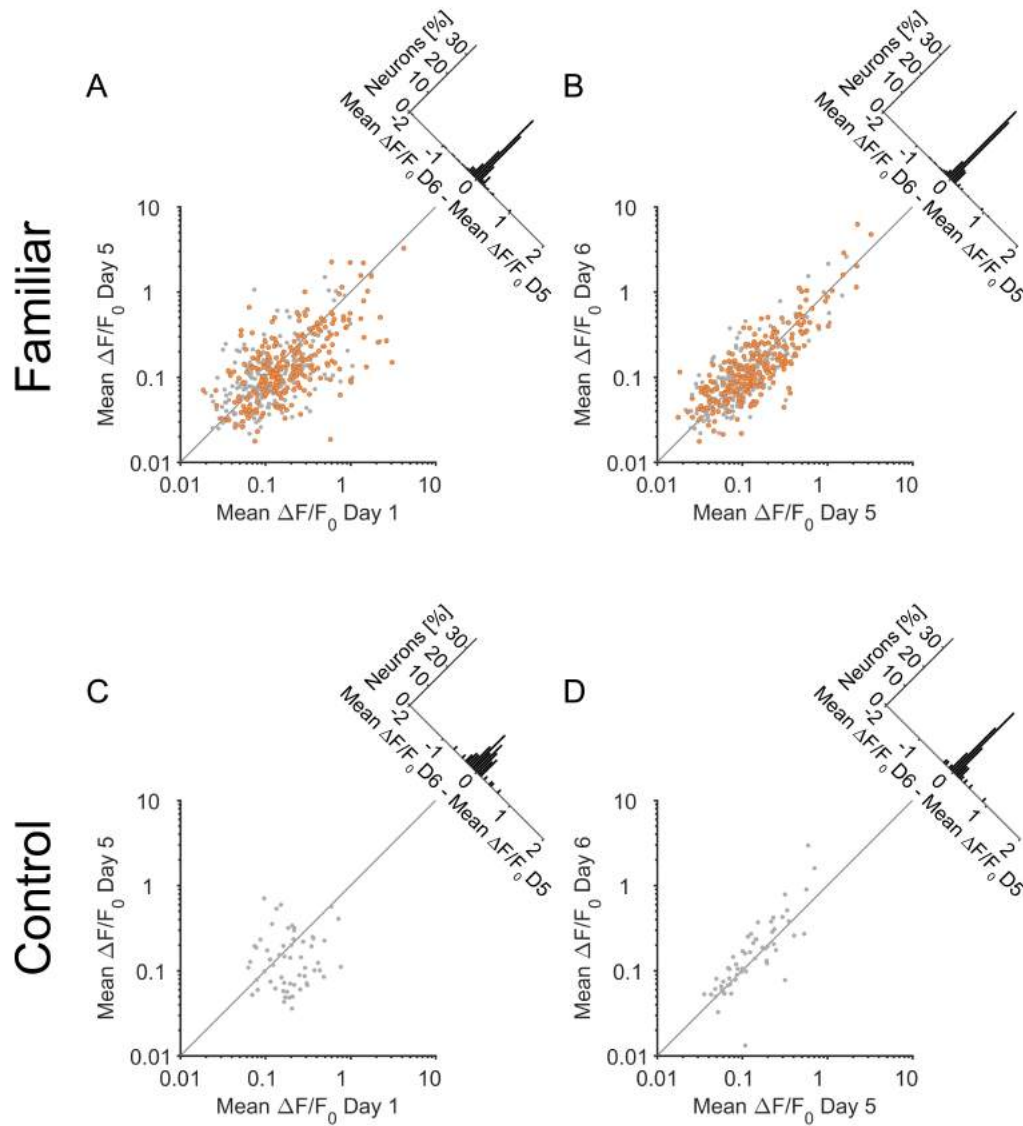


Figure 4.9: Response properties of individual neurons that are orientation selective on at least one day in both familiar (A, B) and control group (C, D); data is taken from stationary periods. Scatter plots of the average amplitude of fluorescence changes ($\Delta F/F_0$) for the preferred orientation of each neuron visually responsive and orientation selective on at least one day (day 1, 5 or 6). A) and C) Day 1 against day 5. B) and D) Day 5 against day 6. Orange: neurons preferring the familiar grating

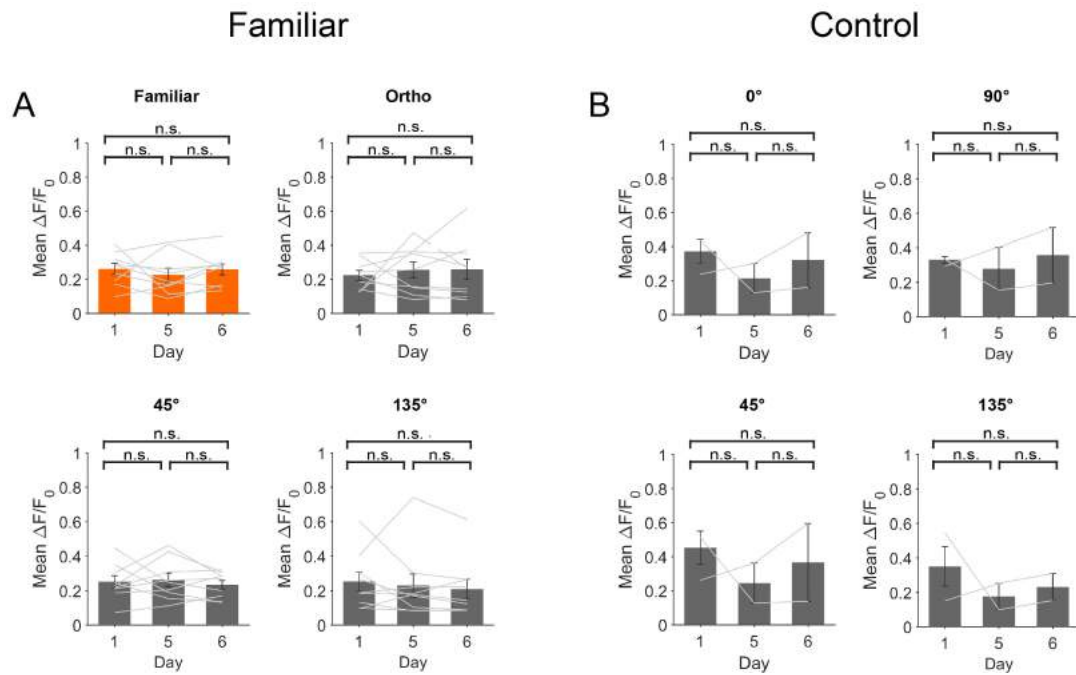


Figure 4.10: Average population response properties across days of all neurons orientation selective on at least one day in both familiar (A) and control group (B) during stationary periods. Average response amplitude ($\Delta F/F_0$) for the preferred orientation of all neurons visually responsive and orientation selective on at least one day (day 1, 5 or 6) during stationary periods. Grey lines represent mean $\Delta F/F_0$ per animal. Error bars indicate s.e.m.; n.s., non-significant, $p > 0.05$, Wilcoxon signed rank test.

We also quantified the percentage of orientation selective neurons per day for both, the familiar (Figure 4.11 A) and control group (Figure 4.11 B). We found a decrease (familiar group day 1: 27 ± 4 , day 5: 22 ± 5 ; control group day 1: 28 ± 9 , day 5: 12 ± 5) in percentage of orientation selective neurons between day 1 and day 5 in both groups, similar to the decrease observed in visually responsive neurons. Furthermore, there was an increase in number of orientation selective neurons on day 6 compared to day 5 observed in the control group. Therefore, the non-significant changes in number of orientation selective neurons in the control group seem to resemble the changes observed in visually responsive neurons. However, there was a significant decrease in orientation selective neurons between day 5 and day 6 observed in the familiar group, compared to the non-significant change in visually responsive neurons.

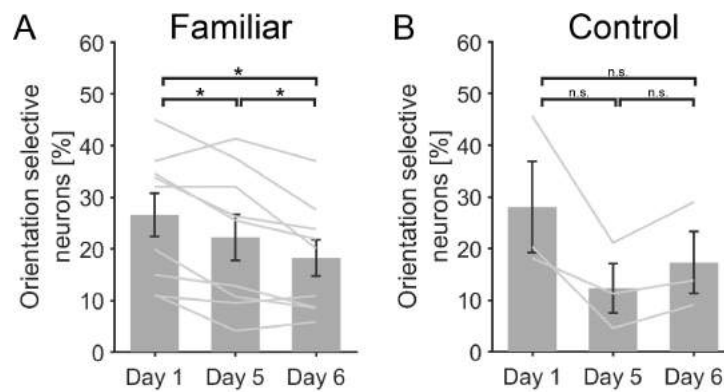


Figure 4.11: Percentage of orientation selective neurons per day. A) Familiar group (N=9). B) Control group (N=3). Grey lines represent the average value per animal per day. Error bars indicate s.e.m.; n.s., non-significant, $p > 0.05$, **, significant, $p < 0.01$, Wilcoxon signed rank test.

4.3.2.3 *Neurons orientation selective on day 1 display stable stimulus-specific neuronal responses across days*

Overall, for neurons preferring the familiar stimulus on day 1, the average response to the familiar stimulus was stable over 5 consecutive days (Figure 4.12 orange trace). Similarly, the response of neurons with a non-familiar orientation preference on day 1 was also stable over 5 consecutive days (Figure 4.12 grey trace). No significant difference was found when comparing the neuronal responses across the daily presentation of the familiar grating (Figure 4.12 A) or when comparing day 1 and day 5 responses to the familiar grating during the orientation mapping protocol (Figure 4.12 B).

Systematic differences in the signal to noise ratio of the calcium transients across animals and days could potentially mask subtle changes in the amplitude of evoked responses. We therefore calculated the stimulus-evoked response amplitude (SER) by normalizing the response of a given grating by the baseline activity preceding the presentation of the stimulus (grey screen period) (see Chapter 2). The SER of neurons preferring the familiar grating on day 1 showed the same stability of responses as that found comparing the mean $\Delta F/F_0$ (Figure 4.12 C). Similarly, comparing the SER to the familiar grating during the orientation mapping protocol on day 1 and day 5 did not reveal any significant difference (Figure 4.12 D).

Therefore, the population response for cells orientation selective for the familiar grating was stable across days; additionally, the population response of the cells selective for all other gratings (non-familiar gratings) on day 1 was also stable after the repeated presentation of the familiar stimulus (ortho day 1: 0.28 ± 0.05 , day 5: 0.22 ± 0.06 ; 45° day 1: 0.34 ± 0.05 , day 5: 0.26 ± 0.05 ; 135° day 1: 0.30 ± 0.07 , day 5: 0.19 ± 0.03) (Figure 4.13). As expected, the same was true for the control group with no significant difference across days. Therefore, regardless of the passive viewing of a repetitive stimulus, the population of V1 neurons maintained a stable responses to preferred orientation, for all oriented gratings.

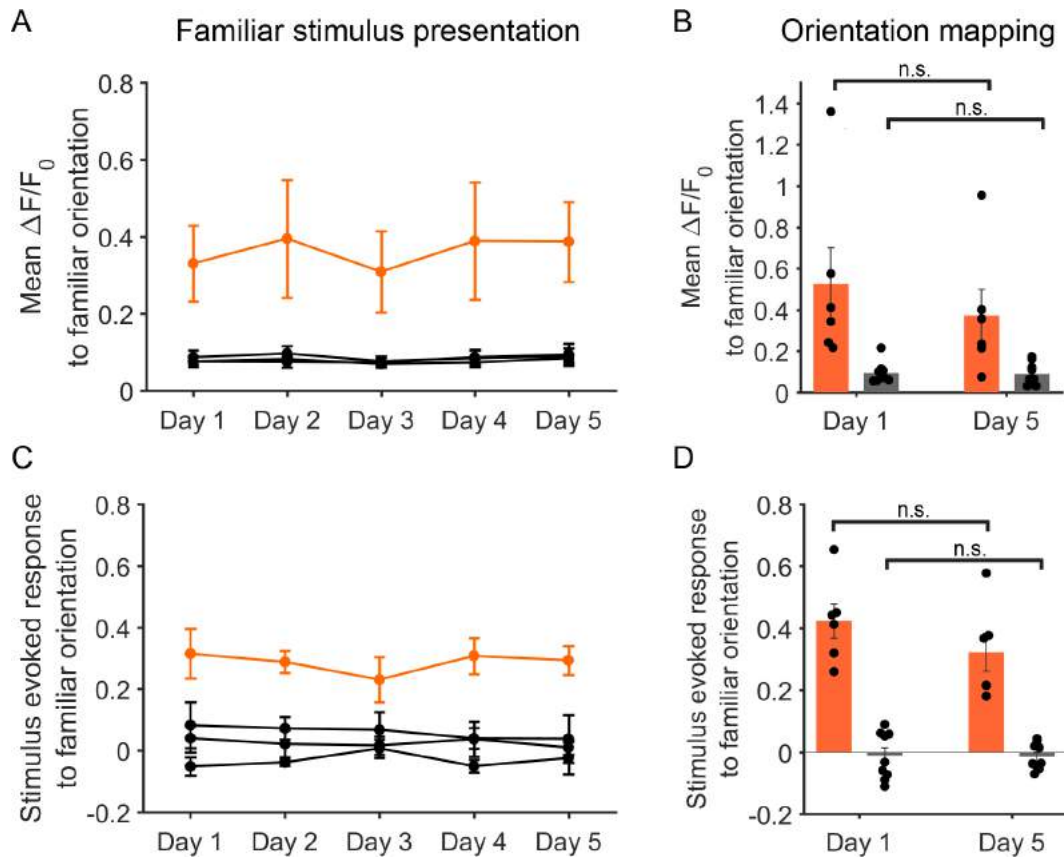


Figure 4.12: Population response properties across days of neurons preferring the familiar grating (orange) and neurons preferring a non-familiar grating (grey) on day 1. A) Mean amplitude of fluorescence changes (mean $\Delta F/F_0$) during the presentation of the familiar grating across 5 consecutive days. B) Mean $\Delta F/F_0$ during the presentation of the familiar orientation and of the non-familiar orientation stimuli on day 1 and 5. Black dots represent mean $\Delta F/F_0$ per animal. Error bars indicate s.e.m.; n.s., non-significant, $p > 0.05$, Wilcoxon signed rank test.

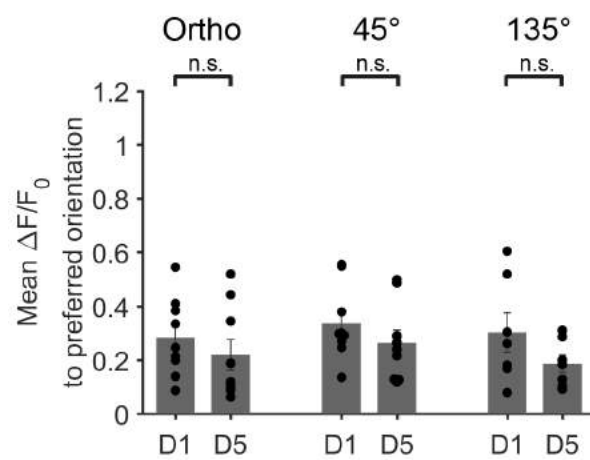


Figure 4.13: Familiar group: population response properties across days of all neurons with a preferred orientation different from the familiar grating on day 1. Mean amplitude of fluorescence changes (mean $\Delta F/F_0$) during the presentation of the preferred grating on day 1 and day 5 during stationary periods. Black dots represent mean $\Delta F/F_0$ per animal. Error bars indicate s.e.m.; n.s., non-significant, $p > 0.05$, Wilcoxon signed rank test.

4.3.3 *Heterogeneous changes in neuronal response properties at the single cell level*

An overall stability of responses at the population level across days can correspond to different scenarios: (1) the same population of neurons display similar amplitudes across days, (2) the same population of neurons display a mixture of responses (increasing and decreasing) resulting in the same average response across days or (3) a fully dynamic network where a mixture of different neurons that are responding differently across all days results in the same average response per day. In order to examine which scenario was occurring, we investigated the changes in evoked responses at the single cell level across days. Indeed, our results show heterogeneous changes in a dynamic network where a mixture of different neurons responding each day changes their responses to their defined preferred orientation. This was true for both the familiar group (Figure 4.14) and the control group (Figure 4.15). For instance, some neurons increase their response amplitude to their preferred orientation between day 1 and day 5 (Figure 4.14, example neuron 1 and 2; Figure 4.15, example neuron 1 and 2), while other neurons decrease their response amplitude between days (Figure 4.14, example neuron 5 and 6; Figure 4.15, example neuron 5 and 6). In contrast, another subset of neurons does not change their response amplitude to their preferred orientation across days (Figure 4.14, example neuron 3 and 4; Figure 4.15, example neuron 3 and 4).

When taking the difference of these responses between days, the results showed that a majority of neurons decrease their response to their preferred orientation between day 1 and day 5 (Figure 4.16 C and D; Figure 4.14 and Figure 4.15, example neurons 5 and 6) (Difference day 5 minus day 1 familiar group: familiar: -0.12 ± 0.06 , ortho: -0.11 ± 0.05 , 45° : -0.07 ± 0.05 , 135° : -0.12 ± 0.05 ; control group: 0° : -0.15 ± 0.07 , 45° : -0.21 ± 0.14 , 90° : -0.04 ± 0.12 , 135° : -0.36 ± 0.27).

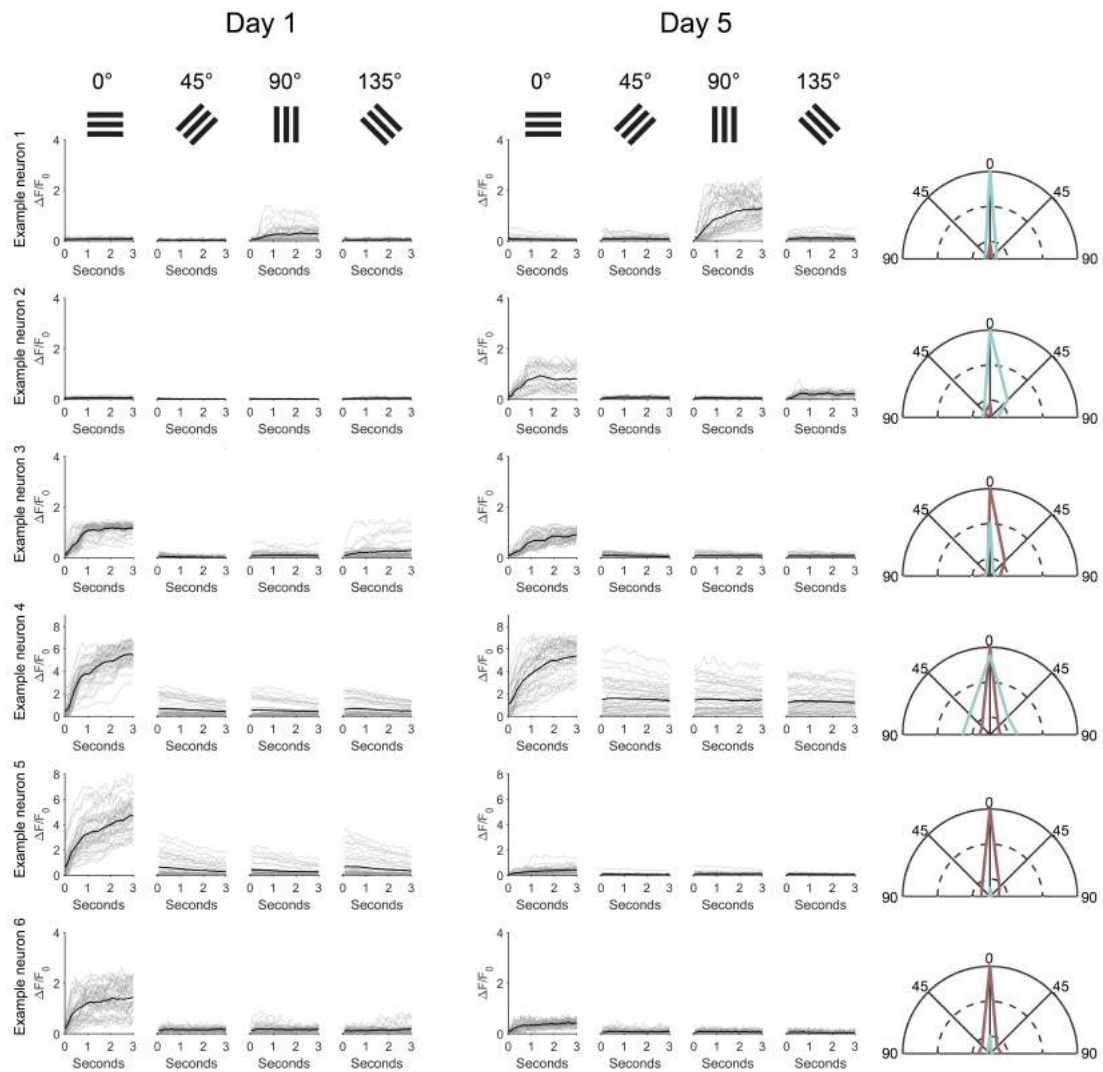


Figure 4.14: Familiar group: heterogeneous changes in response amplitudes to the preferred orientation across days. Each row shows the amplitude of fluorescence changes ($\Delta F/F_0$) to all 4 presented gratings (0°, 45°, 90°, 135°) for six different example neurons, left side: day 1, right side: day 5. Example neuron 1 and 2 show an increase in amplitude from day 1 to day 5, example neuron 3 and 4 show no change in amplitude from day 1 to day 5 and example neuron 5 and 6 show a decrease in amplitude from day 1 to day 5. Black traces: mean $\Delta F/F_0$ across all trials, grey traces: $\Delta F/F_0$ of individual trials. Polar plots show the change in response amplitude to the preferred orientation (normalised to 0) between day 1 (red) and day 5 (blue).

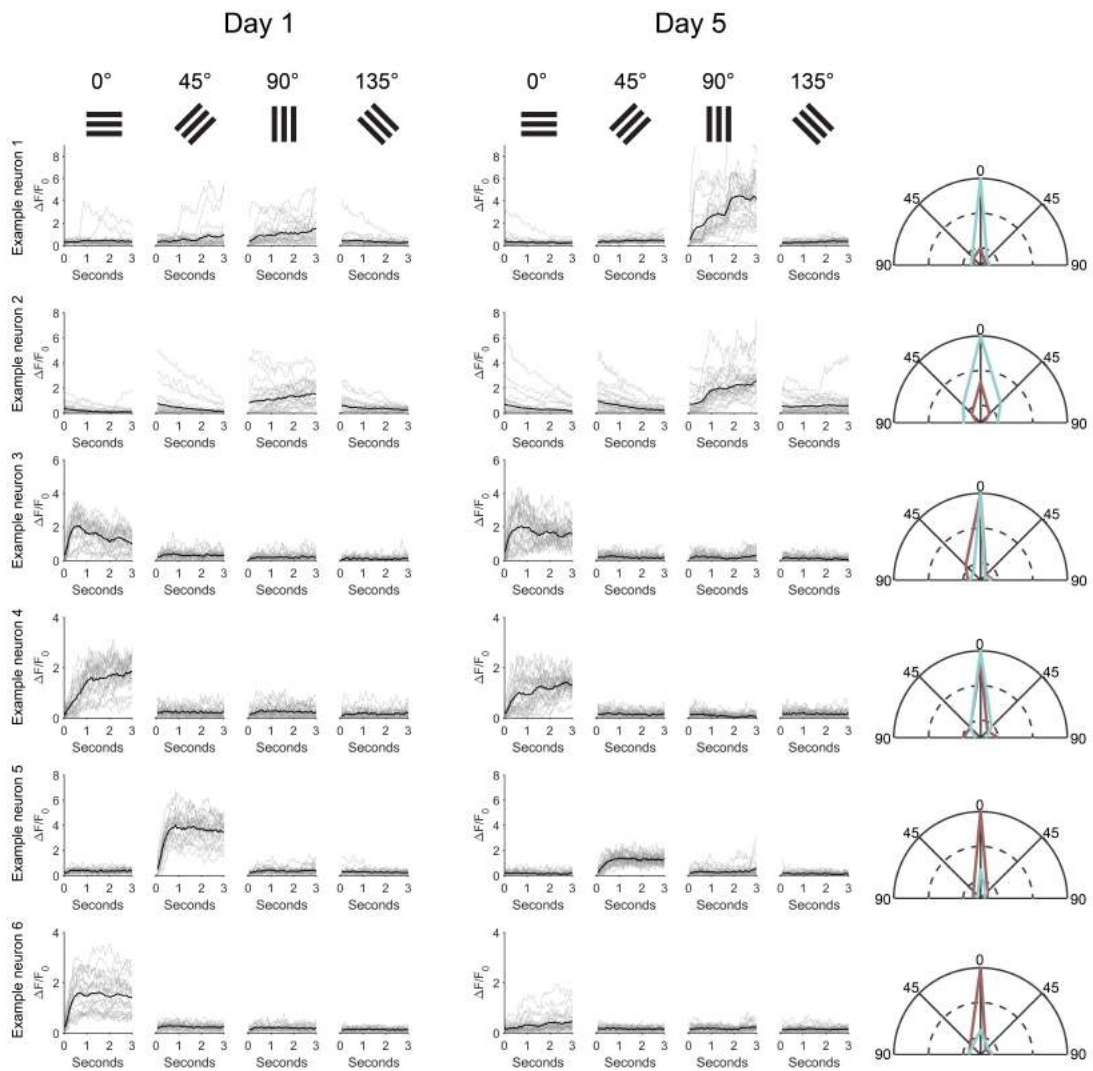


Figure 4.15: Control group: heterogeneous changes in response amplitudes to the preferred orientation across days. Each row shows the amplitude of fluorescence changes ($\Delta F/F_0$) to all 4 presented gratings (0° , 45° , 90° , 135°) for six different example neurons, left side: day 1, right side: day 5. Example neuron 1 and 2 show an increase in amplitude from day 1 to day 5, example neuron 3 and 4 show no change in amplitude from day 1 to day 5 and example neuron 5 and 6 show a decrease in amplitude from day 1 to day 5. Black traces: mean $\Delta F/F_0$ across all trials, grey traces: $\Delta F/F_0$ of individual trials. Polar plots show the change in response amplitude to the preferred orientation (normalised to 0) between day 1 (red) and day 5 (blue).

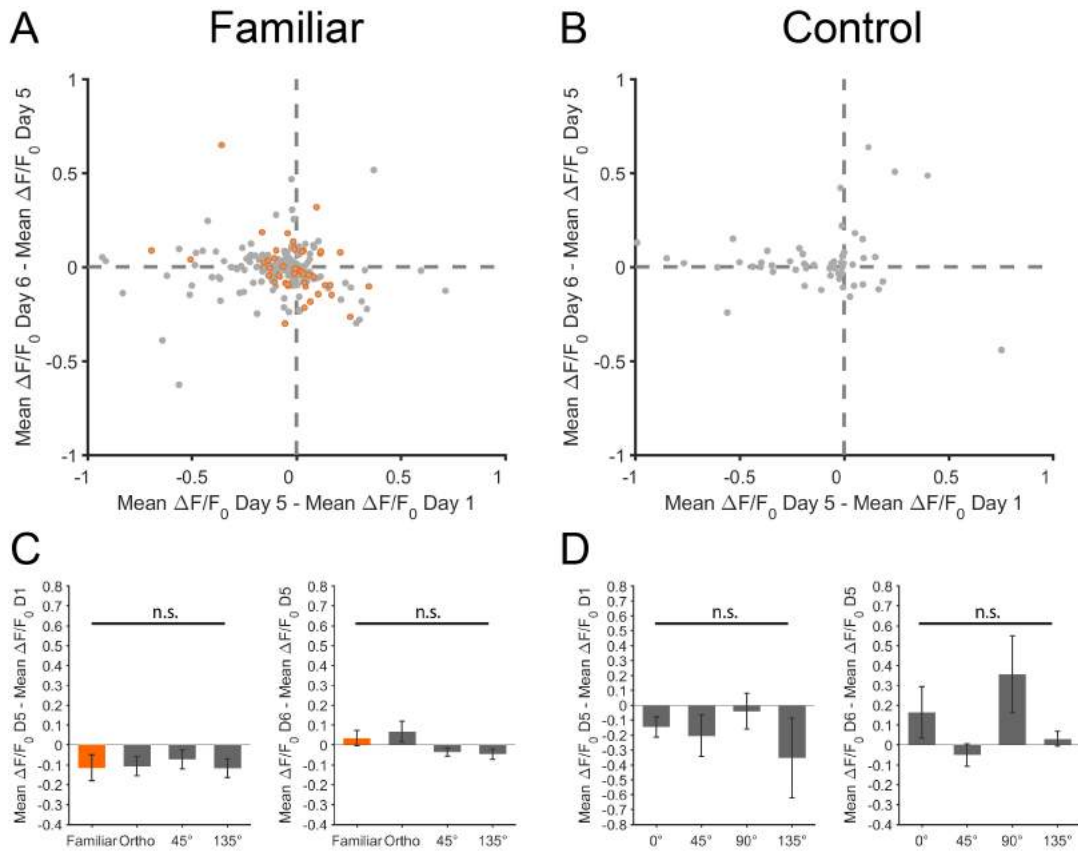


Figure 4.16: Difference in response amplitude of putative excitatory neurons between day 1 and day 5, and day 5 and day 6, for all neurons visually responsive and orientation selective (OSI > 0.3) on at least one day (day 1, 5 or 6) for both, familiar (A and C) and control group (B and D) during stationary periods. Orange dots: neurons orientation selective for the familiar orientation on day 1. A) and B) Scatter plots of the difference in average amplitude of fluorescence changes ($\Delta F/F_0$) of each neuron between day 1 and day 5 plotted against the difference in $\Delta F/F_0$ between day 5 and day 6. A) Familiar group. B) Control group. C) and D) Average difference in $\Delta F/F_0$ of all orientation selective neurons between day 1 and day 5 (i) and day 5 and day 6 (ii). Error bars indicate s.e.m.; n.s., non-significant, $p > 0.05$, Mann-Whitney U-test.

4.3.3.1 Orientation selectivity (OSI) across days

As a consequence of the changes in response amplitude to the preferred orientation, the strength of the orientation selectivity (OSI) and the preferred orientation of individual neurons may also change across days. When we examined the magnitude of the OSI (or selectivity strength) of individual neurons, we found neurons showing a decrease, an increase, as well as neurons showing a stable OSI magnitude across days for both the familiar group (Figure 4.17 A and B) and the control group (Figure 4.17 C and D).

However, on the population level, similar to the other population measures, the average OSI magnitude is largely stable between day 1 and day 5 (Figure 4.18, A familiar group and B control group). There is, however, a significant decrease in OSI magnitude of neurons orientation selective on day 1 for the orientation orthogonal to the familiar as well as for neurons preferentially responding to 135° between day 1 and day 6 (Figure 4.18 A).

In the familiar group, from neurons that are orientation selective on at least one day, 83 % were orientation selective on day 1 (Figure 4.19). One third of neurons orientation selective on day 1 remained orientation selective throughout the experimental timepoints and therefore were also orientation selective on day 5 and day 6 (36 %). Similarly, in the control experimental group 83 % of all neurons orientation selective on at least one day were orientation selective on day 1 (Figure 4.19). About a quarter (27 %) of cells remained orientation selective across all days.

Altogether, these results show an overall reduction in the number of orientation selective neurons between day 1 and day 6. This was true for both experimental groups, the familiar (Figure 4.19) and the control group (Figure 4.19). This decrease was not stimulus-specific, since it was observed in response to all four presented gratings (0° , 45° , 90° , 135°). In addition, the neurons increasing their OSI across days were not biased towards responding to the familiar grating compared to the other orientations. In line with this observation, a similar proportion of neurons in the control group showed an increased OSI.

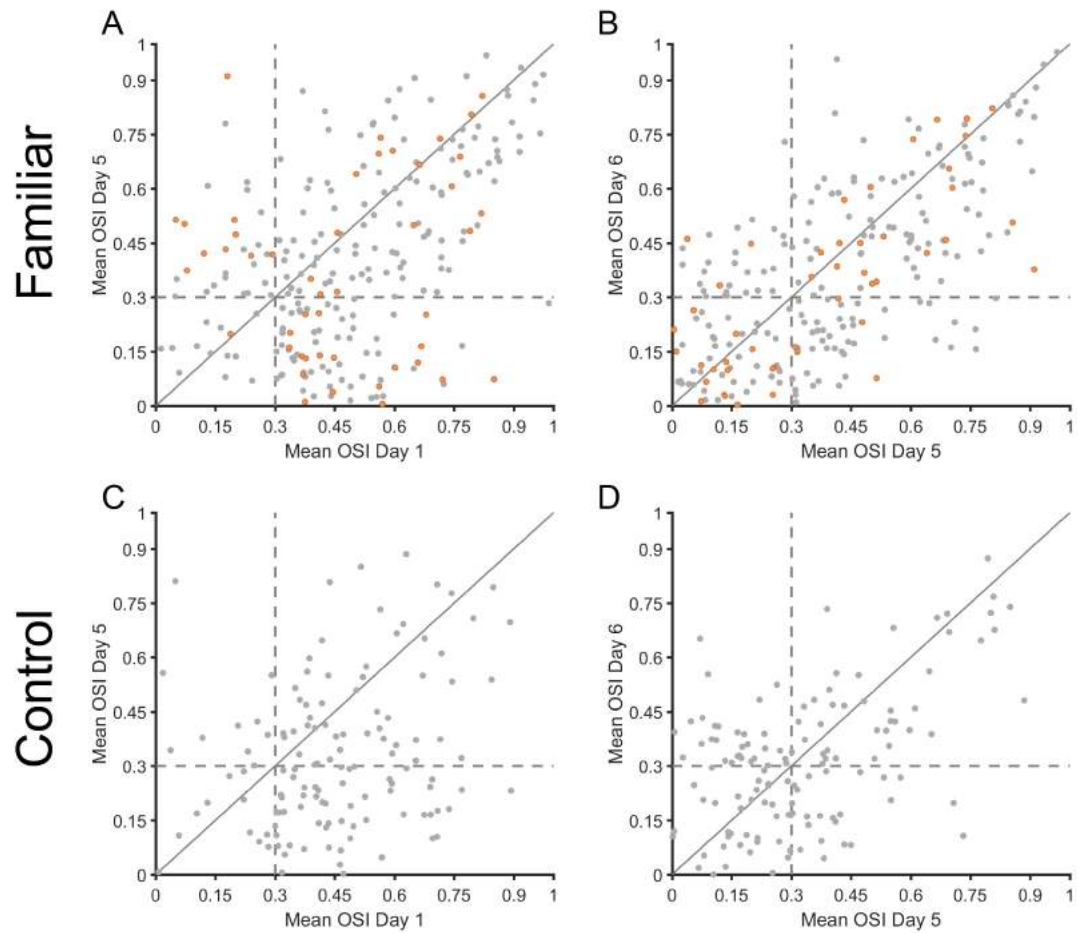


Figure 4.17: Changes in OSI magnitude of individual putative excitatory neurons visually responsive and orientation selective (OSI > 0.3) on at least one day (day 1, 5 or 6) across days for both, familiar (A and B) and control group (C and D) during stationary periods. Orange dots: neurons orientation selective for the familiar orientation on day 1. A) and C) Scatter plots showing the mean OSI magnitude of individual neurons on day 1 against day 5. B) and D) Scatter plots showing the mean OSI magnitude of individual neurons on day 5 against day 6.

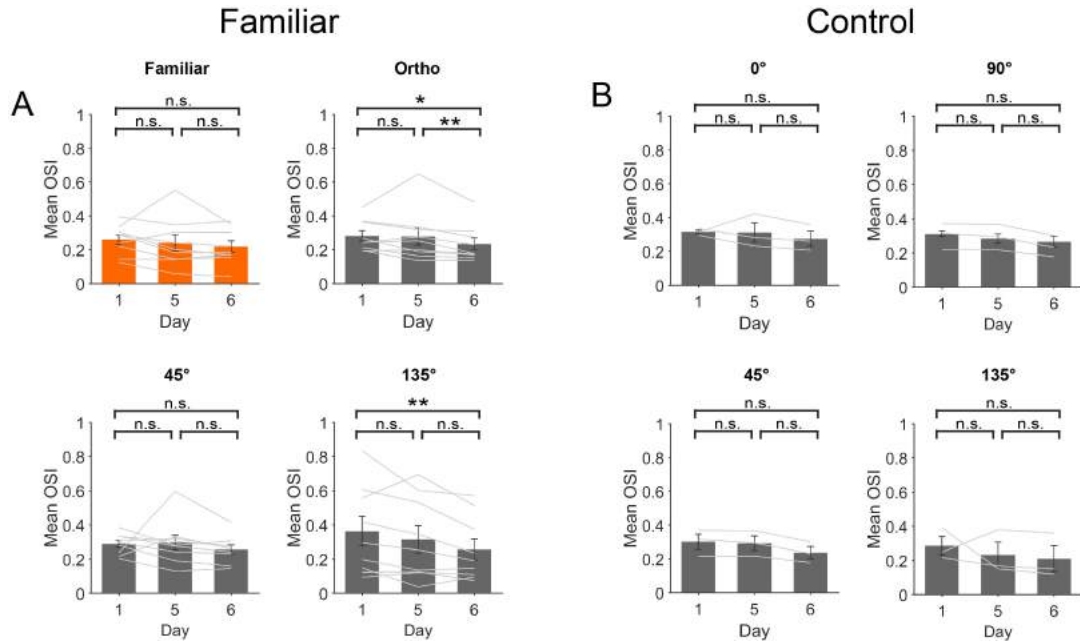


Figure 4.18: Average OSI magnitude across days of all neurons orientation selective on at least one day for both, familiar (A) and control group (B). Error bars indicate s.e.m.; n.s., non-significant, $p > 0.05$, *, significant, $p < 0.05$, **, significant, $p < 0.01$, Wilcoxon signed rank test.

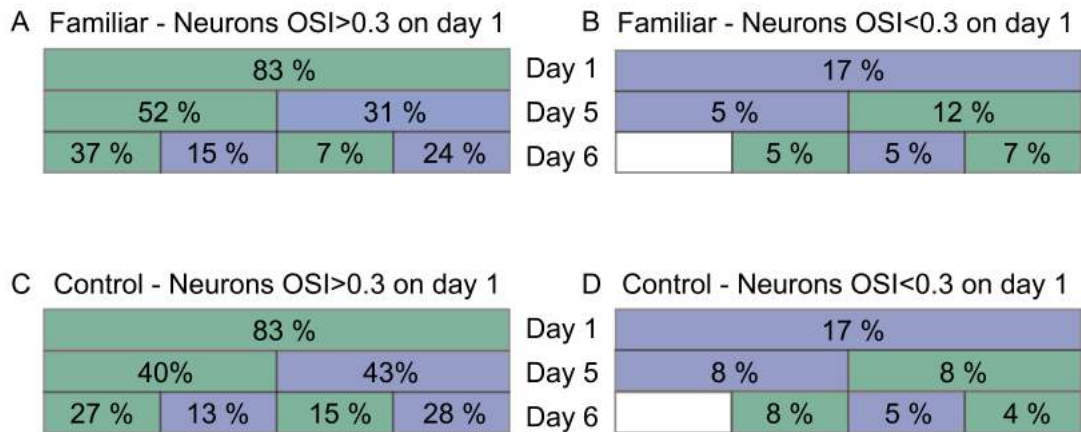


Figure 4.19: Percentage of neurons orientation selective on each day (day 1, 5 or 6) for familiar and control group. Green: percentage of neurons orientation selective. Blue: percentage of neurons not orientation selective. A) Familiar group, neurons orientation selective (OSI > 0.3) on day 1. B) Familiar group, neurons not orientation selective (OSI < 0.3) on day 1. C) Control group, neurons orientation selective (OSI > 0.3) on day 1. D) Control group, neurons not orientation selective (OSI < 0.3) on day 1.

Next, we quantified whether stable neurons that are orientation selective on all three days (day 1, 5 and 6) have a higher mean response amplitude ($\Delta F/F_0$) than neurons not orientation selective on all three days. Again, we found heterogeneous responses with individual neurons displaying lower levels of activity across all three days (Figure 4.20). However, on average neurons orientation selective on day 1, 5 and 6 have a higher mean $\Delta F/F_0$, than neurons not orientation selective on all three days in both groups (Figure 4.21); implying that these cells are more highly active neurons, but also that the passive viewing of a repetitive stimulus did not affect this parameter on an individual cell level.

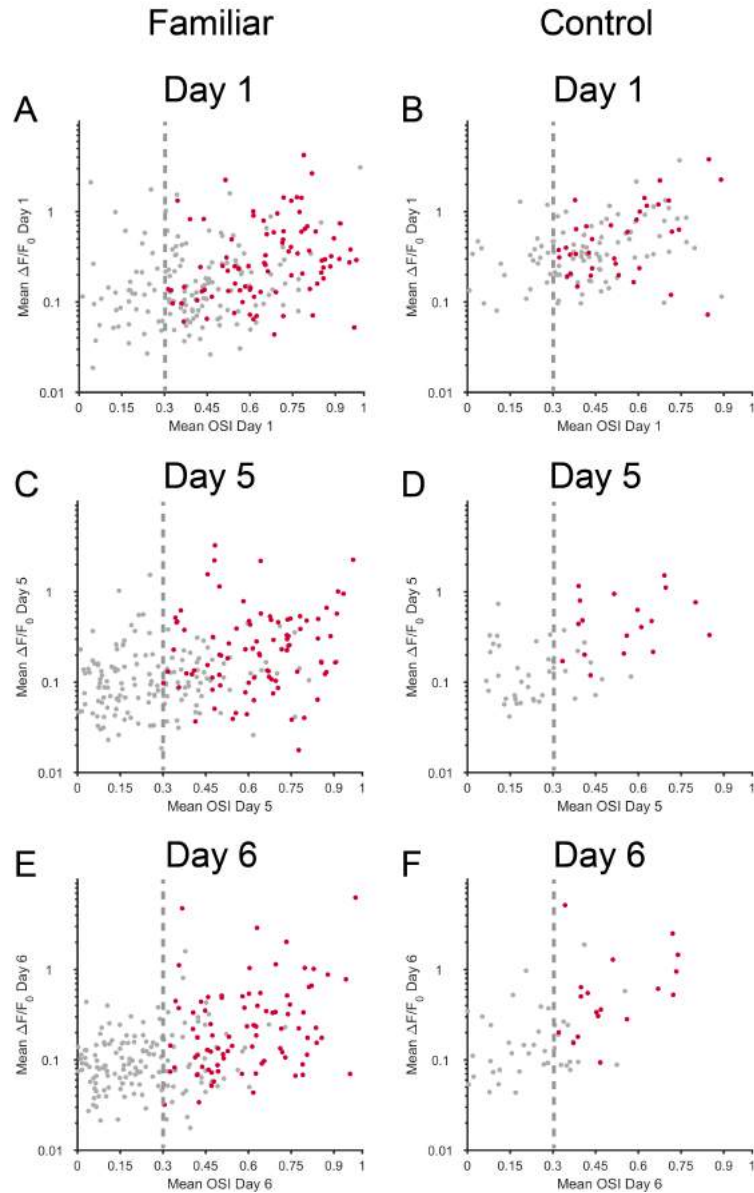


Figure 4.20: Average $\Delta F/F_0$ in relation to OSI of individual putative excitatory neurons orientation selective on at least one day (day 1, 5 or 6) across days for both, familiar (left) and control group (right) during stationary periods. A) and B) Day 1. C) and D) Day 5. E and F) Day 6. Red dots: neurons orientation selective on day 1, 5 and 6.

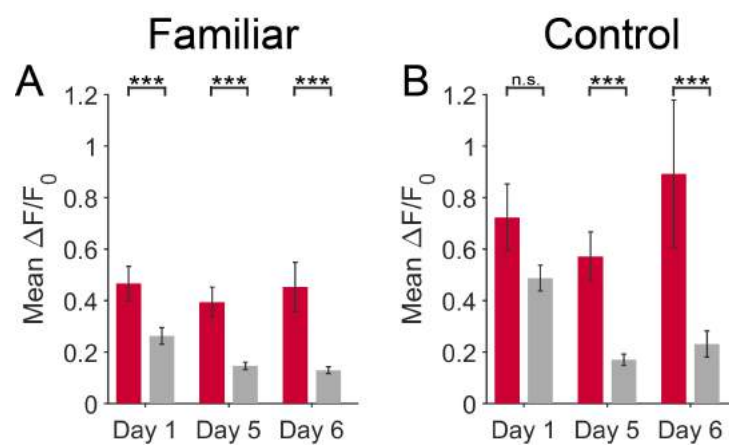


Figure 4.21: Average $\Delta F/F_0$ across days of all neurons orientation selective on at least one day for familiar (A) and control groups (B). Red: neurons orientation selective on day 1, 5 and 6. Grey: neurons not orientation selective on all three days. Error bars indicate s.e.m.; n.s., non-significant, $p > 0.05$, *, significant, $p < 0.05$, **, significant, $p < 0.01$, ***, significant, $p < 0.001$, Mann-Whitney U-test.

4.3.3.2 *Orientation preference across days*

To investigate potential changes in the preferred orientation across days, we examined the changes in preferred orientation between day 1 and day 5 (defined as the difference between the absolute preferred orientation on day 5 to day 1). Thus, a difference of 0° indicates that there was no change in preferred orientation across days, and a difference of 90° indicates that there was a maximal change in preferred orientation (from preferred to orthogonal orientation).

For the familiar group, we found that about 68 % of neurons were stable, meaning they did not change their preferred orientation across days (Figure 4.22 A). A similar proportion of stable neurons (63 %) was found in the control group (Figure 4.22 B), which was exposed to only a grey screen, suggesting that these changes were independent of the visual experience during the 5 consecutive days. Not surprisingly, in both groups we found that the proportion of stable and unstable neurons was dependent on the orientation selectivity of the neurons, with more stably tuned neurons among the highly selective neurons ($OSI > 0.3$). Overall, these results indicate that the higher the OSI magnitude is on day 1, the higher the probability that a neuron is not changing its preferred orientation across days.

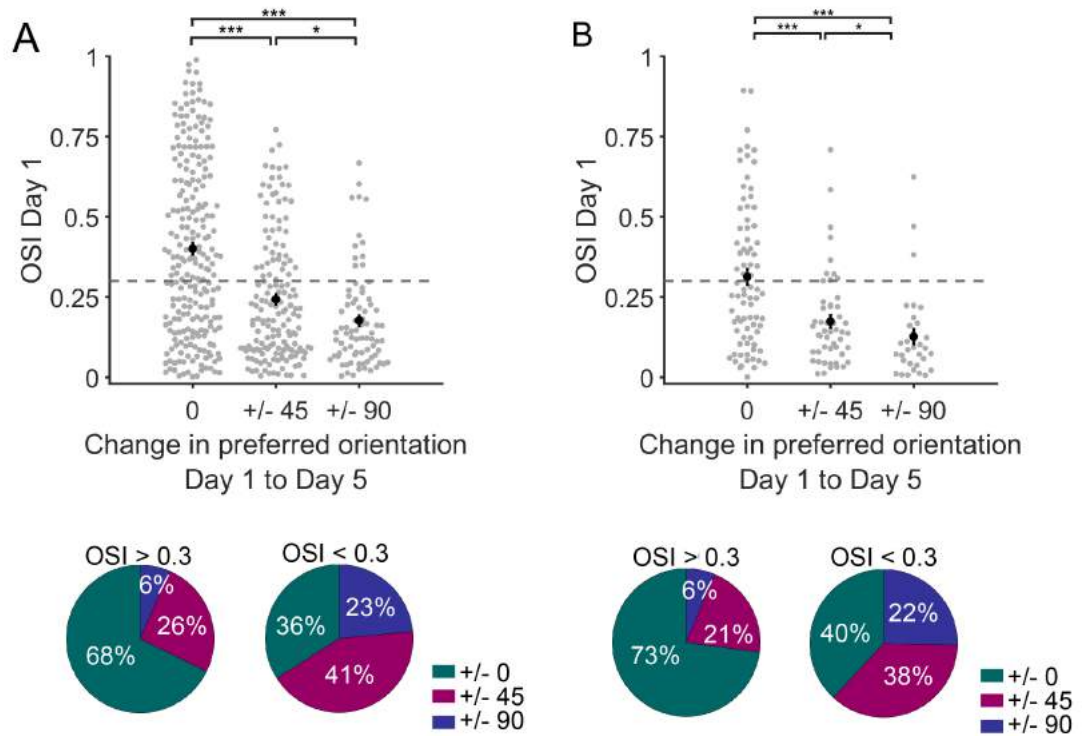


Figure 4.22: Changes in preferred orientation across days. Scatter plot of changes in preferred orientation from day 1 to day 5 of each neuron for the familiar condition as a function of OSI magnitude. ± 0 , no change in preferred orientation; ± 45 , change in preferred orientation by 45° ; ± 90 , change in preferred orientation by 90° . Pie charts display the percentage of orientation selective ($\text{OSI} > 0.3$) and not orientation selective ($\text{OSI} < 0.3$) neurons that: do not change their preferred orientation from day 1 to day 5 (green), change their preferred orientation from day 1 to day 5 by 45° (red) and change their preferred orientation from day 1 to day 5 by 90° (blue). B) Data are presented as in A for control condition. Black dots represent mean $\Delta F/F_0$ per animal. Error bars indicate s.e.m.; *, significant, $p < 0.05$, ***, significant, $p < 0.001$, Mann-Whitney U-test.

4.3.4 Behavioural state-specific modulation of neuronal activity across days

As described in the previous chapters ([Chapter 3](#), see also Pakan et al., 2016), locomotion affects the response properties of V1 neurons. Specifically, responses of excitatory neurons during visual stimulation increase during locomotion. This response gain is specific to the behavioural state of the animal.

To investigate whether the state-specific response of excitatory neurons is stable across days we first verified that enough locomotion and stationary periods were sampled. This is important, since all mice were allowed to voluntarily run on the circular treadmill, thus the total amount of running and the total amount of stationary periods differed across days and between animals ([Figure 4.23](#)). On average, mice spend at least 20 percent of the total amount of time running per day during visual stimulation, thus providing enough data to investigate state-specific modulation of neuronal responses ([Figure 4.23](#)).

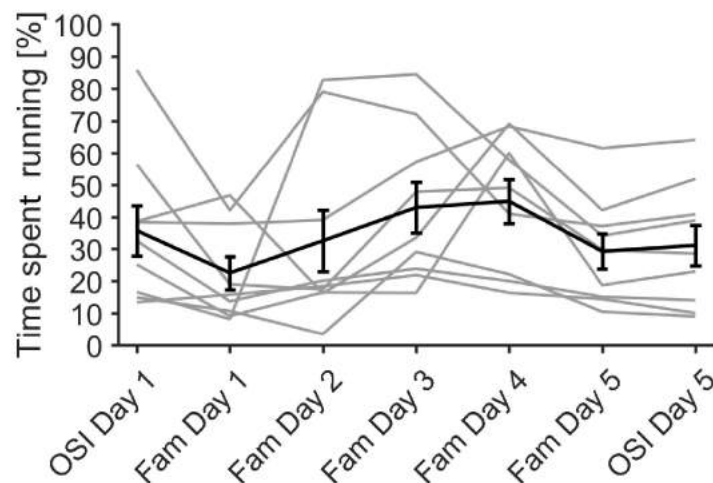


Figure 4.23: Total amount of time spend running in percent per animal across days during visual stimulation. Grey lines: individual animals, black lines: mean across animals, errorbars: s.e.m. Amount of locomotion during visual stimulation trials (gratings), day 1 to 5. On day 1 and 5 the amount spent running is separated into locomotion periods during the orientation mapping stimulus (OSI day 1 and OSI day 5) and locomotion periods during the presentation of the familiar stimulus (Fam day 1 and Fam day 5).

We then compared the responses during locomotion periods of visually responsive neurons across days (Figure 4.24). We found no significant difference in $\Delta F/F_0$ for either, the familiar group (Figure 4.24 A-C) or the control group (Figure 4.24 D-F), indicating that the average population response to all oriented gratings was stable across days during stationary as well as during locomotion periods.

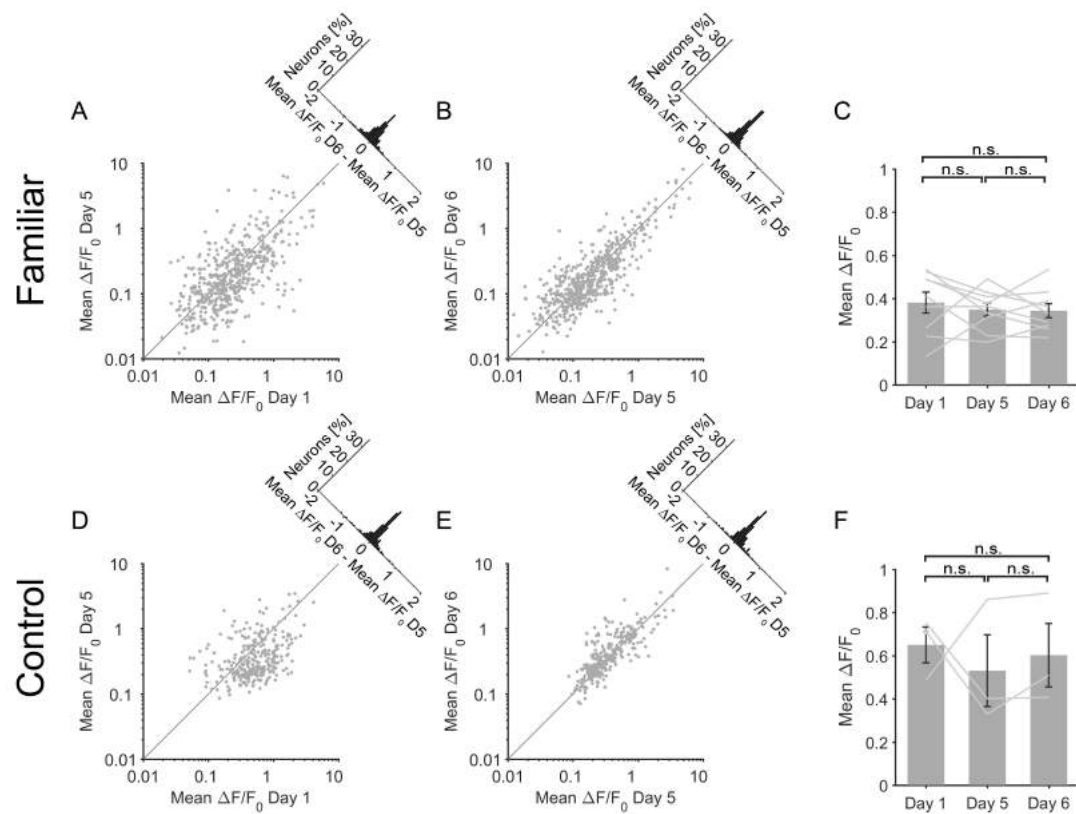


Figure 4.24: Stability of population visual responses across days (putative excitatory neurons) in both familiar (A, B, C) and control group (D, E, F) during locomotion periods. A) and B) Scatter plots of the average amplitude of fluorescence changes ($\Delta F/F_0$) of each neuron visually responsive on at least one day (day 1, 5 or 6). A) Day 1 against day 5. B) Day 5 against day 6. C) Average response amplitude ($\Delta F/F_0$) of all neurons visually responsive on at least one day (day 1, 5 or 6) during locomotion periods. D), E) and F) Date presented as in A), B) and C) for control group (grey screen). Grey lines represent the average value per animal per day. Error bars indicate s.e.m.; n.s., non-significant, $p > 0.05$, Wilcoxon signed rank test.

Next, to investigate whether the state-specific response of excitatory neurons is stable across days we examined the $\Delta F/F_0$ of locomotion periods compared to the $\Delta F/F_0$ of stationary periods (LMI). The results confirmed the findings presented in Chapter 3, showing that locomotion increases the amplitude of $\Delta F/F_0$ during visual stimulation. This was true for both, day 1 and day 5 (Figure 4.25 and Figure 4.26). Our results show no difference in LMI between day 1 and day 5 during visual stimulation, indicating a stability of the effects of locomotion on V1 putative excitatory neuron activity across days, both in the familiar (Figure 4.25) and control group (Figure 4.26).

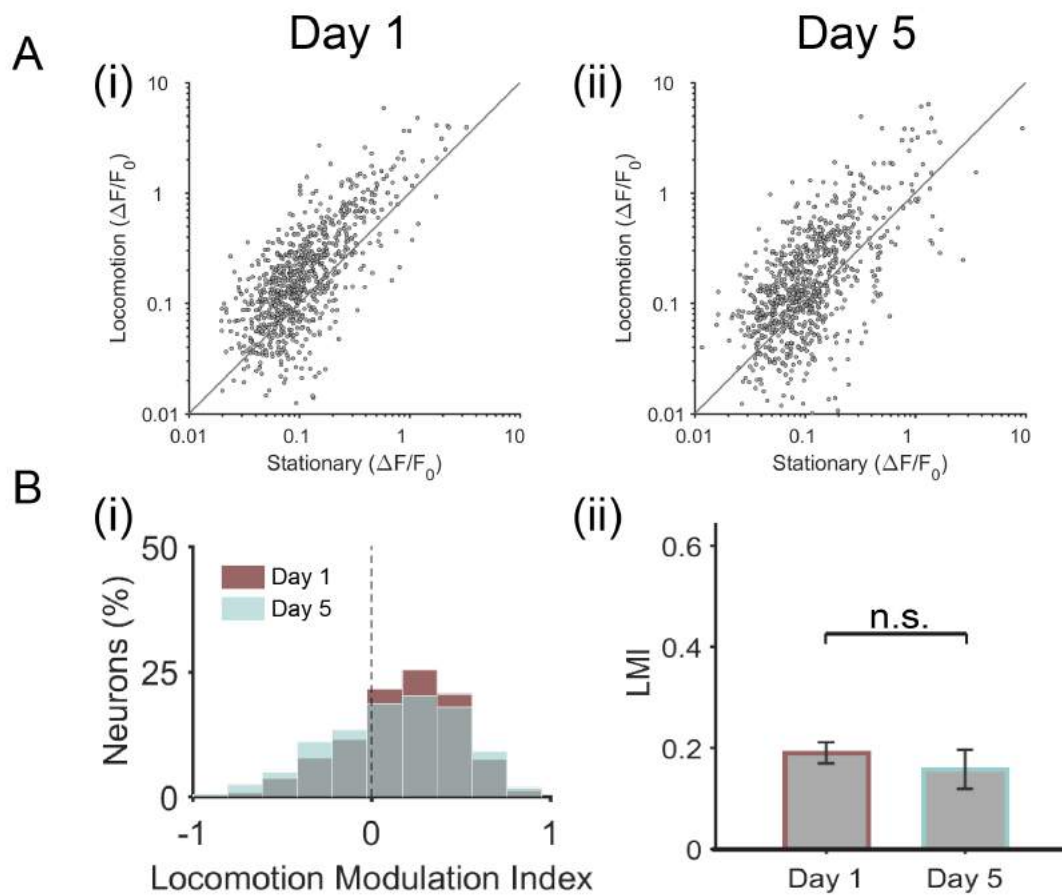


Figure 4.25: Comparison of the LMI of putative excitatory neurons in layer 2/3 of V1 across days (familiar group): A) Scatter plots showing mean ($\Delta F/F_0$) per neuron obtained during stationary periods plotted against mean ($\Delta F/F_0$) obtained during locomotion periods, (i) day 1, (ii) day 5. B) (i) Histogram showing LMI distribution during visual stimulation (day 1 compared to day 5), (ii) mean LMI of all active neurons during visual stimulation on day 1 and day 5 respectively. Error bars s.e.m., n.s., not significant ($p > 0.05$); $n = 9$ mice; Wilcoxon signed rank test.

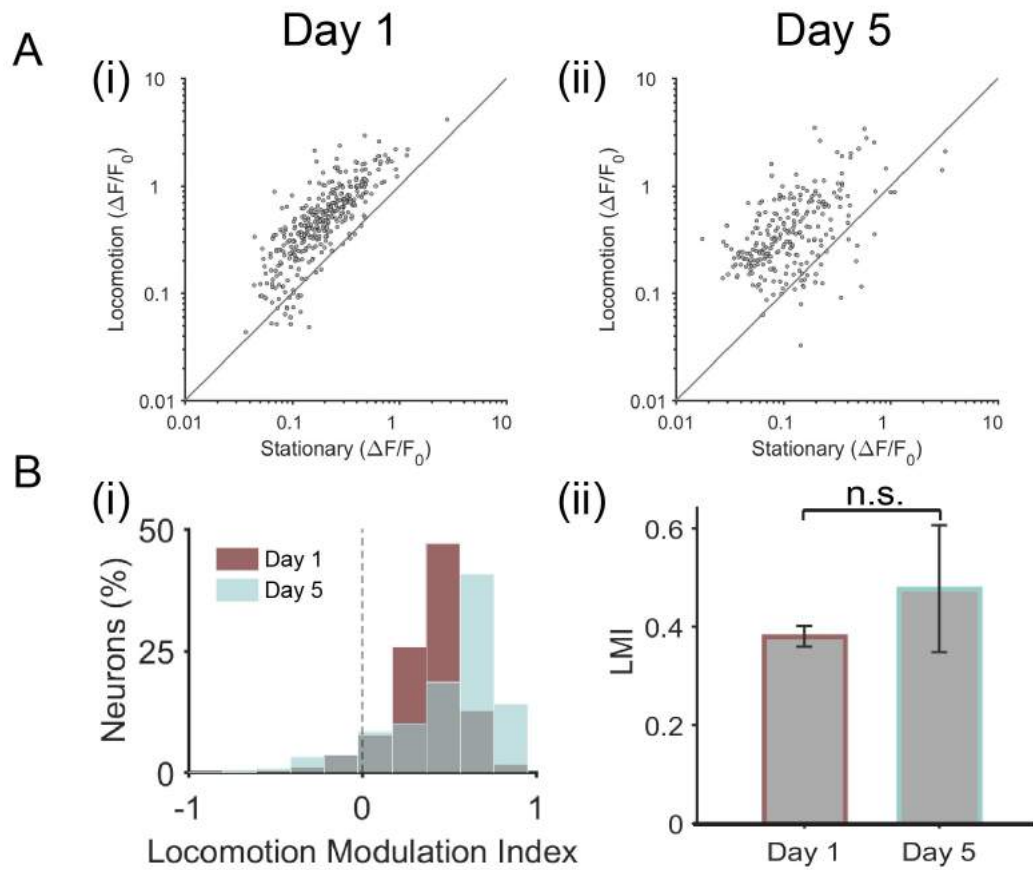


Figure 4.26: Comparison of the LMI of putative excitatory neurons in layer 2/3 of V1 across days (control group): A) Scatter plots showing mean ($\Delta F/F_0$) per neuron obtained during stationary periods plotted against mean ($\Delta F/F_0$) obtained during locomotion periods, (i) day 1, (ii) day 5. B) (i) Histogram showing LMI distribution during visual stimulation (day 1 compared to day 5), (ii) mean LMI of all active neurons during visual stimulation on day 1 and day 5 respectively. Error bars s.e.m., n.s., not significant ($p > 0.05$); $n = 9$ mice; Wilcoxon signed rank test.

Additionally, we wanted to investigate whether the total amount of locomotion had an effect on neuronal response properties of individual V1 neurons. A recent study showed that animals which run more during the presentation of a defined visual stimulus showed an increase in response to that particular stimulus, whereas animals not running during the stimulus presentation would not show a stimulus-specific potentiation. Therefore, we calculated the total amount of time each animal spent running during the presentation of the familiar stimulus (Figure 4.27). The total amount of running time was plotted against the normalized change in $\Delta F/F_0$ from day 1 to day 5, for all visually responsive neurons. We found a small increase in $\Delta F/F_0$ with the amount of time spent running during the presentation of the familiar stimulus ($\Delta F/F_0 = 0.05$, Figure 4.27).

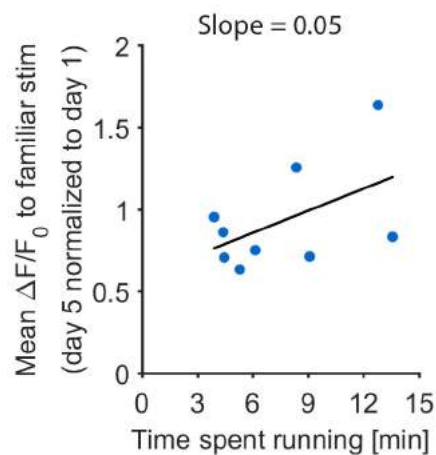


Figure 4.27: Correlation of the total amount of locomotion during the presentation of the familiar stimulus and the amplitude of neuronal responses to familiar stimulus on day 5 normalized to day 1. Each dot corresponds to the data obtained from one mouse.

4.3.5 *Stability and plasticity of interneuron activity across days*

Previous studies have reported experience-dependent changes in inhibitory interneuron activity in V1 (Makino and Komiyama, 2015, Kaplan et al., 2016). To test potential changes in inhibitory activity across days, we imaged three non-overlapping populations of inhibitory interneurons (VIP-, SST-, and PV- inhibitory interneurons) while presenting a visual stimulus (Figure 4.29). Note that inhibitory interneuron activity was only recorded for the familiar condition. As for excitatory neurons, it has been shown, that inhibitory neurons in mice V1 are modulated by locomotion (example traces of individual neurons: Figure 4.28, average data: Chapter 3, Polack, Friedman, and Golshani, 2013, Fu et al., 2014, Pakan et al., 2016). Thus, to avoid any bias caused by an increase or decrease in the proportion of locomotion activity across days, the responses were calculated separately for stationary and locomotion periods. We found no significant difference in $\Delta F/F_0$ for any class of interneurons between day 1 and day 5, both during stationary and during locomotion periods (Figure 4.29). Furthermore, as shown in Chapter 3, we confirmed the increase of visual responses of interneurons during locomotion (positive LMI for VIP-, SST- and PV-expressing interneurons). This modulation of activity by locomotion was not significantly different between day 1 and day 5 (Figure 4.29). However, even though not significant all three interneuron subclasses displayed a slight decrease in LMI values from day 1 to day 5. This is likely due to the slight non-significant decrease in $\Delta F/F_0$ across the days, which was more pronounced during locomotion than to during stationary periods and hence, leads to a reduction on LMI ratio between both.

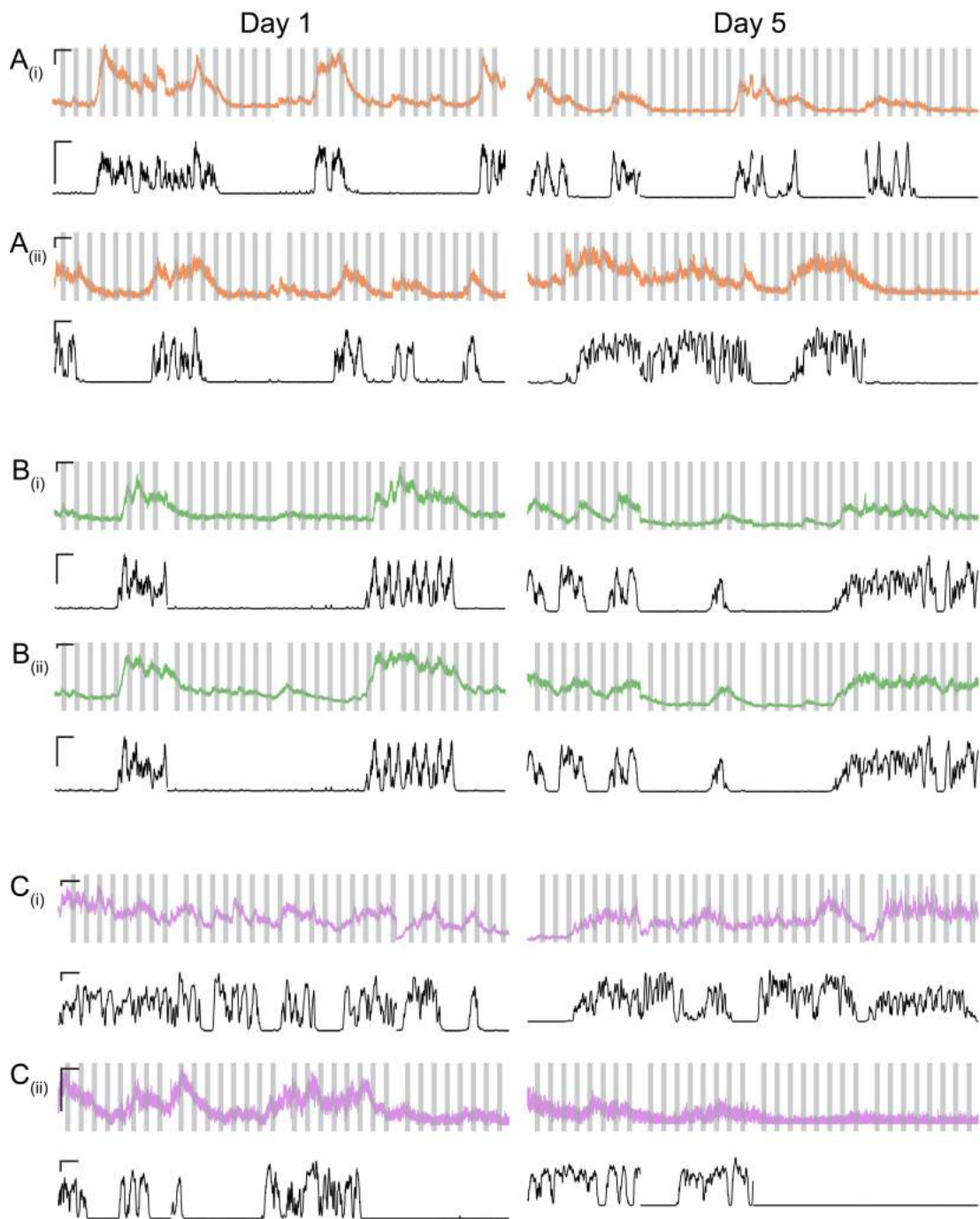


Figure 4.28: Example traces of inhibitory interneurons. A) VIP interneurons, B) SST interneurons. C) PV interneurons. Black trace: running speed (cm/s). Grey bars: oriented gratings.

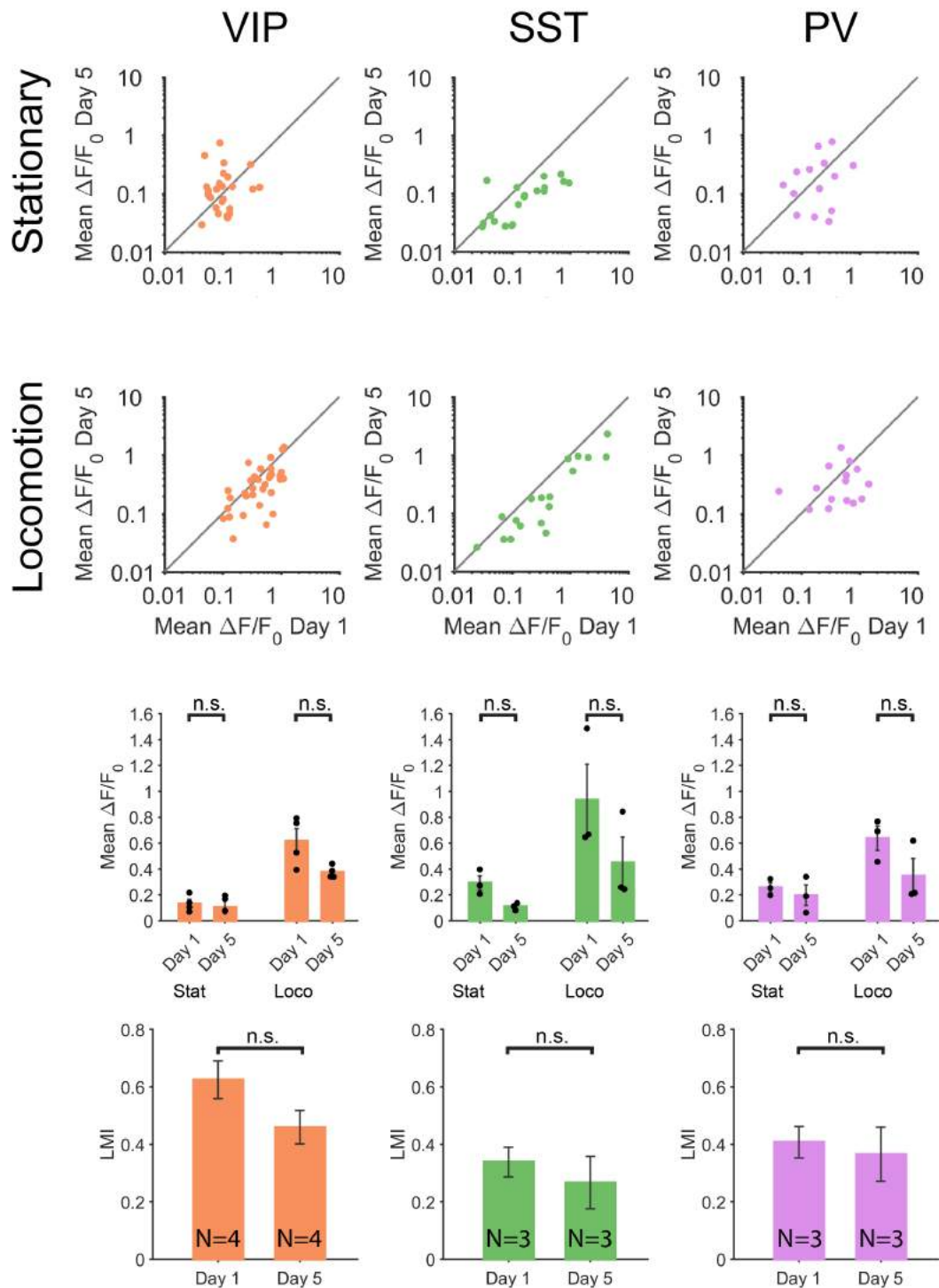


Figure 4.29: Changes in $\Delta F/F_0$ during locomotion and stationary periods of all active interneurons (VIP: orange, SST: green and PV: purple) across days during visual stimulation. Scatter plots of the average amplitude of fluorescence changes ($\Delta F/F_0$) per neuron. Average of $\Delta F/F_0$ per day during stationary and locomotion periods. Black dots represent average $\Delta F/F_0$ per animal. Error bars indicate s.e.m.; n.s., non-significant, $p > 0.05$, Wilcoxon signed rank test.

4.4 DISCUSSION

In this study, we examined changes in neuronal response properties across days before, during and after the daily brief presentation of a visual stimulus in putative excitatory and three non-overlapping inhibitory interneuron subclasses. In summary, we did not find any significant difference between the familiar and the control group (grey screen) indicating a lack of stimulus-specific plasticity in our experimental conditions. At the population level, we found a decrease in the proportion of visually responsive neurons as well as in the proportion of orientation selective neurons. This decrease was significant in the familiar experimental group and not significant in the control group. Furthermore, there was a non-significant increase in number of visually responsive neurons and number of orientation selective neurons observed in the control group between day 5 and day 6, but not in the familiar group. Therefore, the change in orientation selective neurons seems to resemble the change in visually responsive neurons across days in both experimental groups. The major difference between the imaging sessions on day 5 of both experimental groups was that the familiar group is stimulated with a defined grating (familiar grating) while the control group is stimulated with an isoluminant grey screen, before animals of both groups are presented with four differently oriented gratings to test the number of visually responsive neurons as well as orientation preference. This difference in experimental paradigm might affect the number of visually responsive neurons, however further studies increasing the low number of animals in the control group ($N=3$) and further investigating the specific mechanisms underlying the change in stimulus specific neurons responding on different days are needed to fully understand this observation. Since all three animals of the control group display the same drop in visually responsive and orientation selective neurons on day 5 as well as an increase on day 6 and all three animals were recorded on different days, it is unlikely that changes in the experimental setup, such as screen position or image quality, caused these specific changes. Contrary, average population responses to visual stimuli were stable (average $\Delta F/F_0$ to each presented grating orientation, OSI, LMI) across days in both experimental groups.

At the single cell level, we found neurons displaying an increase or decrease in response amplitude to visual stimulation in general (all gratings), as well as neurons showing both an increase and decrease between different experimental days and neurons not changing their response amplitude. However, the range of response amplitudes displayed by individual neurons was similar across days. Furthermore, heterogeneous changes, with some neurons decreasing or increasing, as well as neurons which did not change their response amplitude across days specifically to their preferred orientation, were observed in both experimental groups. The observed decrease or increase in response amplitudes to the preferred orientation was accompanied by neurons losing and gaining orientation selectivity. We found that neurons strongly

preferring a specific orientation (0° , 45° , 90° , 135°) on day 1 ($OSI > 0.3$) were more likely to respond preferentially to the same orientation across days.

Finally, we investigated the response properties of three non-overlapping classes of inhibitory neurons, namely VIP-, SST-, and PV inhibitory neurons, across days. We did not observe significant changes in responses properties between day 1 and day 5 in any of the three subpopulations at the population level. However, the response amplitude of individual neurons also displayed heterogeneous changes across days, with more neurons decreasing their response amplitude than increasing. Especially SST interneurons mainly decreased their response amplitude, however not reaching significance. Additionally, VIP interneurons also show mainly a decrease in response amplitude between day 1 and day 5 during locomotion periods. However, during visual stationary periods a subset of VIP interneurons display an increase in response amplitude between day 1 and day 5. However, further experiments specifically investigating changes in SST and VIP interneurons to increase the number of neurons recorded will be needed to reveal a potential role of both interneuron types in experience-dependent processes and to draw comprehensive conclusions.

4.4.1 *Repetitive passive exposure to sensory stimuli: Adaptation vs Potentiation*

In our study, a brief presentation of a defined visual stimulus (grating) across five consecutive days did not induce a stimulus-specific potentiation of neuronal activity. The absence of significant difference between the familiar and the control group further confirms that our protocol did not induce stimulus-specific changes, neither at the single neuron level nor at the population level. However, earlier studies did find a stimulus-specific response potentiation (SRP) at the population level after the brief presentation of a defined visual stimulus across five consecutive days (Frenkel et al., 2006, Cooke and Bear, 2010). This study was using electrophysiological recordings (local field potentials, LFP) and found the biggest increase in response amplitude in layer 4 of V_1 , while the data presented in this thesis were acquired in layer 2/3. Thus, the potentiation might only take place in layer 4 and not be detected in layer 2/3. However, since layer 4 is the main input-recipient layer of V_1 , it remains to be seen how the potentiation observed in layer 4 is relayed to other layers. In addition, while LFP recordings sample both subthreshold and suprathreshold electrical signals in a relatively large area, calcium imaging only detects suprathreshold events in single neurons. Hence, if the observed potentiation by Bear and colleagues is a subthreshold effect, we would not have been able to detect the effect with calcium imaging. Additionally, it is conceivable that most SRPs in layer 4 of V_1 are arising from the input of the LGN to layer 4. However, it has been shown that SRPs reside in V_1 (Frenkel et al., 2006, Cooke and Bear, 2010, Cooke et al., 2015), thus it is unlikely that the LGN input to layer 4 is the main trigger for SRPs.

The experiments conducted by Bear and colleagues used mice that were maintained

on a 12/12 hour light-dark cycle and experiments were conducted during the light cycle of the animal (Gavornik and Bear, 2014b, Cooke et al., 2015). Stimulus-specific response potentiation was also shown to depend on overnight consolidation during sleep (Aton et al., 2014). Using electrophysiological recordings and spike sorting Aton et al., 2014 could show that more than twice as much principle neurons enhance their responses after sleep compared to when mice were sleep deprived. The mice recorded for this study were not on a 12/12 reversed light-dark cycle. Hence, the experiments were conducted during the dark cycle and thus, interrupted the sleep time of the mice. As shown by Aton et al., 2014, this disruption of sleep might have caused a disruption of the consolidation process and prevented the formation of stimulus-specific effects.

Another recent study did show stimulus-specific potentiation at the single neuron level in V1 layer 2/3 after the brief presentation of a defined stimulus over five consecutive days (Kaneko, Fu, and Stryker, 2017). These results showed that only neurons orientation selective for the grating presented across the five consecutive days increase their response amplitude and that this potentiation was only observed in mice that were running for at least one hour (total of 10 hour presentation, one hour per day for 10 days) during the presentation of the stimulus. In our study, mice were presented for 5 minutes per day with a defined visual stimulus and were free to run. Hence, under our experimental conditions mice run less than 25 minutes during the stimulus presentation. Therefore, it is possible that we did not observe the same effect due to less running time. However, the study conducted by Bear and colleagues (Frenkel et al., 2006, Cooke and Bear, 2010) showing a stimulus-specific response potentiation was performed in head-fixed mice, placed in a tube and not able to run. Thus, it needs to be determined whether the potentiation described in both studies relates to the same mechanisms. An additional difference between both studies is that LFP recordings were performed in awake mice while the two-photon calcium imaging data were acquired in anesthetized mice. It was shown that a general anesthesia significantly reduces inhibitory interneuron activity (Harris and Thiele, 2011, Haider, Häusser, and Carandini, 2013). A reduction in inhibitory inputs may lead to a potentiation in response amplitude. However, it is debatable how a general anesthesia leads to a stimulus-specific effect.

Finally, a third study used a similar protocol in awake mice and found different results. Using two-photon calcium imaging, this study showed a decrease in population response of layer 2/3 V1 neurons across days (Makino and Komiyama, 2015). This decrease was mediated by a decrease in the total number of visually responsive neurons while the overall response of all visually responsive neurons per day stayed constant across days. Importantly, the study was conducted in awake-behaving mice, which were running and the observed reduction of the population response was stimulus-specific. As Makino and Komiyama, 2015 we found a stable response of all visually responsive neurons per day and a decrease in visually responsive neurons. Howe-

ver, we found a decrease in number of visually responsive neurons in the control group presented with an isoluminant grey screen as well as in the familiar group presented with a grating stimulus, arguing against a stimulus-specific effect, whereas Makino and Komiyama, 2015 found a stimulus-specific decrease. The reasons of this discrepancy remain currently unclear.

4.4.2 *Experimental limitations*

One concern when interpreting these results is that increases and decreases in the amplitude of fluorescent changes ($\Delta F/F_0$) could be caused by neurons moving in and out of the focal plane across imaging days. We tried to avoid such bias first during the acquisition of the data and then during the analysis. We used the presence of thin dendrites within the field of view as markers of the focal plane: since dendrites are very thin, ensuring that the same dendrites are visible across days is a good control of the focal plane. However, uneven torsion of cortical tissue may happen across days, so that neurons or dendrites that were initially in the same focal plane become out of focus. That is why careful inspection of each labeled cell was performed during the segmentation of the images acquired across days. As a result, only a limited number of neurons, especially sparse inhibitory interneurons (sometimes only two to three per field of view), could be analyzed. The number of neurons imaged per animal per experiment could be increased using a two-photon imaging setup with an integrated piezo-electric device or an Acousto-Optic Deflectors (AOD)-based set-up, enabling multi-plane imaging (fast imaging of multiple focal planes) (Andermann et al., 2010, Kerlin et al., 2010, Katona et al., 2012).

Another potential source that can bias our results relates to a potential increase in expression level of the genetically encoded calcium indicator (GECI) across days. To minimize such bias, the change in fluorescence over time ($\Delta F/F_0$) was calculated defining the baseline (F_0) across days. The fact that we found neurons showing an increase as well as neurons showing a decrease in $\Delta F/F_0$ amplitude in the same animal over days, suggests that baseline shifts are unlikely to affect our results, because it is unlikely that changes in baseline would lead to both increases and decreases in amplitude at the same time.

Furthermore, variability between animals and between recording days might be introduced by changes in level of arousal of individual animals. For instance, recent studies have shown, that neuronal activity changes across behavioural states such as anaesthesia (Haider, Häusser, and Carandini, 2013), waking (Reimer et al., 2014, Vinck et al., 2015), and locomotion (Polack, Friedman, and Golshani, 2013, Fu et al., 2014, Pakan et al., 2016). While this study separated locomotion and still periods to reveal potential differences in neuronal responses during different behavioural states, differences in arousal level during still periods have not been investigated. However, it was shown that during still periods neuronal response properties of V1 neurons

differed in response reliability and magnitude depending on arousal state (Reimer et al., 2014). Hence, differences in arousal levels during still periods might underlay the variability observed in neuronal responses between animals and recording days. Furthermore, it was shown that arousal and locomotion make distinct contribution to neuronal activity patterns in V1 (Vinck et al., 2015). For example, locomotion leads to an increase in firing activity of regular spiking neurons whereas a state of high arousal result in a suppression of spontaneous activity (Vinck et al., 2015). Therefore, separating locomotion and still periods is an important step towards to dissecting behavioural state dependent changes, but insufficient to account for changes in overall arousal level (Niell, 2015).

Finally, the definition of an orientation selective neuron is based on an arbitrary criterion. In this study, we used an $OSI > 0.3$ to define orientation selective neurons. In the past other thresholds were used to define orientation selective neurons. For example, an OSI threshold of 0.5 (e.g. Rochefort et al., 2011, Niell and Stryker, 2008, Grienberger et al., 2012) and higher for this study would change the results towards a more stable network and less heterogeneity at the single neuron level.

Furthermore, OSI values can be calculated using different formulas. For this study, the OSI was calculated by dividing the difference between the $\Delta F/F_0$ amplitude of the preferred grating to the orthogonal grating by the sum of both. Another OSI calculation uses the circular variance (Ringach, Shapley, and Hawken, 2002). While the first method uses only the response amplitude to the preferred and the orthogonal grating to calculate the OSI, the circular variance takes into account the responses to all presented gratings. Therefore, both methods lead to different results.

4.4.3 Future prospects

In order to reconcile the results of the studies described above, it would be informative to combine the recording of visually evoked potentials (VEP) (Frenkel et al., 2006, Cooke and Bear, 2010, Gavornik and Bear, 2014b) using electrodes with *in vivo* two-photon calcium imaging. This approach enables the correlation of the results gained from the recording of VEPs with the results obtained at the single neuron level using two-photon calcium imaging. Practically, it would be necessary to implant a cranial window and at least two electrodes (recording and reference electrode) in V1. One option would be to record both signals from different hemispheres. When stimulation and recordings take place in the binocular region, it is fair to assume that both visual hemispheres likely respond in a similar way in response to the presented visual stimulation. One of the biggest challenges would be to arrange for enough space for the recording electrodes between the skull and the objective. A new head-plate design and long working distance objectives might be necessary. Another approach would be to record the activity of layer 4 neurons of V1, where the main effect of VEPs stimulus selective response potentiation was found. Furthermore, simultaneous imaging of

layer 2/3 and layer 4 single neurons activity could reveal potential differences in the encoding of a repetitive stimulus between both layers. Simultaneously imaging of layer 2/3 and layer 4 of V1 could be achieved by either using a two-photon imaging setup capable of performing 3D volume imaging (AOD) (Andermann et al., 2010, Ji, Freeman, and Smith, 2016) or a setup fitted with a piezo-electric stage capable of imaging multi-planes nearly simultaneously (Rose et al., 2016). Additionally, two-photon imaging experiments could be used to image chronic changes in LGN labeled axons within V1 in order to investigate whether there are any changes in response properties to repetitive visual stimulation earlier in the visual pathway. To do so, one possibility would be to use mini-scopes in combination with GRIN (gradient index) lenses which enables imaging of subcortical structures, such as the LGN (Jung et al., 2004, Ghosh et al., 2011, Resendez and Stuber, 2015). Finally, it would be interesting to test whether anesthesia does reveal stimulus-specific potentiation by altering inhibition in V1 (Harris and Thiele, 2011, Haider, Häusser, and Carandini, 2013). This would explain the difference between our results and the results of a previous study (Kaneko, Fu, and Stryker, 2017). For this, we could use the same protocol in awake mice while removing inhibition. This could be done either by using DREADDS (Designer Receptor Exclusively Activated by Designer Drugs) (Smith et al., 2016, Armbruster et al., 2007) or cell-type specific optogenetics (Deisseroth, 2011) in inhibitory neurons.

NEURONAL RESPONSE PROPERTIES IN THE ADULT PRIMARY VISUAL CORTEX OF A MOUSE MODEL OF INTELLECTUAL DISABILITY

5.1 INTRODUCTION

The *Syngap* gene (synaptic Ras GTPase-activating protein 1) is frequently mutated in intellectual disorders (ID) associated with global developmental delay and is a risk factor for autism spectrum disorders (ASD) (Pinto et al., 2010, Mefford, Batshaw, and Hoffman, 2012, Hamdan et al., 2011) and severe epilepsy (Carvill et al., 2013). Approximately 3 % of the population in the Western countries are affected by ID, which is characterized by an intelligent quotient (IQ) below 70 (Mefford, Batshaw, and Hoffman, 2012). Family studies suggest that both ASD and ID have a strong heritable component (Bailey et al., 1995).

ID and ASD phenotypes can arise from a mixture of several, potentially diverse genetic as well as environmental factors (Mefford, Batshaw, and Hoffman, 2012), and in a minority of cases they arise from mutations of a single gene (monogenic) (Pinto et al., 2010). While the genetic causes seem diverse and exhibit pleiotropy, they seem to converge on common cellular signalling pathways (Wijetunge et al., 2013 Barnes et al., 2015b). This motivates the study of representative genetic animal models, with the expectation that findings may generalise across a broad range of ASD-associated syndromes.

The investigation of monogenic ASD/ID animal models at the cellular level has revealed several alterations in neuronal properties, such as changes in excitability, synaptic transmission and neural plasticity (Komiyama et al., 2002, Kim et al., 2003, Clement et al., 2012). However, there is only little known about how these changes affect neuronal activity at the circuit level *in vivo*, and how this leads to the diversity of behavioural phenotypes characteristic for ASD/ID. Addressing this gap in knowledge requires a comprehensive understanding of the circuit-level features in the brain of ASD/ID animal models.

In the past years several single gene mutant mice models have been developed, to investigate the pathogenicity of these mutations as well as potential treatments for these diseases. The two most common monogenic syndromes of ASD/ID are Fragile X Syndrome (FXS) (Krueger and Bear, 2011, Wijetunge et al., 2013) and SYNGAP1 haploinsufficiency (Pinto et al., 2010). Mouse models have been generated for both mutations; *Fmr1*^{-/y} (Bakker et al., 1994) and *SynGAP*^{+/-} mice (Kim et al., 2003, Clement et al., 2012, Komiyama et al., 2002).

This chapter will focus on neuronal circuit activity and plasticity in adult SynGAP^{+/-} mice (kindly provided by Dr Seth Grant (Edinburgh University, United Kingdom), a mouse model of ID. We investigated how this mutation affects neural activity in cortical networks, focusing on the primary visual cortex where inputs are easily controllable.

5.1.1 *SynGAP expression and function*

The synaptic GTPase-activating protein (SynGAP) is a neuronal RasGTPase activating protein (RasGAP) that is found at excitatory synapses as part of a macromolecular complex called post-synaptic density (PSD) (Chen et al., 1998, Kim et al., 1998). SynGAP is expressed exclusively in the brain with highest expression levels found in the cortex and the hippocampus (CA1 and dentate gyrus regions) (Chen et al., 1998, Kim et al., 1998).

Ras signaling is essential for the activation of the mitogen-activated protein (MAP) (Figure 5.1). MAP kinase activation leads to the activation of extracellular signal-regulated kinases-1 and -2 (ERK1 and ERK2), which finally leads to the insertion of AMPARs into the postsynaptic membrane, facilitating long-term potentiation (LTP) (Zhu et al., 2002). Thus, the activation of ERK leads to the regulation of activity dependent genes, an important process involved in neuronal plasticity. As a consequence, mutations in the *Syngap* gene are expected to affect both neuronal activity and plasticity (Atkins et al., 1998, Di Cristo et al., 2001, Thomas and Huganir, 2004).

Ras signaling can be triggered by elevated calcium levels, but the exact mechanism remains to be elucidated (Rosen et al., 1994). It was shown that SynGAP, as part of the PSD complex, is in close proximity of N-methyl-D-aspartate receptors (NMDAR) (Moon, Apperson, and Kennedy, 1994, Husi et al., 2000), and signal-transduction molecules such as Ca²⁺ /calmodulin-dependent protein kinase II (CaMKII) (Kennedy, Bennett, and Erondur, 1983, Kennedy, Bennett, and Erondur, 1983). The scaffolding protein PSD-95/SAP-90 is believed to serve as an adapter protein that helps to organize synaptic structures in large macromolecular complexes such as PSD and colocalizes with SynGAP and CaMKII. It is believed that CaMKII phosphorylation is induced after calcium influx through activated NMDA receptors. This results in the phosphorylation of SynGAP and the dissociation of SynGAP from CaMKII (Araki et al., 2015). Phosphorylation of SynGAP down-regulates the activity of RAS-GAP (Figure 5.1). Hence, after calcium influx RAS-GAPs become less active and RAS-GEFs more active which leads to elevated levels of RAS-GTP. Elevated RAS-GTP levels lead to the activation of further downstream proteins finally resulting in the insertion of AMPAR into the postsynaptic membrane (Thomas and Huganir, 2004).

To investigate *Syngap* gene mutations, SynGAP mutant mouse models have been created in the past years on different backgrounds (Komiyama et al., 2002, Kim et al., 2003). Mutant mice lacking either both copies (SynGAP^{-/-}, homozygotes) or one copy

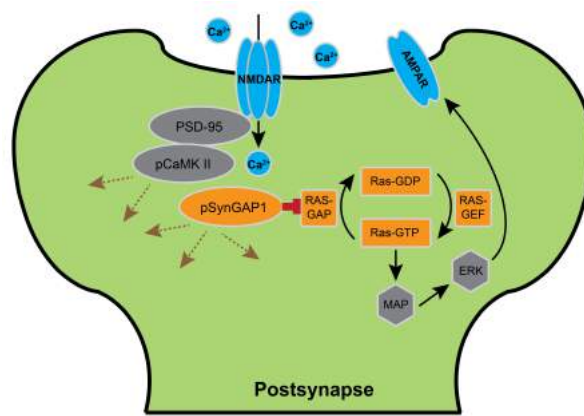


Figure 5.1: Signaling mechanism upon phosphorylation of SynGAP. Upon NMDAR activation, Ca²⁺ enters the postsynapse and triggers the phosphorylation of CaMKII. Phosphorylation of CaMKII leads to the phosphorylation of SynGAP (pSynGAP) which results in elevated levels of Ras-GTP. This leads to the activation of MAP kinase and ERK, which finally results in the insertion of AMPARs into the postsynaptic membrane. Brown arrows indicate other pathways activated by CamKII and SynGAP phosphorylation.

(SynGAP^{+/-}, heterozygotes) of the *Syngap* gene are indistinguishable in phenotype from their wild-type (WT) litter mates at birth and share common neurological deficits. At P03 homozygotes SynGAP^{-/-} show less movement and less food intake compared to their WT litter mates, and therefore, stay smaller in size. Between P05 to P07 homozygotes SynGAP^{-/-} pups die. Heterozygotes SynGAP^{+/-} survive and are fertile. The lethality of homozygotes SynGAP^{-/-} indicates a vital role of the SynGAP protein during development (Komiyama et al., 2002, Kim et al., 2003).

5.1.2 Behavioral impairments in SynGAP^{+/-} mice

ASD is diagnosed clinically using behavioural criteria, such as abnormal social interactions and repetitive behaviour (Fakhoury, 2015). Abnormal social interactions include failure in using facial expression to communicate effectively and reduced interest and difficulties in maintaining social interactions as well as communication deficits. Repetitive behaviours include the preference of patients for repetitive rituals and compulsions together with unwillingness to change motor stereotypies and unusual or very narrow restricted interests. Repetitive behaviours are believed to be a strategy to control the environment and manage arousal levels to overcome anxiety (Mefford, Batshaw, and Hoffman, 2012, McPartland and Volkmar, 2012, Pasciuto et al., 2015). ASD patients often also show signs of hyperactivity (Pasciuto et al., 2015).

In the past years, several behaviour assays evaluating social interactions, communication deficits and repetitive behaviour in mice have been designed to maximize the relevance of these mouse models to the deficits associated with ASD (Pasciuto et al., 2015).

Sociability can be evaluated in three different ways: (1) scoring parameters such as

nose-to-nose sniffing, nose- to-anogenital sniffing, following, passing each other with physical contact, chasing, mounting and wrestling with peers; (2) measuring the time spent with an object vs. time spent with peers, and (3) using the social preference test, where mice are presented with a familiar mouse or object and a novel mouse or object. Since mice are highly social animals, healthy WT mice spend extended times interacting with conspecifics and show a preference for novelty over familiar objects or mice. Assays to evaluate communication deficits include: quantification of ultrasound vocalization, response to novel urinary odors and olfactory habituation. Repetitive behaviour and stereotyped behaviour can be quantified, and insistence on sameness as well as learning and memory deficits can be evaluated using a reversal learning task. Therefore, mice are first trained to follow a certain behavioural routine (such as finding a food reward or an escape platform in the Morris water maze) and then the location is altered, forcing the mice to adapt to the new situation. Anxiety can be evaluated using the open field test. Healthy mice explore novel environments and the explorative behaviour is interpreted as low-anxiety. Reduced levels of explorative behaviour, such as avoiding open fields and bright places are used to score anxiety (Pasciuto et al., 2015). The open field test is also commonly used to assess hyperactivity in mice (Pasciuto et al., 2015).

As in other mouse models of ASD, heterozygote *SynGAP*^{+/-} mice show deficits in social novelty preference (Berryer et al., 2016). While WT mice spend significantly more time with the novel conspecific, heterozygote *SynGAP*^{+/-} mice spend similar amount of time with the novel and the familiar conspecific (Berryer et al., 2016).

Furthermore, *SynGAP*^{+/-} mice were shown to be hyperactive and have reduced levels of anxiety-like behaviour in the open field test (Komiya et al., 2002, Muhia et al., 2010, Berryer et al., 2016). Hyperactivity as well as reduced levels of anxiety-like behaviour are also seen during a systemic blockade of NMDA receptor function. Therefore, these results are in agreement with the theory that *SynGAP*^{+/-} mutations alter NMDA receptor dependent down-stream signalling and hence would lead to similar behavioural phenotypes as a systemic blockade of NMDA receptor function (Muhia et al., 2010).

5.1.3 Cellular impairments in *SynGAP*^{+/-} mice

In the past years, several studies have addressed cellular properties of *SynGAP*^{+/-} mice *in vitro* and *in vivo*. For example, it was shown that synaptic transmission is elevated during development in juvenile *SynGAP*^{+/-} mice, with dendritic spines and synapses forming prematurely due to accumulation of AMPA receptors at the synapse (Vazquez et al., 2004, Carlisle et al., 2008). This is because *SynGAP*^{+/-} mice lack one copy of the *SynGAP* gene and therefore have lower expression levels of *SynGAP*, which leads to a loss of RasGAP activity and thus causes an increase in RAS-GTP leading to the formation of unsilenced synapses through the insertion of AMPA re-

ceptors in the postsynaptic membrane (Carlisle et al., 2008). The amount of silent synapses compared to unsilenced synapses was investigated in thalamocortical slices using a minimal stimulation paradigm at P5 in SynGAP^{+/-} mice and WT mice. Overall, they found approximately double the amount of silent synapses in WT mice compared to SynGAP^{+/-} mice (Clement et al., 2013). In WT mice the insertion of AMPA receptors into the postsynaptic membrane is experience-dependent and leads to the closure of the critical period by reducing the amount of silent synapses (Clement et al., 2013, Huang et al., 2015). The abnormalities in spine formation of SynGAP^{+/-} mice lead to a shortened critical window for synaptic plasticity (Clement et al., 2013) and persist into adulthood (Vazquez et al., 2004, Rumbaugh et al., 2006, Jeyabalan and Clement, 2016). Furthermore, it was shown that the loss of one copy of the *Syngap* gene after the closure of the critical period had only a minimal impact on spine synapse function. At the same time, restoring SynGAP function in adulthood does not improve behaviour or cognition deficits (Clement et al., 2012). In contrast, overexpression of SynGAP results in a reduction in AMPAR expression on the membrane surface, leading to a greater number of silent synapses (Rumbaugh et al., 2006, Clement et al., 2012).

As a consequence, SynGAP^{+/-} mice have significantly more (approximately 20 %) mushroom shaped spines than thin spines (Carlisle et al., 2008). Other studies have shown that thin spines are transient and are more likely to undergo LTP, while mushroom shaped spines are more stable and are less likely to undergo LTP (Holtmaat et al., 2005). In accordance with this, *in vitro* electrophysiological slice recordings made from the hippocampal CA1 region of adult heterozygotes SynGAP^{+/-} mice show a decrease in LTP (Komiyama et al., 2002, Kim et al., 2003).

While previous studies have revealed important deficits at the cellular level in SynGAP^{+/-} mice, much less is known about how these cellular changes affect the activity of neural circuits *in vivo*. In this study, we investigated potential differences in neuronal activity at the population level as well as at the single neuron level between SynGAP^{+/-} mice and WT litter mates, both during spontaneous activity (darkness) and sensory evoked activity (visual stimulation). In addition, we tested potential deficits in adult plasticity in SynGAP^{+/-} mice, using the classical experimental paradigm of monocular deprivation.

5.2 MATERIAL AND METHODS

Experimental procedures including surgery (cranial window, AAV delivery, head-plate attachment) and two-photon imaging in awake behaving mice, were performed as described in [Chapter 2](#). Briefly, two to three weeks prior to imaging, a cranial window surgery was performed and AAVs were locally injected in the binocular region of V1 in order to express GCaMP6 in all neurons (AAV1.Syn.GCaMP6s.WPRE.SV40; Penn Vector Core). Mice were imaged two times, before and after monocular depriva-

tion (MD). During the imaging sessions mice were presented with a visual stimulus (gratings). All experiments were performed with the experimenter blind to genotype. At the end of the experiment mice were transcardially perfused. All procedures were approved by the University of Edinburgh animal welfare committee, and were performed under a UK Home Office project license.

5.2.1 *Animals*

Male heterozygous SynGAP^{+/-} mice (Komiyama et al., 2002) were used for all experiments. On average, mice were 22 weeks old (minimum 17 and maximum 28 weeks). Animals were housed in groups of two to four in conventional cages until the experiment started. At the first day of the experiment (cranial window surgery) animals were started to be single-housed. Water and food were provided *ad libitum* and mice were held on a 12/12 hour light/dark cycle. All procedures were approved by the University of Edinburgh animal welfare committee, and were performed under a UK Home Office project license.

5.2.2 *Habituation of mice to the imaging setup*

Mice were habituated to the head-restraint for approximately 20 minutes for at least one day (and a maximum of 3 days) before the first imaging day. Mice were head-fixed in the two-photon setup and left in the dark, free to run on a circular treadmill. The habituation session was also used to check the cranial window and the neuronal labelling. To habituate the mice to the noise of the mechanical shutter, the shutter was opened and closed several times during the habituation session.

5.2.3 *Monocular deprivation*

MD was performed directly after the imaging session on day 1. Mice were anesthetized with 2 % Isoflurane (IsoFlo, Abbott Laboratories, UK) and the fur around the right eye was removed using scissors. Then, the eyelashes of the right eye were cut using fine forceps and fine scissors and the eye lids sutured. During the surgery, mice were laid on their left side to ensure good access to the right eye. To reduce potential pain, mice were injected with an analgesic (1 ml/ 20 mg mouse Vetergesic, diluted 1:10 with injectable water (Water for Injections 100 % v/v, Norbrook Laboratories Limited, Northern Ireland)). Furthermore, the nails of all four paws were trimmed, to reduce the risk of suture opening due to scratching.

Mice were monocularly deprived for 7 days. During that time, mice were monitored daily to ensure well-being and a tight closure of the suture. Mice found with open sutures were excluded from further experiments (one mouse).

After 7 days, mice were anesthetized and the suture opened using fine scissors. Afterwards, the animal was placed for at least 2 hours (maximum of 3 hours) in a dark box, without any light stimulation, to recover from the anesthesia. After recovery, the animal was immediately prepared for imaging and the imaging session was started as soon as possible (within approximately 15 minutes).

5.2.4 *Chronic two-photon imaging protocol*

The imaging protocol consisted of four parts. First, the animal was stimulated binocularly, then the right eye and left eye were stimulated separately and finally an additional binocular session was performed. For monocular stimulation, each eye was blocked using a black piece of cardboard positioned approximately at a 2 cm distance from the nose of the animal. For each stimulation condition at least 10 recordings in the dark and 12 recordings with visual stimulation were taken.

The visual stimulus was presented on a screen, which was placed in front of the mouse at a 20 cm distance to the nose. The visual stimulus consisted of a sequence of four differently orientated (0° , 45° , 90° , 135°) sinusoidal phase-reversing gratings (1 Hz, 0.03-0.05 cpd), presented in a random order. Each grating was presented for 3 seconds and the inter-stimulus (an isoluminant grey screen) was presented for 5 seconds. Each trial consisted of 2 presentations of each grating with an additional 1 second black screen period at the beginning and at the end of each trial. The total time of one trial was 72 seconds.

5.2.5 *Data analysis*

Acquired data were analysed as described in [Chapter 2](#) of this thesis. Briefly, 2D plane translational-based image alignment (SIMA 1.2.0, Kaifosh et al., 2014) was used to correct for motion artefacts. Next, regions of interests (ROIs) corresponding to neuronal somata were manually selected and pixel intensity within individual ROIs averaged. $\Delta F/F_0$ signal was calculated by taking the difference between F (raw fluorescent signal) and F_0 (baseline fluorescence) divided by F_0 , and neuropil decontamination was performed using non-negative matrix factorization (NMF) run through FISSA. Behavioural state (e.g. stationary versus locomotion) was determined by monitoring the wheel speed. Active neurons were defined as neurons with an average minimum response amplitude ($\Delta F/F_0$) higher than 0.2 during visual stimulation. Visual responsive neurons, stimulus-evoked response (SER), orientation selectivity index (OSI), and locomotion modulation index (LMI) were defined as described in [Chapter 2](#).

5.3 PERSONAL CONTRIBUTION DISCLAIMER

This project was conducted in collaboration with Prof. Peter Kind's laboratory. Specifically, Dr. Chih-Yuan Chiang performed the MD of all mice and Danai Katsanevaki recorded and analyzed five mice included in the dataset. All other data ($n = 22$ mice) were acquired and analysed by myself. We are currently in the process of preparing a peer reviewed journal article including the results discussed here.

5.4 RESULTS

A total of 33 mice were prepared for imaging. Seven mice were excluded due to either head-plate detachment (3 mice) or poor imaging quality (no labelled cells or cloudy cranial window preventing imaging) (4 mice). Day 1 baseline data were recorded for the remaining 26 mice (total of 3260 neurons), of which 12 were SynGAP^{+/-} mice (total of 1427 neurons) and 14 were WT littermates (total of 1919 neurons). MD was performed on 16 mice for 7 consecutive days and the response properties of the same set of neurons were recorded before and after MD (Figure 5.2).

5.4.1 Behaviour correlates of SynGAP^{+/-} mutation

Previous studies have shown that SynGAP^{+/-} mice are hyperactive in the open field (Komiyama et al., 2002, Muhia et al., 2010, Berryer et al., 2016. As shown in Chapter 3, behavioral state modulates neuronal activity in V1. Therefore, we tested whether SynGAP^{+/-} mice display hyperactivity in our experimental conditions, and quantified the time spent running in mutants and WT littermates (Figure 5.3).

On average, SynGAP^{+/-} mice and WT littermates were running the same proportion of time (approximately 20 %) during stimulus presentation on day 1 and day 7. There was no significant difference in the proportion of locomotion during visual stimulation between day 1 and day 7 in either SynGAP^{+/-} mice (day 1: 19.9 ± 3.8 , day 7: 21.7 ± 4.7 ; Wilcoxon signed rank test) or WT littermates mice (day 1: 16.5 ± 3.3 , day 7: 20.7 ± 4.3 ; Wilcoxon signed rank test) (Figure 5.3 A).

Similar results were obtained when comparing only the first 20 min of imaging on day 1 and day 7, both in SynGAP^{+/-} mice and WT littermates (Figure 5.3 B). Again, there was no significant difference in amount of locomotion during visual stimulation between day 1 and day 7 in SynGAP^{+/-} mice (day 1: 20.4 ± 4.6 , day 7: 22.3 ± 5.8 ; Wilcoxon signed rank test) and WT littermates (day 1: 17.9 ± 3.6 , day 7: 20.2 ± 5.6 ; Wilcoxon signed rank test). As before, there was no significant difference in proportion of locomotion during visual stimulation between WT littermates mice and SynGAP^{+/-} on either day (Mann-Whitney U-test; Figure 5.3 B). These results indicate that despite the hyperactivity of SynGAP^{+/-} mice in open fields, mice habituated to

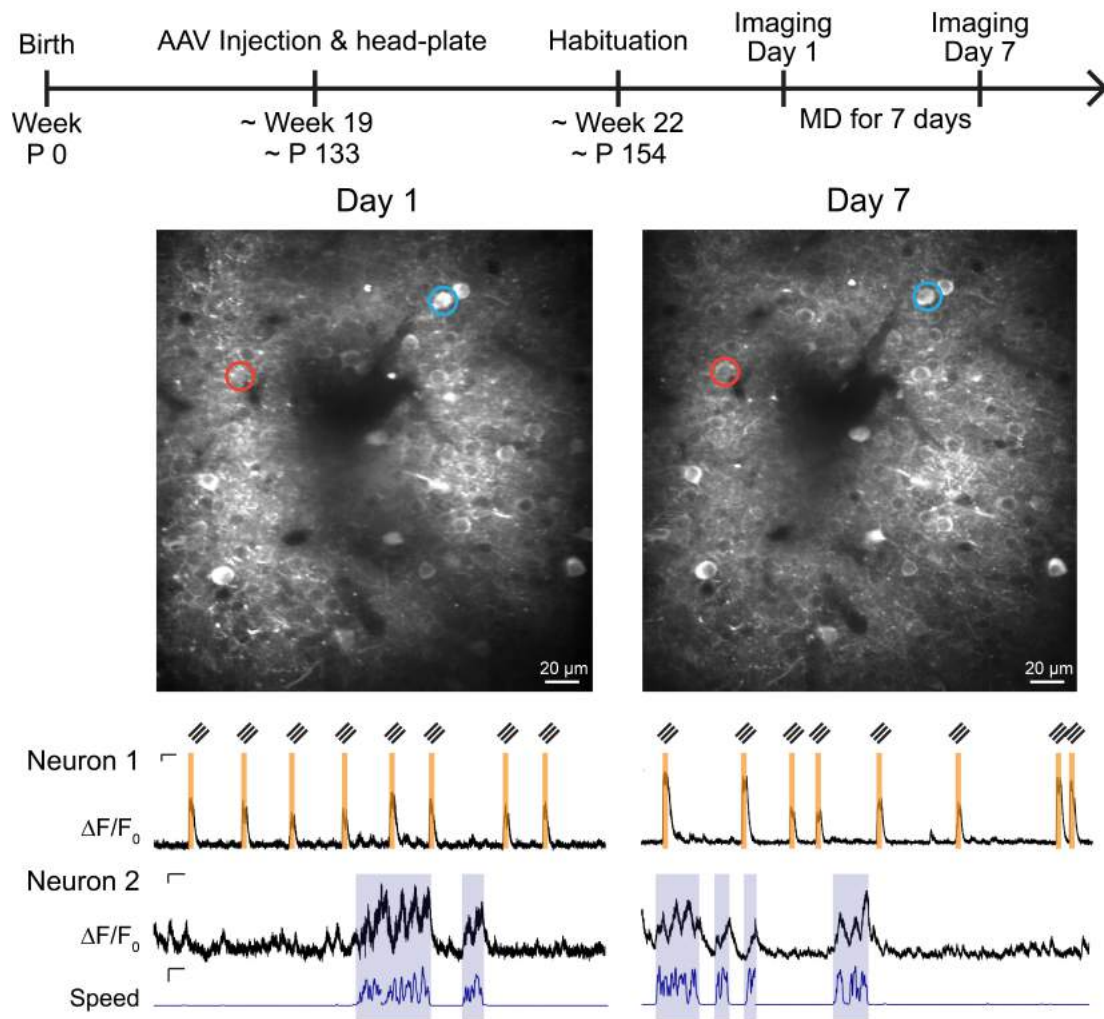


Figure 5.2: Example field of view and example traces before and after MD. Top: Example field of view showing a neuronal population recorded before (left, Day 1) and after (right, Day 7) MD. Bottom: Example $\Delta F/F_0$ traces of an orientation selective neuron (neuron 1) and a locomotion responsive neuron (neuron 2) on day 1 (left) and after MD on day 7 (right). Bottom blue trace displaying wheel speed in cm/s.

the head fixation in the two-photon imaging set-up were not running more than WT littermates.

5.4.2 Comparison of V_1 neuronal activity between $SynGAP^{+/-}$ mice and WT littermates

5.4.2.1 Neuronal activity in V_1 neurons of $SynGAP^{+/-}$ mice is lower compared to WT littermates

We first compared the number of visually responsive neurons on day 1 in V_1 of $SynGAP^{+/-}$ mice and WT littermates. On average we found similar percentage of visually responsive neurons in both $SynGAP^{+/-}$ mice and WT littermates ($SynGAP^{+/-}$ mice: 50.7 %, WT littermates: 53.4 %) (Figure 5.4). Only neurons visually responsive

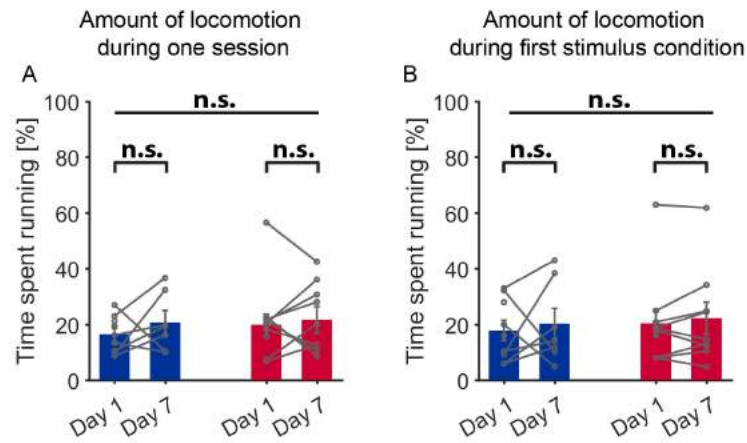


Figure 5.3: Proportion of time spent running in both experimental groups (SynGAP^{+/-} mice and WT littermates). A) Proportion of time spent running during visual stimulation. B) Proportion of time spent running during the first 20 minutes of an imaging session. Blue: WT littermates (N=14), red: SynGAP^{+/-} mice (N=12), grey dots indicate average across all neurons per animal, Error bars: s.e.m.

on day 1 were considered for further analysis.

Next, we determined the baseline activity level of V1 neurons in SynGAP^{+/-} mice and WT littermates. We quantified the population activity in darkness and during binocular visual stimulation, both during stationary and locomotion periods. We found a higher mean $\Delta F/F_0$ during both stationary and locomotion periods in WT littermates compared to SynGAP^{+/-} mice on day 1 both in darkness (stationary periods: WT littermates 0.16 ± 0.04 , SynGAP^{+/-} mice 0.06 ± 0.01 , $p < 0.05$, Mann-Whitney U-test; locomotion periods: WT littermates 0.39 ± 0.09 , SynGAP^{+/-} mice 0.13 ± 0.02 , $p < 0.01$, Mann-Whitney U-test; Figure 5.5 A) and during visual stimulation (stationary periods: WT littermates 0.26 ± 0.06 , SynGAP^{+/-} mice 0.12 ± 0.01 , $p < 0.01$, Mann-Whitney U-test; locomotion periods: WT littermates 0.57 ± 0.11 , SynGAP^{+/-} mice 0.27 ± 0.04 , $p < 0.01$, Mann-Whitney U-test; Figure 5.5 B). Additionally, standard deviation of $\Delta F/F_0$ across trials during stimulus presentation was assessed, to evaluate variability in neuronal responses. We found a lower mean standard deviation in SynGAP^{+/-} mice during stationary periods compared to WT littermates (stationary periods: WT littermates 0.08 ± 0.03 , SynGAP^{+/-} mice 0.01 ± 0.004 , $p < 0.01$, Mann-Whitney U-test; locomotion periods: WT littermates 0.21 ± 0.10 , SynGAP^{+/-} mice 0.03 ± 0.01 , $p < 0.01$, Mann-Whitney U-test; Figure 5.5 C).

5.4.2.2 Orientation selectivity of V1 neurons of SynGAP^{+/-} mice is higher compared to WT littermates

Next, we calculated the orientation selectivity index (OSI) per neuron as described in Chapter 2 for all visually responsive neurons. On average, SynGAP^{+/-} mice showed higher mean OSI values than WT littermates (SynGAP^{+/-} mice: 0.35 ± 0.03 ; WT

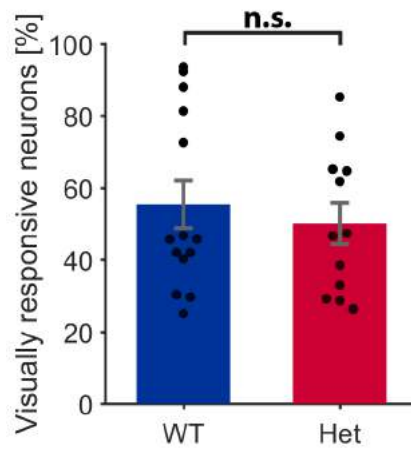


Figure 5.4: Number of visually responsive neurons recorded in $\text{SynGAP}^{+/-}$ mice and WT littermates on day 1. Blue: WT littermates (N=14), red: $\text{SynGAP}^{+/-}$ mice (N=12), black dots indicate average across all neurons per animal, Error bars: s.e.m.

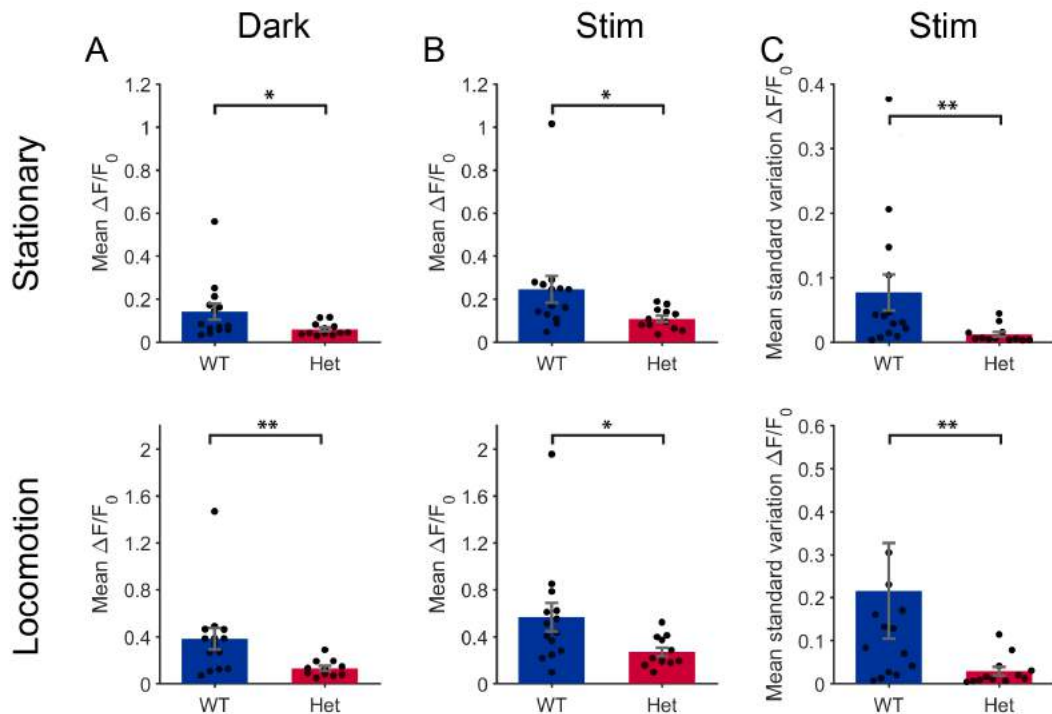


Figure 5.5: Mean neuronal activity of visually responsive neurons of $\text{SynGAP}^{+/-}$ mice (n=10) and WT litter mates (n=13) measured on day 1. A) During darkness: Mean $\Delta F/F_0$ during stationary periods (top) and during locomotion periods (bottom). B and C: During visual stimulation (grating): B) Mean $\Delta F/F_0$ during stationary periods (top) and during locomotion periods (bottom). C) Mean standard deviation of $\Delta F/F_0$ during stationary periods (top) and during locomotion periods (bottom). Blue: WT littermates (N=14), red: $\text{SynGAP}^{+/-}$ mice (N=12), black dots indicate average across all neurons per animal, error bars: s.e.m., *, significant, $p < 0.05$, **, significant, $p < 0.01$, Mann-Whitney U-test.

littermates: 0.23 ± 0.02 , $p < 0.01$, Mann-Whitney U-test; [Figure 5.7 A](#)). Furthermore, standard deviation of OSI across trials was assessed. There was no significant difference in standard deviation of OSI between SynGAP^{+/-} mice and WT littermates (SynGAP^{+/-} mice: 0.18 ± 0.005 ; WT littermates: 0.16 ± 0.01 , $p > 0.05$, Mann-Whitney U-test; [Figure 5.7 B](#)). In addition, the stimulus-evoked response (SER) was calculated for all visually responsive neurons. Since SER is an index giving the ratio between pre and post stimulus onset, SER was calculated without differentiating between locomotion and stationary periods. There was no significant difference in SER between SynGAP^{+/-} mice and WT littermates (SynGAP^{+/-} mice: 0.13 ± 0.04 ; WT littermates: 0.21 ± 0.03 , $p > 0.05$, Mann-Whitney U-test; [Figure 5.7 C](#)).

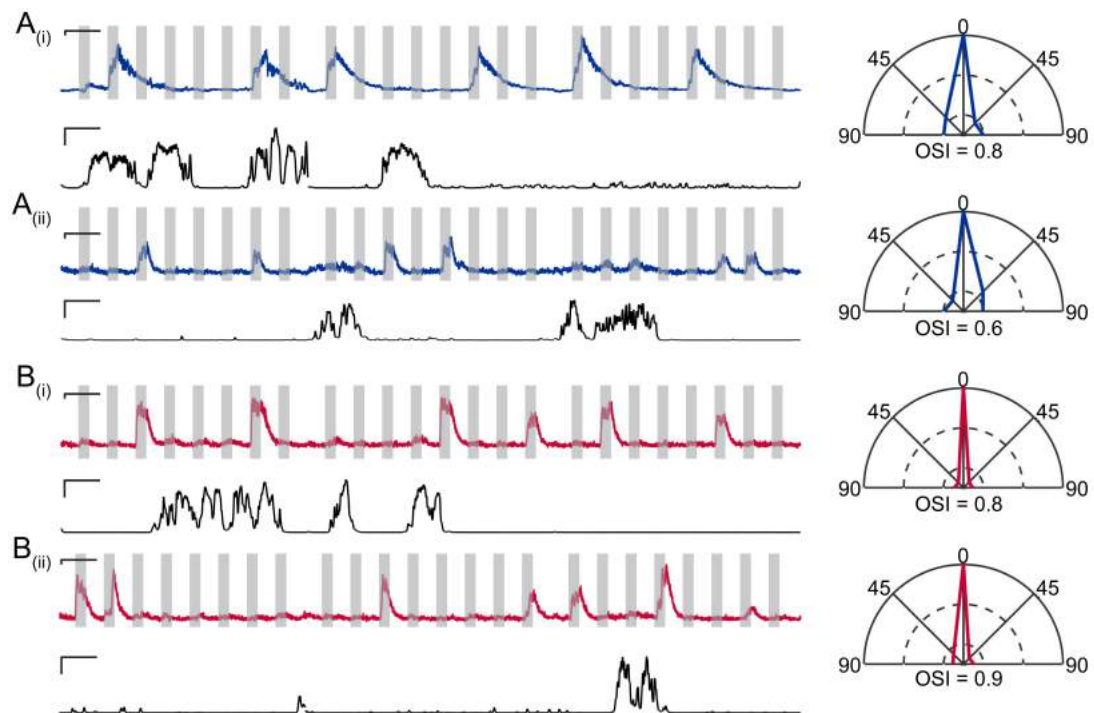


Figure 5.6: Example traces of orientation selective neurons. A) WT mice, B) SynGAP^{+/-} mice. Black trace: running speed (cm/s). Grey bars: oriented gratings. Polar plots show the response amplitude to the four presented gratings normalised to the preferred orientation.

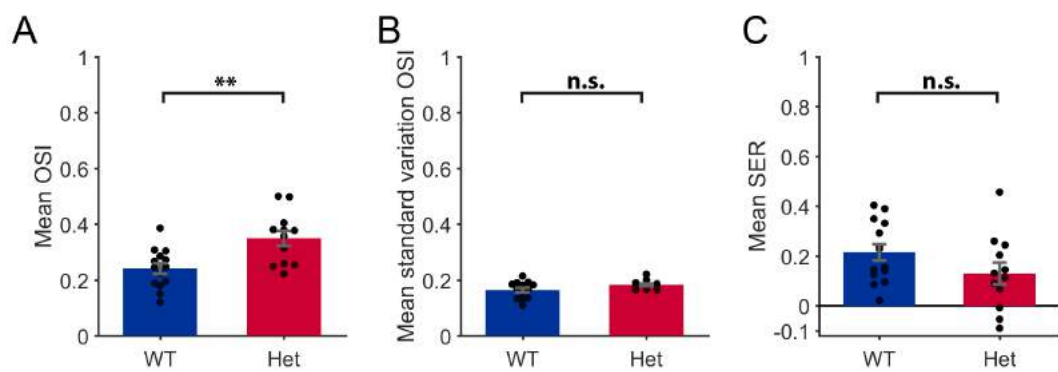


Figure 5.7: OSI and SER of V1 neurons in SynGAP^{+/-} mice and WT littermates measured on day 1. A) Mean OSI magnitude of all visually responsive neurons per animal. B) Standard deviation of mean OSI magnitude per animal. C) Mean SER of all visually responsive neurons per animal. Blue: WT littermates (N=14), Red: SynGAP^{+/-} mice (N=12), error bars: s.e.m. * p < 0.01, n.s., not significant (p > 0.05), Mann-Whitney U-test.

5.4.2.3 No difference in behavioral state dependent modulation of neuronal activity in *SynGAP*^{+/-} mice and WT littermates

We investigated a potential difference in the gain modulation of neuronal responses by locomotion in *SynGAP*^{+/-} mice and WT littermates. We calculated a locomotion modulation index (LMI) as described in [Chapter 2](#) (difference between the mean $\Delta F/F_0$ during locomotion and stationary periods, normalized by the sum of both). We found no significant difference between *SynGAP*^{+/-} mice and WT littermates in LMI during darkness (*SynGAP*^{+/-} mice: 0.27 ± 0.02 ; WT littermates: 0.32 ± 0.05 , $p > 0.05$, Mann-Whitney U-test; [Figure 5.8 A](#)) or during visual stimulation (*SynGAP*^{+/-} mice: 0.34 ± 0.03 ; WT littermates: 0.31 ± 0.04 , $p > 0.05$, Mann-Whitney U-test; [Figure 5.8 B](#)). These results suggest that the mechanisms underlying gain modulation of neuronal activity in V1 during locomotion are unaffected in *SynGAP*^{+/-} mice.

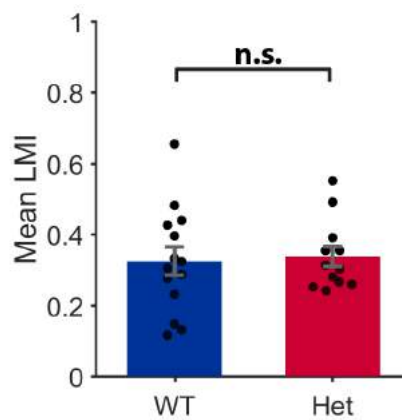


Figure 5.8: LMI of all active neurons of *SynGAP*^{+/-} mice and WT littermates measured on day 1. Blue: WT littermates (N=14), Red: *SynGAP*^{+/-} mice (N=12), grey dots indicated averages across all neurons per animal, error bars: s.e.m., n.s., not significant, $p > 0.05$, **, significant, $p < 0.01$, Mann-Whitney U-test.

5.4.3 *Effect of monocular deprivation on V1 neuronal activity in adult SynGAP^{+/-} mice and WT littermates*

MD was performed to evaluate potential differences in neuronal plasticity between adult SynGAP^{+/-} mice and WT littermates. The SynGAP protein is part of a signalling cascade that ultimately leads to the activation of ERK, which is important for regulating activity dependent genes resulting in the insertion of AMPA receptors into the membrane, which is considered an important mechanism for neuronal plasticity (Atkins et al., 1998, Di Cristo et al., 2001, Thomas and Huganir, 2004). In rodent V1 it was shown that visual experience activates ERK and that activation of ERK is important in mediating experience-dependent plasticity induced by MD during the critical period (Di Cristo et al., 2001). This study aimed to investigate neuronal plasticity induced by MD in adult SynGAP^{+/-} mice, which were shown to display deficits in neuronal plasticity *in vitro*, (Komiyama et al., 2002) and WT littermates to reveal potential deficits in neuronal plasticity *in vivo* in adult mice. These experiments were performed with the idea to compare the results obtained in adults with those obtained in younger animals (during the critical period). Following the MD protocol in adult mice described in Sawtell et al., 2003, Hofer et al., 2006, Rose et al., 2016 we were expecting a shift in ocular dominance at least in WT littermates and aimed to compare this to SynGAP^{+/-} mice. However, since this was a new method in the lab we realised only after performing preliminary experiments that environmental enrichment is critical at this age. Initial experiments were started using adult mice, because the growth process of the juvenile skull needs to be finished by the time of head-plate implantation, since the head-plate attachment would likely cause harm and malformation of the growing skull. Previous studies have shown that environmental enrichment alleviates behavioural phenotypes in another model of intellectual disability and autism spectrum disorders, the FXS mouse (Restivo et al., 2005). For instance, behavioural abnormalities such as an altered pattern of exploration and habituation in the open field arena and neuronal abnormalities in spine density and morphology observed in FXS mice raised in standard cages, are largely rescued when mice are raised in enriched environments. For that reason, we decided to avoid environmental enrichment in the cages of the animals for this set of experiments to avoid experience-dependent effects potentially affecting the neuronal development.

5.4.3.1 *Binocular response properties before and after MD*

In general, after seven days of MD we found a decrease in number of visually responsive neurons (Figure 5.9).

Next, we compared the neuronal response properties of visually responsive neurons of SynGAP^{+/-} mice and WT littermates between day 1 and day 7. During visual stimulation there was no significant difference between day 1 and day 7 in mean $\Delta F/F_0$ during stationary periods or during locomotion periods in neither WT litter mates

(stationary periods: 0.26 ± 0.06 , locomotion periods: 0.57 ± 0.11 , Wilcoxon signed rank test) nor SynGAP^{+/-} mice (stationary periods: 0.12 ± 0.01 , $p < 0.01$, locomotion periods: 0.27 ± 0.0370 , $p < 0.01$, Wilcoxon signed rank test) (Figure 5.10 B). Finally, LMI was calculated to investigate if gain modulation of neuronal responses by locomotion is changing across days. There was no significant difference in LMI measured during visual stimulation between day 1 and day 7 in both genotypes.

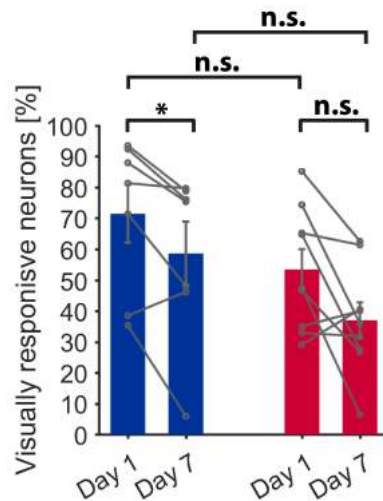


Figure 5.9: Number of visually responsive neurons recorded in SynGAP^{+/-} mice and WT littermates on day 1 and day 7. Blue: WT littermates (N=7), red: SynGAP^{+/-} mice (N=9), grey dots indicate averages across all neurons per animal, error bars: s.e.m.

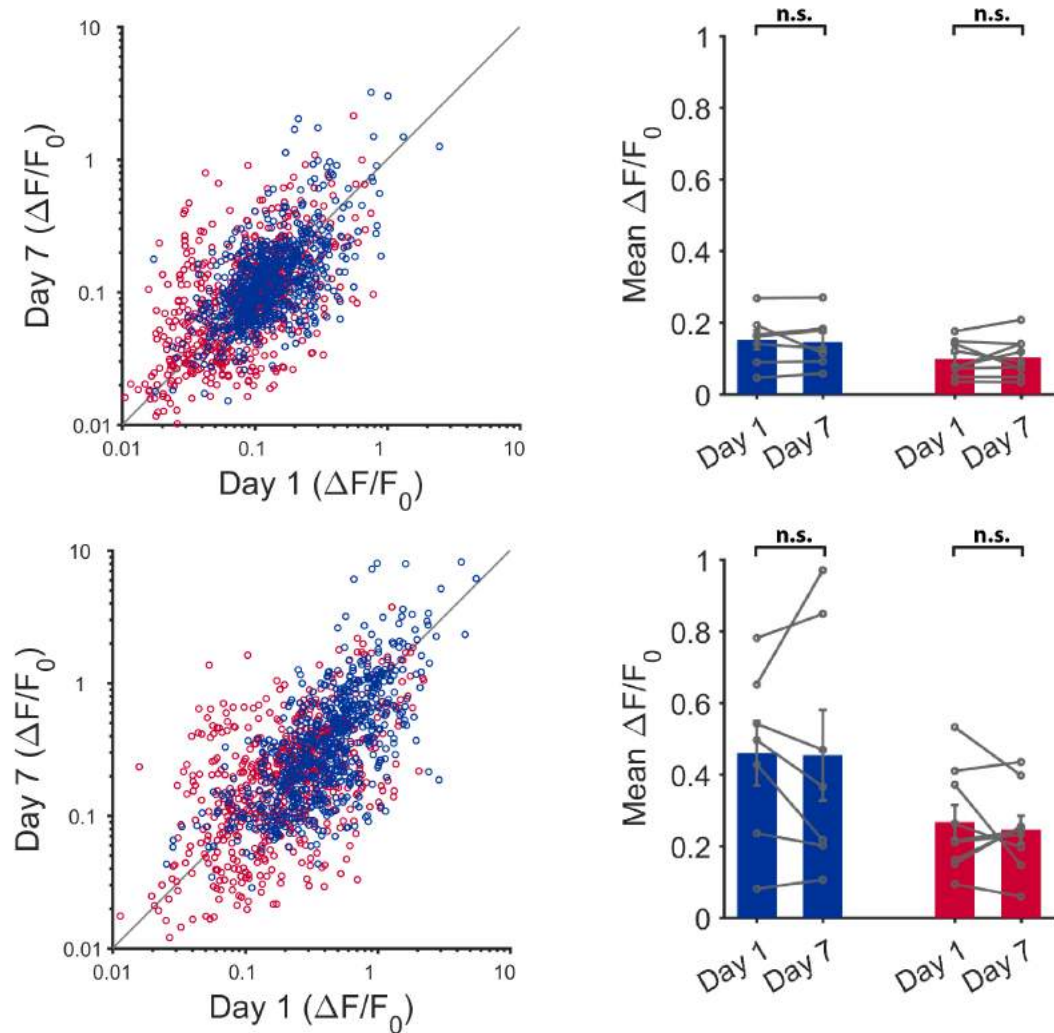


Figure 5.10: Scatter plots showing the mean amplitude of fluorescence changes ($\Delta F/F_0$) of each neuron measured before and after MD. Bar plots showing the mean neuronal activity of visually responsive neurons measured on day 1 and day 7 during darkness and visual stimulation. A) Scatter plots of all neurons and the means per animal for each genotype during visual stimulation: Mean $\Delta F/F_0$ during stationary periods (top) and during locomotion periods (bottom). Blue: WT littermates (N=7), red: SynGAP^{+/-} mice (N=9), grey dots indicate average across all neurons per animal, error bars: s.e.m. $p < 0.05$, n.s. not significant, Wilcoxon signed rank test.

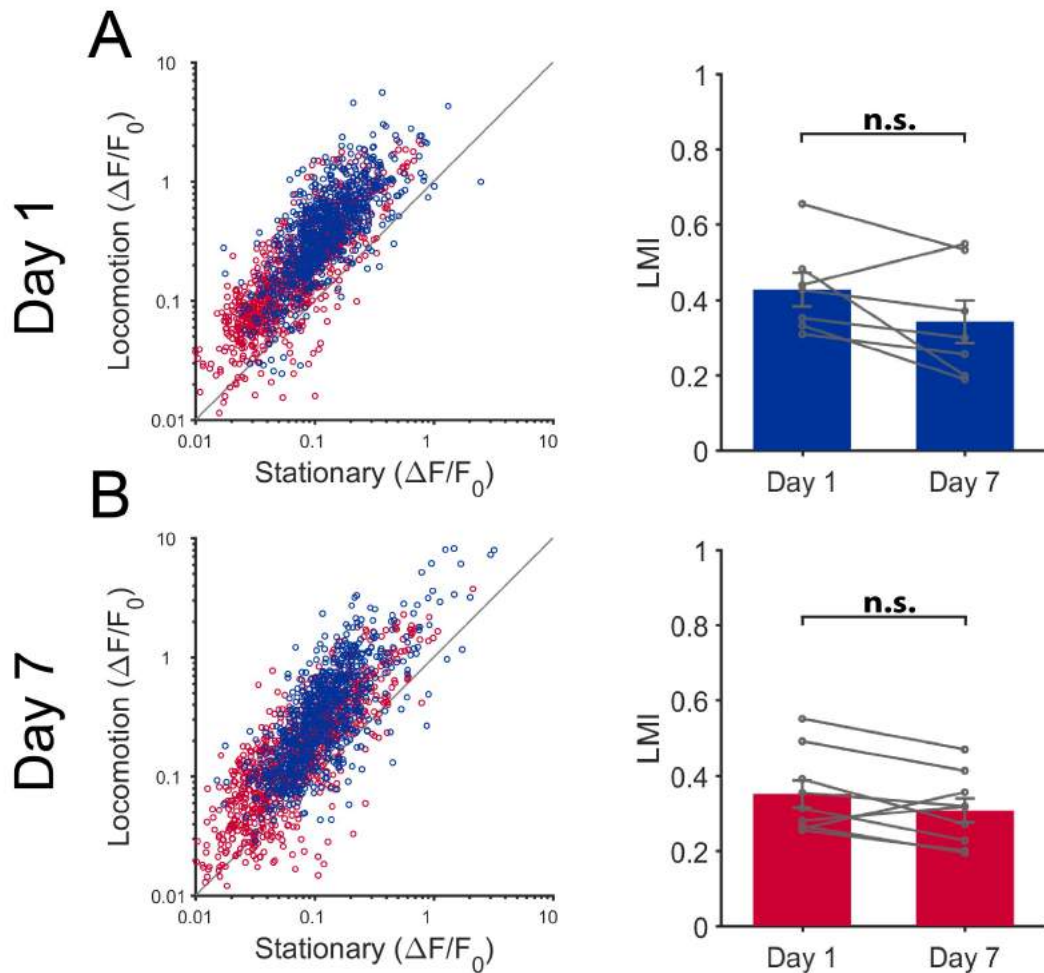


Figure 5.11: A) Scatter plots showing the mean amplitude of fluorescence changes ($\Delta F/F_0$) of each neuron during stationary periods versus locomotion periods in darkness and during visual stimulation (oriented gratings) on day 1 and on day 7. B) Bar plots showing the mean LMI during darkness and visual stimulation measured on day 1 and day 7. Blue: WT littermates (N=7), red: SynGAP^{+/-} mice (N=9), coloured bars: during visual stimulation, black bars: during darkness, grey dots indicate average across all neurons per animal, error bars: s.e.m. * $p < 0.01$, $p < 0.05$, n.s. not significant, Wilcoxon signed rank test.

5.4.3.2 *Monocular response properties before and after MD*

As for binocular responses the results showed on average no significant change in mean $\Delta F/F_0$ between day 1 and day 7 when stimulating either the left eye (stationary periods WT littermates day 1: 0.13 ± 0.04 , day 7: 0.15 ± 0.04 , $p < 0.05$, Wilcoxon signed rank test; SynGAP^{+/-} mice day 1: 0.06 ± 0.01 , day 7: 0.07 ± 0.01 , $p < 0.05$, Wilcoxon signed rank test; locomotion periods WT littermates day 1: 0.34 ± 0.09 , day 7: 0.31 ± 0.09 , $p < 0.05$, Wilcoxon signed rank test; SynGAP^{+/-} mice day 1: 0.11 ± 0.03 , day 7: 0.14 ± 0.03 , $p < 0.05$, Wilcoxon signed rank test; [Figure 5.13 A](#)) or the right eye (stationary periods WT littermates day 1: 0.12 ± 0.03 , day 7: 0.13 ± 0.03 , $p < 0.05$, Wilcoxon signed rank test; SynGAP^{+/-} mice day 1: 0.08 ± 0.02 , day 7: 0.10 ± 0.02 , $p < 0.05$, Wilcoxon signed rank test; locomotion periods WT littermates day 1: 0.30 ± 0.06 , day 7: 0.30 ± 0.09 , $p < 0.05$, Wilcoxon signed rank test; SynGAP^{+/-} mice day 1: 0.20 ± 0.03 , day 7: 0.22 ± 0.04 , $p < 0.05$, Wilcoxon signed rank test; [Figure 5.13 B](#)).

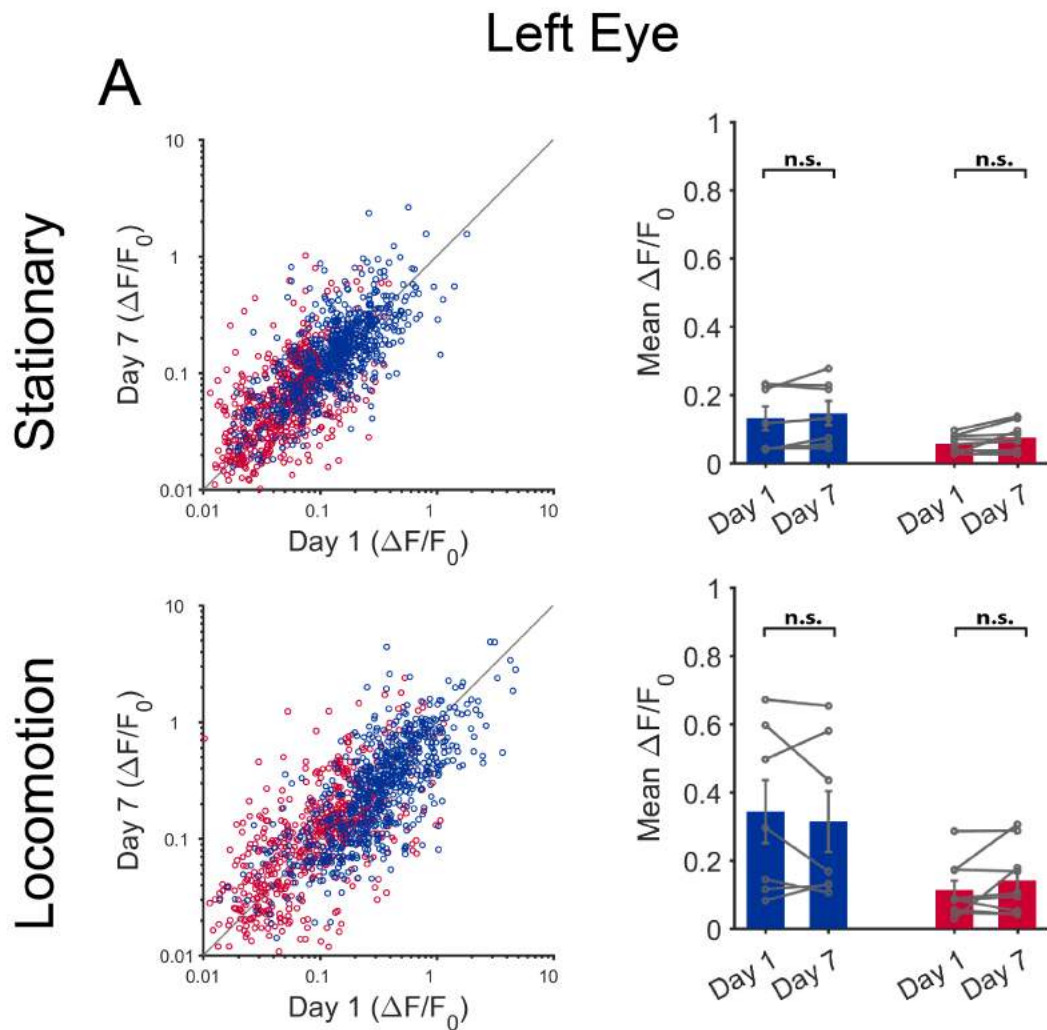


Figure 5.12: Changes in fluorescence ($\Delta F/F_0$) before and after MD of SynGAP^{+/-} mice and WT littermates during visual stimulation of the left eye. Scatter plots showing the mean amplitude of fluorescence changes ($\Delta F/F_0$) of each neuron on day 1 versus day 7 during visual stimulation (oriented gratings) for left eye stimulation during stationary periods (top row) and during locomotion periods (bottom row). Respectively, bar plots showing the mean change in fluorescence ($\Delta F/F_0$). Blue: WT littermates (N=7), red: SynGAP^{+/-} mice (N=9), grey dots indicate average across all neurons per animal, error bars: s.e.m. * $p < 0.01$, $p < 0.05$, n.s. not significant, Wilcoxon signed rank test.

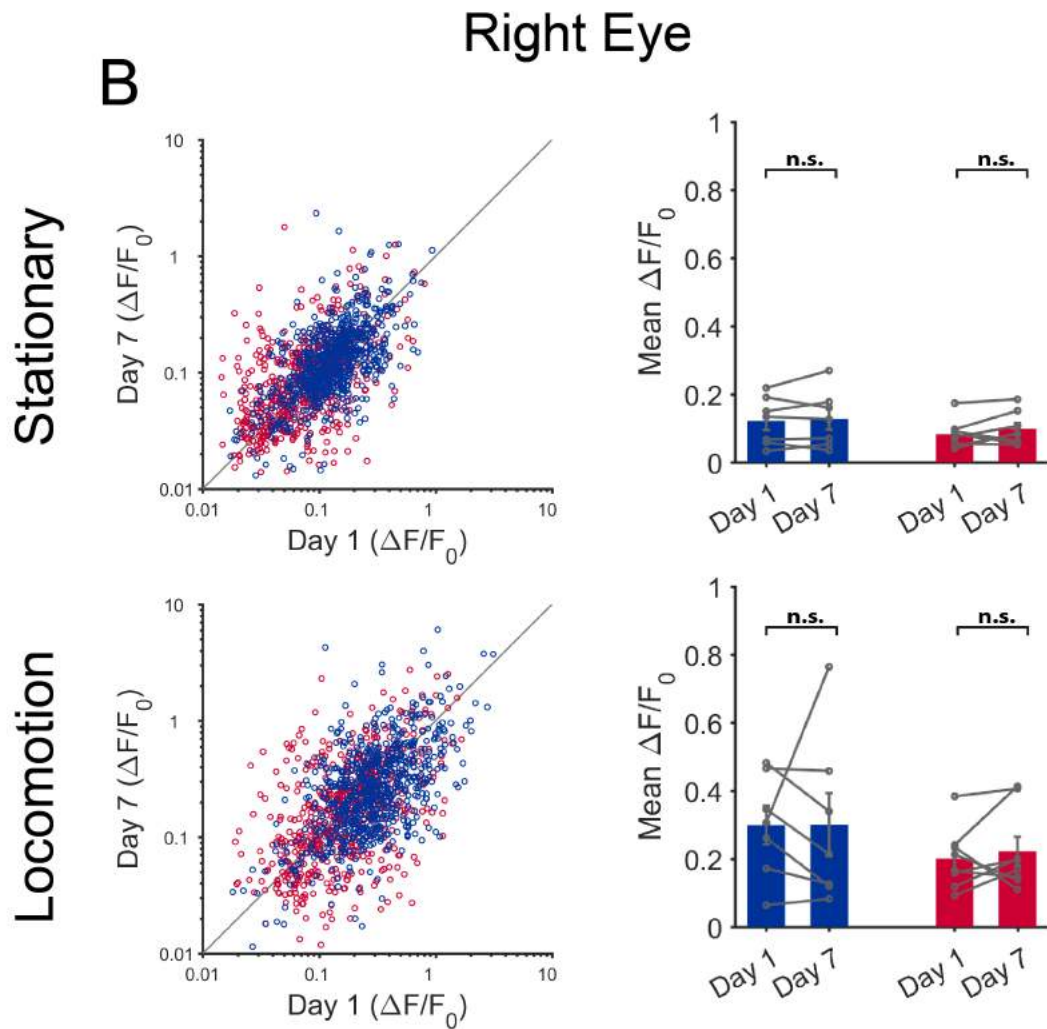


Figure 5.13: Changes in fluorescence ($\Delta F/F_0$) before and after MD of $\text{SynGAP}^{+/-}$ mice and WT littermates during visual stimulation the right eye. Scatter plots showing the mean amplitude of fluorescence changes ($\Delta F/F_0$) of each neuron on day 1 versus day 7 during visual stimulation (oriented gratings), right eye stimulation during stationary periods (top row) and during locomotion periods (bottom row). Respectively, bar plots showing the mean change in fluorescence ($\Delta F/F_0$). Blue: WT littermates (N=7), red: $\text{SynGAP}^{+/-}$ mice (N=8), grey dots indicate average across all neurons per animal, error bars: s.e.m. * $p < 0.01$, $p < 0.05$, n.s. not significant, Wilcoxon signed rank test.

Furthermore, we quantified the effect of MD on the responses to monocular stimulation by calculating an ocular dominance index (ODI). The ODI is defined as the difference between the mean $\Delta F/F_0$ recorded during contralateral eye stimulation and ipsilateral eye stimulation per neuron, normalized by the sum of both. The ODI was used to assess the shift in ocular dominance induced by MD, with an ODI above zero indicating that the dominant input comes from the contralateral eye and an ODI below zero indicating that the dominant input comes from the ipsilateral eye.

On day 1, while SynGAP^{+/-} mice showed the expected bias towards a dominant input of the contralateral eye to binocular V1 (ODI = 0.19 ± 0.03), WT results were more heterogeneous across mice with 3 mice showing larger responses to the ipsilateral eye (ODI = 0.02 ± 0.05).

After seven days of MD, both SynGAP^{+/-} mice and WT littermates showed a trend in decreasing responses to the stimulation of the contralateral eye and increasing responses to the stimulation of the ipsilateral eye. However, this trend in ODI shift was not significant (SynGAP^{+/-} mice day 1: 0.19 ± 0.03 , day 7: 0.14 ± 0.06 ; WT littermates day 1: 0.02 ± 0.05 , day 7: -0.05 ± 0.04 , $p < 0.05$, Wilcoxon signed rank test, $p < 0.05$, Wilcoxon signed rank test; [Figure 5.14](#)).

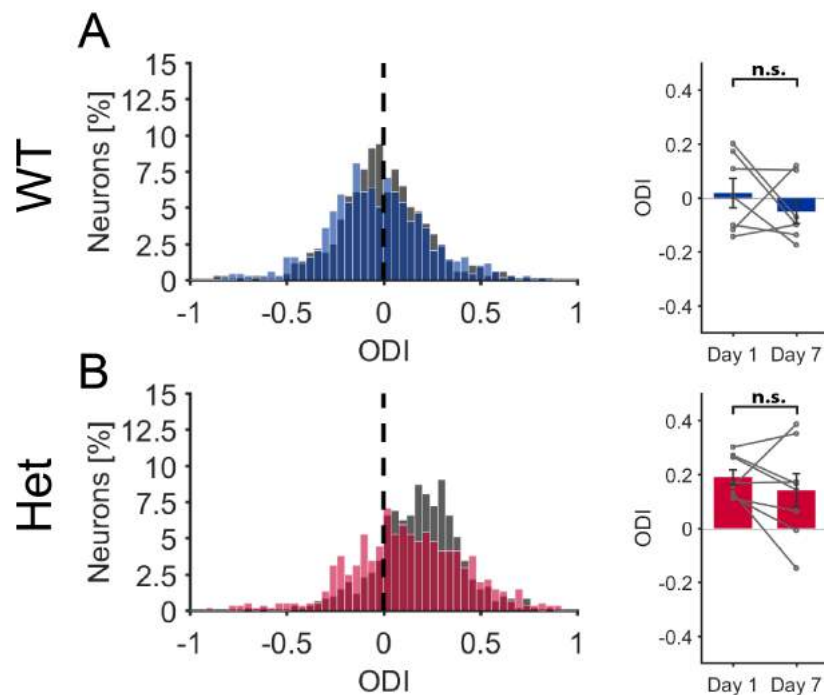


Figure 5.14: Changes in ODI across days of SynGAP^{+/-} mice and WT littermates during visual stimulation. Histograms showing the distribution of ODI values for all visually responsive neurons across animals. Bar plots showing the mean ODI for day 1 and day 7. Blue: WT littermates (N=7), red: SynGAP^{+/-} mice (N=8), grey dots indicate average across all neurons per animal, error bars: s.e.m. $p < 0.05$, n.s. not significant, Wilcoxon signed rank test.

5.5 DISCUSSION

Our results show that the neuronal activity of layer 2/3 neurons in V1 of SynGAP^{+/-} mice is lower compared to WT littermates. This effect across genotypes was robust when data were compared during periods of darkness or during visual stimulation (gratings). We also found a higher variation of neuronal activity during visual stimulation in WT littermates compared to SynGAP^{+/-} mice. In addition, orientation tuning in V1 was found to be higher in SynGAP^{+/-} mice compared to WT littermates. We did not find a difference in neuronal plasticity induced by MD in adult mice between both genotypes.

5.5.1 Lower visually evoked activity but higher orientation tuning in V1 of SynGAP^{+/-} mice

It was previously shown that SynGAP^{+/-} mice exhibit hyperexcitability in the hippocampus (Clement et al., 2012) and medial prefrontal cortex (Ozkan et al., 2014). Additionally, it was recently reported that SynGAP colocalizes with PV positive inhibitory interneurons, and that SynGAP^{+/-} haploinsufficiency leads to a reduced formation of synapses between PV-expressing interneurons and excitatory neurons in the cortex (primary somatosensory cortex (S1)) as well as in the hippocampal CA1 region (Berryer et al., 2016). This reduced inhibitory innervation was suggested to further drive the hyperexcitability of excitatory neurons of SynGAP^{+/-} mice. Additionally, *Syngap* pathogenicity accelerates the maturation of excitatory synapses during development, including several inputs within the hippocampus (Clement et al., 2012) and the thalamo-cortical synapse in L4 somatosensory cortex (Clement et al., 2013). Altogether, in vitro studies suggest that *Syngap* gene mutations increases excitatory synaptic function and promotes neuronal hyperexcitability.

Interestingly, we found both in darkness and during visual stimulation (drifting gratings) a reduced activity of V1 layer 2/3 putative excitatory neurons in SynGAP^{+/-} mice compared to WT littermates. SynGAP^{+/-} mice seem to have an equal amount of visually responsive neurons compared to WT littermates, suggesting that the reduced activity is not a result of less neurons responding to visual stimulation. Possible mechanisms underlying such reduced activity in V1 neurons include reduced subthreshold (synaptic) responses to visual stimulation in excitatory neurons and an increase in inhibition. Potential changes in subthreshold activity could be revealed using patch clamp recordings of pyramidal neurons. Changes in inhibitory neuronal activity could be tested using cre-driver transgenic mice lines to identify specific inhibitory neuronal subpopulations. Furthermore, a recent study showed that SynGAP^{+/-} haploinsufficiency leads to reduced inhibitory innervation by PV positive interneurons onto excitatory neurons (Berryer et al., 2016). Here we labelled and imaged all layer 2/3 V1 neurons, not differentiating between different neuronal subtypes. Hence, the neuronal population recorded is a mixture of excitatory and inhibitory

neurons. A different study conducted by Ozkan et al., 2014 found that *Syngap* haploinsufficiency restricted to forebrain glutamatergic neurons was sufficient to disrupt cognition, while *Syngap* haploinsufficiency in GABAergic neurons had no effect on cognitive abilities. Therefore, future studies investigating the impact of interneuron function on cognitive impairments associated with *Syngap* gene mutation will be of great value for the understanding of neuronal circuit activity in *SynGAP*^{+/-} mice. Despite this general lower level of activity, *V1* neurons in *SynGAP*^{+/-} mice show a higher average OSI across all visually responsive neurons compared to WT littermates. Further analysis using neuronal decoding algorithms, a method that tries to reconstruct sensory information from neuronal network activity, is needed to reveal whether *V1* neuronal populations in *SynGAP*^{+/-} mice encode visual information more efficiently than in WT.

5.5.2 Behavioural correlates of *SynGAP*^{+/-} mutation

Previous studies have shown that *SynGAP*^{+/-} mice are hyperactive in the open field during the first 10 minutes of exploration (Komiyama et al., 2002, Muhia et al., 2010, Berryer et al., 2016). However, our results did not find a significant difference in proportion of locomotion between *SynGAP*^{+/-} mice and WT littermates.

The differences between both experimental conditions likely explain the difference in results. For example, mice were habituated to the head restraint and the two-photon imaging setup for one to three sessions on different days and the proportion of locomotion was not recorded during these habituation sessions. In contrast, the hyperactivity reported in the open field test was assessed during the first 10 minutes of exploration of the new environment (Berryer et al., 2016). Thus, there might be a potential difference in proportion of locomotion between *SynGAP*^{+/-} mice and WT littermates during the first minutes of habituation. Furthermore, during the two-photon imaging experiment mice were head fixed. Therefore, compared to the open field arena, mice were not able to freely explore their surroundings, which likely affects their exploration behaviour and hence can influence the total proportion of time spent running.

Additionally, there was no significant difference in gain modulation through locomotion between WT littermates and *SynGAP*^{+/-} mice during visual stimulation. The amount of gain modulation of neuronal responses in layer 2/3 of *V1* in *SynGAP*^{+/-} mice is similar to the amount of gain modulation observed in previous studies (Niell and Stryker, 2010, Keller, Bonhoeffer, and Hübener, 2012, Bennett, Arroyo, and Hestrin, 2013, Polack, Friedman, and Golshani, 2013, Saleem et al., 2013, Reimer et al., 2014, Pakan et al., 2016). Gain modulation through locomotion in *V1* provides a model system for studying circuit mechanisms underlying behavioural state dependent changes in sensory processing. The fact that there was no significant difference in gain modulation between *SynGAP*^{+/-} mice and WT littermates may indicate that there is

no impairment in state dependent sensory processing in layer 2/3 of V1 in SynGAP^{+/-} mice. However, this study only compared two behavioural states (stationary versus locomotion), but not different arousal states. As discussed in [Chapter 4](#), neuronal response properties of V1 neurons differed in response reliability and magnitude depending on arousal state (Reimer et al., 2014) and that arousal and locomotion make distinct contribution to neuronal activity patterns in V1 (Vinck et al., 2015). Additionally, both studies found that changes in pupil dilation correlate with observed changes in neuronal response properties (Reimer et al., 2014, Vinck et al., 2015). Therefore, it will be informative to correlate the imaging data with pupil dilation in order to correlate the influence of arousal level with V1 neuronal activity of both genotypes. In addition, simultaneous local field potential (LFP) recordings may also reveal differences across genotypes, since it was shown that *Syngap* gene mutation leads to reduced gamma oscillation power during exploratory behaviour (Berryer et al., 2016), while a different study showed that WT mice display an increase in high-frequency oscillations in the gamma range during locomotion (Vinck et al., 2015).

5.5.3 *Heterogeneous changes in monocular responses after seven days of MD in adult SynGAP^{+/-} mice and WT littermates*

The SynGAP protein is part of a signalling cascade that ultimately leads to the activation of ERK, which is important for regulating activity dependent genes (Atkins et al., 1998, Di Cristo et al., 2001, Thomas and Huganir, 2004). In mouse V1 it was shown that visual experience activates ERK and that activation of ERK is important in mediating experience-dependent plasticity induced by MD during the critical period (Di Cristo et al., 2001). *In vitro* studies conducted in hippocampal slices of adult mice found that WT littermates and SynGAP^{+/-} mice show similar synaptic responses when stimulated with patterns of synaptic activation below threshold for LTP induction, but when stimulated with patterns of synaptic activation above threshold for LTP induction SynGAP^{+/-} mice showed a deficit in LTP induction compared to WT littermates (Komiyama et al., 2002).

The present study aimed at investigating neuronal plasticity induced by MD *in vivo* at the circuit level. Comparison of binocular responses ($\Delta F/F_0$) before and after MD revealed no significant changes in either average neuronal activity or gain modulation (LMI). However, comparing the relative responses to the left and right eye, we found a moderate non-significant shift in ODI in both, WT littermates and SynGAP^{+/-} mice. This small non-significant shift in ODI observed in both experimental groups is in agreement with the literature. Mice used in this study were on average P154 (minimum age 119 days, maximum age 196 days), hence way beyond their critical period. Sawtell et al., 2003 showed that a five-day MD is sufficient to induce a significant ODI shift in adult mice (as old as P90). Furthermore, two studies conducting MD in ma-

ture mice concluded that MD of seven or even 14 days is not sufficient to induce an ODI shift in fully mature mice (P₁₃₀) (Hofer et al., 2006, Lehmann and Löwel, 2008). Furthermore, the housing conditions of mice were shown to be crucial in adult ocular dominance plasticity (Kalogeraki et al., 2014, Greifzu et al., 2014). Adult mice housed in an enriched environment show higher levels of ocular dominance plasticity than mice housed in standard cages. The mice included in the present study were housed in standard cages without environmental enrichment, which may further explain the low level of plasticity observed. Additionally, imaging sessions were performed in awake mice and different levels of arousal and stress between imaging of the left and right eye stimulation may mask potential plasticity changes induced by MD.

Finally, this study used adult mice to compare baseline neuronal activity as well as neuronal plasticity in SynGAP^{+/-} mice and WT littermates. *In vitro* studies showed that spine formation happens prematurely in SynGAP^{+/-} mice (Kim et al., 2003, Vazquez et al., 2004, Clement et al., 2012, Clement et al., 2013), leading to a reduction of silent synapses. Silent synapses become unsilenced by the accumulation of AMPA receptors at the synapse and this was shown to shorten the critical period (Clement et al., 2013). In contrary, postsynaptic density protein-95 (PSD-95) knockdown mice show lifelong juvenile-like ocular dominance plasticity throughout adulthood (Huang et al., 2015). PSD-95 is believed to serve as adapter protein and co-localizes with the SynGAP protein and therefore is part of the same downstream signaling pathway. Hence, knockdown of PSD-95 might impair SynGAP activity and since SynGAP is negatively regulating the activity of RAS-GAPs less AMPA receptors are inserted in the postsynaptic membrane and a higher level of silent synapses found in PSD-95 knockdown mice during development. Therefore, it would be interesting to investigate neuronal plasticity in V₁ in juvenile SynGAP^{+/-} mice and WT littermates in long-term studies throughout development, since SynGAP^{+/-} mice might exhibit impairments in neuronal plasticity due to the premature synapse formation and the deficits in ERK signaling (Rumbaugh et al., 2006, Clement et al., 2013). Since it is believed that *Syngap* haplosufficiency causes developmental cognitive abnormalities, it is even more important to investigate changes in neuronal response properties throughout development in long-term chronic studies (Ozkan et al., 2014).

GENERAL DISCUSSION

This thesis investigated experience-dependent plasticity at the population level with single cell resolution in the primary visual cortex (V1) of adult mice. Changes in neuronal response properties of excitatory as well as three non-overlapping inhibitory interneuron subclasses (PV-, SST-, and VIP interneurons) in mouse V1 were monitored both during baseline behaviour in awake behaving mice as well as during a plasticity inducing protocol consisting of the repeated presentation of a visual stimulus using chronic two-photon calcium imaging. Further, we studied neuronal plasticity in the healthy brain as well as in a mouse model of intellectual disability (ID) and autism spectrum disorder using SynGAP^{+/-} mice.

To complete these studies, we first established a two-photon calcium imaging setup for chronic *in vivo* recordings in awake behaving mice. This approach enabled us to follow the same population of neurons across several days and weeks, in order to monitor changes in neuronal response properties before, during and after the induction of experience-dependent plasticity. We also developed analysis tools to extract cell specific activity from densely labeled populations of neurons (Keemink2018). Further improvements on automatic region of interest (ROI) segmentation and fast online analysis of calcium imaging data are currently being developed in several laboratories (Dombeck et al., 2007, Mukamel, Nimmerjahn, and Schnitzer, 2009, Maruyama et al., 2014, Kaifosh et al., 2014, Peron, Chen, and Svoboda, 2015, Pnevmatikakis et al., 2016, Pachitariu et al., 2016). The adoption of standardised analysis methods across labs will strongly benefit the reproducibility of results and the sharing of data; ultimately leading to a more efficient use of *in vivo* data, which is generally collected at a high cost in terms of equipment, staff and animals.

Our first experiments investigated the baseline neuronal response properties in V1 and the importance of behavioural state modulations on neuronal activity in this primary sensory region. We found that during visual stimulation VIP as well as SST inhibitory interneurons increase their activity with locomotion, while during darkness only VIP but not SST depict an increase in activity levels with locomotion. Thus, we concluded that the behavioural state dependent modulation of neuronal responses is context-specific, and functional properties of inhibitory interneurons can not be generalised from one context to another. While this thesis aimed at understanding the microcircuitry involved in V1 neuronal function and plasticity by investigating several neuronal subclasses (e.g. putative excitatory, as well as PV-, SST-, and VIP expressing interneurons), recent studies have shown that neurons belonging to the

same neuronal subtype identified by molecular markers exhibit various patterns of activity, indicating that they might be composed of further subclasses (McGarry et al., 2010, Lee et al., 2010, Rudy et al., 2011, Jiang et al., 2015). A recent study in mouse V1 categorized 15 different subtypes of interneurons, each subtype exhibited a characteristic connectivity pattern with other interneurons and excitatory neurons (Jiang et al., 2015). Therefore, it will be useful to further develop the specificity of molecular neuronal markers, to enable more targeted investigation and manipulation of behaviourally relevant neuronal activity.

Next, we investigated changes in neuronal response properties before, during and after the induction of experience-dependent plasticity in the healthy adult mouse brain using a passive viewing paradigm. We found no stimulus-specific changes in overall response amplitude at the population level. We did see heterogeneous response patterns at the single cell level. However, the control group, presented with an isoluminant grey screen over consecutive days, showed the similar heterogeneous response patterns at the single cell level. This indicates that the observed changes at the single cell level are not caused by the passive viewing paradigm, but are rather normal fluctuations in network activity over days. Other studies, using the similar experimental paradigm, have found diverse results; some studies showing a stimulus-specific increase in neuronal activity and some showing a decrease (Frenkel et al., 2006, Makino and Komiyama, 2015, Kaneko, Fu, and Stryker, 2017). The discrepancy between these recent studies, may be explained by the diversity of functional inputs to mouse V1; in which, activity strongly depends on many factors including stress, level of attention and motivation (Vinck et al., 2015, Makino and Komiyama, 2015), motor activity (Niell and Stryker, 2010, Polack, Friedman, and Golshani, 2013, Fu et al., 2014, Pakan et al., 2016), novelty (Frenkel et al., 2006, Hamm and Yuste, 2016, Kaneko, Fu, and Stryker, 2017) and level of deprivation (lack of enrichment) of housing conditions (Greifzu et al., 2014, Kalogeraki et al., 2014). Each of these factors influences V1 activity and plasticity through various inputs including neuromodulatory (Kilgard and Merzenich, 1998, Bao, Chan, and Merzenich, 2001, Dringenberg, 2006) as well as top-down connections (Zhang et al., 2014, Makino and Komiyama, 2015, Leinweber et al., 2017). Therefore, comprehensive future studies investigating the cell-type specific connectivity and function of bottom-up and top-down inputs to V1 will be necessary for a complete understanding of plasticity in mouse V1. Standardisation of housing conditions and reliable measures of brain states during data acquisition will improve the reproducibility of results across different laboratories.

Finally, we investigated changes in neuronal response properties before and after the induction of experience-dependent plasticity in the healthy adult mouse brain as well as in a mouse model of neurodevelopmental disorder using monocular deprivation (MD). Specifically, we investigated experience-dependent neuronal plasticity

in SynGAP^{+/-} mice, a mouse model of ID, where *in vitro* and *in vivo* studies have shown premature spine formation (Vazquez et al., 2004, Carlisle et al., 2008), a decreased long-term potentiation (LTP) (Komiyama et al., 2002, Kim et al., 2003), and hyperactivity (Komiyama et al., 2002, Muhia et al., 2010, Berryer et al., 2016) as well as deficits in novelty preference (Berryer et al., 2016). We found that the population neuronal activity of SynGAP^{+/-} mice is lower compared to wild-type (WT) littermates. This was unexpected, since it was shown previously that SynGAP^{+/-} mice exhibit hyperexcitability in the hippocampus (Clement et al., 2012). Possible underlying mechanisms for the hypoactivity in V1 of SynGAP^{+/-} mice could be an increase in inhibition or a reduction in synaptic responses to visual stimuli. Hence, further studies, investigating subthreshold activity and interneuron activity, are needed to reveal potential underlying mechanisms. Furthermore, we found a higher mean OSI magnitude in SynGAP^{+/-} mice compared to WT littermates. The higher mean OSI observed in SynGAP^{+/-} mice could be an indication of a strong influence of visual inputs on V1 activity in mutant mice. This might be related to the hypersensitivity to sensory stimuli observed in the large majority of patients affected by autism spectrum disorders. There was no difference in neuronal plasticity induced by MD in adult SynGAP^{+/-} mice and WT littermates, indicating that the observed plasticity deficits in the hippocampus in SynGAP^{+/-} mice may not manifest in the same way in the sensory cortex. However, experimental limitations such as the lack of measures of brain state (associated with stress and level of arousal) during data acquisition may explain the variability of our results. It is also possible that deficits in neuronal plasticity resulting from the impairment of the ERK pathway due to the *Syngap* gene mutation are compensated *in vivo* by other proteins involved in the ERK signalling pathway (e.g. neurofibromin). Additionally, a lack of plasticity in V1 does not preclude plasticity impairments in other cortical areas such as higher visual areas as well as frontal brain regions. Advancements in imaging techniques that would enable imaging several cortical areas simultaneously as well as using neuronal markers to identify neuronal subclasses will help to identify specific brain areas and cell-types as potential therapeutic targets for this disorder.

In recent years, there has been a tremendous development of new *in vivo* data acquisition techniques that will enable researchers to gain new insights into cortical neuronal function and plasticity. Two-photon imaging setups capable of imaging whole cortical columns (Andermann et al., 2010, Kerlin et al., 2010, Katona et al., 2012, Peron et al., 2015), several cortical areas (Stirman et al., 2016), as well as subcortical structures (Flusberg et al., 2005), have recently been developed and will be further applied and refined in the near future. Additionally, new approaches enabling data acquisition in freely behaving animals (Ghosh et al., 2011) and automated data acquisition processes will substantially increase our knowledge of neuronal circuit function (Aoki et al., 2017). The exponentially increasing number of neurons whose activity

can be simultaneously recorded in behaving animals opens a wide field of new questions and challenges, including the need of analysis tools and computational power for big data analysis. The tools developed in machine learning and computational neuroscience will be crucial for this development.

APPENDIX

A.1 SOLUTIONS

Artificial cerebrospinal fluid was mixed as follows (dissolve in 1 liter distilled water) and stored at 4°:

SUBSTANCE	AMOUNT	MOLECULAR MASS
Sodium chloride (NaCl)	7.305	125
Potassium chloride (KCl)	0.33548	4.5
Calcium chloride (CaCl ₂)	0.2219	2.06
Magnesium chloride (MgCl ₂)	0.0952	1
Sodium hydrogen carbonate (NaHCO ₃)	2.1843	26
Sodium di-hydrogen phosphate (NaH ₂ PO ₄)	0.15	1.25

Table 1: Artificial cerebrospinal fluid

Paraformaldehyde solution (4 %) was mixed as follows and stored at 4°: dH₂O was heated in a fume hood to approximately 50° to 55° while stirring. PFA powder was added and next NaOH was added dropwise. After PFA was dissolved and solution was translucent, disodium phosphate and monosodium phosphate were added to solution. The solution was then filtered (filter paper No.1) and cooled to room temperature. Next the PH value was measured and if necessary adjusted to 7.4.

SUBSTANCE	AMOUNT
Distilled water (dH ₂ O)	500 mL
Paraformaldehyde (PFA)	20 g
Disodium phosphate (Na ₂ HPO ₄)	5.465 g
Monosodium phosphate (NaH ₂ PO ₄)	1.585 g
Sodium hydroxide (NaOH)	125ul (10 Molar)

Table 2: Paraformaldehyde solution (4 %)

SCIENTIFIC REPORTS

OPEN

FISSA: A neuropil decontamination toolbox for calcium imaging signals

Sander W. Keemink^{1,2}, Scott C. Lowe^{1,3}, Janelle M. P. Pakan³, Evelyn Dylka³, Mark C. W. van Rossum³ & Nathalie L. Rochefort³

Received: 11 October 2017
Accepted: 6 February 2018
Published online: 22 February 2018

In vivo calcium imaging has become a method of choice to image neuronal population activity throughout the nervous system. These experiments generate large sequences of images. Their analysis is computationally intensive and typically involves motion correction, image segmentation into regions of interest (ROIs), and extraction of fluorescence traces from each ROI. Out of focus fluorescence from surrounding neuropil and other cells can strongly contaminate the signal assigned to a given ROI. In this study, we introduce the FISSA toolbox (Fast Image Signal Separation Analysis) for neuropil decontamination. Given pre-defined ROIs, the FISSA toolbox automatically extracts the surrounding local neuropil and performs blind-source separation with non-negative matrix factorization. Using both simulated and *in vivo* data, we show that this toolbox performs similarly or better than existing published methods. FISSA requires only little RAM, and allows for fast processing of large datasets even on a standard laptop. The FISSA toolbox is available in Python, with an option for MATLAB format outputs, and can easily be integrated into existing workflows. It is available from Github and the standard Python repositories.

Recent developments in *in vivo* imaging and genetically-encoded calcium indicators enable monitoring the activity of hundreds to thousands of neurons in the brains of awake behaving rodents. The activity of sub-types of neurons can be directly related to the animal's behaviour, over temporal scales from hundreds of milliseconds to several weeks^{1–5}. Such imaging experiments produce large sequences of images, the analysis of which typically involves the following steps (Fig. 1A):

- (1) Correction of brain motion artefacts that lead to the misalignment of imaging frames from one time point to the next. For this step, open source software packages are available^{6–13}.
- (2) Segmentation of the imaged field-of-view into regions of interest (ROI), typically containing individual neuronal soma or sub-cellular components (e.g. dendrites and spines). Images can be segmented either manually⁴, semi-automatically¹⁴, or automatically using either morphological criteria⁹ or activity based algorithms^{8,9,15–18}.
- (3) Extraction of the fluorescence changes across time within each ROI. Because two-photon microscopes have an elongated point spread function along the Z-axis, the signals imaged in a given focal plane are contaminated by signals from above and below this plane. The fluorescence signal from a given region of interest is thus usually contaminated by signals from surrounding neurites (axons and dendrites) and sometimes nearby neuronal somata. Correcting for such out-of-focus contamination is particularly critical for experiments in which neuropil activity itself is modulated by the experimental protocol. Decontamination is the focus of the current paper.

Currently, two main approaches are used to correct for neuropil contamination, either by subtracting a neuropil signal from the somatic signal, or by using blind source separation methods. For subtraction, a neuropil region is defined around the region of interest (e.g. a soma), and the spatially averaged neuropil signal is subtracted from the somatic signal^{3,14}. Since the neuropil signal is not spatially uniform^{11,19}, using a local neuropil region is preferable over using a global neuropil signal. The subtraction method has the advantage of being fast and intuitive.

¹Institute for Adaptive and Neural Computation, School of Informatics, University of Edinburgh, Edinburgh, EH8 9AB, UK. ²Bernstein Center Freiburg, Faculty of Biology, University of Freiburg, 79104, Freiburg, Germany. ³Centre for Discovery Brain Sciences, Biomedical Sciences, University of Edinburgh, Edinburgh, EH8 9XD, UK. Sander W. Keemink and Scott C. Lowe contributed equally to this work. Mark C. W. van Rossum and Nathalie L. Rochefort jointly supervised this work. Correspondence and requests for materials should be addressed to S.W.K. (email: swkeemink@scimail.eu) or N.L.R. (email: n.rochefort@ed.ac.uk)

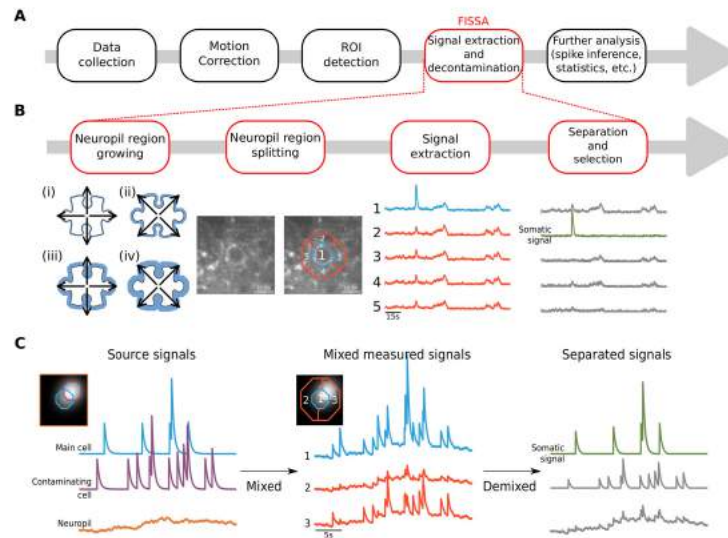


Figure 1. FISSA toolbox overview. (A) Schematic of a generic calcium imaging data analysis workflow. (B) Schematic of the four main steps of the FISSA toolbox workflow. Given a predefined region of interest (ROI), the local neuropil region is defined by expanding the ROI (white shape) alternately in the cardinal and diagonal directions (steps i to iv), until the surrounding area (blue area) is four times the ROI area. The resulting neuropil region is split into four subregions (regions 2, 3, 4, and 5). The signals from each of these regions are separated using non-negative matrix factorization (NMF), and the somatic signal is identified. (C) Schematic representation of blind source separation in FISSA. Left: Model of a somatic signal (blue) contaminated by two types of sources: the surrounding neuropil (orange), and an overlapping soma (purple). Middle: The measured signals in the somatic ROI (region 1) and in the surrounding neuropil (regions 2 and 3) will each be a mix of the three underlying source signals shown in the left panel. Right: NMF separates the mixed signals, recovering the original source signals. From these demixed components the one that best matches the measured ROI signal, relative to the neuropil regions, is identified as the somatic signal.

However, subtraction can lead to negative signals when the neuropil signal is larger than the somatic signal, while in other cases it does not remove all contamination. As a consequence, the subtraction parameters (such as how much weight to give to the subtracted neuropil signal) have to be adjusted for each dataset or even for each cell type (sparse vs densely firing cells¹⁴), which makes standardization of this approach challenging.

A more recent class of decontamination methods is based on blind source separation. These methods aim at finding underlying signal sources from image sequences, typically using either Independent Component Analysis (ICA)^{18,20}, Non-Negative Matrix Factorization (NMF)¹⁵, or model-based NMF^{9,11}. These approaches are standardized and user-independent. They simultaneously estimate ROIs and their associated fluorescence signals, while also accounting for neuropil contamination. However, automated segmentation into somatic ROIs is not always reliable and hand labelling is often still necessary. In addition, in early versions of blind source separation methods, the neuropil was modeled as a one-dimensional signal shared by all pixels with different weights, which can lead to an artificial decrease of correlated somatic signals⁹. Finally, cell-detection methods are computationally intensive for large datasets. Thus, the ideal neuropil decontamination method would be standardized, fast, and work with both manually and automatically drawn ROIs.

For these reasons, we have developed the Fast Image Signal Separation Analysis (FISSA) toolbox for decontaminating calcium signals. FISSA defines a set of neuropil regions around pre-defined somatic ROIs (either from hand-labelling or from automatic detection algorithms), and uses NMF to separate the signals from these regions (Fig. 1B,C). We have tested this toolbox on both simulated and *in vivo* data, and our results show that FISSA performs either similarly or better than existing published methods. Additionally, since only a few signals need to be separated, FISSA is fast and requires only little RAM, so that it is usable on a standard computer or laptop.

Results

FISSA toolbox workflow. The goal of the FISSA toolbox is to remove contamination from the ROI signals. As a consequence of the limited resolution of *in vivo* imaging methods, especially axially²¹, the signal measured from a given region of interest in a single focal plane is in fact a mixture of signals originating from this ROI as

well as from a surrounding volume (Fig. 1C). This volume includes mostly neurites (axons and dendrites) of other cells, and sometimes other somata. To demix these signals, we use the fact that the signals (photon counts) are always positive, and assume that the mixing of the different signals is linear and additive. A method of choice for demixing signals under these assumptions is non-negative matrix factorization^{22,23}, which separates signals by estimating a set of positive signals that best explains the observed mixed signals.

The FISSA toolbox relies on user-defined ROIs that can be imported either from ImageJ or defined as standard Python arrays. For each ROI, FISSA first defines a neuropil region by expanding the shape of each ROI by a fixed amount (Fig. 1B and Methods). The neuropil area is defined as the expanded shape, excluding the original ROI. Next, the neuropil region is divided into subregions of equal area. By default, FISSA defines four subregions each with the same area as the ROI; performance did not improve with more subregions (Fig. 2E).

The signals from each region (the four subregions of the neuropil and the somatic ROI) are then separated using NMF. The NMF method returns how strongly each separated signal was present in each subregion and ROI. Using these estimates, the separated signals are scaled and sorted by relative presence in the ROI compared to the surrounding subregions (see Methods). The signal with the strongest relative presence is taken as the extracted somatic signal (Fig. 1C).

Note that FISSA separates the raw fluorescence signals. The calculation of the relative change in fluorescence ($\Delta f/f_0$) can be done afterwards (see Methods). The extracted and decontaminated signals can be accessed in Python or saved in MATLAB format.

FISSA performance on simulated calcium imaging data. We first used simulated data to evaluate our approach. We modelled a set of neurons with Poisson firing statistics and calcium indicator dynamics based on GCaMP6f (see Methods). In the model, each cell had a well defined spatial structure, but its signal bled into the surrounding region and cells could overlap. A smoothly fluctuating global neuropil signal was included to model background fluctuations. A given pixel might thus contain the global neuropil contamination, and one or more cell signals. Finally, to model photon emission, the calcium indicator signal at each pixel was simulated by Poisson shot noise.

We evaluated the performance of different decontamination methods on three cases with increasing contamination (Fig. 2). We compared the performance of three decontamination methods: 1) subtraction of the local surrounding neuropil signal³⁴, 2) a cell detection and signal separation method including neuropil decontamination called constrained NMF (cNMF⁹), and 3) FISSA extraction. To quantify the performance of each method we calculated the Pearson correlation between the extracted signals and the ROI source signal, with the extracted signals low-pass filtered at 5 Hz to minimize differences due to high frequency noise.

We first considered a single cell whose somatic signal was only contaminated by neuropil fluctuations (Fig. 2A). All three methods successfully decontaminated the ROI signal, resulting in a high correlation between the corrected signal and the ROI source signal (Fig. 2Aiii).

Next, we modelled the same soma but added a partially overlapping neuron (Fig. 2B). The additional contaminating calcium transients reduced the correlation between the measured and the ROI source signal (Fig. 2Biii). Whilst subtracting the neuropil signal still removed slow fluctuations, it did not fully remove the extra transients, resulting in a lower correlation than the other two methods. cNMF and FISSA removed both the background fluctuations and the contaminating transients equally well, while preserving the true transients.

Finally, we added a second non-overlapping signal source with a strong, localized calcium response (Fig. 2C), leading to a neuropil signal with additional large calcium transients (Fig. 2Cii). The subtraction method led to negative transients, and the correlation between its signal and the source signal was lower than for the other two methods. FISSA and cNMF both resulted in very high correlations, with FISSA's being slightly but significantly higher ($p = 0.0051$, Fig. 2Ciii).

We then tested whether the results were consistent across a broader range of simulation parameters (Fig. 3A). While keeping the firing rates of the other cells the same, we varied the firing rates of the cell of interest (panel Ai), its spike transient amplitude (panel Aii), and the imaging frame-rate (panel Aiii). The correlations generally decreased for all methods as the signal-to-noise ratio decreases (through lower firing rates or calcium transient amplitudes). FISSA maintained the highest correlation across all parameter changes, and in particular at low signal-to-noise ratios performed better than other methods. In some cases, the difference between cNMF and FISSA results does not reflect the performance of the signal separation per se but rather shows the limit of the automatic detection method of cNMF. In cases of low signal amplitude or firing rate, cNMF may simply not detect the cell of interest. As a consequence, since there is no segmentation and thus no signal, the correlation with the source signal is very low. However, for the same reasons, a cell with very low firing rates might also not be detected manually. We then tested whether FISSA performed equally well when taking only a subset of the data. Our results show similar performance when downsampling a 120 s data set from 100 Hz to lower frame rates (Fig. 3Aiii). Finally, the shape of the cell of interest, such as more elongated shapes, also did not substantially affect the performance (Fig. 3Aiv).

FISSA has a number of user-adjustable parameters: the number of neuropil regions, the area of the neuropil subregions, and the NMF parameter α which promotes sparseness of the source separation. Performance is robust across parameter values (Fig. 3B), as long as the number of neuropil regions is larger than 3 (the default is 4), for a neuropil subregion area at least half of the original ROI's area (default is the same size as the ROI), and an α between 0.1 and 0.5 (the default is 0.1). Finally, we tested the influence of the ROI's size relative to the cell of interest by varying the threshold used to define the ROI, while keeping the simulated cell shape constant (Fig. 3C). The results show that FISSA performance remains stable for a broad range of ROI sizes, either larger or smaller than the actual cell's shape (Fig. 3C). This robustness of FISSA is a useful property when using hand-labelled ROIs that may be larger or smaller than the actual cell body.

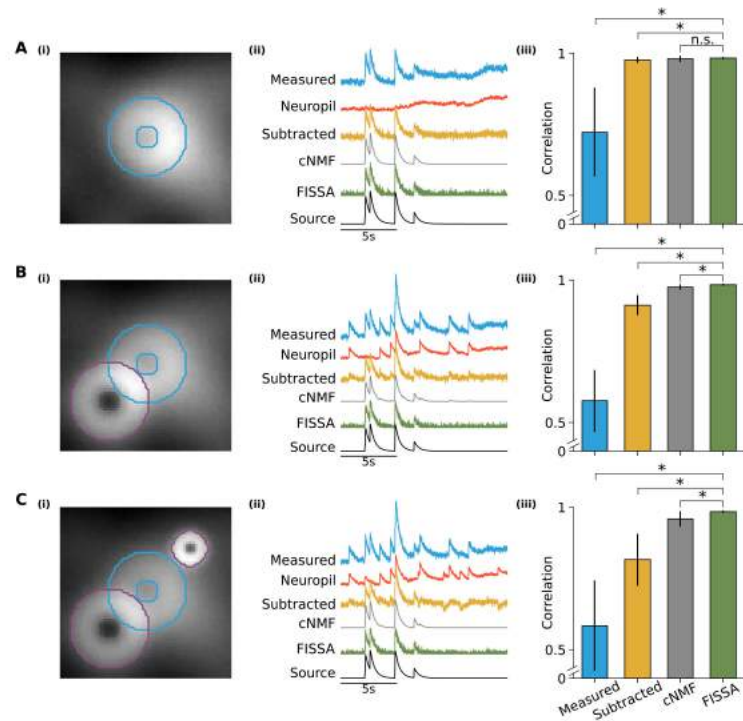


Figure 2. Comparison of FISSA performance with other decontamination methods on simulated calcium imaging data. Rows A, B, and C illustrate three cases with increasing levels of contamination. (A)(i) Image of a region containing a single doughnut-shaped cell firing at 0.5 Hz and a fluctuating neuropil background. The image is an average across all 12000 frames (120 s). The ROI is indicated in blue. (ii) Example fluorescence traces for the blue ROI indicated in panel A(i): average measured signal of the ROI (blue trace, 'Measured'), the average surrounding neuropil signal (red trace), and the signals after neuropil decontamination by three different methods (subtraction in yellow, cNMF in grey, and FISSA in green). The uncontaminated source signal (as defined by the simulation) is shown in black. The cNMF trace has a lower noise level as the cNMF algorithm also includes smoothing. (iii) Average Pearson correlations between the ROI source signal and the extracted ROI signal: before decontamination (first column, 'Measured'; 0.723), and after each decontamination method (neuropil subtraction, cNMF, and FISSA; 0.977, 0.981, and 0.984 respectively). Error bars indicate standard deviation. * $p < 0.05$; ** $p < 0.005$; n.s.: not significant ($p > 0.05$); Wilcoxon signed-rank test, $n = 10$ simulations of 120 s each (with different background neuropil signals, spike times, and photon noise). FISSA vs: measured $p = 0.0033$, subtraction $p = 0.0409$, cNMF $p = 0.0911$. (B) As panel A, but the blue ROI is additionally contaminated by an overlapping cell firing at 0.3 Hz (indicated by the purple outline). Average values for the four methods are 0.576, 0.912, 0.975, and 0.984 respectively. FISSA vs: measured $p = 0.0033$, subtraction $p = 0.0033$, cNMF $p = 0.0033$. (C) As panel B, but an additional bright localized signal firing at 0.3 Hz was added (smaller purple outline). Average values for the four methods are 0.585, 0.816, 0.959, and 0.984 respectively. FISSA vs: measured $p = 0.0051$, subtraction $p = 0.0051$, cNMF $p = 0.0051$.

FISSA performance on *in vivo* calcium imaging data. We next tested FISSA on *in vivo* two-photon calcium imaging data of GCaMP6-labelled layer 2/3 neurons in the mouse primary visual cortex. We used a publicly available dataset which contains simultaneous calcium imaging of GCaMP6-labelled neurons and simultaneous cell-attached electrophysiological recordings^{3,25}, allowing for a direct comparison between the extracted calcium signals and the recorded spikes. To quantify performance we calculated the Pearson correlation between the calcium signals estimated by each method, and the predicted calcium transients inferred from the recorded spikes.

FISSA successfully decontaminated the somatic signal of 20 cells tested: the results showed significantly improved correlation values after FISSA compared to raw data ($p = 0.0006$, Fig. 4B, 'Measured' vs 'FISSA'). On

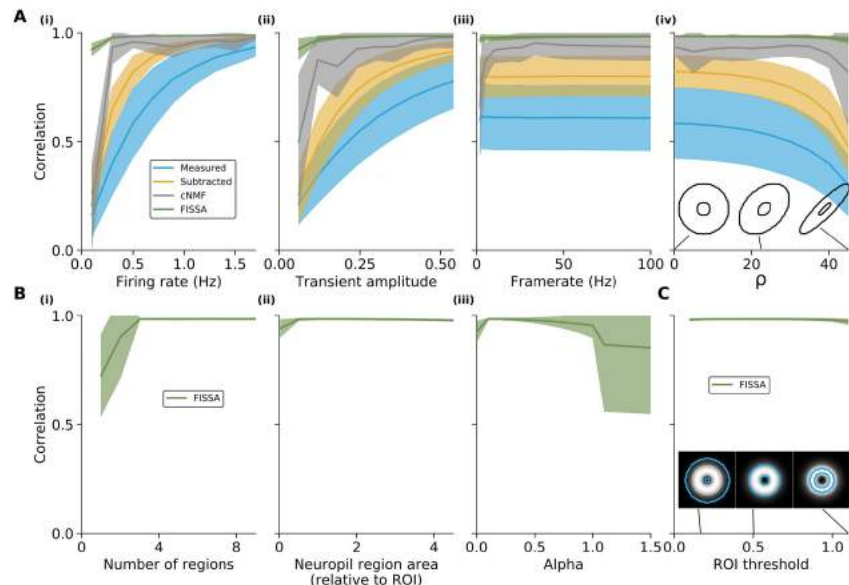


Figure 3. FISSA performance for different simulated data parameters and user-adjustable FISSA parameters, for the signal of the cell of interest from the case in Fig. 2C. **(A)** Correlations between the source and extracted signals before neuropil decontamination ('Measured') and after each decontamination method (neuropil subtraction, cNMF, and FISSA) for different simulation parameters. (i) Correlations for changes in the firing rate of the cell of interest (0.1 to 1.7 Hz, with steps of 0.2 Hz, default is 0.3 Hz). (ii) Correlations for changes in calcium transient magnitude (parameter A , see Eq. 9, 0.06 to 0.54 with steps of 0.06, default is 0.3). (iii) Correlations for changes in imaging framerate (downsampling of 100 Hz initial data to lower frame rates: by 50, 40, 30, 20, 10, 5, 4, 3, 2, and 1). (iv) Correlations for changes in cell shape, by changing the parameter ρ , see Eq. 10 (steps of 5 from 0 to 45, default is 0). The insets show example cell shapes for different ρ values. **(B)** Correlations between the source and extracted signals against different user-adjustable FISSA parameters (x-axes). (i) Number of neuropil subregions while keeping the total area constant, at four times the ROI area. (ii) Area of the neuropil subregions relative to the central ROI (0.025 for the smallest area, steps of 0.5 from 0.5 to 4), for four subregions. (iii) NMF parameter α (with steps of 0.1). **(C)** The effect of suboptimal ROI selection, by varying the threshold at which a cell mask is defined (Parameter T_{mask} in Eq. 14, 0.1 to 1.1 with steps of 0.1, default is 0.5). The insets show the same central cell with the outlines of the mask used for three example thresholds. All panels show the average values over 10 simulations; shaded areas indicate standard error.

this dataset, the results obtained with the cNMF and subtraction methods were not significantly different from those obtained with FISSA (FISSA vs subtraction $p = 0.2959$, FISSA vs cNMF $p = 0.4330$, Fig. 4B). This difference in results, compared to the simulated data in Fig. 2, is due to the relatively sparse labelling leading to a low level of contamination with few overlapping labelled structures in the field of view. As such, the main contamination source consists of background fluctuations, for which all three decontamination methods work well. However, cNMF did result in low correlation values for a small subset of cells. This can be partly explained by the high optical magnification used for the dataset (roughly one to three cells per $30 \mu\text{m}$ by $30 \mu\text{m}$ field of view, at 256 by 256 pixels), while cNMF was designed to be applied to a large field of view with hundreds to thousands of cells. For some cells, the ROIs that cNMF extracted did not fully match the outline of the soma and not all contamination was successfully removed (e.g. grey trace, Fig. 4A).

Finally, we compared the different methods for neuropil decontamination in a dataset of *in vivo* two-photon calcium imaging of layer 2/3 neurons in the primary visual cortex (V1) of awake behaving mice. All neurons were labelled through local injection of adeno-associated viruses (AAV1.Syn.GCaMP6f.WPRE.SV40) in V1⁴. After 2–3 weeks of expression, running speed of the animal and GCaMP6f signals were recorded simultaneously during the presentation of drifting gratings. It is known that visual responses of layer 2/3 neurons in V1 are modulated by locomotion^{4,25–29}. We compared the effect of locomotion on single neuron activity in this dataset before and after neuropil decontamination. The effect of locomotion was quantified for each neuron by the locomotion

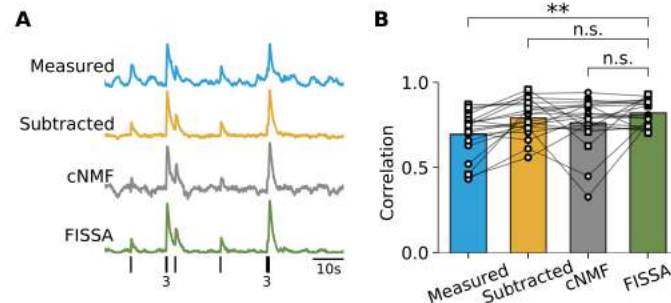


Figure 4. Comparison of neuropil decontamination methods on *in vivo* two-photon calcium imaging data from layer 2/3 neurons in mouse primary visual cortex (data from^{3,24}). (A) Example measured and decontaminated traces of fluorescence changes for cell 20120627_cell14 (frames 14400 to 19200). All traces were low-pass filtered at 5 Hz. The black ticks on the bottom row indicate the spikes measured electrophysiologically, with the number of overlapping spikes indicated below. (B) Correlations between the calcium transients inferred from the recorded spikes (see Methods), and the calcium signals estimated by each method. The data points correspond to GCaMP6s (circles) and GCaMP6f (squares) cells from the dataset^{3,24}. ** $p < 0.005$; n.s.: not significant ($p > 0.05$); Wilcoxon signed-rank test, $n = 20$ cells, FISSA vs measured: $p = 0.0006$, FISSA vs subtraction $p = 0.2959$, FISSA vs cNMF $p = 0.4330$.

modulation index (LMI)⁴, which calculates the normalized difference between the mean change in fluorescence ($\Delta f/f_0$) during locomotion (R_l) and stationary (R_s) periods, as $LMI = (R_l - R_s)/(R_l + R_s)$.

Our results show that before neuropil decontamination almost all cells in this dataset displayed positive LMI (Fig. 5, median LMI 0.29), indicating an increase of activity during locomotion. However, after neuropil decontamination by any of the three methods, LMI values strongly decreased (median LMI was 0.16, 0.04, and 0.09 using neuropil subtraction, cNMF, and FISSA, respectively). These results are in agreement with previous electrophysiological experiments which reported that 20–50% of neurons with visual responses are positively modulated by locomotion in mouse V1^{28,30}. The LMI values obtained with FISSA were not significantly different from those obtained with cNMF ($p = 0.0687$). However, in this dataset, the subtraction method led to significantly higher LMI values than those obtained after FISSA and cNMF ($p = 0.0117$).

Altogether, these results show that correction for neuropil contamination is critical for the analysis of two-photon calcium imaging data, especially for datasets in which the surrounding GCaMP6-labelled neuropil is itself modulated by the experimental conditions (e.g. by sensory stimuli or by the animal's behaviour). In addition, the results obtained with both simulated data and *in vivo* two-photon calcium imaging datasets indicate that FISSA performs either similarly or better than other published methods for neuropil decontamination.

FISSA computational resources and integration into existing workflows. FISSA is freely available at <https://github.com/rochefort-lab/fissa>. The toolbox can be applied to an existing dataset in just a few lines of code:

```

1 # FISSA toolbox import
2 import fissa
3
4 # Specify the location of the ROIs and data files
5 images_location = './exampleData/20150629'
6 rois_location = './exampleData/20150429.zip'
7
8 # Specify the folder where data will be stored
9 output_folder = 'fissa_example'
10
11 # Signal extraction and decontamination
12 experiment = fissa.Experiment(images_location, rois_location, output_folder)
13 experiment.separate()
14
15 # Export results in MATLAB format
16 experiment.save_to_matlab()

```

First, the user defines:

- The imaging data, either as a directory containing tiff files of the acquired images or standard Numpy arrays (Python format that can be generated from other data formats).
- The regions of interest (zip files of ROIs defined in ImageJ or Numpy arrays).
- The results folder where extracted and processed data will be stored.

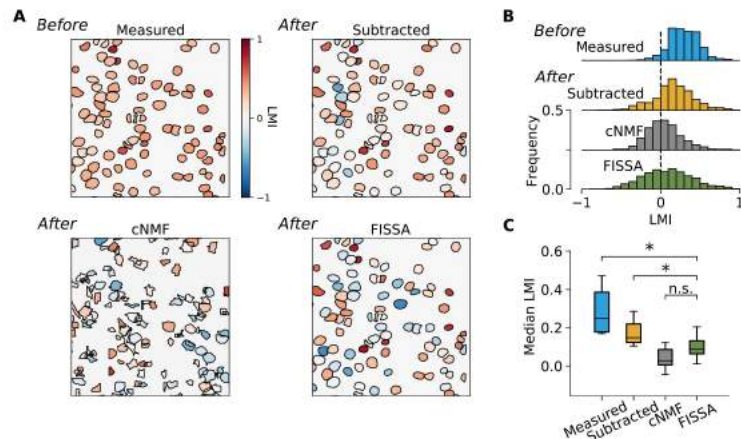


Figure 5. Impact of neuropil decontamination on neuronal responses measured with two-photon calcium imaging, in V1 layer 2/3 of awake behaving mice. Neurons were labelled with GCaMP6f. The effect of locomotion was quantified for each neuron by the locomotion modulation index (LMI). (A) An example field of view with somatic ROIs coloured by the LMI value obtained either before neuropil decontamination ('Measured') or after decontamination. The ROIs for the measured, subtraction, and FISSA methods are identical and were defined by hand. For the cNMF method the ROIs are presented as detected by the algorithm. LMI values were calculated for periods of visual stimulation with oriented gratings (10 to 20 trials per field of view, 60 s/trial). (B) The distributions of LMI values across all layer 2/3 cells in eight mice, before ('Measured') and after each decontamination method. (C) The distributions of median LMI values for the eight mice, before and after decontamination. * $p < 0.05$; n.s.: not significant ($p > 0.05$); Wilcoxon signed-rank test, $n = 8$ mice, FISSA vs measured: $p = 0.0117$, FISSA vs subtraction $p = 0.0117$, FISSA vs cNMF $p = 0.0687$, subtraction vs cNMF $p = 0.0687$.

After this step, only two lines of code are necessary to run the full FISSA analysis pipeline: from neuropil region definition to signal separation and selection. The results can then be accessed within Python or saved in MATLAB format. In the GitHub repository we provide example scripts which demonstrate how to integrate FISSA with existing published workflows such as SIMA⁸ and cNMF⁹.

By default, tiff files are fully loaded into memory before signal extraction. For large tiff files, there is an option to load them frame-by-frame to reduce memory usage. For other formats, there is also the option to define a custom data-loading script.

Since FISSA only has to separate a small number of signals, it can quickly separate signals across large datasets. For example, to extract isolated signals from 40 cells within a 600×600 pixel field of view over 2400 frames, FISSA only takes 40 seconds. This scales sub-linearly with the number of frames, such that for 30000 frames FISSA takes 60 seconds (for these tests FISSA was run on a workstation running Ubuntu 17.04 with a six core Intel Core i7-6800 K CPU@3.40 GHz). FISSA is thus well suited for processing large datasets with long imaging periods. However, as opposed to other methods (cNMF⁹, suite2P¹¹), FISSA does not automatically segment the images into defined ROIs; therefore, the total time for data processing also depends on the method used for defining ROIs as well as on the data loading time.

Discussion

We have developed a fast and easy to use toolbox (FISSA) for neuropil decontamination in calcium imaging datasets. The results obtained with both simulated and *in vivo* two-photon calcium imaging datasets indicate that FISSA performs either similarly or better than previously published methods for neuropil decontamination of calcium signals. In addition, FISSA presents a number of advantages. First, unlike subtraction methods, it provides a standardized, user-independent approach that removes multiple sources of contamination without leading to negative signal artefacts. Other methods based on blind-source separation do provide a standardized approach but require more computational resources and can be very slow to run on large datasets (although recent developments have improved the running time of this type of method^{11,30}).

A further advantage of FISSA is that it uses minimal computational resources and can thus be used on a standard laptop even for large datasets. However, the total analysis time will also depend on the ROI detection method. FISSA does not include an automatic cell detection algorithm: ROIs must be defined beforehand, either manually or through a third-party algorithm. Separating ROI detection and signal extraction can be an advantage for experimental data in which automatic cell detection methods are not sufficiently accurate.

Finally, FISSA's main assumptions are that measured calcium signals are positive and mix both linearly and additively. This is in contrast to other methods, that make specific assumptions about the calcium dynamics in terms of noise level and time scales^{9,31}. Thus, FISSA is more generally applicable across various experimental conditions which may include different fluorescent indicators (such as synthetic dyes or other types of protein-based sensors) as well as other imaging methods (both *in vitro* and *in vivo*). Because the FISSA toolbox can be adapted to different formats of imaging data and regions of interest, it can easily be integrated into existing data analysis workflows.

Methods

FISSA algorithm. *Neuropil subregions definition.* FISSA uses predefined ROIs, obtained from either manual or automatic segmentation. The surrounding region is automatically defined by expanding the shape of each ROI alternately in the cardinal and diagonal directions (Fig. 1B). Next, the neuropil region is divided into N equal area subregions, by taking the polar coordinates relative to the ROI centre and taking the $\frac{1}{N}$ th fraction for each subregion. By default, the total surrounding region is expanded until its area is N times the area of the central ROI (such that each subregion has the same area as the ROI). For the examples in this paper we set $N = 4$, as performance saturated at this N (Fig. 3Bi).

Non-Negative Matrix Factorization implementation. We assume that the spatially averaged signal in a given ROI, $\mathbf{f}_{\text{measured}}(t)$, is given by a linear mixing of a set of underlying source signals

$$\mathbf{f}_{\text{measured}}(t) = W \mathbf{f}_{\text{source}}(t), \quad (1)$$

where $\mathbf{f}_{\text{source}}(t)$ is the set of source signals, and W is the mixing matrix. Blind source separation techniques estimate the mixing matrix V and separated sources $\mathbf{f}_{\text{sep}}(t)$ such that

$$\mathbf{f}_{\text{measured}}(t) \approx V \mathbf{f}_{\text{sep}}(t). \quad (2)$$

For FISSA, we define $\mathbf{f}_{\text{measured}}(t)$ as the $N + 1$ signals from the central ROI and the neuropil subregions, V is the $N + 1$ by $N + 1$ mixing matrix, and $\mathbf{f}_{\text{sep}}(t)$ are the $N + 1$ extracted signals. The separation thus assumes the number of output signals is the same as the number of input signals (measured $N + 1$ signals). If there are fewer than $N + 1$ source signals being mixed (as, for example, in Fig. 2), we did not find this to have a negative impact on performance. The main point is that the number of output signals should not be lower than the number of signal sources. However, in physiological data, the number of signal sources is unknown. For the data sets we have used (*in vivo* data from local labelling of cortical neurons in V1), the number of $N + 1$ (corresponding to 5 regions) gave robust results. However, the option of changing the number of separated signals can be useful in case alternative data sets are likely to include more signal sources.

FISSA performs the blind source separation with Non-Negative Matrix Factorization (NMF), using the implementation in the scikit-learn toolbox³². There is also the option in the FISSA toolbox to use Independent Component Analysis (ICA) instead of NMF. ICA relies on the fact that the distribution of the sum of random variables will be more Gaussian than the individual components. Thus, by finding the most non-Gaussian projections, the sources can be identified. ICA is faster than NMF, but the resulting source signals or mixing coefficients can be negative, which can sometimes lead to negative extracted signals similar to the subtraction method (see Supplementary Fig. 1). NMF makes the stronger assumption that all signals and mixing coefficients are strictly non-negative, a property which is true for calcium imaging data. We therefore recommend using the NMF method, which was used for all results presented in this paper.

To perform NMF the temporal signals over time $\mathbf{f}_{\text{measured}}(t)$ and $\mathbf{f}_{\text{sep}}(t)$ are written as matrices with components

$$F_{i,t} = f_i(t). \quad (3)$$

The NMF algorithm then minimizes an objective E in alternating steps with respect to V and F_{sep} , until E reaches a target threshold^{22,33}. The objective is the total squared difference between the measured signals and the estimated signals F_{measured} , plus additional norms that encourage a sparse solution

$$E = \frac{1}{2} \left\| F_{\text{measured}} - V F_{\text{sep}} \right\|_{\text{Fro}^2}^2 + \alpha l_{\text{ratio}} \|V\|_1 + \alpha l_{\text{ratio}} \|F_{\text{sep}}\|_1 + \alpha (1 - l_{\text{ratio}}) \|V\|_{\text{Fro}^2} + \alpha (1 - l_{\text{ratio}}) \|F_{\text{sep}}\|_{\text{Fro}^2}, \quad (4)$$

where the Frobenius norm is given by $\|A\|_{\text{Fro}^2} = \sqrt{\sum_{i,j} A_{ij}^2}$ and the element-wise L1 norm is given by $\|A\|_1 = \sum_{i,j} |A_{ij}|$. l_{ratio} determines the ratio between the Frobenius norm and the element-wise norm. α is the sparseness regularizer on both the mixing matrix V and the separated signals F_{sep} . We set $\alpha = 0.1$ and $l_{\text{ratio}} = 0.5$. Finally, both the separated signals and the mixing matrix are constrained to be non-negative. Initialization of both the estimated mixing and separated matrix is done by non-negative double singular value decomposition³⁴.

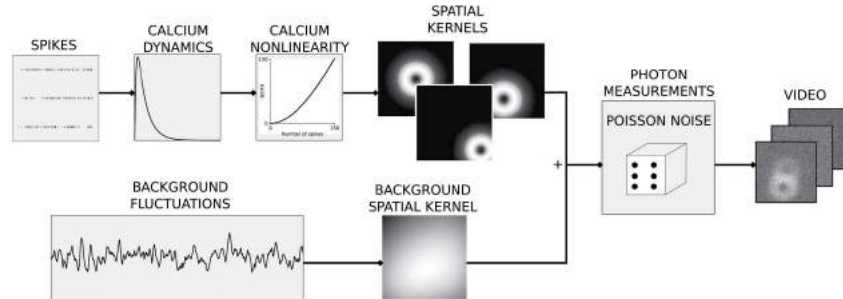


Figure 6. Simulated data generation. For each simulated neuron, a Poisson spike train is generated. The corresponding calcium indicator dynamics are simulated using GCaMP6 rise and decay times, and a nonlinearity. Next, the calcium traces are associated with a spatial kernel consisting of a doughnut shape mask (that models the cellular soma's structure) and a Gaussian that simulates signal spread. Additionally, noisy background fluctuations are generated which vary spatially through a spatial kernel. All resulting signals are summed, and passed through a Poisson generation process to simulate photon emission, resulting in the final image sequence.

Signal selection. Blind source separation returns a set of separated signals, but it does not indicate which one corresponds to the somatic signal and which ones are the contaminating signals. The estimated mixing matrix V provides the weight with which each identified source signal contributes to the mixed signals. Each row in the mixing matrix represents how strongly each of the estimated underlying signals is present in the measured signal. For each signal, we rate its relative presence in the central ROI by normalising the weights across each column of the mixing matrix

$$v'_{ij} = \frac{v_{ij}}{\sum_r v_{rj}}. \quad (5)$$

The values v'_{ij} represent how strongly each signal is present in each region, relative to its average across all regions. The estimated somatic signal is then given by the signal for which v'_{0j} is the highest, multiplied by its contribution to the measured ROI signal

$$f_{\text{est}}(t) = v_{0j_{\text{max}}} f_{\text{sep}}^{j_{\text{max}}}(t), \quad (6)$$

where $f_{\text{sep}}^j(t)$ is the j -th signal as separated by blind source separation, and

$$j_{\text{max}} = \arg \max_j v'_{0j}. \quad (7)$$

Thus, in order to find the signal that corresponds to the somatic signal, we assume that the somatic signal is more strongly represented in the central ROI, compared to the neuropil subregions (otherwise it is unlikely that it would have been chosen as the ROI). For example, the amplitude of the neuropil signal in the somatic ROI might be higher than the somatic signal itself, but this high neuropil signal will also be strongly present in the surrounding subregions. The somatic signal however, will be the one that is mostly present in the somatic ROI, but not in the other subregions.

Baseline. For Fig. 5, to calculate $\Delta f/f_0$, f_0 was estimated as the 5th percentile of the 1Hz low-pass filtered trace. For all extracted traces the f_0 of the non-corrected trace was used.

Multiple trials. In the case of several discrete recording sessions of the same cells, by default FISSA concatenates the trials together. This is done to ensure that the signal extracted for a given trial does not suddenly change across trials (e.g. if a cell is silent during one trial).

Software. The code is implemented in Python 2.7, using the Numpy 1.7, SciPy 0.12, Matplotlib 1.2 and HoloViews 1.6 toolboxes. We implemented NMF and ICA with the Python scikit-learn NMF and fastica functions respectively³².

In addition to the separation algorithm, the FISSA package has two utilities, which may be used independently. First, FISSA has fast TIFF reading scripts, using the open source tiff file package. Second, FISSA has a baseline estimator which estimates f_0 as the 5th percentile of the signal after applying a 1 Hz low-pass filter.

Simulated data. The simulated data generation is illustrated in Fig. 6. Each neuron spike train, $s(t)$, is generated by a Poisson process at a given rate. The calcium dynamics for a given cell are modelled as a difference of exponentials

$$\begin{aligned}\frac{dc_d(t)}{dt} &= -\frac{1}{\tau_d}c_d(t) + s(t) \\ \frac{dc_r(t)}{dt} &= -\frac{1}{\tau_r}c_r(t) + s(t) \\ c(t) &= c_d(t) - c_r(t)\end{aligned}\quad (8)$$

where $c_d(t)$ and $c_r(t)$ model the decay and rise dynamics respectively, $c(t)$ the overall calcium dynamics, and τ_r and τ_d the rise and decay time constants respectively. Using the published model of GCaMP6 dynamics^{35,36}, a polynomial non-linearity to model calcium indicator is applied to obtain the measured calcium indicator signal

$$\begin{aligned}d(t) &= \min [c_{\max}, c(t)] \\ f(t) &= A[d(t) + p_2[d(t)^2 - d(t)] + p_3[d(t)^3 - d(t)]]\end{aligned}\quad (9)$$

where A sets the signal change corresponding to a single spike, and p_2 and p_3 are polynomial parameters. The saturation is applied for $c > c_{\max}$, with $c_{\max} = \frac{-2p_2 - \sqrt{4p_2^2 + 12p_3p_2 + F_3 - 1}}{6p_3}$, otherwise the model starts reducing the output fluorescence beyond c_{\max} . Using the average values from³⁶ we set $p_2 = 0.85$, $p_3 = -0.006$, $\tau_r = 0.0156$ s, and $\tau_d = 0.76$ s for model GCaMP6f dynamics, and $p_2 = 0.81$, $p_3 = -0.056$, $\tau_r = 0.0702$ s, and $\tau_d = 1.87$ s for GCaMP6s dynamics. A was set to 0.3%, 2%, and 4% for the central cell, the overlapping cell (Fig. 2C), and the bright localised signal (Fig. 2C) respectively. For Fig. 2 the simulations ran for 120 seconds at 100 Hz. The firing rates were set at 0.5 Hz, and 0.3 Hz for the central cell and the neighbouring cells, respectively (unless otherwise noted). In order to model the effects of stimulus presentation, and to induce correlations between neurons, all firing rates were periodically doubled for a duration of 15 seconds. For predicting calcium traces from the recorded spikes for Fig. 4, the simulations ran at 60 Hz for as long as each original neuron was recorded electrophysiologically, with the electrophysiologically measured spike-times binned at 60 Hz.

This signal $f(t)$ is convolved with a two-dimensional doughnut-shaped spatial kernel given by the difference between two 2D Gaussians plus a step function

$$K(x, y) = \begin{cases} c + \mathcal{S}(\mu, \Sigma) - \mathcal{S}(\mu, \Sigma/2), & \text{if } \mathcal{S}(\mu, \Sigma) - \mathcal{S}(\mu, \Sigma/2) > T \\ \mathcal{S}(\mu, \Sigma) - \mathcal{S}(\mu, \Sigma/2), & \text{otherwise} \end{cases}\quad (10)$$

where $\mathcal{S}(\mu, \Sigma) = \exp\left(-\frac{1}{2}(x - \mu)^T \Sigma^{-1}(x - \mu)\right)$, $\mu = [\mu_x, \mu_y]$ indicates the x and y positions, and $\Sigma = \begin{bmatrix} \sigma^2 & \rho \\ \rho & \sigma^2 \end{bmatrix}$ sets the spatial spread. The offset $c = 0.2$ models the physical structure of a cell soma, the threshold $T = 0.5$ determines its extent, and the Gaussian models the spread of a cell's calcium signal beyond its structure to model cross contamination between nearby structures. $K(x, y)$ was additionally normalized so that $\max(K) = 1$. For Fig. 2 the central cell had $\sigma^2 = 50$ and $\mu_x = \mu_y = 0$ (indicating the middle of the field of view), the overlapping cell had $\sigma^2 = 50$ and $\mu_x = \mu_y = 13$, and the small cell $\sigma^2 = 10$ and $\mu_x = \mu_y = -15$. Unless otherwise noted ρ is always set to 0.

We simulate the background neuropil contamination $B(t)$ as

$$\frac{dB(t)}{dt} = \eta dW(t),\quad (11)$$

where η is a constant (set to 0.05) and $W(t)$ is a Wiener process. A square wave signal of magnitude 0.1 and a period of 15 seconds was also added to simulate stimulus presentation. To vary the background signal spatially, the background signal is convolved with a spatial kernel given by the sum of $M = 10$ Gaussians

$$K_{\text{bg}}(x, y) = \sum_{i=1}^M \exp\left[-\frac{(x - \mu_{xi})^2 + (y - \mu_{yi})^2}{2\sigma_i^2}\right].\quad (12)$$

with $\sigma_i^2 \in [100, 200]$ and μ_{xi}, μ_{yi} give the mean x and y positions which were randomly drawn within the image limits (80 by 80 pixels). Finally, we obtained the calcium response at a given pixel at position x, y and time t as

$$F(x, y, t) = \sum_i K_i(x, y) f_{\text{true},i}(t) + K_{\text{bg}}(x, y) B(t),\quad (13)$$

where the sum over i is across structures. To simulate photon emission, F is used as the rate in a Poisson noise process to generate the final pixel responses. Signals for each ROI are estimated based on the mask

$$M_i(x, y) = \begin{cases} 1, & \text{if } K_i(x, y) > T_{\text{mask}}, \\ 0, & \text{otherwise} \end{cases}\quad (14)$$

where T_{mask} determines its extent (set to 0.5 unless otherwise noted).

Other decontamination methods used to compare FISSA performance. *Neuropil subtraction.* Given a ROI's spatially averaged signal $f_{\text{ROI}}(t)$ and a surrounding neuropil region, the neuropil's spatially averaged signal $f_{\text{npil}}(t)$ was subtracted to give the estimated signal

$$f_{\text{est}}(t) = f_{\text{ROI}}(t) - k f_{\text{npil}}(t), \quad (15)$$

where k is a constant. The value of this constant has been determined manually in previous publications^{3,14}. When analysing our simulated data, we set $k=1$, since this value removed the background fluctuations (Fig. 2A). For the experimental *in vivo* data, we set $k=0.7$, as previously published³. For the neuropil region we used the total surrounding region (all subregions) as defined by the FISSA algorithm.

Constrained non-negative matrix factorization. For details of the cNMF algorithm see the original publication⁹. We applied cNMF to the simulated (Fig. 2) dataset using the `demo_script.m` script from the cNMF toolbox. For the *in vivo* data presented in Figs 4 and 5 the memory usage was much higher than for the simulated dataset due to higher resolution field of views and more frames. We thus performed the analysis in patches, rather than analysing the whole field of view. For this, we used the `run_pipeline.m` script from the cNMF toolbox. cNMF often detected more regions than just the soma of interest. In these cases we chose the region that resulted in the highest performance (highest Pearson correlation values for all subpanels (iii) in Figs 2 and 4B).

***In vivo* calcium imaging data.** All procedures were performed in accordance with the animal care and handling guidelines of the University of Edinburgh animal welfare committee, and were performed under a UK Home Office project license.

For the data in Fig. 5, all surgical and imaging procedures are detailed in our previous publication⁴. Briefly, adeno-associated viruses (AAV1.Syn.GCaMP6f.WPRE.SV40, University of Pennsylvania Vector Core, PA, USA) were locally injected in V1 at three different depths (-50 , -400 , and $-600 \mu\text{m}$) in 8 mice (8- to 10-week-old). The mice were obtained by crossing Cre-driver transgenic mice lines (Sst<tm2.1(cre)Zjh> [RRID:IMSR_JAX:013044] $n=3$, Pvalb<tm1(cre)Arbr> (PV-Cre) [RRID:IMSR_JAX:008069] $n=1$, or Vip<tm1(cre)Zjh> [RRID:IMSR_JAX:010908] $n=4$) with Rosa-CAG-LSL-tdTomato [RRID:IMSR_JAX:007914] mice. All mice were originally obtained from Jackson Laboratory, ME, USA. Mice were group housed (typically 2–4 mice) and both male and female mice were used for the experiments. After 2–3 weeks of expression, the running speed and GCaMP6f signals were simultaneously recorded, during the presentation of drifting gratings (the total visual stimulation times were 720–1200 seconds per imaged field of view⁹). For the results presented in Fig. 5, we did not exclude tdTomato-positive neurons such that all GCaMP6f labelled neurons were included in the analysis.

Motion correction. To perform motion correction for the *in vivo* data presented in Figs 4 and 5 we used the discrete Fourier method from the SIMA toolbox⁸.

Data availability statement. The toolbox described in this paper is available at <https://github.com/rochefort-lab/fissa>.

References

- Huber, D. *et al.* Multiple dynamic representations in the motor cortex during sensorimotor learning. *Nature* **484**, 473–478 (2012).
- Margolis, D. J. *et al.* Reorganization of cortical population activity imaged throughout long-term sensory deprivation. *Nat Neurosci* **15**, 1539–1546 (2012).
- Chen, T. *et al.* Ultrasensitive fluorescent proteins for imaging neuronal activity. *Nature* **499**, 295–300 (2013).
- Pakan, J. *et al.* Behavioural state modulation of inhibition is context-dependent and cell-type specific in mouse V1. *Elife* **5**, e14985 (2016).
- Attinger, A., Wang, B. & Keller, G. Visuomotor coupling shapes the functional development of mouse visual cortex. *Cell* **169**, 1291–1302 (2017).
- Dombeck, D., Khabaz, A., Collman, F., Adelman, T. & Tank, D. Imaging large-scale neural activity with cellular resolution in awake, mobile mice. *Neuron* **56**, 43–57 (2007).
- Greenberg, D. & Kerr, J. Automated correction of fast motion artifacts for two-photon imaging of awake animals. *Journal of Neuroscience Methods* **176**, 1–15 (2009).
- Kaifosh, P., Zaremba, J. D., Danielson, N. B. & Losonczy, A. SIMA: Python software for analysis of dynamic fluorescence imaging data. *Frontiers in neuroinformatics* **8** (2014).
- Pnevmatikakis, E. A. *et al.* Simultaneous Denoising, Deconvolution, and Demixing of Calcium Imaging Data. *Neuron* **89**, 285–299 (2015).
- Muir, D., Roth, M., Helmchen, F. & Kampa, B. Model-based analysis of pattern motion processing in mouse primary visual cortex. *Frontiers in neural circuits* **9** (2015).
- Pachitariu, M. *et al.* Suite2p: beyond 10,000 neurons with standard two-photon microscopy. *bioRxiv*, <https://doi.org/10.1101/061507> (2016).
- Dubbs, A., Guevara, J. & Yuste, R. moCo: Fast motion correction for calcium imaging. *Frontiers in Neuroinformatics* **10** (2016).
- Pnevmatikakis, E. & Giovannucci, A. NormCorre: An online algorithm for piecewise rigid motion correction of calcium imaging data. *bioRxiv*, <https://doi.org/10.1101/108514> (2017).
- Peron, S., Freeman, J., Iyer, V., Guo, C. & Svoboda, K. A cellular resolution map of barrel cortex activity during tactile behavior. *Neuron* **86**, 783–799 (2015).
- Maruyama, R. *et al.* Detecting cells using non-negative matrix factorization on calcium imaging data. *Neural Networks* **55**, 11–19 (2014).
- Diego, F. & Hamprecht, F. Sparse space-time deconvolution for calcium image analysis. *NIPS* **27**, 64–72 (2014).
- Apthorpe, N. *et al.* Automatic neuron detection in calcium imaging data using convolutional networks. *NIPS* **29** (2016).
- Mukamel, E. A., Nimmerjahn, A. & Schnitzer, M. J. Automated Analysis of Cellular Signals from Large-Scale Calcium Imaging Data. *Neuron* **63**, 747–760 (2009).
- Peron, S., Chen, T. & Svoboda, K. Comprehensive imaging of cortical networks. *Current opinion in neurobiology* **32**, 115–123 (2015).

20. Stetter, M. *et al.* Principal component analysis and blind separation of sources for optical imaging of intrinsic signals. *NeuroImage* **11**, 482–490 (2000).
21. Ji, N., Sato, T. & Betzig, E. Characterization and adaptive optical correction of aberrations during *in vivo* imaging in the mouse cortex. *PNAS* **109**, 22–27 (2012).
22. Cichocki, A. & Anh-Huy, P. H. A. N. Fast local algorithms for large scale nonnegative matrix and tensor factorizations. *IEICE transactions on fundamentals of electronics, communications and computer sciences* **92**, 708–721 (2009).
23. Langville, A. N., Meyer, C. D., Albright, R., Cox, J. & Duling, D. Algorithms, initializations, and convergence for the nonnegative matrix factorization. *arXiv 1407.7299* (2014).
24. Svoboda, H. K. Simultaneous imaging and loose-seal cell-attached electrical recordings from neurons expressing a variety of genetically encoded calcium indicators. *GENIE project, Janelia Farm Campus, CRCNS.org* (2015).
25. Niell, C. M. & Stryker, M. P. Modulation of visual responses by behavioral state in mouse visual cortex. *Neuron* **65**, 472–479 (2010).
26. Keller, G., Bonhoeffer, T. & Hübener, M. Sensorimotor mismatch signals in primary visual cortex of the behaving mouse. *Neuron* **74**, 809–815 (2012).
27. Ayaz, A., Saleem, A., Schölvink, M. & Carandini, M. Locomotion controls spatial integration in mouse visual cortex. *Current Biology* **23**, 890–894 (2013).
28. Erisken, S. *et al.* Effects of locomotion extend throughout the mouse early visual system. *Current Biology* **24**, 2899–2907 (2014).
29. Fu, Y. *et al.* A cortical circuit for gain control by behavioral state. *Cell* **156**, 1139–1152 (2014).
30. Dadarlat, M. & Stryker, M. Locomotion enhances neural encoding of visual stimuli in mouse v1. *Journal of Neuroscience* **37**, 3764–3775 (2017).
31. Friedrich, J. *et al.* Multi-scale approaches for high-speed imaging and analysis of large neural populations. *PLoS Comput Biol* **13** (2017).
32. Pedregosa, F. *et al.* Scikit-learn: Machine learning in Python. *Journal of Machine Learning Research* **12**, 2825–2830 (2011).
33. Lin, C. Projected gradient methods for non-negative matrix factorization. *Neural Computation* **19**, 2756–2779 (2007).
34. Boutsidis, C. & Gallopoulos, E. Svd based initialization: A head start for nonnegative matrix factorization. *Pattern Recognition* **41**, 1350–1362 (2008).
35. Akerboom, J. *et al.* Optimization of a GCaMP Calcium Indicator for Neural Activity Imaging. *The Journal of Neuroscience* **32**, 13819–13840 (2012).
36. Deneux, T. *et al.* Accurate spike estimation from noisy calcium signals for ultrafast three-dimensional imaging of large neuronal populations *in vivo*. *Nature Communications* **7** (2016).

Acknowledgements

This work was funded by the BBSRC grant BB/N023161/1 to M.v.R. and N.R., by the Wellcome Trust and the Royal Society (Sir Henry Dale fellowship to N.R.), the Marie Curie Actions of the European Union's FP7 program (MC-CIG 631770 to N.R. and IEF 624461 to J.P.), the Shirley Foundation, the Patrick Wild Center, the RS MacDonald Charitable Trust Seedcorn Grant, the Simons Initiative for the Developing Brain (to N.R.), and the Graduate School of Life Sciences, University of Edinburgh (to E.D.). S.K. was supported by the EuroSpin Erasmus Mundus program and S.K. and S.L. were funded by the EPSRC Doctoral Training Centre in Neuroinformatics (EP/F500386/1 and BB/F529254/1).

Author Contributions


N.R. and S.K. designed the project. S.K. and S.L. were jointly responsible for coding the toolbox. J.P., E.D., and N.R. acquired and analysed the *in vivo* data. S.K., J.P., N.R. and E.D. tested the different versions of the toolbox and provided feedback on the results. S.K., M.v.R., and N.R. wrote the paper, with input from all authors.

Additional Information

Supplementary information accompanies this paper at <https://doi.org/10.1038/s41598-018-21640-2>.

Competing interests: The authors declare no competing interests.

Publisher's note: Springer Nature remains neutral with regard to jurisdictional claims in published maps and institutional affiliations.

 **Open Access** This article is licensed under a Creative Commons Attribution 4.0 International License, which permits use, sharing, adaptation, distribution and reproduction in any medium or format, as long as you give appropriate credit to the original author(s) and the source, provide a link to the Creative Commons license, and indicate if changes were made. The images or other third party material in this article are included in the article's Creative Commons license, unless indicated otherwise in a credit line to the material. If material is not included in the article's Creative Commons license and your intended use is not permitted by statutory regulation or exceeds the permitted use, you will need to obtain permission directly from the copyright holder. To view a copy of this license, visit <http://creativecommons.org/licenses/by/4.0/>.

© The Author(s) 2018

BIBLIOGRAPHY

- [1] I. D. Abella. "Optical double-photon absorption in cesium vapor." In: *Physical Review Letters* 9.11 (1962), pp. 453–455. ISSN: 00319007. DOI: [10.1103/PhysRevLett.9.453](https://doi.org/10.1103/PhysRevLett.9.453).
- [2] Stephen R. Adams. "How calcium indicators work." In: *Cold Spring Harbor Protocols* 5.3 (2010), pp. 1–6. ISSN: 15596095. DOI: [10.1101/pdb.top70](https://doi.org/10.1101/pdb.top70).
- [3] Walther Akemann, Hiroki Mutoh, Amelie Perron, Jean Rossier, and Thomas Knöpfel. "Imaging brain electric signals with genetically targeted voltage-sensitive fluorescent proteins." In: *Nature Methods* 7.8 (2010), pp. 643–649. ISSN: 15487091. DOI: [10.1038/nmeth.1479](https://doi.org/10.1038/nmeth.1479).
- [4] Henry J. Alitto and Yang Dan. "Cell-type-specific modulation of neocortical activity by basal forebrain input." In: *Frontiers in Systems Neuroscience* 6 (2013), pp. 1–12. ISSN: 1662-5137. DOI: [10.3389/fnsys.2012.00079](https://doi.org/10.3389/fnsys.2012.00079).
- [5] Mark L. Andermann, Aaron M. Kerlin, Demetris K. Roumis, Lindsey L. Glickfeld, and R. Clay Reid. "Functional specialization of mouse higher visual cortical areas." In: *Neuron* 72.6 (2010), pp. 1025–1039. ISSN: 08966273. DOI: [10.1016/j.neuron.2011.11.013](https://doi.org/10.1016/j.neuron.2011.11.013).
- [6] Antonella Antonini and Michael P. Stryker. "Rapid remodeling of axonal arbors in the visual cortex." In: *Science* 260 (1993). DOI: [10.1126/science.8511592](https://doi.org/10.1126/science.8511592).
- [7] Ryo Aoki, Tadashi Tsubota, Yuki Goya, and Andrea Benucci. "An automated platform for high-throughput mouse behavior and physiology with voluntary head-fixation." In: *Nature Communications* 8.1 (2017), p. 1196. ISSN: 2041-1723. DOI: [10.1038/s41467-017-01371-0](https://doi.org/10.1038/s41467-017-01371-0).
- [8] Yoichi Araki, Menglong Zeng, Mingjie Zhang, and Richard L. Huganir. "Rapid dispersion of SynGAP from synaptic spines triggers AMPA receptor insertion and spine enlargement during LTP." In: *Neuron* 85.1 (2015), pp. 173–190. ISSN: 10974199. DOI: [10.1016/j.neuron.2014.12.023](https://doi.org/10.1016/j.neuron.2014.12.023).
- [9] B. N. Armbruster, X. Li, M. H. Pausch, S. Herlitze, and B. L. Roth. "Evolving the lock to fit the key to create a family of G protein-coupled receptors potently activated by an inert ligand." In: *Proceedings of the National Academy of Sciences* 104.12 (2007), pp. 5163–5168. ISSN: 0027-8424. DOI: [10.1073/pnas.0700293104](https://doi.org/10.1073/pnas.0700293104).
- [10] Sergio Arroyo, Corbett Bennett, and Shaul Hestrin. "Nicotinic modulation of cortical circuits." In: *Frontiers in Neural Circuits* 8.30 (2014), pp. 1–6. ISSN: 1662-5110. DOI: [10.3389/fncir.2014.00030](https://doi.org/10.3389/fncir.2014.00030).

- [11] Bassam V. Atallah, Massimo Scanziani, and Matteo Carandini. "Interneuron subtypes and orientation tuning." In: *Nature* 508.1 (2014), pp. 2012–2015. ISSN: 14764687. DOI: [10.1038/nature13129](https://doi.org/10.1038/nature13129).
- [12] Bassam V. Atallah, William Bruns, Matteo Carandini, and Massimo Scanziani. "Parvalbumin-expressing interneurons linearly transform cortical responses to visual stimuli." In: *Neuron* 73.1 (2012), pp. 159–170. ISSN: 08966273. DOI: [10.1016/j.neuron.2011.12.013](https://doi.org/10.1016/j.neuron.2011.12.013).
- [13] D. Atasoy, Y. Aponte, H. H. Su, and S. M. Sternson. "A FLEX switch targets channelrhodopsin-2 to multiple cell types for imaging and long-range circuit mapping." In: *Journal of Neuroscience* 28.28 (2008), pp. 7025–7030. ISSN: 0270-6474. DOI: [10.1523/JNEUROSCI.1954-08.2008](https://doi.org/10.1523/JNEUROSCI.1954-08.2008).
- [14] Coleen M. Atkins, Joel C. Selcher, Joseph J. Petraitis, James M. Trzaskos, and J. David Sweatt. "The MAPK cascade is required for mammalian associative learning." In: *Nature neuroscience* 1.7 (1998), pp. 602–609. ISSN: 1097-6256. DOI: [10.1038/2836](https://doi.org/10.1038/2836).
- [15] Sara J. Aton, Aneesha Suresh, Christopher Broussard, and Marcos G. Frank. "Sleep promotes cortical response potentiation following visual experience." In: *Sleep* 37.7 (2014), pp. 1163–1170. ISSN: 0161-8105. DOI: [10.5665/sleep.3830](https://doi.org/10.5665/sleep.3830).
- [16] A. Bailey, A Le Couteur, I Gottesman, P Bolton, E Simonoff, E Yuzuda, and M Rutter. "Autism as a strongly genetic disorder: evidence from a British twin study." In: *Psychol Med* 25.1 (1995), pp. 63–77.
- [17] Ce Bakker, C Verheij, R Willemsen, R van der Helm, F Oerlemans, M Vermeij, A Bygrave, At Hoogeveen, E Reyniers, K De Boule, R D'Hooge, P Cras, D van Velzen, G Nagels, Jj Martin, Pp De Deyn, Jk Darby, Ba Oostra, and Pj Willems. "Fmrl Knockout Mice : A Model to Study Fragile X Mental Retardation." In: *Cell* 78.1 (1994), pp. 23–33. ISSN: 00928674. DOI: [10.1016/0092-8674\(94\)90569-X](https://doi.org/10.1016/0092-8674(94)90569-X).
- [18] Shaowen Bao, Vincent T. Chan, and Michael M. Merzenich. "Cortical remodeling induced by activity of ventral tegmental dopamine neurons." In: *Nature* 412.6842 (2001), pp. 79–83. ISSN: 00280836. DOI: [10.1038/35083586](https://doi.org/10.1038/35083586).
- [19] Samuel J. Barnes, Rosanna P. Sammons, R. Irene Jacobsen, Jennifer Mackie, Georg B. Keller, and Tara Keck. "Subnetwork-specific homeostatic plasticity in mouse visual cortex in vivo." In: *Neuron* 86.5 (2015), pp. 1290–1303. ISSN: 10974199. DOI: <https://doi.org/10.1016/j.neuron.2015.05.010>.
- [20] Stephanie A. Barnes, Lasani S. Wijetunge, Adam D. Jackson, Danai Katsanavaki, Emily K. Osterweil, Noboru H. Komiyama, Seth G. N. Grant, Mark F. Bear, U. Valentin Nagerl, Peter C. Kind, and David J. A. Wyllie. "Convergence of Hippocampal Pathophysiology in Syngap^{+/-} and Fmr1^{-/y} Mice."

- In: *Journal of Neuroscience* 35.45 (2015), pp. 15073–15081. ISSN: 0270-6474. DOI: [10.1523/JNEUROSCI.1087-15.2015](https://doi.org/10.1523/JNEUROSCI.1087-15.2015).
- [21] Corbett Bennett, Sergio Arroyo, and Shaul Hestrin. “Controlling brain states.” In: *Neuron* 83.2 (2014), pp. 260–261. ISSN: 10974199. DOI: [10.1016/j.neuron.2014.07.007](https://doi.org/10.1016/j.neuron.2014.07.007).
- [22] Corbett Bennett, Sergio Arroyo, and Shaul Hestrin. “Subthreshold mechanisms underlying state-dependent modulation of visual responses.” In: *Neuron* 80.2 (2013), pp. 350–357. ISSN: 08966273. DOI: [10.1016/j.neuron.2013.08.007](https://doi.org/10.1016/j.neuron.2013.08.007).
- [23] Martin H. Berryer, Bidisha Chattopadhyaya, Paul Xing, Ilse Riebe, Ciprian Bosoi, Nathalie Sanon, Judith Antoine-Bertrand, Maxime Lévesque, Massimo Avoli, Fadi F. Hamdan, Lionel Carmant, Nathalie Lamarche-Vane, Jean-Claude Lacaille, Jacques L. Michaud, and Graziella Di Cristo. “Decrease of SYNGAP1 in GABAergic cells impairs inhibitory synapse connectivity, synaptic inhibition and cognitive function.” In: *Nature Communications* 7 (2016), pp. 1–14. ISSN: 2041-1723. DOI: [10.1038/ncomms13340](https://doi.org/10.1038/ncomms13340).
- [24] Guoqiang Bi and Muming Poo. “Synaptic modifications in cultured hippocampal neurons: dependence on spike timing, synaptic strength, and postsynaptic cell type.” In: *The Journal of Neuroscience* 18.24 (1998), pp. 10464–10472. ISSN: 0270-6474. DOI: [10.1038/25665](https://doi.org/10.1038/25665).
- [25] Colin Blakemore and Grahame F. Cooper. “Development of the brain depends on the visual environment.” In: *Nature* 228.24 (1970), pp. 361–362.
- [26] Colin Blakemore and Richard C. V. Sluyters. “Innate and environmental factors in the development of the kittens visual cortex.” In: (1975), pp. 663–716.
- [27] Tobias Bonhoeffer and Amiram Grinvald. “Iso-orientation domains in cat visual cortex are arranged in pinwheel-like patterns.” In: *Nature* 353.6343 (1991), pp. 429–431. ISSN: 0028-0836. DOI: [10.1038/353429a0](https://doi.org/10.1038/353429a0).
- [28] David H. Brainard. “The Psychophysics Toolbox.” In: *Spatial Vision* 10.4 (1997), pp. 433–436. ISSN: 01691015. DOI: [10.1163/156856897X00357](https://doi.org/10.1163/156856897X00357).
- [29] Jianhua Cang, Rene C. Renteria, Megumi Kaneko, Xiaorong Liu, David R. Copenhagen, and Michael P. Stryker. “Development of precise maps in visual cortex requires patterned spontaneous activity in the retina.” In: *Neuron* 48.5 (2005), pp. 797–809. DOI: [10.1016/j.neuron.2005.09.015](https://doi.org/10.1016/j.neuron.2005.09.015).
- [30] Jessica A. Cardin, Marie Carlen, Konstantinos Meletis, Ulf Knoblich, Feng Zhang, Karl Deisseroth, Li-Huei Tsai, and Christopher I. Moore. “Driving fast-spiking cells induces gamma rhythm and controls sensory responses.” In: *Nature* 459.7247 (2009), pp. 663–668. ISSN: 1476-4687. DOI: [10.1038/nature08002](https://doi.org/10.1038/nature08002).

- [31] Holly J. Carlisle, Pasquale Manzerra, Edoardo Marcora, and Mary B. Kennedy. "SynGAP Regulates Steady-State and Activity-Dependent Phosphorylation of Cofilin." In: *Journal of Neuroscience* 28.50 (2008), pp. 13673–13683. ISSN: 0270-6474. DOI: [10.1523/JNEUROSCI.4695-08.2008](https://doi.org/10.1523/JNEUROSCI.4695-08.2008).
- [32] Pico Caroni, Flavio Donato, and Dominique Muller. "Structural plasticity upon learning: Regulation and functions." In: *Nature Reviews Neuroscience* 13.7 (2012), pp. 478–490. DOI: [10.1038/nrn3258](https://doi.org/10.1038/nrn3258).
- [33] Gemma L. Carvill et al. "Targeted resequencing in epileptic encephalopathies identifies de novo mutations in CHD2 and SYNGAP1." In: *Nature Genetics* 45.7 (2013), pp. 825–830. ISSN: 10614036. DOI: [10.1038/ng.2646](https://doi.org/10.1038/ng.2646). URL: [g.2646](https://www.nature.com/articles/ng.2646).
- [34] Hong Jung Chen, Michelle Rojas-Soto, Asako Oguni, and Mary B. Kennedy. "A synaptic Ras-GTPase activating protein (p135 SynGAP) inhibited by CaM kinase II." In: *Neuron* 20.5 (1998), pp. 895–904. ISSN: 08966273. DOI: [10.1016/S0896-6273\(00\)80471-7](https://doi.org/10.1016/S0896-6273(00)80471-7).
- [35] Tsai-Wen Chen, Trevor J. Wardill, Yi Sun, Stefan R. Pulver, Sabine L. Renninger, Amy Baohan, Eric R. Schreiter, Rex A. Kerr, Michael B. Orger, Vivek Jayaraman, Loren L. Looger, Karel Svoboda, and Douglas S. Kim. "Ultrasensitive fluorescent proteins for imaging neuronal activity." In: *Nature* 499.7458 (2013), pp. 295–300. ISSN: 1476-4687. DOI: [10.1038/nature12354](https://doi.org/10.1038/nature12354). eprint: [arXiv:1011.1669v3](https://arxiv.org/abs/1011.1669v3).
- [36] Xiaowei Chen, Ulrich Leischner, Zsuzsanna Varga, Hongbo Jia, Diana Deca, Nathalie L. Rochefort, and Arthur Konnerth. "LOTOS-based two-photon calcium imaging of dendritic spines in vivo." In: *Nature Protocols* 7.10 (2012), pp. 1818–29. ISSN: 1750-2799. DOI: [10.1038/nprot.2012.106](https://doi.org/10.1038/nprot.2012.106).
- [37] Alexander A. Chubykin, Emma B. Roach, Mark F. Bear, and Marshall G. Hussain Shuler. "A cholinergic mechanism for reward timing within primary visual cortex." In: *Neuron* 77.4 (2013), pp. 723–735. ISSN: 08966273. DOI: [10.1016/j.neuron.2012.12.039](https://doi.org/10.1016/j.neuron.2012.12.039).
- [38] James P. Clement, Massimiliano Aceti, Thomas K. Creson, Emin D. Ozkan, Yulin Shi, Nicholas J. Reish, Antoine G. Almonte, Brooke H. Miller, Brian J. Wiltgen, Courtney A. Miller, Xiangmin Xu, and Gavin Rumbaugh. "Pathogenic SYNGAP1 mutations impair cognitive development by disrupting maturation of dendritic spine synapses." In: *Cell* 151.4 (2012), pp. 709–723. DOI: [10.1016/j.cell.2012.08.045](https://doi.org/10.1016/j.cell.2012.08.045).
- [39] James P. Clement, Emin D. Ozkan, Massimiliano Aceti, Courtney A. Miller, and Gavin Rumbaugh. "SYNGAP1 Links the maturation rate of excitatory synapses to the duration of critical-period synaptic plasticity." In: *Journal of Neuroscience* 33.25 (2013), pp. 10447–10452. ISSN: 0270-6474. DOI: [10.1523/JNEUROSCI.0765-13.2013](https://doi.org/10.1523/JNEUROSCI.0765-13.2013).

- [40] Christine M. Constantinople and Randy M. Bruno. "Deep cortical layers are activated directly by thalamus." In: *Science* 340 (2013), pp. 1591–1594. DOI: [10.1126/science.1236425](https://doi.org/10.1126/science.1236425).
- [41] Sam F. Cooke and Mark F. Bear. "How the mechanisms of long-term synaptic potentiation and depression serve experience-dependent plasticity in primary visual cortex." In: *Philosophical transactions of the Royal Society of London. Series B, Biological sciences* 369 (2014), pp. 1–12. DOI: [10.1098/rstb.2013.0284](https://doi.org/10.1098/rstb.2013.0284).
- [42] Sam F. Cooke and Mark F. Bear. "Visual experience induces long-term potentiation in the primary visual cortex." In: *J Neurosci* 30.48 (2010), pp. 16304–16313. ISSN: 0270-6474. DOI: [10.1523/JNEUROSCI.4333-10.2010](https://doi.org/10.1523/JNEUROSCI.4333-10.2010).
- [43] Sam F. Cooke, Robert W. Komorowski, Eitan S. Kaplan, Jeffrey P. Gavnornik, and Mark F. Bear. "Visual recognition memory, manifested as long-term habituation, requires synaptic plasticity in V1." In: *Nature neuroscience* 18.2 (2015), pp. 262–271. ISSN: 1097-6256. DOI: [10.1038/nn.3920](https://doi.org/10.1038/nn.3920).
- [44] R. James Cotton, Emmanouil Froudarakis, Patrick Storer, Peter Saggau, and Andreas S. Tolias. "Three-dimensional mapping of microcircuit correlation structure." In: *Frontiers in Neural Circuits* 7.October (2013), pp. 1–13. ISSN: 1662-5110. DOI: [10.3389/fncir.2013.00151](https://doi.org/10.3389/fncir.2013.00151).
- [45] M Cynader and D E. Mitchell. "Prolonged sensitivity to monocular deprivation in dark-reared cats." In: *Journal of Neurophysiology* 43.4 (1980).
- [46] Maria C. Dadarlat and Michael P. Stryker. "Locomotion enhances neural encoding of visual stimuli in mouse V1." In: 37.14 (2017), pp. 3764–3775. ISSN: 0270-6474. DOI: [10.1101/102673](https://doi.org/10.1101/102673).
- [47] Marco Dal Maschio, Angela Michela De Stasi, Fabio Benfenati, and Tommaso Fellin. "Three-dimensional in vivo scanning microscopy with inertia-free focus control." In: *Optics Letters* 36.17 (2011), p. 3503. ISSN: 0146-9592. DOI: [10.1364/OL.36.003503](https://doi.org/10.1364/OL.36.003503).
- [48] Hod Dana, Boaz Mohar, Yi Sun, Sujatha Narayan, Andrew Gordus, Jeremy P. Hasseman, Getahun Tsegaye, Graham T. Holt, Amy Hu, Deepika Walpita, Ronak Patel, John J. Macklin, Cornelia I. Bargmann, Misha B. Ahrens, Eric R. Schreier, Vivek Jayaraman, Loren L. Looger, Karel Svoboda, and Douglas S. Kim. "Sensitive red protein calcium indicators for imaging neural activity." In: *eLife* 5 (2016). ISSN: 2050084X. DOI: [10.7554/eLife.12727](https://doi.org/10.7554/eLife.12727).
- [49] Corinna Darian-Smith and Charles D. Gilbert. "Axonal sprouting accompanies functional reorganization in adult cat striate cortex." In: *Nature* 368.6473 (1994), pp. 737–740. ISSN: 0028-0836. DOI: [10.1038/368737a0](https://doi.org/10.1038/368737a0).
- [50] Aniruddha Das and Charles D. Gilbert. *Long-range horizontal connections and their role in cortical reorganization revealed by optical recording of cat primary visual cortex*. 1995. DOI: [10.1038/375780a0](https://doi.org/10.1038/375780a0).

- [51] Karl Deisseroth. "Optogenetics." In: *Nature Methods* 8.1 (2011), pp. 26–29. ISSN: 1548-7091. DOI: [10.1038/nmeth.f.324](https://doi.org/10.1038/nmeth.f.324).
- [52] Thomas Deneux, Attila Kaszas, Gergely Szalay, Gergely Katona, Tamas Lakner, Amiram Grinvald, Balazs Rozsa, and Ivo Vanzetta. "Accurate spike estimation from noisy calcium signals for ultrafast three-dimensional imaging of large neuronal populations in vivo." In: *Nature Communications* 7 (2016), pp. 1–17. DOI: [10.1038/ncomms12190](https://doi.org/10.1038/ncomms12190).
- [53] Winfried Denk. "Principles of multiphoton-excitation fluorescence microscopy." In: *Cold Spring Harbor Protocols* 10 (2007). DOI: [10.1101/pdb.top23](https://doi.org/10.1101/pdb.top23).
- [54] Winfried Denk, David W. Piston, and Watt W. Webb. "Multi-photon molecular excitation in laser-scanning microscopy." In: *Handbook of Biological Confocal Microscopy: Third Edition* (2006), pp. 535–549. DOI: [10.1007/978-0-387-45524-2_28](https://doi.org/10.1007/978-0-387-45524-2_28).
- [55] Winfried Denk, James H. Strickler, and Watt W. Webb. "Two-photon laser scanning fluorescence microscopy." In: *Science* 248 (1990), pp. 73–76. DOI: [10.1126/science.2321027](https://doi.org/10.1126/science.2321027).
- [56] Winfried Denk and Karel Svoboda. "Photon upmanship: Why multiphoton imaging is more than a gimmick." In: *Neuron* 18.3 (1997), pp. 351–357. ISSN: 08966273. DOI: [10.1016/S0896-6273\(00\)81237-4](https://doi.org/10.1016/S0896-6273(00)81237-4).
- [57] Claire L. Dent, Anthony R. Isles, and Trevor Humby. "Measuring risk-taking in mice: Balancing the risk between seeking reward and danger." In: *European Journal of Neuroscience* 39.4 (2014), pp. 520–530. ISSN: 0953816X. DOI: [10.1111/ejn.12430](https://doi.org/10.1111/ejn.12430).
- [58] Graziella Di Cristo, Nicoletta Berardi, Laura Cancedda, Tommaso Pizzorusso, Elena Putignano, Gina M. Ratto, and Lamberto Maffei. "Requirement of ERK activation for visual cortical plasticity." In: *Science* 292.5525 (2001), pp. 2337–40. ISSN: 0036-8075. DOI: [10.1126/science.1059075](https://doi.org/10.1126/science.1059075).
- [59] Dimitar Dimitrov, You He, Hiroki Mutoh, Bradley J. Baker, Lawrence Cohen, Walther Akermann, and Thomas Knöpfel. "Engineering and characterization of an enhanced fluorescent protein voltage sensor." In: *PLoS ONE* 2.5 (2007), pp. 2–6. ISSN: 19326203. DOI: [10.1371/journal.pone.0000440](https://doi.org/10.1371/journal.pone.0000440).
- [60] JingJin J. Ding, Andrew F. Luo, LiYan Y. Hu, DaCheng C. Wang, and Feng Shao. "Structural basis of the ultrasensitive calcium indicator GCaMP6." In: *Science China Life Sciences* 57.3 (2014), pp. 269–274. ISSN: 16747305. DOI: [10.1007/s11427-013-4599-5](https://doi.org/10.1007/s11427-013-4599-5).
- [61] Daniel A. Dombeck, Anton N. Khabbaz, Forrest Collman, Thomas L. Adelman, and David W. Tank. "Imaging large-scale neural activity with cellular resolution in awake, mobile mice." In: *Neuron* 56.1 (2007), pp. 43–57. ISSN: 08966273. DOI: [10.1016/j.neuron.2007.08.003](https://doi.org/10.1016/j.neuron.2007.08.003).

- [62] Ursula C. Drager. "Receptive fields of single cells and topography in mouse visual cortex." In: *The Journal of Comparative Neurology* 160.3 (1975), pp. 269–290. ISSN: 0021-9967 (Print). DOI: [10.1002/cne.901600302](https://doi.org/10.1002/cne.901600302).
- [63] Florian Engert and Tobias Bonhoeffer. "Dendritic spine changes associated with hippocampal long-term synaptic plasticity." In: *Nature* 399.6731 (1999), pp. 66–70. DOI: [10.1038/19978](https://doi.org/10.1038/19978).
- [64] Sinem Erisken, Agne Vaiceliunaite, Ovidiu Jurjut, Matilde Fiorini, Steffen Katzner, and Laura Busse. "Effects of locomotion extend throughout the mouse early visual system." In: *Current Biology* 24.24 (2014), pp. 2899–2907. ISSN: 09609822. DOI: [10.1016/j.cub.2014.10.045](https://doi.org/10.1016/j.cub.2014.10.045).
- [65] J. Sebastian Espinosa and Michael P. Stryker. "Development and plasticity of the primary visual cortex." In: *Neuron* 75.2 (2012), pp. 230–49. ISSN: 1097-4199. DOI: [10.1016/j.neuron.2012.06.009](https://doi.org/10.1016/j.neuron.2012.06.009).
- [66] Michela Fagiolini and Takao K. Hensch. "Inhibitory threshold for critical-period activation in primary visual cortex Critical period." In: 674.1991 (2000), pp. 5–8.
- [67] Michela Fagiolini, Tommaso Pizzorusso, Nicoletta Beraadi, Luciano Domenici, and Lamberto Maffei. "Functional postnatal development of the rat primary visual cortex and the role of visual experience : dark rearing and monocular deprivation." In: 34.6 (1994), pp. 709–720.
- [68] Michela Fagiolini, Hiroyuki Katagiri, Hiroyuki Miyamoto, Hisashi Mori, Seth G. N. Grant, Masayoshi Mishina, and Takao K. Hensch. "Separable features of visual cortical plasticity revealed by N-methyl-D-aspartate receptor 2A signaling." In: *Proceedings of the National Academy of Sciences of the United States of America* 100.5 (2003), pp. 2854–2859. ISSN: 00278424. DOI: [10.1073/pnas.0536089100](https://doi.org/10.1073/pnas.0536089100).
- [69] Joshua Faguet, Bruno Maranhao, Spencer L. Smith, and Joshua T. Trachtenberg. "Ipsilateral eye cortical maps are uniquely sensitive to binocular plasticity." In: *Journal of Neurophysiology* 101.2 (2008), pp. 855–861. ISSN: 0022-3077. DOI: [10.1152/jn.90893.2008](https://doi.org/10.1152/jn.90893.2008).
- [70] Marc Fakhoury. "Autistic spectrum disorders: A review of clinical features, theories and diagnosis." In: *International Journal of Developmental Neuroscience* 43 (2015), pp. 70–77. ISSN: 1873474X. DOI: [10.1016/j.ijdevneu.2015.04.003](https://doi.org/10.1016/j.ijdevneu.2015.04.003).
- [71] Erika E. Fanselow, Kristen A. Richardson, and Barry W. Connors. "Selective, state-dependent activation of somatostatin-expressing inhibitory interneurons in mouse neocortex." In: *Journal of Neurophysiology* 100.5 (2008), pp. 2640–2652. ISSN: 0022-3077. DOI: [10.1152/jn.90691.2008](https://doi.org/10.1152/jn.90691.2008).

- [72] Jose Fernando, Maya Vetencourt, Alessandro Sale, Alessandro Viegi, Laura Baroncelli, Roberto De Pasquale, Olivia F. O. Leary, Eero Castren, and Lamberto Maffei. "The antidepressant fluoxetine restores plasticity in the adult visual cortex." In: *Science* 510 (2008), pp. 385–389. DOI: [10.1126/science.1150516](https://doi.org/10.1126/science.1150516).
- [73] A Fiorentini and N Berardi. *Perceptual learning specific for orientation and spatial frequency*. 1980. DOI: [10.1038/287043a0](https://doi.org/10.1038/287043a0).
- [74] Aris Fiser, David Mahringer, Hassana K. Oyibo, Anders V. Petersen, Marcus Leinweber, and Georg B. Keller. "Experience-dependent spatial expectations in mouse visual cortex." In: *Nature Neuroscience* 19.12 (2016), pp. 1658–1664. ISSN: 1097-6256. DOI: [10.1038/nn.4385](https://doi.org/10.1038/nn.4385).
- [75] Benjamin A. Flusberg, Eric D. Cocker, Wibool Piyawattanametha, Juergen C. Jung, Eunice L.M. Cheung, and Mark J. Schnitzer. "Fiber-optic fluorescence imaging." In: *Nature Methods* 2.12 (2005), pp. 941–950. ISSN: 15487091. DOI: [10.1038/nmeth820](https://doi.org/10.1038/nmeth820).
- [76] Yves Frégnac, Daniel Shulz, Simon Thorpe, and Elie Bienenstock. "A cellular analogue of visual cortical plasticity." In: *Nature* 333.6171 (1988), pp. 367–370. ISSN: 0028-0836. DOI: [10.1038/333367a0](https://doi.org/10.1038/333367a0).
- [77] Mikhail Y. Frenkel and Mark F. Bear. "How monocular deprivation shifts ocular dominance in visual cortex of young mice." In: *Neuron* 44.6 (2004), pp. 917–923. ISSN: 08966273. DOI: [10.1016/j.neuron.2004.12.003](https://doi.org/10.1016/j.neuron.2004.12.003).
- [78] Mikhail Y. Frenkel, Nathaniel B. Sawtell, Antonia Cinira M. Diogo, Bongjune Yoon, Rachael L. Neve, and Mark F. Bear. "Instructive effect of visual experience in mouse visual cortex." In: *Neuron* 51.3 (2006), pp. 339–349. ISSN: 08966273. DOI: [10.1016/j.neuron.2006.06.026](https://doi.org/10.1016/j.neuron.2006.06.026).
- [79] Johannes Friedrich, Pengcheng Zhou, and Liam Paninski. "Fast online deconvolution of calcium imaging data." In: *PLoS Computational Biology* 13.3 (2017), pp. 1–26. DOI: [10.1371/journal.pcbi.1005423](https://doi.org/10.1371/journal.pcbi.1005423).
- [80] Robert C. Froemke and Yang Dan. "Spike-timing-dependent synaptic modification induced by natural spike trains." In: *Nature* 416.6879 (2002), pp. 433–438. ISSN: 00280836. DOI: [10.1038/416433a](https://doi.org/10.1038/416433a).
- [81] Yu Fu, Jason M. Tucciarone, J. Sebastian Espinosa, Nengyin Sheng, Daniel P. Darcy, Roger A. Nicoll, Z. Josh Huang, and Michael P. Stryker. "A cortical circuit for gain control by behavioral state." In: *Cell* 156.6 (2014), pp. 1139–1152. ISSN: 10974172. DOI: [10.1016/j.cell.2014.01.050](https://doi.org/10.1016/j.cell.2014.01.050).
- [82] Yu Fu, Megumi Kaneko, Yunshuo Tang, Arturo Alvarez-Buylla, and Michael P. Stryker. "A cortical disinhibitory circuit for enhancing adult plasticity." In: *eLife* 2015.4 (2015), pp. 1–12. ISSN: 2050084X. DOI: [10.7554/eLife.05558](https://doi.org/10.7554/eLife.05558).

- [83] Christopher S. Furmanski, Denis Schluppeck, and Stephen A. Engel. "Learning strengthens the response of primary visual cortex to simple patterns." In: *Canadian Field-Naturalist* 128.2 (2014), pp. 189–190. ISSN: 00083550. DOI: [10.1016/j.cfn.2014.05.001](https://doi.org/10.1016/j.cfn.2014.05.001).
- [84] Laetitia Gabernet, Shantanu P. Jadhav, Daniel E. Feldman, Matteo Carandini, and Massimo Scanziani. "Somatosensory integration controlled by dynamic thalamocortical feed-forward inhibition." In: *Neuron* 48.2 (2005), pp. 315–327. ISSN: 08966273. DOI: [10.1016/j.neuron.2005.09.022](https://doi.org/10.1016/j.neuron.2005.09.022).
- [85] L. J. Garey and T. P. S. Powell. "An experimental study of the termination of the lateral geniculo-cortical pathway in the cat and monkey." In: *Proceedings of the Royal Society of London. Series B, Biological Sciences* 179.1054 (2017), pp. 41–63.
- [86] Jeffrey P. Gavornik and Mark F. Bear. "Higher brain functions served by the lowly rodent primary visual cortex." In: *Learning & memory (Cold Spring Harbor, N.Y.)* 21.10 (2014), pp. 527–33. ISSN: 1549-5485. DOI: [10.1101/lm.034355.114](https://doi.org/10.1101/lm.034355.114).
- [87] Jeffrey P. Gavornik and Mark F. Bear. "Learned spatiotemporal sequence recognition and prediction in primary visual cortex." In: *Nature Neuroscience* 17.5 (2014), pp. 732–737. ISSN: 1097-6256. DOI: [10.1038/nn.3683](https://doi.org/10.1038/nn.3683).
- [88] Kunal K. Ghosh, Laurie D. Burns, Eric D. Cocker, Axel Nimmerjahn, Yaniv Ziv, Abbas El Gamal, and Mark J. Schnitzer. "Miniaturized integration of a fluorescence microscope." In: *Nature Methods* 8.10 (2011), pp. 871–878. ISSN: 1548-7091. DOI: [10.1038/nmeth.1694](https://doi.org/10.1038/nmeth.1694).
- [89] Charles D. Gilbert and Wu Li. "Top-down influences on visual processing." In: *Nature Reviews Neuroscience* 14.5 (2013), pp. 350–363. ISSN: 1471003X. DOI: [10.1038/nrn3476](https://doi.org/10.1038/nrn3476).
- [90] Charles D. Gilbert and Torsten N. Wiesel. "Receptive field dynamics in adult primary visual cortex." In: *Nature* 359 (1992), pp. 150–152. DOI: [10.1038/356150a0](https://doi.org/10.1038/356150a0).
- [91] Lindsey L. Glickfeld, Mark L. Andermann, Vincent Bonin, and R. Clay Reid. "Cortico-cortical projections in mouse visual cortex are functionally target specific." In: *Nature Neuroscience* 16.2 (2013), pp. 219–226. ISSN: 10976256. DOI: [10.1038/nn.3300](https://doi.org/10.1038/nn.3300).
- [92] Lindsey L. Glickfeld, J. David Roberts, Peter Somogyi, and Massimo Scanziani. "Interneurons hyperpolarize pyramidal cells along their entire somatodendritic axis." In: *Nature Neuroscience* 12.1 (2009), pp. 21–23. ISSN: 1097-6256. DOI: [10.1038/nn.2230](https://doi.org/10.1038/nn.2230).
- [93] Melvyn A. Goodale and A. David Milner. "Separate visual pathways for perception and action." In: *Trends in Neurosciences* 15 (1992), pp. 20–5. ISSN: 01662236. DOI: [10.1016/0166-2236\(92\)90344-8](https://doi.org/10.1016/0166-2236(92)90344-8).

- [94] Maria Göppert-Mayer. "Ueber elementarakte mit zwei quantenspruengen." PhD thesis. 1930, pp. 273–294.
- [95] Joshua A. Gordon and Michael P. Stryker. "Experience-dependent plasticity of binocular responses in the primary visual cortex of the mouse." In: *Journal of Neuroscience* 16.10 (1996), pp. 3274–3286. ISSN: 0270-6474. DOI: [10.1523/JNEUROSCI.0961-96.1996](https://doi.org/10.1523/JNEUROSCI.0961-96.1996).
- [96] Franziska Greifzu, Justyna Pielecka-Fortuna, Evgenia Kalogeraki, Katja Krempler, Plinio D. Favaro, Oliver M. Schluter, and Siegrid Löwel. "Environmental enrichment extends ocular dominance plasticity into adulthood and protects from stroke-induced impairments of plasticity." In: *Proceedings of the National Academy of Sciences* 111.3 (2014), pp. 1150–1155. ISSN: 0027-8424. DOI: [10.1073/pnas.1313385111](https://doi.org/10.1073/pnas.1313385111).
- [97] Christine Grienberger, Nathalie L. Rochefort, Helmuth Adelsberger, Horst A. Henning, Daniel N. Hill, Julia Reichwald, Matthias Staufenbiel, and Arthur Konnerth. "Staged decline of neuronal function in vivo in an animal model of Alzheimer's disease." In: *Nature Communications* 3 (2012), pp. 1–10. ISSN: 2041-1723. DOI: [10.1038/ncomms1783](https://doi.org/10.1038/ncomms1783).
- [98] Jaime Grutzendler, Narayanan Kasthuri, and Wen Biao Gan. "Long-term dendritic spine stability in the adult cortex." In: *Nature* 420.6917 (2002), pp. 812–816. ISSN: 00280836. DOI: [10.1038/nature01276](https://doi.org/10.1038/nature01276).
- [99] Zengcai V. Guo, S. Andrew Hires, Nuo Li, Daniel H. O'Connor, Takaki Komiyama, Eran Ophir, Daniel Huber, Claudia Bonardi, Karin Morandell, Diego Gutnisky, Simon Peron, Ning Long Xu, James Cox, and Karel Svoboda. "Procedures for behavioral experiments in head-fixed mice." In: *PLoS ONE* 9.2 (2014). ISSN: 19326203. DOI: [10.1371/journal.pone.0088678](https://doi.org/10.1371/journal.pone.0088678).
- [100] Bilal Haider, Michael Häusser, and Matteo Carandini. "Inhibition dominates sensory responses in the awake cortex." In: *Nature* 493.7430 (2013), pp. 97–100. ISSN: 1476-4687. DOI: [10.1038/nature11665](https://doi.org/10.1038/nature11665).
- [101] Fadi F. Hamdan, Hussein Daoud, Amlie Piton, Julie Gauthier, Sylvia Dobrzeńska, Marie Odile Krebs, Ridha Joober, Jean Claude Lacaille, Amlie Nadeau, Jeff M. Milunsky, Zhenyuan Wang, Lionel Carmant, Laurent Mottron, Miriam H. Beauchamp, Guy A. Rouleau, and Jacques L. Michaud. "De novo syngap1 mutations in nonsyndromic intellectual disability and autism." In: *Biological Psychiatry* 69.9 (2011), pp. 898–901. ISSN: 00063223. DOI: [10.1016/j.biopsych.2010.11.015](https://doi.org/10.1016/j.biopsych.2010.11.015).
- [102] Jordan P. Hamm and Rafael Yuste. "Somatostatin interneurons control a key component of mismatch negativity in mouse visual cortex." In: *Cell Reports* 16.3 (2016), pp. 597–604. ISSN: 22111247. DOI: [10.1016/j.celrep.2016.06.037](https://doi.org/10.1016/j.celrep.2016.06.037).

- [103] Kenneth D. Harris and Thomas D. Mrsic-Flogel. "Cortical connectivity and sensory coding." In: *Nature* 503.7474 (2013), pp. 51–8. ISSN: 1476-4687. DOI: [10.1038/nature12654](https://doi.org/10.1038/nature12654).
- [104] Kenneth D. Harris and Alexander Thiele. "Cortical state and attention." In: *Nature Reviews Neuroscience* 12.9 (2011), pp. 509–523. ISSN: 1471-003X. DOI: [10.1038/nrn3084](https://doi.org/10.1038/nrn3084).
- [105] Hai-Yan He, William Hodos, and Elizabeth M. Quinlan. "Visual deprivation reactivates rapid ocular dominance plasticity in adult visual cortex." In: *Journal of Neuroscience* 26.11 (2006), pp. 2951–2955. ISSN: 0270-6474. DOI: [10.1523/JNEUROSCI.5554-05.2006](https://doi.org/10.1523/JNEUROSCI.5554-05.2006).
- [106] D. O. Hebb. *The organization of behaviour*. 1949, p. 62. ISBN: 0471367273. DOI: [citeulike-article-id:1282862](https://doi.org/citeulike-article-id:1282862).
- [107] Fritjof Helmchen and Winfried Denk. "Deep tissue two-photon microscopy." In: *Nature Methods* 2.12 (2005). DOI: [10.1038/NMETH818](https://doi.org/10.1038/NMETH818).
- [108] Peter W. Hickmott. "Synapses of horizontal connections in adult rat somatosensory cortex have different properties depending on the source of their axons." In: *Cerebral Cortex* 20.3 (2010), pp. 591–601. ISSN: 10473211. DOI: [10.1093/cercor/bhp125](https://doi.org/10.1093/cercor/bhp125).
- [109] Daniel Hillier, Michele Fiscella, Antonia Drinnenberg, Stuart Trenholm, Santiago B Rompani, Zoltan Raics, Gergely Katona, Josephine Juettner, Andreas Hierlemann, Balazs Rozsa, and Botond Roska. "Causal evidence for retina-dependent and -independent visual motion computations in mouse cortex." In: *Nature Neuroscience* 20.September 2016 (2017), pp. 960–968. ISSN: 1097-6256. DOI: [10.1038/nn.4566](https://doi.org/10.1038/nn.4566).
- [110] Helmut V. B. Hirsch and D N Spinelli. "Visual experience modifies distribution of horizontally and vertically oriented receptive fields in cats." In: *Science* 168.3933 (1970), pp. 869–871. ISSN: 0036-8075. DOI: [10.1126/science.168.3933.869](https://doi.org/10.1126/science.168.3933.869).
- [111] Sonja B. Hofer, Thomas D. Mrsic-Flogel, Tobias Bonhoeffer, and Mark Hübner. "Experience leaves a lasting structural trace in cortical circuits." In: *Nature* 457.7227 (2009), pp. 313–7. ISSN: 1476-4687. DOI: [10.1038/nature07487](https://doi.org/10.1038/nature07487).
- [112] Sonja B. Hofer, Thomas D. Mrsic-Flogel, Tobias Bonhoeffer, and Mark Hübner. "Prior experience enhances plasticity in adult visual cortex." In: *Nature Neuroscience* 9.1 (2006), pp. 127–32. ISSN: 1097-6256. DOI: [10.1038/nn1610](https://doi.org/10.1038/nn1610).
- [113] Anthony J.G.D. Holtmaat, Joshua T. Trachtenberg, Linda Wilbrecht, Gordon M. Shepherd, Xiaoqun Zhang, Graham W. Knott, and Karel Svoboda. "Transient and persistent dendritic spines in the neocortex in vivo." In: *Neuron* 45.2 (2005), pp. 279–291. ISSN: 08966273. DOI: [10.1016/j.neuron.2005.01.003](https://doi.org/10.1016/j.neuron.2005.01.003).

- [114] Stephen D Van Hooser, J Alexander F Heimel, Sooyoung Chung, Sacha B Nelson, and Louis J Toth. "Orientation selectivity without orientation maps in visual cortex of a highly visual mammal." In: 25.1 (2005), pp. 19–28. DOI: [10.1523/JNEUROSCI.4042-04.2005](https://doi.org/10.1523/JNEUROSCI.4042-04.2005).
- [115] Xiaojie Huang, Sophia K. Stodieck, Bianka Goetze, Lei Cui, Man Ho Wong, Colin Wenzel, Leon Hosang, Yan Dong, Siegrid Löwel, and Oliver M. Schlüter. "Progressive maturation of silent synapses governs the duration of a critical period." In: *Proceedings of the National Academy of Sciences* 112.24 (2015), pp. 3131–3140. DOI: [10.1073/pnas.1506488112](https://doi.org/10.1073/pnas.1506488112).
- [116] D H Hubel, T N Wiesel, and Michael P. Stryker. "Anatomical demonstration of orientation columns in macaque monkey." In: *The Journal of Comparative Neurology* 177.3 (1978), pp. 361–380. DOI: [10.1002/cne.901770302](https://doi.org/10.1002/cne.901770302).
- [117] David H. Hubel and Torsten N. Wiesel. "Receptive fields and functional architecture of monkey striate cortex." In: *Journal of Physiology* 195 (1968), pp. 215–243. ISSN: 0022-3751. DOI: [papers://47831562-1F78-4B52-B52E-78BF7F97A700/Paper/p352](https://doi.org/papers://47831562-1F78-4B52-B52E-78BF7F97A700/Paper/p352).
- [118] David H. Hubel and Torsten N. Wiesel. "Receptive fields, binocular interaction and functional architecture in the cat's visual cortex." In: *The Journal of Physiology* (1962), pp. 106–154. ISSN: 0022-3751. DOI: [10.1523/JNEUROSCI.1991-09.2009](https://doi.org/10.1523/JNEUROSCI.1991-09.2009).
- [119] Mark Hübener. "Mouse visual cortex." In: *Current Opinion in Neurobiology* 13.4 (2003), pp. 413–420. ISSN: 09594388. DOI: [10.1016/S0959-4388\(03\)00102-8](https://doi.org/10.1016/S0959-4388(03)00102-8).
- [120] Andrew D. Huberman and Cristopher M. Niell. "What can mice tell us about how vision works?" In: *Trends in Neurosciences* 34.9 (2011), pp. 464–473. ISSN: 01662236. DOI: [10.1016/j.tins.2011.07.002](https://doi.org/10.1016/j.tins.2011.07.002).
- [121] Andrew D. Huberman, Mihai Manu, Selina M. Koch, Michael W. Susman, Amanda Brosius Lutz, Erik M. Ullian, Stephen A. Baccus, and Ben A. Barres. "Architecture and activity-mediated refinement of axonal projections from a mosaic of genetically identified retinal ganglion cells." In: *Neuron* 59.3 (2008), pp. 425–438. ISSN: 08966273. DOI: [10.1016/j.neuron.2008.07.018](https://doi.org/10.1016/j.neuron.2008.07.018).
- [122] Andrew D. Huberman, Wei Wei, Justin Elstrott, Ben K. Stafford, Marla B. Feller, and Ben A. Barres. "Genetic identification of an on-off direction-selective retinal ganglion cell subtype reveals a layer-specific subcortical map of posterior motion." In: *Neuron* 62.3 (2009), pp. 327–334. ISSN: 08966273. DOI: [10.1016/j.neuron.2009.04.014](https://doi.org/10.1016/j.neuron.2009.04.014).
- [123] Allen L. Humphrey, Leslie C. Skeen, and Thomas T. Norton. "Topographic organization of the orientation column system in the striate cortex of the Tree Shrew (*Tupaia glis*) I I deoxyglucose mapping." In: *The Journal of Comparative Neurology* 192 (1980), pp. 549–566. DOI: [10.1002/cne.901920312](https://doi.org/10.1002/cne.901920312).

- [124] Holger Husi, Malcolm A. Ward, Jyoti S. Choudhary, Walter P. Blackstock, and Seth G. Grant. "Proteomic analysis of NMDA receptor-adhesion protein signaling complexes." In: *Nature Neuroscience* 3.7 (2000), pp. 661–669. ISSN: 1097-6256. DOI: [10.1038/76615](https://doi.org/10.1038/76615).
- [125] Masatoshi Inoue, Atsuya Takeuchi, Shin Ichiro Horigane, Masamichi Ohkura, Keiko Gengyo-Ando, Hajime Fujii, Satoshi Kamijo, Sayaka Takemoto-Kimura, Masanobu Kano, Junichi Nakai, Kazuo Kitamura, and Haruhiko Bito. "Rational design of a high-affinity, fast, red calcium indicator R-CaMP2." In: *Nature Methods* 12.1 (2014), pp. 64–70. ISSN: 15487105. DOI: [10.1038/nmeth.3185](https://doi.org/10.1038/nmeth.3185).
- [126] Jesse Jackson, Inbal Ayzenshtat, Mahesh M. Karnani, and Rafael Yuste. "VIP+ interneurons control neocortical activity across brain states." In: *Journal of Neurophysiology* 115.6 (2016), pp. 3008–3017. ISSN: 0022-3077. DOI: [10.1152/jn.01124.2015](https://doi.org/10.1152/jn.01124.2015).
- [127] Kyle R. Jenks, Taekeun Kim, Elissa D. Pastuzyn, Hiroyuki Okuno, Andrew V. Taibi, Haruhiko Bito, Mark F. Bear, and Jason D. Shepherd. "Arc restores juvenile plasticity in adult mouse visual cortex." In: *Proceedings of the National Academy of Sciences* 114.34 (2017), pp. 9182–9187. DOI: [10.1073/pnas.1700866114](https://doi.org/10.1073/pnas.1700866114).
- [128] C J Jeon, E Strettoi, and R H Masland. "The major cell populations of the mouse retina." In: *Journal of Neuroscience* 18.21 (1998), pp. 8936–8946. ISSN: 0270-6474. DOI: [1702462](https://doi.org/10.1523/JNEUROSCI.1702-98.2000).
- [129] Nallathambi Jeyabalan and James P. Clement. "SynGAP1: Mind the Gap." In: *Frontiers in Cellular Neuroscience* 10. February (2016), pp. 1–16. ISSN: 1662-5102. DOI: [10.3389/fncel.2016.00032](https://doi.org/10.3389/fncel.2016.00032).
- [130] Na Ji, Jeremy Freeman, and Spencer L. Smith. "Technologies for imaging neural activity in large volumes." In: *Nature Neuroscience* 19.9 (2016), pp. 1154–64. ISSN: 1097-6256. DOI: [10.1038/nn.4358](https://doi.org/10.1038/nn.4358).
- [131] Xiaolong Jiang, Shan Shen, Cathryn R. Cadwell, Philipp Berens, Fabian Sinz, Alexander S. Ecker, Saumil Patel, and Andreas S. Tolias. "Principles of connectivity among morphologically defined cell types in adult neocortex." In: *Science* 353.6304 (2015), pp. 1108–1108. ISSN: 0036-8075. DOI: [10.1126/science.aaf6102](https://doi.org/10.1126/science.aaf6102).
- [132] Jürgen C Jung, Amit D Mehta, Emre Aksay, Raymond Stepnoski, and Mark J. Schnitzer. "In vivo mammalian brain imaging using one- and two-photon fluorescence microendoscopy." In: *Journal Neurophysiology* 92.5 (2004), pp. 3121–3133. ISSN: 0022-3077. DOI: [10.1152/jn.00234.2004](https://doi.org/10.1152/jn.00234.2004). In.
- [133] Patrick Kaifosh, Jeffrey D. Zaremba, Nathan B. Danielson, and Attila Losonczy. "SIMA: Python software for analysis of dynamic fluorescence imaging data." In: *Frontiers in neuroinformatics* 8. September (2014), p. 80. ISSN: 1662-5196. DOI: [10.3389/fninf.2014.00080](https://doi.org/10.3389/fninf.2014.00080).

- [134] W. Kaiser and C. Garrett. "Two-photon excitation in CaF₂:Eu²⁺." In: *Physical Review Letters* 7.6 (1961), pp. 229–231. ISSN: 0031-9007. DOI: [10.1103/PhysRevLett.7.229](https://doi.org/10.1103/PhysRevLett.7.229).
- [135] Evgenia Kalogeraki, Justyna Pielecka-Fortuna, Janika M. Hüppe, and Siegrid Löwel. "Physical exercise preserves adult visual plasticity in mice and restores it after a stroke in the somatosensory cortex." In: *Frontiers in Aging Neuroscience* 8 (2016), pp. 1–15. ISSN: 16634365. DOI: [10.3389/fnagi.2016.00212](https://doi.org/10.3389/fnagi.2016.00212).
- [136] Evgenia Kalogeraki, Franziska Greifzu, Franziska Haack, and Siegrid Löwel. "Voluntary physical exercise promotes ocular dominance plasticity in adult mouse primary visual cortex." In: *Journal of Neuroscience* 34.46 (2014), pp. 15476–15481. ISSN: 0270-6474. DOI: [10.1523/JNEUROSCI.2678-14.2014](https://doi.org/10.1523/JNEUROSCI.2678-14.2014).
- [137] Megumi Kaneko, Yu Fu, and Michael P. Stryker. "Locomotion induces stimulus-specific response enhancement in adult visual cortex." In: *Journal of Neuroscience* 37.13 (2017), pp. 3532–3543. DOI: [10.1523/JNEUROSCI.3760-16.2017](https://doi.org/10.1523/JNEUROSCI.3760-16.2017).
- [138] Christoph Kapfer, Lindsey L. Glickfeld, Bassam V. Atallah, and Massimo Scanziani. "Supralinear increase of recurrent inhibition during sparse activity in the somatosensory cortex." In: *Nature Neuroscience* 10.6 (2007), pp. 743–753. ISSN: 1097-6256. DOI: [10.1038/nn1909](https://doi.org/10.1038/nn1909).
- [139] Eitan S. Kaplan, Sam F. Cooke, Robert W. Komorowski, Alexander A. Chubykin, Aurore Thomazeau, Lena A. Khibnik, Jeffrey P. Gavornik, and Mark F. Bear. "Contrasting roles for parvalbumin-expressing inhibitory neurons in two forms of adult visual cortical plasticity." In: *eLife* 5 (2016), pp. 1–27. ISSN: 2050084X. DOI: [10.7554/eLife.11450](https://doi.org/10.7554/eLife.11450).
- [140] Uma R. Karmarkar and Yang Dan. "Experience-dependent plasticity in adult visual cortex." In: *Neuron* 52.4 (2006), pp. 577–585. ISSN: 08966273. DOI: [10.1016/j.neuron.2006.11.001](https://doi.org/10.1016/j.neuron.2006.11.001).
- [141] Matthias Kaschube, Michael Schnabel, Siegrid Löwel, David M. Coppola, Leonard E. White, and Fred Wolf. "Universality in the evolution of orientation columns in the visual cortex." In: *Science* 330 (2010), pp. 1113–1116. DOI: [10.1126/science.1194869](https://doi.org/10.1126/science.1194869).
- [142] Gergely Katona, Gergely Szalay, Pál Maák, Attila Kaszás, Máté Veress, Dániel Hillier, Balázs Chiovini, E. Sylvester Vizi, Botond Roska, and Balázs Rózsa. "Fast two-photon in vivo imaging with three-dimensional random-access scanning in large tissue volumes." In: *Nature Methods* 9.2 (2012), pp. 201–208. ISSN: 15487091. DOI: [10.1038/nmeth.1851](https://doi.org/10.1038/nmeth.1851).
- [143] Yasuo Kawaguchi. "Selective cholinergic modulation of cortical GABAergic cell subtypes." In: *Journal of Neurophysiology* (1997), pp. 1743–1747. DOI: [10.1152/jn.1997.78.3.1743](https://doi.org/10.1152/jn.1997.78.3.1743).

- [144] Yasuo Kawaguchi, Fuyuki Karube, and Yoshiyuki Kubota. "Dendritic branch typing and spine expression patterns in cortical nonpyramidal cells." In: *Cerebral Cortex* 16.5 (2006), pp. 696–711. DOI: [10.1093/cercor/bhj015](https://doi.org/10.1093/cercor/bhj015).
- [145] Yasuo Kawaguchi and Yoshiyuki Kubota. "GABAergic cell subtypes and their synaptic connections in rat frontal cortex." In: *Cerebral Cortex* 7.6 (1997), pp. 476–486. ISSN: 10473211. DOI: [10.1093/cercor/7.6.476](https://doi.org/10.1093/cercor/7.6.476).
- [146] Yasuo Kawaguchi, Hironobu Katsumaru, Toshio Kosaka, Claus W. Heizmann, and Kiyoshi Hama. "Fast spiking cells in rat hippocampus (CA1 region) contain the calcium-binding protein parvalbumin." In: *Brain Research* 416.2 (1987), pp. 369–374. ISSN: 00068993. DOI: [10.1016/0006-8993\(87\)90921-8](https://doi.org/10.1016/0006-8993(87)90921-8).
- [147] Tara Keck, Taro Toyozumi, Lu Chen, Brent Doiron, Daniel E. Feldman, Kevin Fox, Wulfram Gerstner, Philip G. Haydon, Mark Hübener, Hey-Kyoung Lee, John E. Lisman, Tobias Rose, Frank Sengpiel, David Stellwagen, Michael P. Stryker, Gina G. Turrigiano, and Mark C. van Rossum. "Integrating Hebbian and homeostatic plasticity: the current state of the field and future research directions." In: *Philosophical Transactions of the Royal Society B: Biological Sciences* 372.1715 (2017), p. 20160158. ISSN: 0962-8436. DOI: [10.1098/rstb.2016.0158](https://doi.org/10.1098/rstb.2016.0158).
- [148] Tara Keck, Volker Scheuss, R. Irene Jacobsen, Corette J. Wierenga, Ulf T. Eysel, Tobias Bonhoeffer, and Mark Hübener. "Loss of sensory input causes rapid structural changes of inhibitory neurons in adult mouse visual cortex." In: *Neuron* 71.5 (2011), pp. 869–882. ISSN: 08966273. DOI: [10.1016/j.neuron.2011.06.034](https://doi.org/10.1016/j.neuron.2011.06.034).
- [149] Tara Keck, Thomas D. Mrsic-Flogel, Miguel Vaz Afonso, Ulf T. Eysel, Tobias Bonhoeffer, and Mark Hübener. "Massive restructuring of neuronal circuits during functional reorganization of adult visual cortex." In: *Nature Neuroscience* 11.10 (2008), pp. 1162–1167. ISSN: 1097-6256. DOI: [10.1038/nn.2181](https://doi.org/10.1038/nn.2181).
- [150] Tara Keck, Georg B. Keller, R. Irene Jacobsen, Ulf T. Eysel, Tobias Bonhoeffer, and Mark Hübener. "Synaptic scaling and homeostatic plasticity in the mouse visual cortex in vivo." In: *Neuron* 80.2 (2013), pp. 327–334. ISSN: 08966273. DOI: [10.1016/j.neuron.2013.08.018](https://doi.org/10.1016/j.neuron.2013.08.018).
- [151] Sander W. Keemink, Scott C. Lowe, Janelle M. P. Pakan, Evelyn Dylida, Mark C. W. Van Rossum, and Nathalie L. Rochefort. "FISSA: A neuropil decontamination toolbox for calcium imaging signals." In: *Scientific Reports* 8.3493 (2018), pp. 1–12. DOI: [10.1038/s41598-018-21640-2](https://doi.org/10.1038/s41598-018-21640-2).
- [152] Georg B. Keller, Tobias Bonhoeffer, and Mark Hübener. "Sensorimotor mismatch signals in primary visual cortex of the behaving mouse." In: *Neuron* 74.5 (2012), pp. 809–815. ISSN: 08966273. DOI: [10.1016/j.neuron.2012.03.040](https://doi.org/10.1016/j.neuron.2012.03.040).

- [153] M B Kennedy, M K Bennett, and N E Erond. "Biochemical and immunochemical evidence that the "major postsynaptic density protein" is a subunit of a calmodulin-dependent protein kinase." In: *Proceedings of the National Academy of Sciences of the United States of America* 80.23 (1983), pp. 7357–7361. ISSN: 0027-8424. DOI: [10.1073/pnas.80.23.7357](https://doi.org/10.1073/pnas.80.23.7357).
- [154] Adam Kepecs and Gordon Fishell. "Interneuron cell types are fit to function." In: *Nature* 505.7483 (2014), pp. 318–26. ISSN: 1476-4687. DOI: [10.1038/nature12983](https://doi.org/10.1038/nature12983).
- [155] Aaron M. Kerlin, Mark L. Andermann, Vladimir K. Berezovskii, and R. Clay Reid. "Broadly tuned response properties of diverse inhibitory neuron subtypes in mouse visual cortex." In: *Neuron* 67.5 (2010), pp. 858–871. ISSN: 08966273. DOI: [10.1016/j.neuron.2010.08.002](https://doi.org/10.1016/j.neuron.2010.08.002).
- [156] Jason N. D. Kerr and Winfried Denk. "Imaging in vivo: watching the brain in action." In: *Nature reviews. Neuroscience* 9.3 (2008), pp. 195–205. ISSN: 1471-003X. DOI: [10.1038/nrn2338](https://doi.org/10.1038/nrn2338).
- [157] Michael P. Kilgard and Michael M. Merzenich. "Plasticity of temporal information processing in the primary auditory cortex." In: *Nat Neurosci* 1.8 (1998), pp. 727–731. ISSN: 1097-6256. DOI: [10.1038/3729](https://doi.org/10.1038/3729).
- [158] Hyunsoo Kim and Haesun Park. "Sparse non-negative matrix factorizations via alternating non-negativity-constrained least squares for microarray data analysis." In: *Bioinformatics* 23.12 (2007), pp. 1495–1502. ISSN: 13674803. DOI: [10.1093/bioinformatics/btm134](https://doi.org/10.1093/bioinformatics/btm134).
- [159] Jee Hae Kim, Dezhi Liao, Lit Fui Lau, and Richard L. Huganir. "SynGAP: A synaptic RasGAP that associates with the PSD-95/SAP90 protein family." In: *Neuron* 20.4 (1998), pp. 683–691. ISSN: 08966273. DOI: [10.1016/S0896-6273\(00\)81008-9](https://doi.org/10.1016/S0896-6273(00)81008-9).
- [160] Jee Hae Kim, Hey-Kyoung Lee, Kogo Takamiya, and Richard L. Huganir. "The role of synaptic GTPase-activating protein in neuronal development and synaptic plasticity." In: *The Journal of Neuroscience* 23.4 (2003), pp. 1119–1124. ISSN: 1529-2401. DOI: [23/4/1119\[pii\]](https://doi.org/10.1523/JNEUROSCI.23/4/1119[pii]).
- [161] Thomas Knöpfel. "Genetically encoded optical indicators for the analysis of neuronal circuits." In: *Nature Reviews Neuroscience* 13.10 (2012), pp. 687–700. ISSN: 1471003X. DOI: [10.1038/nrn3293](https://doi.org/10.1038/nrn3293).
- [162] Ho Ko, Sonja B. Hofer, Bruno Pichler, Katherine A. Buchanan, P. Jesper Sjoestrom, and Thomas D. Mrsic-Flogel. "Functional specificity of local synaptic connections in neocortical networks." In: *Nature* 473.7345 (2011), pp. 87–91. ISSN: 1476-4687. DOI: [10.1038/nature09880](https://doi.org/10.1038/nature09880).

- [163] Noboru H. Komiyama, Ayako M. Watabe, Holly J. Carlisle, Karen Porter, Paul Charlesworth, Jennifer Monti, Douglas J. C. Strathdee, Colin M. O'Carroll, Stephen J. Martin, Richard G. M. Morris, Thomas J. O'Dell, and Seth G. N. Grant. "SynGAP regulates ERK/MAPK signaling, synaptic plasticity, and learning in the complex with postsynaptic density 95 and NMDA receptor." In: *The Journal of Neuroscience* 22.22 (2002), pp. 9721–9732. ISSN: 1529-2401. DOI: [10.1523/JNEUROSCI.22.22.9721-1999](https://doi.org/10.1523/JNEUROSCI.22.22.9721-1999).
- [164] Satoru Kondo, Takashi Yoshida, and Kenichi Ohki. "Mixed functional micro-architectures for orientation selectivity in the mouse primary visual cortex." In: *Nature Communications* 7 (2016), p. 13210. ISSN: 2041-1723. DOI: [10.1038/ncomms13210](https://doi.org/10.1038/ncomms13210).
- [165] Anne K. Kreile, Tobias Bonhoeffer, and Mark Hübener. "Altered visual experience induces instructive changes of orientation preference in mouse visual cortex." In: *The Journal of Neuroscience* 31.39 (2011), pp. 13911–13920. DOI: [10.1523/JNEUROSCI.2143-11.2011](https://doi.org/10.1523/JNEUROSCI.2143-11.2011).
- [166] Dilja D. Krueger and Mark F. Bear. "Toward fulfilling the promise of molecular medicine in fragile X syndrome." In: *Annual review of medicine* 62 (2011), pp. 411–429. ISSN: 0066-4219. DOI: [10.1146/annurev-med-061109-134644](https://doi.org/10.1146/annurev-med-061109-134644).
- [167] Matthew E. Larkum, Walter Senn, and Hans R. Lüscher. "Top-down dendritic input increases the gain of layer 5 pyramidal neurons." In: *Cerebral Cortex* 14.10 (2004), pp. 1059–1070. ISSN: 10473211. DOI: [10.1093/cercor/bhh065](https://doi.org/10.1093/cercor/bhh065).
- [168] A. Moses Lee, Jennifer L. Hoy, Antonello Bonci, Linda Wilbrecht, Michael P. Stryker, and Cristopher M. Niell. "Identification of a brainstem circuit regulating visual cortical state in parallel with locomotion." In: *Neuron* 83.2 (2014), pp. 455–466. ISSN: 10974199. DOI: [10.1016/j.neuron.2014.06.031](https://doi.org/10.1016/j.neuron.2014.06.031).
- [169] Sangkyun Lee, Jochen F. Meyer, Jiyoung Park, and Stelios M. Smirnakis. "Visually driven neuropil activity and information encoding in mouse primary visual cortex." In: *Frontiers in Neural Circuits* 11.July (2017), pp. 1–18. ISSN: 1662-5110. DOI: [10.3389/fncir.2017.00050](https://doi.org/10.3389/fncir.2017.00050).
- [170] Seung-Hee Lee, Alex C. Kwan, Siyu Zhang, Victoria Phoumthippavong, John G. Flannery, Sotiris C. Masmanidis, Hiroki Taniguchi, Z. Josh Huang, Feng Zhang, Edward S. Boyden, Karl Deisseroth, and Yang Dan. "Activation of specific interneurons improves V1 feature selectivity and visual perception." In: *Nature* 488.7411 (2012), pp. 379–383. ISSN: 0028-0836. DOI: [10.1038/nature11312](https://doi.org/10.1038/nature11312).
- [171] SooHyun Lee, Jens Hjerling-Leffler, Edward Zagher, Gord Fishell, and Bernardo Rudy. "The largest group of superficial neocortical GABAergic interneurons expresses ionotropic serotonin receptors." In: *Journal of Neuroscience* 30.50 (2010), pp. 16796–16808. ISSN: 0270-6474. DOI: [10.1523/JNEUROSCI.1869-10.2010](https://doi.org/10.1523/JNEUROSCI.1869-10.2010).

- [172] Soohyun Lee, Illya Kruglikov, Z Josh Huang, Gord Fishell, and Bernardo Rudy. "A disinhibitory circuit mediates motor integration in the somatosensory cortex." In: *Nature Neuroscience* 16.11 (2013), pp. 1662–1670. ISSN: 1097-6256. DOI: [10.1038/nn.3544](https://doi.org/10.1038/nn.3544).
- [173] Wei Chung Allen Lee, Hayden Huang, Guoping Feng, Joshua R. Sanes, Emery N. Brown, Peter T. So, and Elly Nedivi. "Dynamic remodeling of dendritic arbors in GABAergic interneurons of adult visual cortex." In: *PLoS Biology* 4.2 (2006), pp. 271–280. ISSN: 15457885. DOI: [10.1371/journal.pbio.0040029](https://doi.org/10.1371/journal.pbio.0040029).
- [174] Konrad Lehmann and Siegrid Löwel. "Age-dependent ocular dominance plasticity in adult mice." In: *PLoS ONE* 3.9 (2008). ISSN: 19326203. DOI: [10.1371/journal.pone.0003120](https://doi.org/10.1371/journal.pone.0003120).
- [175] Marcus Leinweber, Daniel R. Ward, Jan M. Sobczak, Alexander Attinger, and Georg B. Keller. "A sensorimotor circuit in mouse cortex for visual flow Predictions." In: *Neuron* 95.6 (2017), 1420–1432.e5. ISSN: 10974199. DOI: [10.1016/j.neuron.2017.08.036](https://doi.org/10.1016/j.neuron.2017.08.036).
- [176] Marcus Leinweber, Pawel Zmarz, Peter Buchmann, Paul Argast, Mark Hübener, Tobias Bonhoeffer, and Georg B. Keller. "Two-photon calcium imaging in mice navigating a virtual reality environment." In: *Journal of visualized experiments : JoVE* 84 (2014), pp. 1–6. ISSN: 1940-087X. DOI: [10.3791/50885](https://doi.org/10.3791/50885).
- [177] Christiaan N. Levelt and Mark Hübener. "Critical-period plasticity in the visual cortex." In: *Annual Review of Neuroscience* 35.1 (2012), pp. 309–330. ISSN: 0147-006X. DOI: [10.1146/annurev-neuro-061010-113813](https://doi.org/10.1146/annurev-neuro-061010-113813).
- [178] Ya-tang Li, Leena A. Ibrahim, Bao-hua Liu, Li I. Zhang, and Huizhong Whit Tao. "Linear transformation of thalamocortical input by intracortical excitation." In: *Nature Neuroscience* 16.9 (2013), pp. 1324–30. ISSN: 1546-1726. DOI: [10.1038/nn.3494](https://doi.org/10.1038/nn.3494).
- [179] Anthony D. Lien and Massimo Scanziani. "Tuned thalamic excitation is amplified by visual cortical circuits." In: *Nature Neuroscience* 16.9 (2013), pp. 1315–23. ISSN: 1546-1726. DOI: [10.1038/nn.3488](https://doi.org/10.1038/nn.3488).
- [180] Loren L. Looger and Oliver Griesbeck. "Genetically encoded neural activity indicators." In: *Current Opinion in Neurobiology* 22.1 (2012), pp. 18–23. ISSN: 09594388. DOI: [10.1016/j.conb.2011.10.024](https://doi.org/10.1016/j.conb.2011.10.024).
- [181] Liqun Luo, Edward M. Callaway, and Karel Svoboda. "Genetic dissection of neural circuits." In: *Neuron* 57.5 (2008), pp. 634–660. ISSN: 08966273. DOI: [10.1016/j.neuron.2008.01.002](https://doi.org/10.1016/j.neuron.2008.01.002).
- [182] Yunyong Ma, Hang Hu, Albert S. Berrebi, Peter H. Mathers, and Ariel Agmon. "Distinct subtypes of somatostatin-containing neocortical interneurons revealed in transgenic mice." In: *Journal of Neuroscience* 26.19 (2006), pp. 5069–5082. ISSN: 0270-6474. DOI: [10.1523/JNEUROSCI.0661-06.2006](https://doi.org/10.1523/JNEUROSCI.0661-06.2006).

- [183] Arianna Maffei, Kiran Nataraj, Sacha B. Nelson, and Gina G. Turrigiano. "Potentiation of cortical inhibition by visual deprivation." In: *Nature* 443:7107 (2006), pp. 81–84. DOI: [10.1038/nature05079](https://doi.org/10.1038/nature05079).
- [184] Hiroshi Makino and Takaki Komiyama. "Learning enhances the relative impact of top-down processing in the visual cortex." In: *Nature Neuroscience* 2015.6 (2015), pp. 173–180. ISSN: 1546-170X. DOI: [10.1038/nn.4061](https://doi.org/10.1038/nn.4061).
- [185] Fred Marbach and Anthony M. Zador. "A self-initiated two-alternative forced choice paradigm for head-fixed mice." In: *bioRxiv* (2016), p. 073783. DOI: [10.1101/073783](https://doi.org/10.1101/073783).
- [186] Henry Markram, Maria Toledo-Rodriguez, Yun Wang, Anirudh Gupta, Gilad Silberberg, and Caizhi Wu. "Interneurons of the neocortical inhibitory system." In: *Nature Reviews Neuroscience* 5.10 (2004), pp. 793–807. ISSN: 1471-003X. DOI: [10.1038/nrn1519](https://doi.org/10.1038/nrn1519).
- [187] James H. Marshel, Marina E. Garrett, Ian Nauhaus, and Edward M. Callaway. "Functional specialization of seven mouse visual cortical areas." In: *Neuron* 72.6 (2011), pp. 1040–1054. ISSN: 08966273. DOI: [10.1016/j.neuron.2011.12.004](https://doi.org/10.1016/j.neuron.2011.12.004).
- [188] Ryuichi Maruyama, Kazuma Maeda, Hajime Moroda, Ichiro Kato, Masashi Inoue, Hiroyoshi Miyakawa, and Toru Aonishi. "Detecting cells using non-negative matrix factorization on calcium imaging data." In: *Neural Networks* 55 (2014), pp. 11–19. ISSN: 18792782. DOI: [10.1016/j.neunet.2014.03.007](https://doi.org/10.1016/j.neunet.2014.03.007).
- [189] Richard H. Masland. "The fundamental plan of the retina." In: *Nature Neuroscience* 4.9 (2001), pp. 877–886. ISSN: 1097-6256. DOI: [10.1038/nn0901-877](https://doi.org/10.1038/nn0901-877).
- [190] Ulrike Matthies, Jenny Balog, and Konrad Lehmann. "Temporally coherent visual stimuli boost ocular dominance plasticity." In: *Journal of Neuroscience* 33.29 (2013), pp. 11774–11778. DOI: [10.1523/JNEUROSCI.4262-12.2013](https://doi.org/10.1523/JNEUROSCI.4262-12.2013).
- [191] Mark Mazurek, Marisa Kager, and Stephen D. Van Hooser. "Robust quantification of orientation selectivity and direction selectivity." In: *Frontiers in Neural Circuits* 8 (2014), pp. 1–17. ISSN: 1662-5110. DOI: [10.3389/fncir.2014.00092](https://doi.org/10.3389/fncir.2014.00092).
- [192] David A. McCormick, Zhong Wang, and John Huguenard. "Neurotransmitter control of neuronal activity and excitability." In: *Cerebral Cortex* 3 (1993), pp. 387–398.
- [193] Cortina L. McCurry, Jason D. Shepherd, Daniela Tropea, Kuan Hong Wang, Mark F. Bear, and Mriganka Sur. "Loss of Arc renders the visual cortex impervious to the effects of sensory experience or deprivation." In: *Nature neuroscience* 13.4 (2010), pp. 450–7. ISSN: 1546-1726. DOI: [10.1038/nn.2508](https://doi.org/10.1038/nn.2508).

- [194] Laura M. McGarry, Adam M. Packer, Elodie Fino, Voldodymyr Nikolenko, Tanya Sippy, and Rafael Yuste. “Quantitative classification of somatostatin-positive neocortical interneurons identifies three interneuron subtypes.” In: *Frontiers in Neural Circuits* 4 (2010), pp. 1–19. ISSN: 16625110. DOI: [10.3389/fncir.2010.00012](https://doi.org/10.3389/fncir.2010.00012).
- [195] Aaron W. McGee, Yupeng Yang, Quentin S. Fischer, Nigel W. Daw, and Stephen M. Strittmatter. “Experience-driven plasticity of visual cortex limited by myelin and Nogo receptor.” In: *Science* 309.5744 (2005), pp. 2222–2226. ISSN: 0036-8075. DOI: [10.1126/science.1114362](https://doi.org/10.1126/science.1114362).
- [196] Matthew J. McGinley, Martin Vinck, Jacob Reimer, Renata Batista-Brito, Edward Zagher, Cathryn R. Cadwell, Andreas S. Tolias, Jessica A. Cardin, and David A. McCormick. “Waking state: Rapid variations modulate neural and behavioral responses.” In: *Neuron* 87.6 (2015), pp. 1143–1161. ISSN: 10974199. DOI: [10.1016/j.neuron.2015.09.012](https://doi.org/10.1016/j.neuron.2015.09.012).
- [197] James McPartland and Fred R. Volkmar. *Chapter 23 – Autism and related disorders*. 3rd ed. Vol. 106. Elsevier B.V., 2012, pp. 407–418. ISBN: 9780444520029. DOI: [10.1016/B978-0-444-52002-9.00023-1](https://doi.org/10.1016/B978-0-444-52002-9.00023-1).
- [198] Heather C. Mefford, Mark L. Batshaw, and Eric P. Hoffman. “Genomics, Intellectual Disability, and Autism.” In: (2012), pp. 733–743. ISSN: 1533-4406. DOI: [10.1056/NEJMra1114194](https://doi.org/10.1056/NEJMra1114194).
- [199] Jerome Mertz. *A practical guide: Building a two-photon laser-scanning microscope*. 2005, pp. 71–74.
- [200] C. Metin, P. Godement, and M. Imbert. “The primary visual cortex in the mouse receptive field properties and functional organization.” In: 1987 (2000), pp. 594–612.
- [201] Goichi Miyoshi, Jens Hjerling-Leffler, Theofanis Karayannis, Vitor H. Sousa, Simon J. B. Butt, James Battiste, Jane E. Johnson, Robert P. Machold, and Gord Fishell. “Genetic fate mapping reveals that the caudal ganglionic eminence produces a large and diverse population of superficial cortical interneurons.” In: *Journal of Neuroscience* 30.5 (2010), pp. 1582–1594. ISSN: 0270-6474. DOI: [10.1523/JNEUROSCI.4515-09.2010](https://doi.org/10.1523/JNEUROSCI.4515-09.2010).
- [202] Il Soo Moon, Michelle L. Apperson, and Mary B. Kennedy. “The major tyrosine-phosphorylated protein in the postsynaptic density fraction is N-methyl-D-aspartate receptor subunit 2B.” In: *Proceedings of the National Academy of Sciences of the United States of America* 91.9 (1994), pp. 3954–3958. ISSN: 0027-8424. DOI: [10.1073/pnas.91.9.3954](https://doi.org/10.1073/pnas.91.9.3954).
- [203] Bernardo Morales, Se-young Choi, and Alfredo Kirkwood. “Dark rearing alters the development of GABAergic transmission in visual cortex.” In: 22.18 (2002), pp. 8084–8090.

- [204] Nicolás A. Morgenstern, Jacques Bourg, and Leopoldo Petreanu. “Improving membrane voltage measurements using FRET with new fluorescent proteins.” In: *Nature Neuroscience* 19.8 (2016), pp. 1034–1040. ISSN: 15461726. DOI: [10.1038/nn.4339](https://doi.org/10.1038/nn.4339).
- [205] Hirofumi Morishita, Julie M. Miwa, Nathaniel Heintz, and Takao K. Hensch. “Lynx1, a cholinergic brake, limits plasticity in adult visual cortex.” In: *Science* 330.6008 (2010), pp. 1238–1240. ISSN: 0036-8075. DOI: [10.1126/science.1195320](https://doi.org/10.1126/science.1195320).
- [206] Brad C. Motter. “Focal attention produces spatially selective processing in visual cortical areas V1, V2, and V4 in the presence of competing stimuli.” In: *Journal of Neurophysiology* 70.3 (1993), pp. 909–919. ISSN: 0022-3077. DOI: [0022-3077/93](https://doi.org/10.1152/jn.1993.70.3.909).
- [207] George D. Mower. “The effect of dark rearing on the time course of the critical period in cat visual cortex.” In: *Developmental Brain Research* 58 (1991), pp. 151–158.
- [208] Thomas D. Mrsic-Flogel, Sonja B. Hofer, Kenichi Ohki, R. Clay Reid, Tobias Bonhoeffer, and Mark Hübener. “Homeostatic regulation of eye-specific responses in visual cortex during ocular dominance plasticity.” In: *Neuron* 6.54 (2007), pp. 961–972. DOI: [10.1016/j.neuron.2007.05.028](https://doi.org/10.1016/j.neuron.2007.05.028).
- [209] Mary Muhia, Benjamin K. Yee, Joram Feldon, Foivos Markopoulos, and Irene Knuesel. “Disruption of hippocampus-regulated behavioural and cognitive processes by heterozygous constitutive deletion of SynGAP.” In: *European Journal of Neuroscience* 31.3 (2010), pp. 529–543. ISSN: 0953816X. DOI: [10.1111/j.1460-9568.2010.07079.x](https://doi.org/10.1111/j.1460-9568.2010.07079.x).
- [210] Eran Mukamel, Axel Nimmerjahn, and Mark J. Schnitzer. “Automated analysis of cellular signals from large-scale calcium imaging data.” In: *Neuron* 63.6 (2009), pp. 747–760. ISSN: 08966273. DOI: [10.1016/j.neuron.2009.08.009](https://doi.org/10.1016/j.neuron.2009.08.009). Automated.
- [211] William Muñoz, Robin Tremblay, Daniel Levenstein, and Bernardo Rudy. “Layer-specific modulation of neocortical dendritic inhibition during active wakefulness.” In: 959 (2017), pp. 954–959.
- [212] Masanori Murayama, Enrique Perez-Garci, Thomas Nevian, Tobias Bock, Walter Senn, and Matthew E. Larkum. “Dendritic encoding of sensory stimuli controlled by deep cortical interneurons.” In: *Nature* 457 (2009), pp. 1137–1141. ISSN: 0028-0836. DOI: [10.1038/nature07663](https://doi.org/10.1038/nature07663).
- [213] K. M.Naga Srinivas Nadella, Hana Roš, Chiara Baragli, Victoria A. Griffiths, George Konstantinou, Theo Koimtzis, Geoffrey J. Evans, Paul A. Kirkby, and R. Angus Silver. “Random-access scanning microscopy for 3D imaging in

- awake behaving animals." In: *Nature Methods* 13.12 (2016), pp. 1001–1004. ISSN: 15487105. DOI: [10.1038/nmeth.4033](https://doi.org/10.1038/nmeth.4033).
- [214] J. L. Nathanson, Y. Yanagawa, K. Obata, and E. M. Callaway. "Preferential labeling of inhibitory and excitatory cortical neurons by endogenous tropism of adeno-associated virus and lentivirus vectors." In: *Neuroscience* 161.2 (2009), pp. 441–450. ISSN: 03064522. DOI: [10.1016/j.neuroscience.2009.03.032](https://doi.org/10.1016/j.neuroscience.2009.03.032).
- [215] Cristopher M. Niell. "Cell types, circuits, and receptive fields in the mouse visual cortex." In: *Annual Review of Neuroscience* 38.1 (2015), pp. 413–431. ISSN: 0147-006X. DOI: [10.1146/annurev-neuro-071714-033807](https://doi.org/10.1146/annurev-neuro-071714-033807).
- [216] Cristopher M. Niell and Michael P. Stryker. "Highly selective receptive fields in mouse visual cortex." In: *Journal of Neuroscience* 28.30 (2008), pp. 7520–7536. ISSN: 0270-6474. DOI: [10.1523/JNEUROSCI.0623-08.2008](https://doi.org/10.1523/JNEUROSCI.0623-08.2008).
- [217] Cristopher M. Niell and Michael P. Stryker. "Modulation of visual responses by behavioral state in mouse visual cortex." In: *Neuron* 65.4 (2010), pp. 472–479. ISSN: 08966273. DOI: [10.1016/j.neuron.2010.01.033](https://doi.org/10.1016/j.neuron.2010.01.033).
- [218] Jess Nithianantharajah and Anthony J. Hannan. "Enriched environments, experience-dependent plasticity and disorders of the nervous system." In: *Nature Reviews Neuroscience* 7.9 (2006), pp. 697–709. ISSN: 1471-003X. DOI: [10.1038/nrn1970](https://doi.org/10.1038/nrn1970).
- [219] Daniel H. O'Connor, Daniel Huber, and Karel Svoboda. "Reverse engineering the mouse brain." In: *Nature* 461.7266 (2009), pp. 923–929. ISSN: 0028-0836. DOI: [10.1038/nature08539](https://doi.org/10.1038/nature08539).
- [220] Martin Oheim, Emmanuel Beaurepaire, Emmanuelle Chaigneau, Jerome Mertz, and Serge Charpak. "Two-photon microscopy in brain tissue: parameters influencing the imaging depth." In: *Journal of Neuroscience Methods* 111 (2001), pp. 29–37. ISSN: 01650270. DOI: [10.1016/S0165-0270\(01\)00495-2](https://doi.org/10.1016/S0165-0270(01)00495-2).
- [221] Kenichi Ohki, Sooyoung Chung, Yeang H. Ch'ng, Prakash Kara, and R. Clay Reid. "Functional imaging with cellular resolution reveals precise micro-architecture in visual cortex." In: *Nature* 433.7026 (2005), pp. 597–603. ISSN: 0028-0836. DOI: [10.1038/nature03274](https://doi.org/10.1038/nature03274).
- [222] Szabolcs Olah, Miklos Fuele, Gergely Komlosi, Csaba Varga, Rita Baldi, Pal Barzo, and Gabor Tamas. "Regulation of cortical microcircuits by unitary GABA-mediated volume transmission." In: *Nature* 461.7268 (2009), pp. 1278–81. ISSN: 1476-4687. DOI: [10.1038/nature08503](https://doi.org/10.1038/nature08503).
- [223] Emin D. Ozkan, Thomas K. Creson, Enikő A. Kramár, Camilo Rojas, Ron R. Seese, Alex H. Babyan, Yulin Shi, Rocco Lucero, Xiangmin Xu, Jeffrey L. Noebels, Courtney A. Miller, Gary Lynch, and Gavin Rumbaugh. "Reduced cognition in Syngap1 mutants is caused by isolated damage within developing forebrain excitatory neurons." In: *Neuron* 82.6 (2014), pp. 1317–1333. ISSN: 10974199. DOI: [10.1016/j.neuron.2014.05.015](https://doi.org/10.1016/j.neuron.2014.05.015).

- [224] Marius Pachitariu, Carsen Stringer, Sylvia Schröder, Mario Dipoppa, L. Federico Rossi, Matteo Carandini, and Kenneth D Harris. “Suite2p: beyond 10,000 neurons with standard two-photon microscopy.” In: *bioRxiv* (2016), p. 061507. ISSN: 0092-8674. DOI: [10.1101/061507](https://doi.org/10.1101/061507).
- [225] D. E. Pafundo, M. A. Nicholas, R. Zhang, and S. J. Kuhlman. “Top-down-mediated facilitation in the visual cortex is gated by subcortical neuromodulation.” In: *Journal of Neuroscience* 36.10 (2016), pp. 2904–2914. ISSN: 0270-6474. DOI: [10.1523/JNEUROSCI.2909-15.2016](https://doi.org/10.1523/JNEUROSCI.2909-15.2016).
- [226] Janelle M. P. Pakan, Scott C. Lowe, Evelyn Dylida, Sander W. Keemink, Stephen P. Currie, Christopher A. Coutts, and Nathalie L. Rochefort. “Behavioral-state modulation of inhibition is context-dependent and cell type specific in mouse visual cortex.” In: *eLife* 5 (2016), pp. 1–18. ISSN: 2050084X. DOI: [10.7554/eLife.14985](https://doi.org/10.7554/eLife.14985).
- [227] E. Pasciuto, S. C. Borrie, A. K. Kanellopoulos, A. R. Santos, E. Cappuyns, L. D’Andrea, L. Pacini, and C. Bagni. “Autism Spectrum Disorders: Translating human deficits into mouse behavior.” In: *Neurobiology of Learning and Memory* 124 (2015), pp. 71–87. ISSN: 10959564. DOI: [10.1016/j.nlm.2015.07.013](https://doi.org/10.1016/j.nlm.2015.07.013).
- [228] Simon P. Peron, Jeremy Freeman, Vijay Iyer, Caiying Guo, and Karel Svoboda. “A cellular resolution map of barrel cortex activity during tactile behavior.” In: *Neuron* 86.3 (2015), pp. 783–799. ISSN: 10974199. DOI: [10.1016/j.neuron.2015.03.027](https://doi.org/10.1016/j.neuron.2015.03.027).
- [229] Simon Peron, Tsai-Wen Chen, and Karel Svoboda. “Comprehensive imaging of cortical networks.” In: *Current Opinion in Neurobiology* 32 (2015), pp. 115–123. ISSN: 09594388. DOI: [10.1016/j.conb.2015.03.016](https://doi.org/10.1016/j.conb.2015.03.016).
- [230] Carl C H Petersen and Sylvain Crochet. “Synaptic computation and sensory processing in neocortical layer 2/3.” In: *Neuron* 78.1 (2013), pp. 28–48. ISSN: 08966273. DOI: [10.1016/j.neuron.2013.03.020](https://doi.org/10.1016/j.neuron.2013.03.020).
- [231] Warner L. Peticolas, John P. Goldsborough, and K. E. Rieckhoff. “Double photon excitation in organic crystals.” In: *Physical Review Letters* 10.2 (1963), pp. 43–45. ISSN: 00319007. DOI: [10.1103/PhysRevLett.10.43](https://doi.org/10.1103/PhysRevLett.10.43).
- [232] Leopoldo Petreanu, Tianyi Mao, Scott M. Sternson, and Karel Svoboda. “The subcellular organization of neocortical excitatory connections.” In: *Nature* 457.7233 (2009), pp. 1142–1145. ISSN: 0028-0836. DOI: [10.1038/nature07709](https://doi.org/10.1038/nature07709).
- [233] Carsten K. Pfeffer, Mingshan Xue, Miao He, Z. Josh Huang, and Massimo Scanziani. “Inhibition of inhibition in visual cortex: The logic of connections between molecularly distinct interneurons.” In: *Nature Neuroscience* 16.8 (2013), pp. 1068–76. ISSN: 1546-1726. DOI: [10.1038/nn.3446](https://doi.org/10.1038/nn.3446).

- [234] Hyun-Jae Pi, Balázs Hangya, Duda Kvitsiani, Joshua I. Sanders, Z. Josh Huang, and Adam Kepecs. “Cortical interneurons that specialize in disinhibitory control.” In: *Nature* 503.7477 (2013), pp. 521–524. ISSN: 0028-0836. DOI: [10.1038/nature12676](https://doi.org/10.1038/nature12676).
- [235] Dalila Pinto et al. “Functional impact of global rare copy number variation in autism spectrum disorder.” In: *Nature* 466.7304 (2010), pp. 368–372. ISSN: 1476-4687. DOI: [10.1038/nature09146](https://doi.org/10.1038/nature09146). **Functional**.
- [236] Lucas Pinto, Michael J Goard, Daniel Estandian, Min Xu, Alex C Kwan, Seung-Hee Lee, Thomas C Harrison, Guoping Feng, and Yang Dan. “Fast modulation of visual perception by basal forebrain cholinergic neurons.” In: *Nature Neuroscience* 16.12 (2013), pp. 1857–1863. ISSN: 1097-6256. DOI: [10.1038/nn.3552](https://doi.org/10.1038/nn.3552).
- [237] Eftychios A. Pnevmatikakis, Daniel Soudry, Yuanjun Gao, Timothy A. Machado, Josh Merel, David Pfau, Thomas Reardon, Yu Mu, Clay Lacefield, Weijian Yang, Misha Ahrens, Randy Bruno, Thomas M. Jessell, Darcy S. Peterka, Rafael Yuste, and Liam Paninski. “Simultaneous denoising, Deconvolution, and demixing of calcium imaging data.” In: *Neuron* 89.2 (2016), p. 299. ISSN: 10974199. DOI: [10.1016/j.neuron.2015.11.037](https://doi.org/10.1016/j.neuron.2015.11.037).
- [238] Pierre-Olivier Polack, Jonathan Friedman, and Peyman Golshani. “Cellular mechanisms of brain state-dependent gain modulation in visual cortex.” In: *Nature Neuroscience* 16.9 (2013), pp. 1331–1339. ISSN: 1097-6256. DOI: [10.1038/nn.3464](https://doi.org/10.1038/nn.3464).
- [239] Jasper Poort, Adil G. Khan, Marius Pachitariu, Ivana Orsolich, Julija Krupic, Marius Bauza, Maneesh Sahani, Georg B. Keller, Thomas D. Mrsic-Flogel, and Sonja B. Hofer. “Learning enhances sensory and multiple non-sensory representations in primary visual cortex article learning enhances sensory and multiple non-sensory representations in primary visual cortex.” In: *Neuron* 86.6 (2015), pp. 1478–1490. ISSN: 0896-6273. DOI: [10.1016/j.neuron.2015.05.037](https://doi.org/10.1016/j.neuron.2015.05.037).
- [240] Steve M. Potter. “Vital imaging: two photons are better than one.” In: *Current Biology* 6 (1996), pp. 1595–8. ISSN: 0960-9822. DOI: [10.1016/S0960-9822\(02\)70782-3](https://doi.org/10.1016/S0960-9822(02)70782-3).
- [241] Nicholas J. Priebe and Aaron W. McGee. “Mouse vision as a gateway for understanding how experience shapes neural circuits.” In: *Frontiers in Neural Circuits* 8.123 (2014), p. 123. ISSN: 1662-5110. DOI: [10.3389/fncir.2014.00123](https://doi.org/10.3389/fncir.2014.00123).
- [242] Adam Ranson. “Stability and plasticity of contextual modulation in the mouse visual cortex.” In: *CellReports* 18.4 (2016), pp. 1–31. ISSN: 22111247. DOI: [10.1016/j.celrep.2016.12.080](https://doi.org/10.1016/j.celrep.2016.12.080).

- [243] Adam Ranson, Claire E. J. Cheetham, Kevin Fox, and Frank Sengpiel. "Homeostatic plasticity mechanisms are required for juvenile, but not adult, ocular dominance plasticity." In: *Proceedings of the National Academy of Sciences of the United States of America* 109.4 (2012), pp. 1311–1316. DOI: [10.1073/pnas.1112204109](https://doi.org/10.1073/pnas.1112204109).
- [244] S. Chenchal Rao, Louis J. Toth, and Mriganka Sur. "Optically imaged maps of orientation preference in primary visual cortex of cats and ferrets." In: *The Journal of Comparative Neurology* 387 (1997), pp. 358–370.
- [245] Jacob Reimer, Emmanouil Froudarakis, Cathryn R. Cadwell, Dimitri Yatsenko, George H. Denfield, and Andreas S. Tolias. "Pupil fluctuations track fast switching of cortical states during quiet wakefulness." In: *Neuron* 84.2 (2014), pp. 355–362. ISSN: 10974199. DOI: [10.1016/j.neuron.2014.09.033](https://doi.org/10.1016/j.neuron.2014.09.033).
- [246] Shanna L. Resendez and Garret D. Stuber. "In vivo calcium imaging to illuminate neurocircuit activity dynamics underlying naturalistic behavior." In: *Neuropsychopharmacology* 40.1 (2015), pp. 238–239. ISSN: 0893-133X. DOI: [10.1038/npp.2014.206](https://doi.org/10.1038/npp.2014.206).
- [247] Leonardo Restivo, Francesca Ferrari, Enrica Passino, Carmelo Sgobio, Ben A. Oostra, Claudia Bagni, and Martine Ammassari-Teule. "Enriched environment promotes behavioral and morphological recovery in a mouse model for the fragile X syndrome." In: *Proceedings of the National Academy of Sciences of the United States of America* 102.32 (2005), pp. 11557–11562. DOI: <https://doi.org/10.1073/pnas.0504984102>.
- [248] John H. Reynolds and David J. Heeger. "The normalization model of attention." In: *Neuron* 61.2 (2009), pp. 168–185. ISSN: 08966273. DOI: [10.1016/j.neuron.2009.01.002](https://doi.org/10.1016/j.neuron.2009.01.002).
- [249] Dario L Ringach, Robert M Shapley, and Michael J Hawken. "Orientation selectivity in macaque V1: diversity and laminar dependence." In: *The Journal of Neuroscience* 22.13 (2002), pp. 5639–5651. ISSN: 1529-2401. DOI: [20026567](https://doi.org/10.1523/JNEUROSCI.2002-02.2002).
- [250] Nathalie L. Rochefort, Madoka Narushima, Christine Grienberger, Nima Marandi, Daniel N. Hill, and Arthur Konnerth. "Development of direction selectivity in mouse cortical neurons." In: *Neuron* 71.3 (2011), pp. 425–432. ISSN: 08966273. DOI: [10.1016/j.neuron.2011.06.013](https://doi.org/10.1016/j.neuron.2011.06.013).
- [251] Nathalie L. Rochefort, Olga Garaschuk, Ruxandra-Iulia Milos, Madoka Narushima, Nima Marandi, Bruno Pichler, Yury Kovalchuk, and Arthur Konnerth. "Sparsification of neuronal activity in the visual cortex at eye-opening." In: *Proceedings of the National Academy of Sciences of the United States of America* 106.35 (2009), pp. 15049–54. ISSN: 1091-6490. DOI: [10.1073/pnas.0907660106](https://doi.org/10.1073/pnas.0907660106).

- [252] Sebastián A. Romano, Verónica Pérez-Schuster, Adrien Jouary, Jonathan Boulanger-Weill, Alessia Candeo, Thomas Pietri, and Germán Sumbre. “An integrated calcium imaging processing toolbox for the analysis of neuronal population dynamics.” In: *PLoS Computational Biology* 13.6 (2017). ISSN: 15537358. DOI: [10.1371/journal.pcbi.1005526](https://doi.org/10.1371/journal.pcbi.1005526).
- [253] Tobias Rose, Juliane Jäpel, Mark Hübener, and Tobias Bonhoeffer. “Cell-specific restoration of stimulus preference after monocular deprivation in the visual cortex.” In: *Science* 1319 (2016). DOI: [10.1126/science.aad3358](https://doi.org/10.1126/science.aad3358).
- [254] Laura B. Rosen, David D. Ginty, Michael J. Weber, and Michael E. Greenberg. “Membrane depolarization and calcium influx stimulate MEK and MAP kinase via activation of Ras.” In: *Neuron* 12.6 (1994), pp. 1207–1221. ISSN: 08966273. DOI: [10.1016/0896-6273\(94\)90438-3](https://doi.org/10.1016/0896-6273(94)90438-3).
- [255] Morgane M. Roth, Johannes C. Dahmen, Dylan R. Muir, Fabia Imhof, Francisco J. Martini, and Sonja B. Hofer. “Thalamic nuclei convey diverse contextual information to layer 1 of visual cortex.” In: *Nature Neuroscience* 19.2 (2015), pp. 299–307. ISSN: 1097-6256. DOI: [10.1038/nn.4197](https://doi.org/10.1038/nn.4197).
- [256] Pablo Rubio-Garrido, Flor Pérez-De-Manzo, César Porrero, Maria J. Galazo, and Francisco Clascá. “Thalamic input to distal apical dendrites in neocortical layer 1 is massive and highly convergent.” In: *Cerebral Cortex* 10.10 (2009), pp. 2380–2395. ISSN: 10473211. DOI: [10.1093/cercor/bhn259](https://doi.org/10.1093/cercor/bhn259).
- [257] Bernardo Rudy, Gordon Fishell, SooHyun Lee, and Jens Hjerling-Leffler. “Three groups of interneurons account for nearly 100% of neocortical GABAergic neurons.” In: *Developmental Neurobiology* 71.1 (2011), pp. 45–61. ISSN: 19328451. DOI: [10.1002/dneu.20853](https://doi.org/10.1002/dneu.20853).
- [258] Gavin Rumbaugh, J. Paige Adams, Jee H. Kim, and Richard L. Huganir. “SynGAP regulates synaptic strength and mitogen-activated protein kinases in cultured neurons.” In: *Proceedings of the National Academy of Sciences* 103.12 (2006), pp. 4344–4351. ISSN: 0027-8424. DOI: [10.1073/pnas.0600084103](https://doi.org/10.1073/pnas.0600084103).
- [259] Caroline A. Runyan, James Schummers, Audra Van Wart, Sandra J. Kuhlman, Nathan R. Wilson, Z. Josh Huang, and Mriganka Sur. “Response features of parvalbumin-expressing interneurons suggest precise roles for subtypes of inhibition in visual cortex.” In: *Neuron* 67.5 (2010), pp. 847–857. ISSN: 08966273. DOI: [10.1016/j.neuron.2010.08.006](https://doi.org/10.1016/j.neuron.2010.08.006).
- [260] Aman B. Saleem, Asli Ayaz, Kathryn J. Jeffery, Kenneth D. Harris, and Matteo Carandini. “Integration of visual motion and locomotion in mouse visual cortex.” In: *Nature Neuroscience* 16.12 (2013), pp. 1864–1869. ISSN: 1097-6256. DOI: [10.1038/nn.3567](https://doi.org/10.1038/nn.3567).

- [261] Rosanna P. Sammons and Tara Keck. "Adult plasticity and cortical reorganization after peripheral lesions." In: *Current Opinion in Neurobiology* 35 (2015), pp. 136–141. ISSN: 18736882. DOI: [10.1016/j.conb.2015.08.004](https://doi.org/10.1016/j.conb.2015.08.004).
- [262] Nathaniel B. Sawtell, Mikhail Y. Frenkel, Benjamin D. Philpot, Kazu Nakazawa, Susumu Tonegawa, and Mark F. Bear. "NMDA receptor-dependent ocular dominance plasticity in adult visual cortex." In: *Neuron* 38.6 (2003), pp. 977–985. ISSN: 0896-6273. DOI: [S0896627303003234\[pii\]](https://doi.org/10.1016/j.neuron.2003.06.011).
- [263] Manuela Scali, Laura Baroncelli, Maria Cristina Cenni, Alessandro Sale, and Lamberto Maffei. "A rich environmental experience reactivates visual cortex plasticity in aged rats." In: *Experimental Gerontology* 47.4 (2012), pp. 337–341. ISSN: 05315565. DOI: [10.1016/j.exger.2012.01.007](https://doi.org/10.1016/j.exger.2012.01.007).
- [264] Aniek A. Schoups, Rufin Vogels, and Guy A. Orban. "Human perceptual learning in identifying the oblique orientation: retinotopy, orientation specificity and monocularly." In: *The Journal of Physiology* 483 (Pt 3 (1995), pp. 797–810. ISSN: 0022-3751. DOI: [10.1113/jphysiol.1995.sp020623](https://doi.org/10.1113/jphysiol.1995.sp020623).
- [265] Aniek A. Schoups, Rufin Vogels, Ning Qian, and Guy A. Orban. "Practising orientation identification improves orientation coding in V1 neurons." In: *Nature* 412.6846 (2001), pp. 549–553. ISSN: 0028-0836. DOI: [10.1038/35087601](https://doi.org/10.1038/35087601).
- [266] Sven Schütt, Tobias Bonhoeffer, and Mark Hübener. "Mapping retinotopic structure in mouse visual cortex with optical imaging." In: *Journal of Neuroscience* 22.15 (2002), pp. 6549–6559. ISSN: 1529-2401. DOI: [20026635](https://doi.org/10.1523/JNEUROSCI.0800-02.2002).
- [267] Robert Shapley. "Visual sensitivity and parallel retinocortical channels." In: *Annual Review of Psychology* 41.1 (1990), pp. 635–658. ISSN: 0066-4308. DOI: [10.1146/annurev.ps.41.020190.003223](https://doi.org/10.1146/annurev.ps.41.020190.003223).
- [268] Marshall G. Shuler and Mark F. Bear. "Reward timing in the primary visual cortex." In: *Science* 311.12 (2006), pp. 1606–1609. DOI: [10.1038/nature04781](https://doi.org/10.1126/science.1126216). **Decoding.**
- [269] Ikuko T. Smith, Leah B. Townsend, Ruth Huh, Hongtu Zhu, and Spencer L. Smith. "Stream-dependent development of higher visual cortical areas." In: *Nature Neuroscience* 20.2 (2017), pp. 1–11. ISSN: 1097-6256. DOI: [10.1038/nrn.4469](https://doi.org/10.1038/nrn.2017.10).
- [270] Kyle S. Smith, David J. Bucci, Bryan W. Luikart, and Stephen V. Mahler. "DRE-ADDS: Use and application in behavioral neuroscience." In: *Behavioral Neuroscience* 130.2 (2016), pp. 137–155. ISSN: 1939-0084. DOI: [10.1037/bne0000135](https://doi.org/10.1037/bne0000135).
- [271] Spencer L. Smith, Ikuko T. Smith, Tiago Branco, and Michael Häusser. "Dendritic spikes enhance stimulus selectivity in cortical neurons in vivo." In: *Nature* 503.7474 (2013), pp. 115–20. ISSN: 1476-4687. DOI: [10.1038/nature12600](https://doi.org/10.1038/nature12600).

- [272] Nicholas J. Sofroniew, Daniel Flickinger, Jonathan King, and Karel Svoboda. "A large field of view two-photon mesoscope with subcellular resolution for in vivo imaging." In: *eLife* 5 (2016). ISSN: 2050084X. DOI: [10.7554/eLife.14472](https://doi.org/10.7554/eLife.14472).
- [273] Kazuhiro Sohya, Katsuro Kameyama, Yuchio Yanagawa, Kunihiro Obata, and Tadaharu Tsumoto. "GABAergic neurons are less selective to stimulus orientation than excitatory neurons in layer II/III of visual cortex, as revealed by in vivo functional Ca²⁺ imaging in transgenic mice." In: *Journal of Neuroscience* 27.8 (2007), pp. 2145–2149. ISSN: 0270-6474. DOI: [10.1523/JNEUROSCI.4641-06.2007](https://doi.org/10.1523/JNEUROSCI.4641-06.2007).
- [274] Chenchen Song, Samuel Barnes, and Thomas Knöpfel. "Mammalian cortical voltage imaging using genetically encoded voltage indicators: a review honoring professor Amiram Grinvald." In: *Neurophotonics* 4.3 (2017), p. 031214. ISSN: 2329-423X. DOI: [10.1117/1.NPh.4.3.031214](https://doi.org/10.1117/1.NPh.4.3.031214).
- [275] M Stetter, I Schiessl, T Otto, Frank Sengpiel, Mark Hübener, Tobias Bonhoeffer, and K Obermayer. "Principal component analysis and blind separation of sources for optical imaging of intrinsic signals." In: *NeuroImage* 11 (2000), pp. 482–490. ISSN: 1053-8119. DOI: [10.1006/nimg.2000.0551](https://doi.org/10.1006/nimg.2000.0551).
- [276] Jeffrey N. Stirman, Leah B. Townsend, and Spencer L. Smith. "A touchscreen based global motion perception task for mice." In: *Vision Research* 127 (2016), pp. 74–83. ISSN: 18785646. DOI: [10.1016/j.visres.2016.07.006](https://doi.org/10.1016/j.visres.2016.07.006).
- [277] Jeffrey N. Stirman, Ikuko T. Smith, Michael W. Kudenov, and Spencer L. Smith. "Wide field-of-view, multi-region, two-photon imaging of neuronal activity in the mammalian brain." In: *Nature Biotechnology* 34.8 (2016), pp. 857–862. ISSN: 1087-0156. DOI: [10.1038/nbt.3594](https://doi.org/10.1038/nbt.3594).
- [278] Jeffrey N. Stirman, Ikuko T. Smith, Michael W. Kudenov, and Spencer L. Smith. "Wide field-of-view, multi-region two-photon imaging of neuronal activity." In: *bioRxiv preprint* (2014).
- [279] Sophia Katharina Stodieck, Franziska Greifzu, Bianka Goetze, Karl Friedrich Schmidt, and Siegrid Löwel. "Brief dark exposure restored ocular dominance plasticity in aging mice and after a cortical stroke." In: *Experimental Gerontology* 60 (2014), pp. 1–11. DOI: [10.1016/j.exger.2014.09.007](https://doi.org/10.1016/j.exger.2014.09.007).
- [280] Karel Svoboda and Ryohei Yasuda. "Principles of two-photon excitation microscopy and its applications to neuroscience." In: *Neuron* 50.6 (2006), pp. 823–39. ISSN: 0896-6273. DOI: [10.1016/j.neuron.2006.05.019](https://doi.org/10.1016/j.neuron.2006.05.019).
- [281] Karel Svoboda, Winfried Denk, David Kleinfeld, and David W. Tank. *In vivo dendritic calcium dynamics in neocortical pyramidal neurons*. 1997. DOI: [10.1038/385161a0](https://doi.org/10.1038/385161a0).

- [282] Nicholas V. Swindale. "Is the cerebral cortex modular ?" In: *Trends in Neurosciences* 13.12 (1990), pp. 487–492. DOI: [https://doi.org/10.1016/0166-2236\(90\)90082-L](https://doi.org/10.1016/0166-2236(90)90082-L).
- [283] Hiroki Taniguchi, Miao He, Priscilla Wu, Sangyong Kim, Raehum Paik, Ken Sugino, Duda Kvitsani, Yu Fu, Jiangteng Lu, Ying Lin, Goichi Miyoshi, Yasuyuki Shima, Gord Fishell, Sacha B. Nelson, and Z. Josh Huang. "A Resource of Cre driver lines for genetic targeting of GABAergic neurons in cerebral cortex." In: *Neuron* 71.6 (2011), pp. 995–1013. ISSN: 08966273. DOI: [10.1016/j.neuron.2011.07.026](https://doi.org/10.1016/j.neuron.2011.07.026).
- [284] Patrick Theer, Mazahir T. Hasan, and Winfried Denk. "Two-photon imaging to a depth of 1000 microm in living brains by use of a Ti:Al₂O₃ regenerative amplifier." In: *Optics Letters* 28.12 (2003), pp. 1022–1024. ISSN: 0146-9592. DOI: [10.1364/OL.28.001022](https://doi.org/10.1364/OL.28.001022).
- [285] Gareth M. Thomas and Richard L. Huganir. "MAPK cascade signalling and synaptic plasticity." In: *Nature Reviews Neuroscience* 5.3 (2004), pp. 173–183. ISSN: 1471-003X. DOI: [10.1038/nrn1346](https://doi.org/10.1038/nrn1346).
- [286] Lin Tian, S. Andrew Hires, and Loren L. Looger. "Imaging neuronal activity with genetically encoded calcium indicators." In: *Cold Spring Harbor Protocols* 7.6 (2012), pp. 647–656. ISSN: 19403402. DOI: [10.1101/pdb.top069609](https://doi.org/10.1101/pdb.top069609).
- [287] Robin Tremblay, Soohyun Lee, and Bernardo Rudy. "GABAergic interneurons in the neocortex: From cellular properties to circuits." In: *Neuron* 91.2 (2016), pp. 260–292. DOI: [10.1016/j.neuron.2016.06.033](https://doi.org/10.1016/j.neuron.2016.06.033).
- [288] Stefan Treue and Julio C. Martínez Trujillo. "Feature-based attention influences motion processing gain in macaque visual cortex." In: *Nature* 399.6736 (1999), pp. 575–579. ISSN: 0028-0836. DOI: [10.1038/21176](https://doi.org/10.1038/21176).
- [289] Gina G. Turrigiano. "Homeostatic synaptic plasticity: Local and global mechanisms for stabilizing neuronal function." In: *Cold Spring Harbor Perspectives in Biology* 4.1 (2012), pp. 1–17. ISSN: 19430264. DOI: [10.1101/cshperspect.a005736](https://doi.org/10.1101/cshperspect.a005736).
- [290] Stephen D. Van Hooser. "Similarity and diversity in visual cortex: Is there a unifying theory of cortical computation?" In: *Neuroscientist* 13.6 (2007), pp. 639–656. ISSN: 10738584. DOI: [10.1177/1073858407306597](https://doi.org/10.1177/1073858407306597).
- [291] Luis E. Vazquez, Hong-Jung Chen, Irina Sokolova, Irene Knuesel, and Mary B. Kennedy. "SynGAP regulates spine formation." In: *Journal of Neuroscience* 24.40 (2004), pp. 8862–8872. ISSN: 0270-6474. DOI: [10.1523/JNEUROSCI.3213-04.2004](https://doi.org/10.1523/JNEUROSCI.3213-04.2004).

- [292] Martin Vinck, Renata Batista-Brito, Ulf Knoblich, and Jessica A. Cardin. "Arousal and locomotion make distinct contributions to cortical activity patterns and visual encoding." In: *Neuron* 86.3 (2015), pp. 740–754. ISSN: 10974199. DOI: [10.1016/j.neuron.2015.03.028](https://doi.org/10.1016/j.neuron.2015.03.028).
- [293] Quanxin Wang and Andreas Burkhalter. "Area map of mouse visual cortex." In: *Journal of Comparative Neurology* 502.2 (2007), pp. 275–290. ISSN: 0021-9967. DOI: [10.1002/cne](https://doi.org/10.1002/cne).
- [294] Quanxin Wang, Olaf Sporns, and Andreas Burkhalter. "Network analysis of corticocortical connections reveals ventral and dorsal processing streams in mouse visual cortex." In: *Journal of Neuroscience* 32.13 (2012), pp. 4386–4399. ISSN: 0270-6474. DOI: [10.1523/JNEUROSCI.6063-11.2012](https://doi.org/10.1523/JNEUROSCI.6063-11.2012).
- [295] Robert H. Waterston et al. "Initial sequencing and comparative analysis of the mouse genome." In: *Nature* 420.6915 (2002), pp. 520–562. ISSN: 00280836. DOI: [10.1038/nature01262](https://doi.org/10.1038/nature01262).
- [296] Torsten N. Wiesel and David H. Hubel. "Effects of visual deprivation on morphology and physiology of cells in the cat's lateral geniculate body." In: *Methods* 26 (1963), pp. 978–993.
- [297] Torsten N. Wiesel and David H. Hubel. "Extent of recovery from the effects of visual deprivation in kittens." In: *Journal of Neurophysiology* (1964).
- [298] Torsten N. Wiesel and David H. Hubel. "Singel-cell responses in striate cortex of kittens deprived of vision in one eye." In: *Journal of Neurophysiology* 26 (1963), pp. 1003–1017.
- [299] Lasani S. Wijetunge, Sumantra Chattarji, David J.A. Wyllie, and Peter C. Kind. "Fragile X syndrome: From targets to treatments." In: *Neuropharmacology* 68 (2013), pp. 83–96. ISSN: 00283908. DOI: [10.1016/j.neuropharm.2012.11.028](https://doi.org/10.1016/j.neuropharm.2012.11.028).
- [300] Alan Woodruff, Qing Xu, Stewart A. Anderson, and Rafael Yuste. "Depolarizing effect of neocortical chandelier neurons." In: *Frontiers in Neural Circuits* 3 (2009), pp. 1–10. ISSN: 16625110. DOI: [10.3389/neuro.04.015.2009](https://doi.org/10.3389/neuro.04.015.2009).
- [301] Han Xu, Hyo Young Jeong, Robin Tremblay, and Bernardo Rudy. "Neocortical somatostatin-expressing GABAergic interneurons disinhibit the thalamorecipient layer 4." In: *Neuron* 77.1 (2013), pp. 155–167. ISSN: 08966273. DOI: [10.1016/j.neuron.2012.11.004](https://doi.org/10.1016/j.neuron.2012.11.004).
- [302] Xiangmin Xu, Keith D. Roby, and Edward M. Callaway. "Mouse cortical inhibitory neuron type that coexpresses somatostatin and calretinin." In: *The Journal of Comparative Neurology* 502.2 (2007), pp. 275–290. ISSN: 0021-9967. DOI: [10.1002/cne](https://doi.org/10.1002/cne).
- [303] Emre Yaksi and Rainer W. Friedrich. "Reconstruction of firing rate changes across neuronal populations by temporally deconvolved Ca²⁺ imaging." In: *Nature Methods* 3.5 (2006), pp. 377–383. ISSN: 1548-7091. DOI: [10.1038/nmeth874](https://doi.org/10.1038/nmeth874).

- [304] Homare Yamahachi, Sally A. Marik, Justin N.J. McManus, Winfried Denk, and Charles D. Gilbert. "Rapid axonal sprouting and pruning accompany functional reorganization in primary visual cortex." In: *Neuron* 64.5 (2009), pp. 719–729. ISSN: 08966273. DOI: [10.1016/j.neuron.2009.11.026](https://doi.org/10.1016/j.neuron.2009.11.026).
- [305] Yumiko Yoshimura, Tomohisa Ohmura, and Yukio Komatsu. "Two forms of synaptic plasticity with distinct dependence on age, experience, and NMDA receptor subtype in rat visual cortex." In: *The Journal of Neuroscience* 23.16 (2003), pp. 6557–6566. ISSN: 1529-2401. DOI: [23/16/6557\[pii\]](https://doi.org/10.1523/JNEUROSCI.2316-03.2003).
- [306] Hatim A. Zariwala, Linda Madisen, Kurt F. Ahrens, Amy Bernard, Edward S. Lein, Allan R. Jones, and Hongkui Zeng. "Visual tuning properties of genetically identified layer 2/3 neuronal types in the primary visual cortex of Cre-transgenic mice." In: *Frontiers in Systems Neuroscience* 4 (2011), pp. 1–16. ISSN: 1662-5137. DOI: [10.3389/fnsys.2010.00162](https://doi.org/10.3389/fnsys.2010.00162).
- [307] Siyu Zhang, Min Xu, Tsukasa Kamigaki, Johnny Phong Hoang Do, Wei-Cheng Chang, Sean Jenvay, Kazunari Miyamichi, Liqun Luo, and Yang Dan. "Long-range and local circuits for top-down modulation of visual cortex processing." In: *Science* 345.6197 (2014), pp. 660–665. DOI: [10.1126/science.1254126](https://doi.org/10.1126/science.1254126).
- [308] J. Julius Zhu, Yi Qin, Mingming Zhao, Linda Van Aelst, and Roberto Malinow. "Ras and Rap control AMPA receptor trafficking during synaptic plasticity." In: *Cell* 110.4 (2002), pp. 443–455. ISSN: 00928674. DOI: [10.1016/S0092-8674\(02\)00897-8](https://doi.org/10.1016/S0092-8674(02)00897-8).
- [309] Warren R. Zipfel, Rebecca M. Williams, and Watt W. Webb. "Nonlinear magic: multiphoton microscopy in the biosciences." In: *Nature Biotechnology* 21.11 (2003), pp. 1369–1377. ISSN: 1087-0156. DOI: [10.1038/nbt899](https://doi.org/10.1038/nbt899).
- [310] Pawel Zmarz and Georg B. Keller. "Mismatch receptive fields in mouse visual cortex." In: *Neuron* 92.4 (2016), pp. 766–772. ISSN: 10974199. DOI: [10.1016/j.neuron.2016.09.057](https://doi.org/10.1016/j.neuron.2016.09.057).